GAS TURBINE COMBUSTOR PORT FLOWS

by

A.Spencer

Department Aeronautical and Automotive Engineering and Transport Studies
Loughborough University

Summary

Competitive pressure and stringent emissions legislation have placed an urgent demand on research to improve our understanding of the gas turbine combustor flow field. Flow through the air admission ports of a combustor plays an essential role in determining the internal flow patterns on which many features of combustor performance depend. This thesis explains how a combination of experimental and computational research has helped improve our understanding, and ability to predict, the flow characteristics of jets entering a combustor.

The experiments focused on a simplified generic geometry of a combustor port system. Two concentric tubes, with ports introduced into the inner tube's wall, allowed a set of radially impinging jets to be formed within the inner tube. By investigating the flow with LDA instrumentation and flow visualisation methods a quantitative and qualitative picture of the mean and turbulent flow fields has been constructed. Data were collected from the annulus, port and core regions. These data provide suitable validation information for computational models, allow improved understanding of the detailed flow physics and provide the global performance parameters used traditionally by combustor designers.

Computational work focused on improving the port representation within CFD models. This work looked at the effect of increasing the grid refinement, and improving the geometrical representation of the port. The desire to model realistic port features led to the development of a stand-alone port modelling module. Comparing calculations of plain-circular ports to those for more realistic chuted port geometry, for example, showed that isothermal modelling methods were able to predict the expected changes to the global parameters measured. Moreover, these effects are seen to have significant consequences on the predicted combustor core flow field.

Acknowledgements

Help, suggestions and discussions with all friends and colleagues that have been involved with the Rolls-Royce UTC has been greatly appreciated along with the airflow lab humour. I am especially grateful to Jim for his invaluable guidance throughout this work. Thanks must go to the combustion department at Rolls-Royce plc. for useful suggestions, and along with DERA, for supporting this work. Final thanks to friends and family for your understanding and encouragement.

Nomenclature

A	area	U,V,W	mean velocity components in rectangular cartesian co-ordinates, (x,y,z)
B	bleed ratio		
C_c	contraction coefficient	u,v,w	RMS velocity components
C_d	discharge coefficient	U,V_r,W_θ	mean velocity components in cylindrical polar co-ordinates, (x,r,θ)
C_v	velocity coefficient		
C_L	lift coefficient		
CFD	computational fluid dynamics	x,y,z	rectangular cartesian coordinates
nD	n-Dimensional	x,r,θ	cylindrical polar co-ordinates
D,d	diameter	x,h,z	generalised co-ordinates
h	annulus height	α	jet injection angle
ΔH	drop in head	β	jet skew angle
HeNe	Helium-Neon	ε	dissipation of k
J	momentum flux ratio	ρ	density
k	turbulent kinetic energy		
LDA	laser doppler anemometry		
$\dot{m}$	mass flow rate		
M	momentum flux		
pdf	probability distribution function	Subscripts	
psd	power spectral density	a,an	annulus inlet
p	static pressure	b	bleed
P	total pressure	c	core inlet
ΔP	$P_a - p_c$ (liner pressure drop)	h	hole, port
$\dot{Q}$	volumetric flow rate	j	jet
R	jet to cross flow velocity ratio	L	Laser coordinates
r.m.s.	root mean square		

Contents

Chapter 1

Introduction   1

Chapter 2

Experimental Facilities and Methodology   17

Chapter 3

Experimental Results   55

Chapter 4

Mathematical Modelling   147

Chapter 5

Port Modelling   159

Chapter 6

Computational Results   **185**

Chapter 7

Conclusions   **287**

References   **293**

List of Figures

Chapter 5

Chapter 6

Chapter 7

Chapter 1

Introduction

1.1 Gas Turbine Combustors

During the last half of this century the development of gas turbine combustors has advanced gradually rather than as a result of major innovations. This is despite the 1974 fuel crisis and the environmental awareness of the 1990's, both of which could have provided the initiative for a breakthrough in combustor design and technology. One conclusion which could be drawn from this statement is that our understanding of the fundamental processes occurring within a combustor has not been developed sufficiently to make 'quantum leaps' in the field - particularly when considering the increase in combustion research each event brought. In practice, we find that manufacturers often introduce fixes to existing combustor designs to combat poor performance or meet more stringent emission regulations. For example, in order to reduce emissions from General Electric's CF6-80C2 engine, two changes have been made; the combustor head has been redesigned to incorporate more burners and the dilution holes have been 'reworked', (GE 1996). These changes represent modifications to the existing design rather than as a result of considered research into innovative combustor designs. Similar examples can be found amongst all gas turbine manufacturers, even though each invests significantly in combustor research. Indeed, there are many different currently proposed designs for low emission combustors, though they are often seen as technological risks. Again this could be considered a result of lack of confidence in our ability to predict accurately the overall performance of a given combustor design.

It is widely accepted that aerodynamics play, if not the most critical, an important role in the operation of a combustor; Lefebvre (1983), for example, states;

> *"Aerodynamic processes play a vital role in the design and*
> *performance of gas turbine combustion systems. It is probably no*
> *great exaggeration to state that when good aerodynamic design*
> *is allied to a matching fuel-injection system, a trouble-free*
> *combustor requiring only nominal development is virtually*
> *assured."*

When we look closer at the aerodynamics of a combustor it is evident that a fundamental set of flow features are present in all types of combustion systems. This is due to the primary requirements of all combustors being the same, and most of these requirements being controlled or affected by aerodynamic processes. Some of these important flow features will be the focus of this study, but before introducing them in more detail, a brief description of a typical aero-gas turbine combustor will now be presented to explain the terminology used throughout this thesis.

Figure 1.1 shows a cross-section through a contemporary combustor, as used in Rolls-Royce RB-211 engines. The pre-diffuser and dump diffuser of this design are required to decelerate the air flow supplied by the compressor. This is to prevent significant pressure losses that would be generated by high flow velocities. Approximately one fifth of this air is then allowed to pass into the combustor head (or dome) which conditions the flow to help produce a fuel spray (often cone-shaped), downstream of the fuel injector and air swirler arrangement. The remaining air flows around the outside of the combustor liner along the inner and outer annuli in order to supply the air admission ports in the combustor liner. Air is supplied to the combustion chamber for various purposes along the annuli. Some air is used to keep the combustor liner walls cool by producing a film of 'cool' air on the inside wall of the combustor liner. However, this study will focus upon the flow associated with the primary, intermediate and dilution ports which are used to generate aerodynamic zones within the combustor, which are depicted in figure 1.2. The primary ports are required to generate a region of low velocity, but highly recirculating air to produce a stable primary combustion region. The intermediate zone then serves to burn any unburnt hydro-carbons and reduce dissociation of the combustion products which can occur at certain operating conditions. Finally to reduce the outlet temperature and create a desirable exit temperature profile, the gases pass through a dilution zone. This will ensure that the turbine blades are not subjected to excessive, life reducing, temperatures.

The features described in figures 1.1 and 1.2 are common to all conventional aero gas turbine combustion systems, despite there being two distinct categories; tubular and annular. The combustor shown in figure 1.1 is an annular one, and is the favoured design for modern aero-engines. Both the compactness and the reduced pressure loss

in comparison to that of the tubular design make it the default choice. The tubular design consists of several cylindrical liners (each often referred to as a 'can') inside a cylindrical casing. Most early aero-engines employed this type of combustor, having between seven and sixteen cans per engine (Lefebvre 1995). However the tubular design, by modern standards, is considered too heavy. Despite this they are often used on industrial engines due to the ease of maintenance and accessibility. The air admission ports in the liners of both tubular and annular combustors are supplied by flow along the external annuli, and in both cases this flow is injected into a confined cross-flow. The fundamental flow processes occurring are thus common to both combustor types, and a study of the flow through the air-admission ports of one type of combustor will be equally applicable to the other.

The balance of flow split into each zone is crucial to the successful operation of the combustion chamber; if incorrect, the results can be disastrous. For example, high levels of pollutants, short combustor life, flame instability, poor relight characteristics, low life of turbine blades are just some of the problems which may result. The flow splits and strengths of recirculation in each zone are to a great extent determined by the positioning and relative sizing of the primary, intermediate and dilution ports, although swirl introduced via the fuel injector also plays a role. Furthermore, the way the flow is fed to the ports determines the velocity profiles of the jets issuing from them. Obviously for a designer to stipulate an initial design he must have good understanding of how jet characteristics will effect the important internal flow patterns. This can come from three main sources; experience, experimentation and computational models.

Combustor design is often referred to as a 'black art'. This is because experience still plays the main role in the preliminary design of a combustor. Experimentation then supplies some of the basic empirical rules to aid a more detailed design. Further development of the combustor is then facilitated by an overwhelmingly experimental study. Computational modelling is being used more frequently, but Computational Fluid Dynamics (CFD) methods are still unproven where highly turbulent, recirculating flows are concerned, as found in a combustion chamber.

1.2 Previous Work

Work reported on combustor aerodynamics has usually focused on either the internal or external flow fields around a combustor liner. Very few, either experimental or theoretical, have focused on coupled internal and external flow fields. Indeed, little is reported about the external (annulus) flow field when compared to that reported on internal flow fields.

Many investigations of jets in cross-flow have been reported, which are relevant to internal combustor flow fields. This review will therefore briefly focus on jets in cross-flow to highlight the important and influencing flow features created by jets injected into a combustion chamber. It will then look at investigations of geometry that is more realistic and typical of gas turbine combustors, much of which in recent years has had an emphasis on modelling the flow field. Finally a look at publications of direct similarity to the present study will follow.

1.2.1 Jets in cross-flows

Jets in cross-flow can be found in many engineering applications, and have therefore received a substantial number of investigations. Indeed, whole conferences have been dedicated to studies of them. For example, in the proceedings of: "Computational and Experimental Assessment of Jets in Cross-flow" (AGARD 1993) forty relevant pieces of work are presented, e.g. (Margason 1993). This is an indication of how important jets in cross-flows are to many engineering applications. Much of most recent work is biased toward establishing the most appropriate computational modelling techniques for the various applications of jets in cross-flow. Typical areas where the phenomenon occurs are: Vertical/Short Take-Off and Landing (VSTOL) aircraft applications, effluent discharge from chimneys into the atmosphere, certain film cooling arrangements and in combustion chambers. Each application has its own complications to that of an idealised jet in cross-flow, e.g. compressibility, buoyancy and thermodynamic effects respectively. For the case of combustion chambers, the aerodynamic complication arises due to the jets issuing into a confined cross-flow, creating regions of jet impingement and interaction with other jets or walls.

A comprehensive experimental study into jets in cross-flows was carried out by Andreopoulos and Rodi (1984). This work presents information on the flow field around a circular jet issuing normally into a cross-flow at velocity ratios (jet to cross-flow), R, of 0.5, 1.0 and 2.0. Measurements of all three mean and fluctuating velocity components were taken, thus allowing a three-dimensional picture of the flow field to be constructed along with information on the nature of the turbulence field and shear stresses. Although these low velocity ratios are more relevant to film cooling, this work is mentioned here to illustrate the nature of the flow field around a single jet in a cross-flow. Figure 1.3 is taken from Andreopoulos and Rodi (1984); it shows a circular jet penetrating into a quasi semi-infinite cross-flow, with R = 2.0, a ratio typical of a combustor's dilution jets. Since the jet presents itself as a blockage to the free stream flow, a force is exerted on the jet. This force deflects the jet such that the further the jet enters the cross-flow, the closer its core is aligned to the mean free stream flow. The cross stream flow is deflected around the jet, particularly in the near wall region, creating a wake of two co-rotating vortices; similar in nature to those of a Von Karman vortex street. Rather than being shed however, they are entrained by the jet and form what are known as bound vortices. It is this vortex pair that forms the characteristic kidney-shaped cross-section that develops in the downstream jet core. The shear layer and the generated vortices create the favourable mixing conditions which makes this jet configuration suitable for dilution ports where the hot cross-flow needs to be diluted by the colder jet flow.

Some workers have attempted to describe the nature of a jet by investigating the trajectory of its locus of maximum velocity (e.g. Platten and Keffer 1971). For the case of heated jets other workers define the jet trajectory by the locus of extrema in temperature (e.g. Ramsey and Goldstein 1971). The correlations found to fit these loci are noted to be strongly related to the momentum flux ratio, J, $(J=\rho_j V_j^2/\rho_{fs} U_{fs}^2)$, as expected the higher the free stream momentum flux in relation to that of the jet, the more the jet will be deflected. A small dependence is found on the density ratio for the case of a heated jet, hence there is some difference between the correlations for the loci defined by the extrema in temperature and the extrema in velocity.

A more relevant and physically meaningful characterisation was performed by Srinivasan et al. (1982,1984,1985). Here the study was of jets issuing into a confined duct carrying cross-flow, again using simplistic geometry (a rectangular duct of constant cross-section) but of proportions and flow conditions similar to those found in a combustor. Srinivasan et al. again used the definition of the locus of extrema in temperature to investigate the jet trajectory but also looked at the temperature distribution on a plane downstream of the jet. This is of prime interest to combustion engineers as it indicates the level of mixing generated by the jet - a uniform temperature profile downstream from a heated jet indicates complete mixing. When the jet issued into a confined duct it was found that the jet was deflected more than in the case where it issued into an infinite domain for the same flow conditions. This is as expected since there will be some interaction between the jet and the opposing wall. An additional complication is introduced when two opposed jets impinge, and the correlations mentioned above for non-interacting jets will be invalidated. Sivasegaram and Whitelaw (1986) looked at rows of opposing jets using flow visualisation techniques to establish the effects of slight mis-alignment of jets and unequal jet velocities. It was found with only small mis-alignments substantial flow asymmetries were produced. Moreover a numerical investigation by Quick et al. (1993) found that there is a physical unsteadiness when two opposing jets collide. This unsteadiness was observed to have a time scale comparable to the ratio of the square of the duct height to the square root of the jet momentum flux J. This was seen as a periodic oscillation in velocity near to the impingement point. Experimental evidence showed an unsteady aspect to the flow but did not indicate any dominant frequency. High levels of turbulence in the experimental investigation were found to partly mask the underlying periodic oscillations in the pseudo mean flow. It is, therefore, noted that the interaction of two jets can lead to complex phenomena; high levels of turbulence, recirculation, unsteady/periodic flow conditions. A comprehensive review of jets in cross-flows can be found in Margason (1993).

One common feature of the above work is that all authors have attempted to produce or model a jet or jets with uniform exit conditions. No work has been found which focuses on the effect of variations in the jet exit characteristics at this fundamental level. Typically for a combustion chamber, and many other applications, the jet will

exhibit characteristics formed in the supply route to the jet exit plane. For example, higher velocities will be found toward the centre of the port, and the jet will enter at an angle due to the cross-flow momentum of the supply air. This problem is addressed to some extent in the work summarised below, but due to the additional geometrical complexities it is difficult to understand the full implications of realistic jet representation in isolation.

1.2.2 Combustor Aerodynamics

Many of the aerodynamic investigations reported on internal combustor flows have been concerned with computational modelling with some associated experimental findings to validate the models. Coupland and Priddin (1986) combined a standard turbulence model with a combustion and emission model to predict the flow field, turbulence levels, exit temperature profile and NO_x emissions from a production combustor. The k-ε turbulence model of Launder and Spalding (1974) was found to be adequate for predicting what was reported to be a pressure-driven core flow field. This was found, in part, to be due to the high degree of interactions occurring between the jets, recirculation zones and swirl dominating the flow pattern. The predicted flow field for both isothermal and combusting cases agreed well with the water analogy experiments used for validation of the predictions. This supported the now common practice of using water flow testing as a means of developing combustors. The flow splits entering the combustor had to be determined in order to specify the boundary conditions for the calculation. This was done by using a 1D model for the external combustor flow. The method is described by Lowe(1994) but its basic methodology will be outlined. A description of the annulus cross-section is provided to allow the flow area at each axial location along the combustor to be calculated. By using empirical airflow correlations for the various air-admission ports into the combustor a prediction of the mass flows and pressure drops may be obtained for each port. The advantage of this method is that it can quickly estimate the expected flow splits of a given geometry. The disadvantages are that the method provides limited detail of the jet characteristics, allows for no coupling between the internal and external flow field and relies heavily upon empirical correlations. For example, port discharge coefficients, C_d, (the ratio between the actual mass flow and ideal mass flow which

would pass through a port), have to be estimated from empirically found relationships. It is well known however (Hay and Spencer 1992) that very small geometric variations of a port can bring about quite large changes in its C_d. Under certain operating conditions it is known that undesirable flow features also occur, particularly in the form of port vortices, as noted by Carrotte (1990b), Baker (1992b), Doerr (1995), Lowe (1994) causing a significant reduction in the C_d of the port. Obviously, it is difficult to include this unpredictable behaviour within empirical correlations used by the 1D method.

To address part of this problem, Karki (1990) described a method to allow the diffuser and combustor flow to interact. However, this interaction was facilitated by communicating the mass flow splits between separate calculations of a simplified 2D axis-symmetrical model of the annulus flow and a full 3D model of a combustion chamber. Several iterations were performed until the mass flow splits between each of the ports were consistent with each of the pressure fields. Although this method provides a crude coupling of the internal-external flow, no detail of the jet entry velocity profile into the combustion chamber can be evaluated. Properly coupled calculations will be discussed in the next section, but provide the only method of generating port exit profile information and allowing true coupling between the internal and external flow. An alternative approach adopted by Shyy (1988) was to use experimental data to specify the combustor inlet conditions. Five hole probe data was used to specify the port velocity profiles on curvilinear body fitted (and port fitted) grids. Unfortunately the grid resolution around the ports was low such that any profile was only crudely represented. This method, with increasing grid resolution and with accurately measured boundary conditions, is ideal for predicting the internal flow, but there is a significant overhead required in generating the necessary experimental data for each and every combustor geometry. Furthermore, modifications to the combustor liner may also affect the external flow distributions such that further experiments may be required. In this sense, also, the calculation is uncoupled. Again, Shyy verified that the k-ε turbulence model was adequate for predicting the overall flow field and exit temperature pattern characteristics. Shyy concluded that the detailed information yielded by this method was useful to help understand, explain and parameterise the interactions among the many variables within the combustor. No indication is given in

this work, however, on the effect of increasing grid resolution, particularly around the port region. Substantial effort was made to obtain the jet velocity profiles for this work but no indication was given of how important these were to the global flow field.

Numerous publications report work on modelling the internal flow of either the full, or dilution zone of realistic combustors. But other than the work of Shyy et al., the geometrical representation of the port has been accomplished by using a crude castellated approach. This is where a rectangular grid is used, and by declaring certain boundary cells as blockages and others as part of the jet exit, a 'castellated' approximation to the hole shape is formed. This method was used by Coupland & Priddin (1986), as previously described, along with McGuirk & Palma (1992), Jones et al.(1989), Koutmos & McGuirk (1989) and Lin & Lu(1993). Beside the obvious poor port geometrical representation, care has to be taken in sizing the port to give the correct open area of the port exit plane. This body of work on the internal flow calculations is also often short of detailed experimental validation data. One reason for this is the expense involved in generating data sets for detailed configurations, in terms of both model construction and actually making measurements in often inaccessible regions. This also accounts for very little information being available for reacting combustors, despite production tests being regularly carried out. With the additional problem of extreme temperatures, few detailed quantitative measurements have been reported in open literature.

To reduce the divide between the flexibility of modelling techniques and the relative expensive experimental approaches, a simplified geometry is required to allow detailed measurements to be made against which models can be bench-marked, before being applied to realistic combustor geometry.

Bicen et al. (1989) report experiments on a geometry generic to can-type combustors. The model contained just enough complexity to represent the main features of a combustor including a swirler-driven primary zone and two rows of radially inflowing jets. The model was constructed with plexi-glass and water was used as the working medium, which allowed laser doppler anemometer measurements to be made to obtain details of the velocity and turbulence fields. A similar generic geometry was also

investigated by McGuirk & Palma (1992) (the same geometry used by other workers for combusting studies) to make further measurements of a turbulent flow field along with higher order moments of the velocity probability distributions. The data obtained indicated flow unsteadiness generated by jet instability, with frequencies within the range of 10-150 Hz at the primary jet impingement. Also the dilution jets exhibited an unsteadiness in penetration depth with a frequency of 7 Hz. The fundamental cause of this instability is unclear but agrees with the work by Quick (1993).

The work described so far has been on either simplified jets in cross-flow or, complicated combustor-like geometry. In order to look solely at the port flow characteristics found in combustion chambers, some workers have simplified combustor geometry further to provide a link between these two approaches, removing effects due to complicated geometries whilst retaining the important flow characteristics not studied in the more fundamental jet in cross-flow approach.

1.2.3 Annulus/Port Flows

The previous sections have described work performed without explicitly including the annulus flow field in either the modelling or the experimental work. The similar experimental setup of Koutmos and McGuirk (1989) and McGuirk and Palma (1992) is one exception to this, where the combustor's air admission ports are fed from an annulus containing cross-flow. However the two rows of ports are each fed from a separate annuli, such that there can be no interaction between the primary and dilution ports. This final review section will therefore focus on work reported which looks at the coupled behaviour of the annulus and core flows.

Manners (1987) provided one of the first computational studies of coupled internal and external flows. The geometry which was modelled is shown in figure 1.4. A rectangular domain allowed an orthogonal mesh to be easily fitted to the geometry, except around the half-port, which was approximated by a castellated grid as previously described. Mass flow splits were set to produce flow scenarios typical of both primary and dilution jets. Both the standard k-ε and second moment closure were used for the turbulence model, though each gave kinetic energy levels an order of magnitude different. As no experimental data was available, it is difficult to say which,

if either, was the correct result. Manners concluded that some of the features of the flow field which depend primarily on the relative momentum of the flow streams are not sensitive to some degree of numerical error. For example, the initial angle of the jets, the overall trajectory of the jet and, to a degree, the pressure drop across the combustor were in agreement with those predicted by the 1D model mentioned earlier. However, features such as the exit temperature traverse may not be correctly predicted due to the accumulation of numerical errors involved. Although Manners adopted the castellated hole approximation in the rectangular grid, by the same method, he was able to represent a plunged port. This change in shape of port from a plain to plunged hole, even though very crudely modelled was seen to have a strong influence on the behaviour of the jet as expected.

In the Ph.D. thesis by Merdjani (1989), a body of work is described involved with the investigation of jet mixing in an isothermal model of a gas turbine combustor dilution zone. This work involved both an experimental and computational approach to help examine the flow physics. The test geometry comprised a pipe flow with eight radially inflowing jets supplied by an annular manifold containing cross-flow. Some of the air in the manifold was bled past the jet entries and exhausted through the jacket of the manifold. An automatic traverse mechanism allowed probes to be introduced into the inner core region from a mounting position further downstream. A comprehensive mapping of the flow field in radial planes was carried out - with five hole probes being used for the mean velocity field and triple hot wire anemometers for the turbulence field. Jet to core flow velocity ratios, R, from 2 to 5 were tested with predominately no annulus bleed. The experimental results suggested the existence of a toroidal recirculation upstream of the jet impingement for R greater than or equal to 4. However, the intrusive nature of the probe meant that measurements could not be made in back flow regions. Indeed, high yaw angles onto the probes, particularly at the jet inflow, may have introduced significant errors in the results. Merdjani also reported flow asymmetries in the supply annulus and had to introduce splitter plates to ensure each of the 8 jets had equal mass flow through them. No measurements could be made in the annulus or at the port exit, therefore little could be said about the cause of the asymmetry. For Merdjani's computational study, a symmetrical sector of 22.5° was modelled. A flat jet profile was imposed at the jet boundary and this feature was

blamed for poor results at high jet to core flow velocity ratios. The experimental results had pointed towards a significantly anisotropic turbulence field which the k-ε turbulence model could not resolve, and was blamed as contributing towards poor agreement between the computational and experimental studies.

Baker (1989, 1992) again considered isothermal flows in both simplified geometry, similar to that of Merdjani(1990), and a more realistic 'can' combustor configuration. An emphasis was placed on studying the internal/external interaction of can-type combustors and the turbulence closure used for the turbulence modelling. The experimental approach was to use water as the working medium to allow non-intrusive LDA measurements to be made - with optical access achieved by constructing the models with plexi-glass. The effects of varying the annulus height were studied with the simplified geometry, whilst also providing CFD validation data. Problems were encountered when investigating the flow in the can combustor. It was noted that the second row of jets penetrated the core flow more strongly than expected. This was thought to be due to the isothermal model not matching the volumetric expansion that occurs upstream of the dilution jets in the reacting case, which tends to deflect the jets further. The numerical work focused on comparing the k-ε and Reynolds-Stress turbulence models, applied to initially simple flow problems, building up to modelling the flow in a 3D combustor. It was found that the k-ε model performed satisfactorily when predicting the flow field, and the Reynolds Stress model under predicted the turbulent kinetic energies expected. It was also concluded that improving the boundary conforming abilities of the computational grid would have significant benefit which would outweigh the subtleties involved with turbulence modelling. In addition to realising the need to improve the feature resolution, it was found advisable to include the annulus in the flow calculation to allow good representation of the jet profile at entry to the combustor.

1.3 Objectives

Analytical methods of predicting the annulus port flows found in combustion systems are, at present, crude in their representation. Design procedures in the gas turbine industry often employ 1D empirical formulae to predict the flow splits between various

ports, jet trajectories and mass flows. These may be determined with some accuracy but jet velocity profiles can only be approximated. The overall objective of this study is therefore to investigate the effect of hole geometry, annulus hole interactions and assess appropriate numerical methods to calculate such flows. Detailed information on velocity profiles and turbulence distribution for the flow field is to be gathered to enable more accurate calculations of future combustor designs to be performed. An experimental investigation in parallel with this work will not only provide validation for the theoretical predictions but also indicate important flow regions in the annulus/ port flow which need to be predicted to ensure a correct overall picture may be obtained.

1.4 Structure of Thesis

The experimental and computational work reported in this thesis will remain separate until the final chapter where the conclusions and recommendations for further work are discussed.

The experimental investigation will be described in chapters 2 and 3. Chapter 2 focuses on the experimental apparatus and techniques used as part of this study. Results will be presented from the commissioning of the test rig designed and built for this study. Also the preliminary work will be discussed which allowed the main test matrix to be specified. Chapter 3 then presents and discusses all of the new data obtained from the main test programme.

Chapters 4, 5 and 6 will discuss the computational work performed. Chapter 4 introduces the modelling concepts which underpin the computational study carried out. Chapter 5 describes the development of port modelling techniques which were necessary in order to complete the computational study. Chapter 6 will then describe the results of the computational work undertaken. Where appropriate these results are compared to those of the experimental study.

Finally chapter 7 will re-iterate any conclusions drawn from the results of this work and make recommendations on how this field of knowledge may be further expanded.
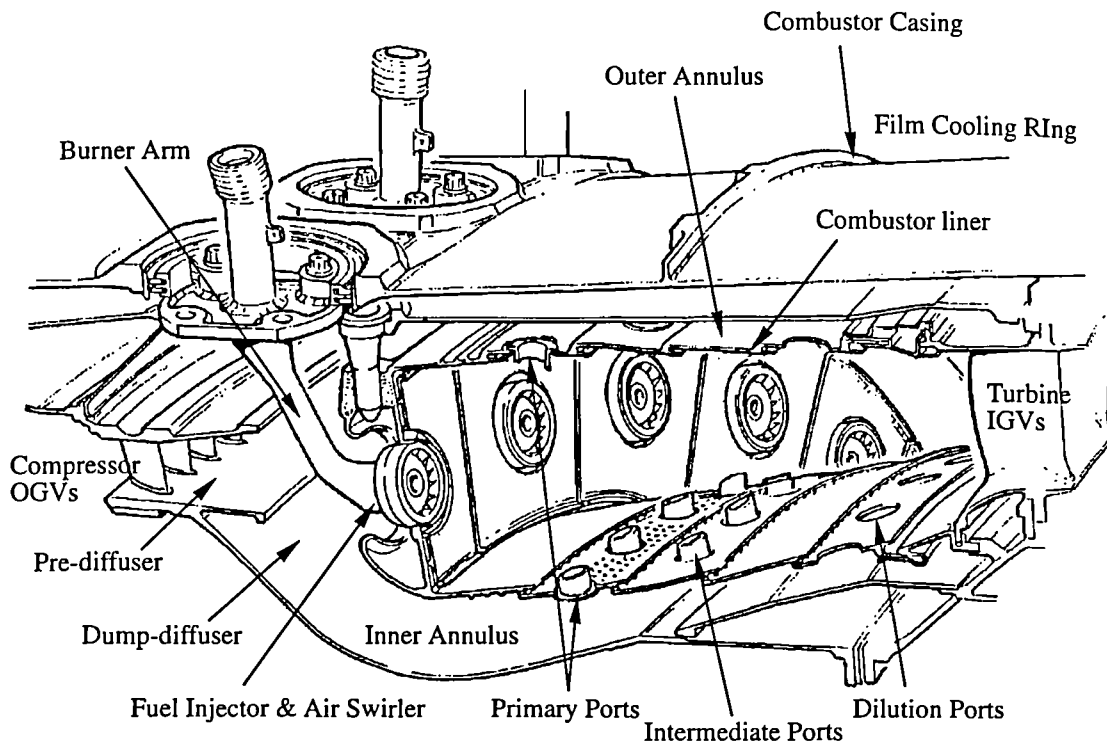
Figure 1.1 Annular Combustor Typical of Current Rolls-Royce RB211 Engines.
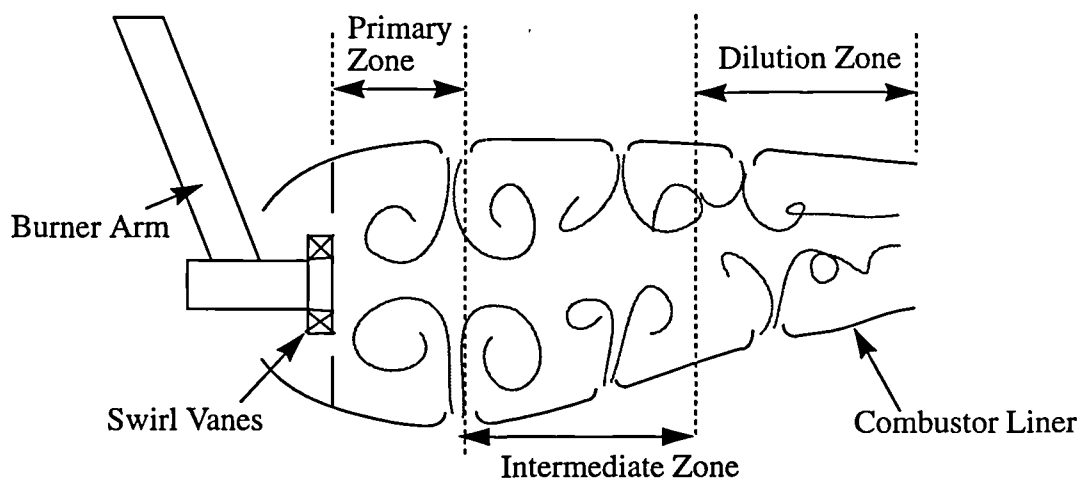
Figure 1.2 The Aerodynamic Zones of a Combustor
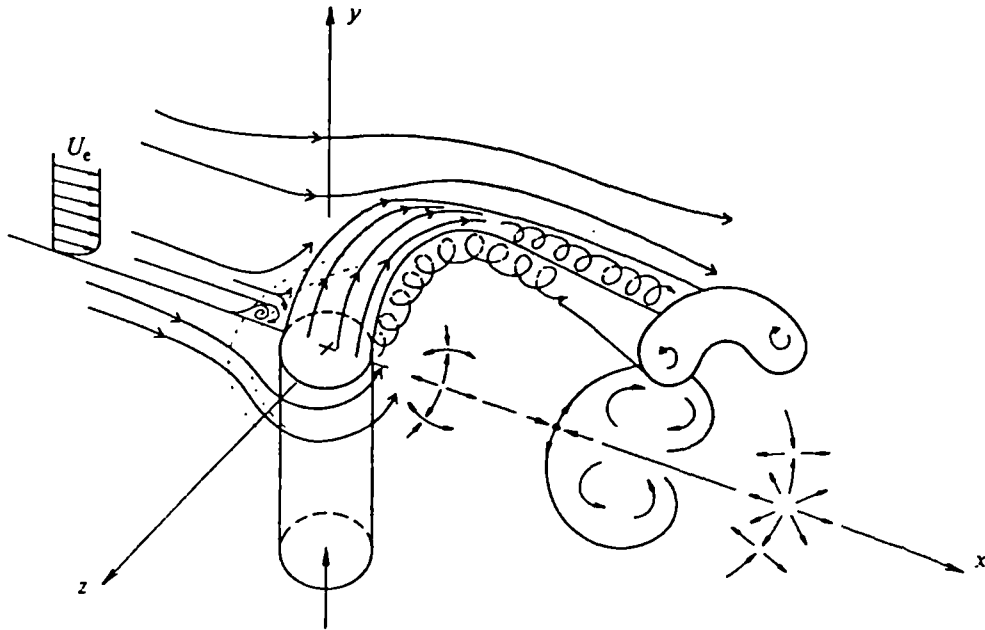
**Figure 1.3 Flow Development of a Jet Issuing Into Cross-flow
from Andreopoulos (1984)**
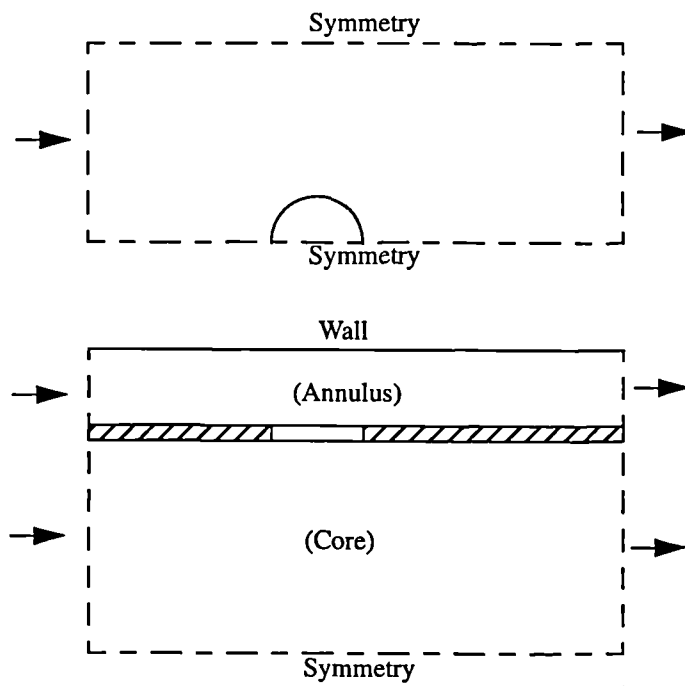
Figure 1.4 Coupled Annulus/Core Geometry Modelled by Manners (1987)

Chapter 2

Experimental Facilities and Methodology

2.1 Introduction

Annulus/port flows, in isolation, have received little experimental investigation; as a result there is only a small amount of available data with which CFD predictions can be compared and validated, e.g. Baker (1992) and Merdjani (1989). High quality experimental data is vital to code validation exercises, so that the CFD calculations can be quantitatively assessed, and also to indicate the important flow characteristics that should be predicted by computational models. Not only is the data valuable for CFD validation but also for combustor designers who wish to design away from the undesirable flow conditions described in the previous chapter. Despite the knowledge that undesirable flow conditions do occur in the feed annuli of both test rigs and combustors alike, no work has been reported which explains how they are formed. It is also widely accepted that the annulus and core flows interact, Close (1991), but little is understood of the mechanisms by which this occurs, and whether through port vortices are one of these mechanisms.

In order to address the points made above an experimental program will be presented which had the following aims;

- generate a data set of velocity and turbulence measurements for validation of CFD predictions.

- make detailed measurements of important flow areas, such as jet exit profiles including details of the turbulence field.

- take measurements of global performance parameters which have been traditionally used by design engineers, e.g. the discharge coefficient.

2.2 The Test Rig

The experimental facility to be described was designed and built at Loughborough as part of this study. It was based upon the facilities used by Baker(1992) for his experimental investigation of annulus/port flows, i.e. an isothermal, vertically flowing, constant head, water flow rig. However, several significant changes have been introduced to improve flow controllability, optical access and maintenance.

The approach velocities in the annulus of a combustor are typically of the order 10m/s and up to 150m/s through the principle air admission ports, Boyce (1995). At a temperature of 400° C this converts to a jet Mach number of just below 0.3. At Mach

numbers around 0.3 and below it is common practice to ignore the effects of compressibility. Given this, water has often been chosen as the working fluid to facilitate the measurements of previous workers. For example, Coupland and Priddin(1986) supported the use of water analogy as a useful tool in understanding the flow field of a combustor. Since this work, water has been used in numerous other combustor studies, e.g. Baker(1992), Koutmos(1989) and Stull(1985). Water was also chosen as the working medium for this study, allowing a purely aerodynamic study to be conducted, neglecting any effects due to heat transfer and compressibility. Employing water also has additional advantages. Firstly, domestic water has a naturally high particulate concentration suitable for laser doppler anemometer (LDA) measurements, the primary measurement method for this study. Thus the use of additional 'seeding' material can be avoided. This high seeding concentration results in favourable signal to noise ratios, increasing the validated data rate of the system, see Turner(1990). Secondly, water allows gravity to be used as a stable driving force. A pump's delivery rate will vary with time, so the variations are eliminated by the overflow branch of the system, with the result that the mass flow through the working section can be kept constant over very large periods of time. Finally, with practical considerations in mind, low speed flows in geometry of manageable scale can be used to create Reynolds numbers close to those found within combustors.

A pipe network algorithm was used in the initial stages of design to enable choices of pipe sizes which would give the desired flow rates with acceptable pressure losses. The algorithm also confirmed that the head available by placing the header tank below the ceiling of the laboratory was sufficient to provide the required mass flows. Baker (1992) described problems setting up the desired mass flow rates through his rig with only three valves. However, use of the pipe network algorithm provided an understanding of how the rig could, in theory, be controlled and set to a specific flow condition using only three valves, and perhaps explain why problems had been previously experienced. This explanation will be left until section 2.6, when the reader has a better understanding of the rig layout.

Figure 2.1 shows a schematic of the rig, it will be described here by following the water through a circuit of the rig (bracketed letters in this description refer to the key

for figure 2.1). Water is pumped to the header tank with a 1.7kW pump (P), though there is a bypass valve which allows water to be returned to the sump tank (D). This ensures the pump can be started under a low load, and also be run at a low load if only a small delivery flow is required to the header tank. The supply flow rate to the header tank is adjusted, using valves D and E, to ensure there is a constant spillage over the overflow divider in the header tank, providing a constant header tank water level (13). This level was monitored with a water level indicator, fitted with an alarm to help prevent possible spillage.

The remaining flow can then either flow down the core pipe or the annular gap between the core pipe and the outer pipe to the main test section of the rig. A flow restricting mechanism in the header tank allowed the inlet mass flow split between the annulus and core to be controlled (J). At entry to these pipes, flow straighteners (I), were used to prevent any possible swirl velocity component being transported into the test section. The water then flows vertically downwards through 1.6m of tube, (this represents 18 core pipe diameters or 53 annulus heights) to the working section. After the annulus and core flows interact at the working section, they are channelled back to the sump tank separately as core and annulus return flows. This is accomplished by a small manifold, H, at the bottom of the vertical piping which separates the outer and inner pipe flow paths.

Control valves, (F&G), in the annulus and core return flow pipes allow the mass flow through each to be set. With these set, the total mass flow through the test section is determined. The pressure drop across two orifice plates (O - made to BS1042), are measured in the return pipes with inverted water manometers to allow the annulus and core return mass flows to be calculated. Finally, all flows returning to the sump tank and the supply to the header tank are filtered using fine mesh bags to remove any debris forming in the system.

2.3 The Test Section

The working section is shown in detail in figure 2.2. It comprises of two circular pipes 600mm long, the inner one being held concentric with the outer at each end via a set of NACA 0015 struts. The inner pipe contains the ports approximately half way along its

length. Unique to this rig is the ability to rotate the inner pipe. This ability allows the exploration of more of the flow field than possible on the previous annulus/port flow rig of Baker (1992). The lower struts connect the ring gear situated in a sealed flange to the bottom of the inner pipe. Which, by turning a worm gear, allows the inner pipe of the test section, along with the support struts, to be rotated. This removes the need to be able to rotate the laser about the axis of the two pipes to measure velocities on different azimuthal planes: a practice which would introduce further difficulty since the wall of the water jacket would need to rotate with the laser. (section 2.4.2 describes the optical setup in greater detail). Instead, the inner pipe is rotated, hence offering a different azimuthal plane to the optical axis of the laser. Both upper and lower bearings were constructed from two brass rings, as detailed for the upper bearing in figure 2.2. This had to be done for several reasons; to provide a close tolerance fit for the bearing surface - which could not be done with perspex, to keep the perspex circular and to provide the strength necessary to support the struts. Each of the brass rings was spiggoted and pinned to the perspex pipe, such that both the lower and upper struts rotated with the inner pipe. The whole of the working section is encased in a square acrylic jacket filled with water to reduce refraction effects at the air-acrylic interface, which is standard practice, Bicen (1981), ensuring that the optical axis is perpendicular to the outer wall of the jacket. This perpendicularity would have been difficult to maintain had the laser rotated about the rig.

The test section is designed such that the inner pipe can be quickly exchanged; the two pipes are split at the upper flange of the working section, (A), then the lower part of the rig is slid sideways along guide rails such that the inner pipe can be lifted out and replaced. Four test sections were used for this study: the first was blank with no ports, the remaining three each had six ports equi-spaced around the core tube. One with circular ports, one with D shaped ports and one in which the circular ports had chutes, shown in figure 2.3. The diameter of the ports was chosen to be large compared to the control volume of the LDA system (minor and major axis of approximately 1 and 3mm).

A final variable in the rig geometry was the ability to introduce swirl in the annulus by replacing the upper support struts with a set of swirl vanes. Fifteen NACA 65-8 10

(thickened) vanes were used to produce approximately $15°$ of swirl, figure 2.4. These vanes were designed by Carrotte(1994) as IGVs for a full annular combustor model.

The coordinate systems and nomenclature adopted in the experimental work are depicted in figure 2.5. Cylindrical polar co-ordinates were used for referencing the control volume position and velocity vector, (x,r,θ), as shown. For convenience the laser position was described by rectangular cartesian co-ordinates, (x_L,y_L,z_L), which were aligned with the traverse directions of a milling table on which the optical bench was mounted. The origins were aligned such that $x_L=y_L=0$ when $r=0$ and $x=z_L=0$ at the centre-line height of the 6 ports. Some co-ordinate conversion was therefore necessary in order to relate laser co-ordinates to rig co-ordinates. $\theta=0$ was taken in the negative x_L(laser optical axis) direction, increasing in the standard right handed sense about the x (rig centre-line) axis. Five mass flows have been included to illustrate the subscript definitions chosen for each station; **c** - core inlet, **an** - annulus inlet, **j** - jet, **o** - core outlet and **b** - annulus bleed.

2.4 LDA Instrumentation

2.4.1 Laser Doppler System

A one-dimensional Laser Doppler Anemometer (LDA) system was used as the main, non-intrusive interrogation method. The LDA system could be used in either differential forward scatter or back scatter modes, see figure 2.6 for a diagram of the apparatus setup. Forward scatter mode was adequate for most measurements, offering high data rates, though in certain situations back scatter mode was more convenient. The advantage of backscatter mode is that the receiving optics do not need altering once they have been setup since they are common with the transmitting optics. Therefore, when traversing the laser through regions of substantial refraction, constant re-alignment of the receiving optics is not required. The disadvantage of this method though is that additional seeding material is required in the form of latex spheres or TiO_2. Even with the additional seeding data rates were still found to be an order of magnitude less than when operating in forward scatter (data rates of 2kHz compared with 20kHz).

An optical bench with rigid support for the laser and photo multiplier was secured to the top of a milling table traverse mechanism to give three axes of movement (x_L, y_L, z_L). To remove possible errors due to backlash in the gearing, two digital position indicators were used. These were fixed to the milling table to display x_L and z_L with an accuracy of ± 0.01mm. It was found difficult to mount successfully a digital indicator on the y_L traverse, as it was sandwiched between the other two traverse mechanisms. A mechanical dial test indicator was therefore used to locate the y_L reference point at the end of each traverse in this direction to eliminate any backlash effects. An additional axis of movement was provided by the ability to rotate the test section about its axis.

To set the control volume to the origin of the rig co-ordinates, a light sensitive diode, shown in figure 2.6, was used. The photo-multiplier was replaced by the diode so that as the control volume passed through a perspex/water interface the light flare produced would be indicated by the meter. An accuracy of around 0.2mm was achievable when locating this point, depending on the surface quality. If the perspex surface was scratched, for example, then the flare could saturate the meter before the peak value of light being reflected was obtained. Firstly $y_L = 0$ could be found by bisecting the two points at which the laser beams glanced off each side of the inner pipe across its diameter. This point is the same whether the laser beams are orientated vertically or horizontally with respect to each other. $x_L = 0$ could then be found by the same method, though this time the control volume will cross the interface normally as it traverses it in the x_L direction. In this case the laser must be in the orientation it will be used in to take the measurements. $z_L = 0$ could then be found by adjusting both the x_L and z_L position of the laser until one beam glanced off the top of a port and one beam glanced off the bottom of a port whose axis was in line with the optical axis. At this point the laser could be rotated in its mounting and the beams should trace the perimeter of the circular port.

A Uniphase 20mW He-Ne laser was used, along with a Dantec 55X optical system to generate the control volume at the beam intersection, as shown schematically in figure 2.6. The photomultiplier used had a pre-amplifier built in which allowed it to be used

in both forward and back-scatter modes. The characteristics of the optical system are given in table 2.1.

Table 2.1 Laser Characteristics

Property	Value
Power Output	20mW
Wavelength	632.8nm
Diameter of beam at $1/e^2$	0.68mm
Half angle of beam intersection	5.53^o
Minor axis of control volume	0.30mm
Major axis of control volume	3.12mm
Fringe spacing	3.28μm
No. Fringes	46

The error introduced because of statistical uncertainty in calculating the mean velocity, U, from N randomly sampled data is given by Yanta, (1973) as:

$$\text{error} = \frac{1.96\sqrt{u^2}}{\sqrt{N}} \frac{}{U}$$

where u is the fluctuating component about the mean. Enough samples were taken to keep the error below 4%. However, with high levels of turbulence occurring and potential flow unsteadiness, it was also often necessary to ensure the data was collected over a time period significantly greater than the period of oscillation, in order to capture all of the frequencies associated with the flow. This was done by accepting a predetermined number, N, of samples at a given rate, rather than accepting the first N samples measured.

The other errors associated with making LDA measurements had a negligible effect on the error compared to that produced by the statistical uncertainty. For example, broadening of the probability distribution function due to velocity gradients, was found to introduce a maximum of 0.1% error to the measurements for the expected flow field. Corrections for broadening of the probability distribution function were therefore not used for this study.

2.4.2 Optical Corrections to LDA Measurements

When using a laser doppler anemometer to measure the fluid flow inside an acrylic test rig the laser beams are refracted as they pass through fluid/acrylic interfaces. It is necessary to make corrections to account for this, since refraction may change the position, orientation and the fringe spacing of the control volume. The physics of refraction at optical interfaces (i.e. where there is a change in refractive index) is well known and described by Snell's law, Durst (1976). Equations have been derived to allow positional and velocity magnitude corrections to be made to LDA measurements taken from inside a single cylinder and reported by several authors, Bicen (1981) and Boadway and Karahan (1981). A set of twelve equations is presented in Bicen (1981) which describe three correction factors for four recommended orientations of the laser. Two of the corrections evaluate the positional shift of the control volume in the radial and circumferential directions and, the final one, the velocity correction factor. The four orientations of the laser are suggested because the trigonometrical analysis is simplified, and these are depicted in figure 2.7. In this study, when measuring inside the core region (through two cylindrical walls) or in the far annulus in which the laser needs to pass fully through the core pipe (through three cylindrical walls) these equations will not apply. Moreover, it is possible in certain orientations that one beam may pass through the wall of the inner pipe but the other through a port. In order to understand and correct for the optical effects of having two concentric tubes, a simple ray tracing program was written. The program uses three dimensional vector analysis to trace both beams through the specified geometry. To verify the program, a comparison was performed, shown in figure 2.8. In this figure, Bicen's equations for the radial and azimuthal correction factors when measuring the radial velocity are compared to the ray tracing algorithm's results for an identical arrangement.

An advantage of using a general computational method is that it can calculate the correction factors required when the control volume is not on the optical axis or on the diameter perpendicular to it, impossible to do with the trigonometric equations described. A further benefit of this approach is that it allows the laser coordinates (x_L, y_L, z_L) to be found necessary to interrogate specific rig coordinates (x, r, θ). This is done by applying the algorithm in an iterative process, by specifying the required laser

beam intersection point and then repeatedly optimising the laser head coordinates until the control volume is calculated to be at the required location.

Figure 2.9 shows an example of the results of this iterative ray tracing method to find the laser coordinates necessary to interrogate a particular point within the flow. It proved impossible to measure the port exit radial velocity profile directly, due to the large refraction of the laser beams indicated in figure 2.8 as R_i is approached. At positions where there are large refractions of the beams, not only is the positional shift important but the fringe spacing in the measurement volume become highly distorted. This is further emphasised by examining the loci A, indicated in figure 2.9, close to the inner wall of either of the tubes. The loci is of the control volume when making radial velocity measurements on the axis perpendicular to that of the optical axis, for the rig geometry. To combat this it was proposed to measure the port exit radial velocity at $\pm 45^\circ$ to the radial component, and then calculate the radial component from these two values (this calculation method is described in the next section). However, to do this required making measurements at an angle of 45° to the optical axis. By employing the above, iterative, method the ray paths shown, B_1 and B_2, were calculated, hence giving the required laser position.

2.5 Data Reduction

2.5.1 Calculating the Port Exit Velocity Profile

As described in the previous section, the port exit radial velocity could not be directly measured. However, by measuring the mean and r.m.s. velocities at $\pm \theta^\circ$ to the radial component, $V_{+\theta}$, $v_{+\theta}$, $V_{-\theta}$ and $v_{-\theta}$, and the circumferential velocities, W and w at the

same point, the radial velocity, V, the radial normal stress, vv, and the radial-circumferential shear stress, vw, can be evaluated from the following relationships;

$$V = \frac{\left(\overline{V_{+\theta}} + \overline{V_{-\theta}} \right)}{2\cos\theta}$$

$$\overline{v^2} = \frac{\overline{v_{+\theta}}^2 + \overline{v_{-\theta}}^2 - 2\overline{w^2}\sin^2\theta}{2\cos^2\theta}$$

$$\overline{vw} = \frac{\overline{v_{+\theta}}^2 - \overline{v_{-\theta}}^2}{4\cos\theta\sin\theta}$$

$V_\theta = (V+v)\cos\theta + (W+w)\sin\theta$

$V_{-\theta} = (V+v)\cos(-\theta) + (W+w)\sin(-\theta)$
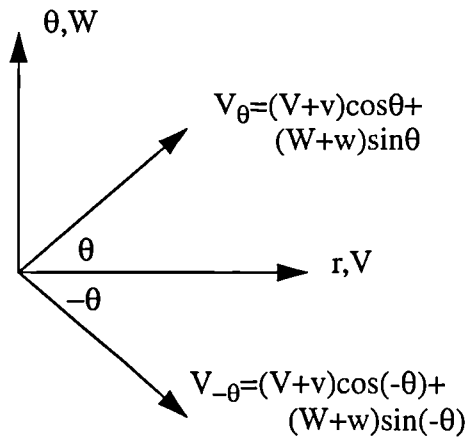
where the overbars denote time averaged values. For a derivation of these relationships see Durst (1976). In order to measure V_θ and $V_{-\theta}$ the axis of the port under investigation was rotated until it was at angles of either $45°$ or $-45°$ (the value chosen for θ) to the optical axis. W, as usual, was measured with the port axis in line with the optical axis, i.e. $\theta=0$. The (x_L, y_L) positions of the laser to make each of these three measurements was calculated by the method described and illustrated in the previous section. At each of these positions the laser was traversed across the vertical diameter of the port ($-10 < z_L < 10$mm) to enable the construction of the exit velocity profile to be carried out.

2.5.2 Construction of Velocity Vectors and Turbulence Field

With only a 1D LDA system, each of the three velocity components was measured on separate traverses through the test section. Because the correction factors for optical shifting of the control volume were different in each case, the three velocity components were generally measured at slightly different locations along each traverse. Indeed, the test section had to be rotated through $90°$ such that the radial velocity could be measured on the diameter perpendicular to the optical axis. A method was therefore required to allow each velocity component to be transposed onto a common, regular grid. A true 3D velocity vector could then be constructed and defined at each point on this grid.

The method adopted was to fit a cubic spline to the data set of each 1D traverse. The FORTRAN routines for doing this, spline.f and splint.f, were taken from Press (1992). Boundary conditions had to be given for the ends of each curve in order to calculate the cubic spline. A zero gradient constraint was used when the end point was taken at a plane of assumed symmetry, at the centre line for example. Otherwise a zero value was added to the end of the profile to represent a wall velocity. This is in effect an extrapolation of the data, since no measurements were made closer than 3mm to a concave wall. These values have been included in the results section to complete the field plots, but obviously care is needed when interpreting the results near to the walls.

By stacking up a series of consecutive parallel traverses of all of the measured velocity components a full 3D vector field could be constructed onto a 2D rectangular mesh. Furthermore the turbulent kinetic energy, k, could then be calculated from; $k = 1/2 (u^2 + v^2 + w^2)$, (u,v and w being the r.m.s. value of the fluctuating part of U,V and W), for each point in the grid. In some cases one velocity component was not or could not be measured. In these cases two alternative methods for calculating k were used. If nothing was known about the third velocity component the flow was assumed to have isotropic turbulence, e.g. $k = 3/4 (u^2 + v^2)$. Otherwise the un-measured fluctuating component was assumed to be equal to the known closest of the other two measured values, $k = 1/2 (u^2 + 2v^2)$. This second method was used predominantly in the core flow when the circumferential velocity was not measured. The un-measured fluctuating component, w, had previously been observed to be approximately equal to v, but often quite different to u. For this reason the second method gave a better estimate of k than the first.

2.5.3 Evaluation Of Inlet Mass Flow Rates From Velocity Profiles

Two methods were used for evaluating the core and annulus inlet mass flows. A quick method was used to enable the rig to be quickly set to the desired conditions, then a more lengthy method to determine the mass flow more accurately.

To obtain a quick estimate of the actual inlet mass flows to the working section the following table can be used. The table below shows how to convert the maximum velocities in the core and annulus pipe to bulk mean velocities and mass flows. The

values of $\hat{U}_c$ and $\hat{U}_a$ are measured at core pipe centre-line and half annulus height respectively, as far upstream as possible from the ports, (at x=-150mm).

TABLE 1. Inlet Profile Characteristics

Pipe	$U_b/\hat{U}$	$\dot{m}$ [kg/s]
Core	0.81	$5.15 \times \hat{U}$ [m/s]
Annulus	0.84	$6.33 \times \hat{U}$ [m/s]

The factors given in the table were established by comparing the respective velocity measurements with the mass flow calculated from the orifice plate pressure drop. This was done with the blank test section in place such that there was no mass transfer between the core and annulus streams. The error in using this method was estimated to be around 5% due to a slight dependence of the axial velocity profile on the range of Reynolds numbers used and also due to the suggested accuracy of the orifice plates.

A more accurate method was to assume the flow at inlet to be axis-symmetric and to integrate the measured inlet velocity profiles to obtain the mass flow from,

$$\dot{m} = \int_{Area} \rho U.dA = \rho\pi\int_{-\frac{D}{2}}^{\frac{D}{2}} Ur.dr$$

where, by integrating across the diameter an average of two radial profiles is being taken. The assumption of axis-symmetry was good for the core flow, however, for the annulus flow, a correction due to the presence of the 6 strut wakes was necessary. The circumferential variation of axial velocity is shown for the mid-annulus height in figure 2.10. During measurement it was ensured that the profile across the annulus was measured between struts. Assuming that the velocity deficit of the wakes is constant along the span of the strut, then when integrating the measured velocity profile, the calculated mass flow would be expected to be approximately 2% higher than the actual. Hence the value obtained from integration of the annulus axial velocity profile requires division by a factor of 1.02.

2.5.4 Evaluation Of Exit Mass Flow Rates Using Orifice Plates

Given the pressure drop across an orifice plate made to BS1042, the same standard provides a set of equations to calculate the mass flowing through it. However this

process is quite lengthy, so in order to speed the conversion from inches of water to actual mass flow, a function in the form of; $\dot{m} = A\,(\Delta H)^{\,B}$ was fitted to 2000 points calculated for each orifice plate from BS1042. The values of A and B along with orifice plate properties are tabulated below;

TABLE 2. Orifice Plate / Manometer Parameters

Pipe	D[mm]	d[mm]	β (=d/D)	A	B
Core	52.8	35.0	0.663	0.48348	0.492347
Annulus	52.8	27.5	0.521	0.27263	0.495661

where; $\dot{m}$ is in kg/s and ΔH is in inches of water (the scale used on the manometers). The error associated in using this method as opposed to that of BS1042 was found to be below 1 percent, provided the pressure drop across each plate is greater than 1.5 inches of water.

Again, by using a blank test section, and using the values of A and B specified above, the mass flows given by the above equations for both the annulus and core flows compare to those calculated by integration of velocity profiles to within 3%

2.5.5 Calculation of the Port Discharge Coefficient

The discharge coefficient of a port is defined as the ratio between the actual mass flowing through it to the amount which would if the flow was ideal, i.e.;

$$C_d = \frac{\dot{m}_{j\text{-}actual}}{\dot{m}_{j\text{-}ideal}}$$

Using the energy equation for ideal incompressible flow, it can be shown;

$$\dot{m}_{ideal} = A\sqrt{2\rho\left(P_{an} + \frac{1}{2}\rho V_{an}^2 - P_c\right)} = A\sqrt{2\rho\Delta P_j}$$

where A is the port's geometrical area. To calculate the ideal mass flow a method was needed to measure both the static pressure drop across the liner and the annulus inlet dynamic pressure. The later is easily obtained by using the bulk average velocity for V_{an}, calculated from the annulus inlet mass flow, $(V_{an} = \dot{m}_{an}/\rho A_{an})$. Theoretically, the mass weighted annulus velocity should be used (rather than the area weighted), but

since the annulus dynamic head is typically 5% of the liner static pressure drop, a small error in its value will have no significant effect on the ideal mass flow. Measuring the pressure loss, p_{an} - p_c, and defining how to do so, however, presents a small problem. Namely; Where should the pressure tappings be positioned? And how to measure the pressure drop accurately in a water analogy rig? A computational prediction of the expected pressure distribution helped with the first of these questions. It can be seen in figure 2.11 that the pressure in the core is uniform both upstream and down stream of the jet's influence. In between it is possible to see a pressure recovery at the jet impingement, and a low pressure region in the lee of the jet. The pressure at the jet core is also seen to be quite similar to that of the upstream pressure. Therefore the core tapping was positioned 2.5 hole diameters upstream of the hole centre line, away from any potential flow unsteadiness. The position of the annulus tapping was not as crucial, as the annulus pressure field was quite uniform. To avoid introducing any concern over the difference in gravitational head between the tappings it was decided to position it at the same height. The arrangement can be seen in figure 2.12. A Farnell pressure transducer was used to measure the pressure difference between these static pressure tappings. Because the pressure transducer only worked with air, an air trap had to be setup to prevent damage to the unit. This also had to be done so the water level in each connecting tube was level, such that with no flow through the rig the pressure in each line was equal. Air vents, shown in figure 2.12, were therefore opened prior to running the rig to allow the water level in each pipe reach that of the header tank. The vents were then closed and the rig set to the desired flow condition with the air traps intact.

The actual mass flow through the ports, though not directly measured, can be easily calculated from a knowledge of two of the four mass flows passing into and out of the test rig. The difference between the core inlet and exit mass flows was used as the jet mass flow since these were measured with the greatest accuracy.

2.6 Operation of Rig

Setting the rig to a desired condition was a process which took about two or three iterations to achieve. The reason for this is as follows. Firstly, the desired mass flows

would be calculated. The core exit and annulus exit mass flows could then be set using standard valves and measuring devices along the return pipes of the rig. At this point the total mass flow through the test section has been set, but the ratio between the core inlet to annulus inlet mass flows will not necessarily be correct. To correct this the core inlet valve could be adjusted to bring this ratio in to line. In the test set-up, flow can pass through the test section via three paths; enter and exit through the core pipe, enter the annulus then pass through the port and exit through the core pipe, or, enter and exit via the annulus. If the ratio of flow passing through each of these paths is changed then the loss through the system, as a whole, will also change. Therefore adjusting valve J in figure 2.1 will alter the not only the mass flow split between the core inlet and annulus inlet mass flows but also the combined mass flow. Hence valves F and G may require slight re-adjustment to bring the return mass flows back to the desired values. This may, yet again, upset the inlet mass flow split, and another cycle of this routine would be necessary. With experience this procedure could be carried out to give the desired mass flows within a couple of minutes. This description of setting up may explain why Baker (1992) had problems setting a similar rig on a particular condition. At high jet velocity to cross flow ratios the mass flow split between the annulus and core inlet was very sensitive to changes in the position of valve J. For this reason the initial design of valve J was changed. The original design was a tapered plug which could be lowered into the exit of the core header tank. However, the forces on the valve, when nearly shut, were large which caused deflections in the support mechanism. This in turn created oscillations in the mass flowing into the core. The replacement valve consisted of two discs sitting concentrically on top of each other. Both had a matching set of holes, so by rotating the top disc the area open to the flow was altered. This mechanism was not prone to the flow altering its position and removed any oscillations set up in the flow with the previous arrangement.

Once the desired mass flows had been set they remained constant for a period of several hours whilst any measurements were made. To ensure the head in the tank did not drop a water level indicator was employed. The device also had an alarm to warn if the water level rose above the overflow spill. If the overflow pipe could not carry the spillage away then without this warning the flow would eventually spill over the header tank.

The rig was designed to be able to operate with a core inlet mass flow of up to 3kg/s and an annulus inlet mass flow of up to 2kg/s. These values were chosen such that a minimum jet Reynolds number of 2.0×10^4 could be achieved along with the required range of jet to core cross flow velocity ratios, 1.0 to 10.0. These values imply that the core return must be capable of carrying up to 5kg/s and the annulus return up to 2kg/s, depending upon the amount of bleed flow. Initial tests with a blank test section, i.e. one with no ports, demonstrated that the maximum core flow achievable is 5.3 kg/s and the maximum annulus flow is 2.6 kg/s.With the flow return valves fully open, it is the orifice plates which offer most resistance to the flow. Therefore if either of the two mass flows were required to be higher then the orifice plate diameter could be increased. The maximum pump delivery is 7.5 kg/s hence the two combined inlet or return flows can not exceed this without upgrading the pump.

2.7 Flow Visualisation Techniques

Flow visualisation is an invaluable tool for understanding the nature of a particular flow. One principle method was used to visualise the flow, though the results were recorded with two media. By running the test rig with a minimum water level in the sump tank, (11 figure 2.1), air bubbles were generated in the water by the weir flow splashing into the lower level. By using a small amount of soap, the surface tension of the mixture is such that a certain size of bubble remains in the system for a sufficient time span for it to pass through the working section. By fine tuning the operating conditions it was possible to generate a sufficient and constant number of bubbles. The area around the test rig was darkened with curtaining and a halogen light sheet was used to illuminate the required plane of the test section. In order to increase the visibility of the bubbles the camera had to be positioned at a slight angle from the normal to the light sheet. Typically an angle of 10 to 15° was used for best effect, such that the angle between the light box and the camera was 100-105° about the rig axis. A video camera was found most useful for recording the flow since still photos only captured snapshots of an instant in time of the flow field. Because of the highly turbulent nature of the flow, interpretation of this snapshot was very difficult.

2.8 Preliminary Results

Numerous problems were encountered with the rig after initial construction which had to be eliminated. Tiny air bubbles in the system prevented accurate measurements being taken at first and required immediate attention. The primary causes of bubble generation were found to be in the two tanks where splashing had to be minimised. In the sump tank baffle plates were introduced to maximise the residence time of the water in the tank, this allowed any bubbles in the water to rise to the surface. By also introducing a weir the water is also forced to flow near to the surface such that smaller bubbles also reach the surface before being drawn back into the pump. Level 11, indicated in figure 2.1, also had to be kept high, because (as described in the previous section) reducing this level conversely allowed the generation of bubbles due to splashing.

In the header tank splashing was generated by the delivery pipe feeding high velocity water into the tank. This was minimised by constructing a perforated bucket around the end of the pipe, to reduce the exit velocity and distribute the water evenly. A calm water surface resulted from this measure, which is important to ensure there is an even and steady pressure distribution in the header tank. Further care was taken to ensure all pipe joints were air tight, particularly around the pump, through which air could be drawn into the system. With these measures, and by filling the rig two or three hours before operation to allow the dissolved air to escape, the problem of air in the system was removed. With the ability to take measurements in the rig it was discovered the flow was far from symmetric and higher levels of turbulence than expected were found in the working section. Several factors were to blame for this. Firstly the inner tube was found not to be concentric with the outer nor sufficiently circular. A significant re-manufacture was required with cast acrylic tube to replace the inner, extruded acrylic pipe. The cast acrylic, despite being more expensive and slightly thicker, was manufactured with higher tolerance than the extruded tube. Some leakage was also observed through the inner pipe bearing surfaces. This was seen to be causing un-symmetric flow in the core pipe, upstream of the test ports. To prevent this, water proof grease had to be used on the inner pipe bearing surfaces. Care had to be taken when applying the grease: if applied too liberally then beads would form around the pipe

joints, upsetting the velocity profile existing near the pipe walls. Finally, to improve symmetry, flow straighteners were introduced to the entrance of the core and annulus pipes. these produced a more even inlet velocity profile to the tubes and controlled the level of turbulence entering the pipes. The last measures to be made were to improve the controllability of the rig. The first addition was a water level meter in the header tank which allows the operator to ensure the tank is at the over flow level, and also to control the filling of the tank. All of the control valves had smaller by-pass valves fitted which allowed finer control of the mass flows. With these modifications made, the rig reached the state at which the reported results were obtained. The following sections describe some of the results obtained to demonstrate the rig is appropriate for this investigation.

2.8.1 Inlet flow conditions

Figure 2.13 shows a graph of the mean axial velocity and r.m.s. component at inlet to the blank test section (inlet taken to be x=-150mm). Zero velocities have been added to this graph to illustrate the position of the walls of the pipes. Acceptable turbulence intensities of 4 and 5% are seen at the centre of the core and annulus passages, with the expected distributions, increasing towards the walls of the pipes. Measurements close to the walls were not possible with the current setup since the control volume was 3.12mm along its major axis, and the minor axis could not be brought close to the walls because in this orientation high levels of refraction occur. Very similar profiles were measured across the diameter perpendicular to the optical axis and with the inner pipe rotated to various positions indicating a good level of symmetry. Care had to be taken however when measuring the annulus profiles due to the presence of the six wakes causing a maximum velocity deficit of 6% at the axial location of the ports, as shown previously in figure 2.10. Similar profiles at various flow rates were measured to allow the orifice plates to be calibrated. Whilst the core flow is not expected to be fully developed with only 18 pipe diameters from entry to working section, the annulus profile would be expected to be developed having 53 annulus heights to do so. Figure 2.14 shows the level of secondary velocity components at inlet to the test section. The level of swirl and radial velocity are typically less than 1% of the mean

axial velocity, small enough to be comparable to the error involved in measuring the axial velocity with the LDA system.

The flow through the system was found to be very stable over large periods of time, after the first hour of running. Temperature increase of the water was found to be the cause of small changes in mass flow during a warming up period. Monitoring of the water temperature over several hours of running showed that it increased quite quickly until it was about 5°C above the laboratory temperature then rose very slowly. A warming up period of about an hour also gave further time for air trapped in the system to escape, leading to favourable testing conditions.

2.8.2 Effects of rotation of the test section

The ability to rotate the test section proved to be a useful tool but it was important to establish what consequences this had on the flow and symmetry of the flow, since only the inner pipe rotated.

During the initial rig design only four, non-rotating struts were specified. This was found to produce large variations in the symmetry of both the annulus and core flow fields. When the six ports were rotated a variety of arrangements were possible; with struts in and out of line with certain ports. It was therefore decided to have six struts, to force them to turn with the test section, and to locate them out of line with the ports. With this layout the core flow was seen to be symmetric with the jets meeting at the centre-line of the pipe. It was important however to establish the effects on the annulus flow. It had previously been established, Daly (1994), that the most sensitive region to asymmetry in the annulus was on the outer wall above the ports. In this region, with low annulus bleed flows, a separation bubble is formed above each port. The size of each bubble was found to be very sensitive to flow asymmetry, such that in any one test the size of each bubble would be different, despite otherwise symmetric flow. It was therefore decided to examine results obtained by traversing axially along a line 3mm away from the outer wall above several ports. Each of these ports was then rotated through several angles, to establish whether the flow pattern rotated with the core pipe or remained fixed relative to the outer tube. In the type of profile described a

lower velocity over, and behind the hole indicates a stronger influence of the presence of the hole, i.e. a slightly higher mass flow may be expected through it.

Before considering the effects of rotation it was necessary to determine the extent of variation in the size of these recirculation bubbles for one test condition, without rotating the core pipe. A bleed flow, (the proportion of annulus inlet flow bypassing the port) of 50% was chosen, because, at this value, flow visualisation had shown that the recirculation bubbles were just being formed. At higher bleed ratios no recirculation was found, at values lower than 50% recirculation bubbles were always found. In figure 2.15(a) the profiles over three separate ports are presented. Each was measured when the angle between the hole designated number 1 was at $\alpha=60^{\circ}$ to the optical axis. It is evident that there was a measurable variation around the annulus of these profiles. It is evident that a recirculation existed over hole 2 for example, whereas the profile over hole 4 did not show evidence of separation. Despite this measurable asymmetry in the annulus the core flow for this test was found to be symmetric, with the jets impinging at the core pipe centre line. This evidence suggests that the level of asymmetry in the annulus was insufficient to create a significant uneven distribution of mass flow through each hole.

Figure 2.15(b) presents the same results, but this time hole 3 has been rotated into the position which holes 2,3 and 4 were at in the previous case. For this α had to be 120°, 60° and 0° respectively. With the core pipe being rotated it is possible to see there is a much smaller variation in the measured profiles. Two main conclusions can be drawn from this result. Firstly, despite taking care to ensure symmetric inflow characteristics to the annulus, at this very unsteady flow location above each port asymmetry is evident. Secondly, and quite importantly, it is evident that the flow field can be considered to be fixed relative to the core pipe.

This information therefore suggests that it is a valid procedure to measure the axial and circumferential velocity components on the diameter aligned with the optical axis, then rotate the core pipe through 90° to measure the radial velocity on the diameter perpendicular to the optical axis. This test was repeated with a component of azimuthal velocity (i.e. swirl) and the same result was observed.

2.8.3 Comparison with previous studies

Figure 2.16 gives an indication that the rig is able to repeat the results of those obtained by Baker (1992) in a similar study, for a similar geometry. It shows the axial velocity distribution along the pipe centre line for a jet to core flow velocity ratio of 4.8. There are two main differences between the test setups for these results; firstly the annulus height, 20mm in this study; this was 30mm in Baker's. Secondly the liner thickness was 5mm in this study, 3 in Baker's. However a good agreement between the results can be seen for the internal core flow. The size of the upstream recirculation region for example is very similar for both cases. The absolute values of the minimum and maximum velocities on the centre line are slightly different however. Slightly higher turbulence levels were observed in this investigation which will have increased the amount of turbulent diffusion occurring, acting to decrease the peak velocities found at the centre-line.

2.9 Closure

The philosophy behind the design, manufacture and development of the test rig used for this study has now been discussed in sufficient depth to recreate or reuse them. Preliminary results have shown inlet conditions are steady and symmetrical with levels of turbulence unlikely to have any effect on the highly turbulent, recirculating flow fields which will be present in the working section. An outline of the novel approach for correcting for the effects of refraction on the position of the LDA control volume has also been given. Using this correction technique, along with the ability to rotate the inner portion of the working section, it has been shown that a method for constructing the three velocity components using a 1D LDA probe in a repeatable fashion has been devised. Finally, reproduction and good agreement with previous measurements of a very similar flow scenario has given reassurance of the experimental methodologies adopted. The results of the experimental investigation are presented and discussed in the following chapter.
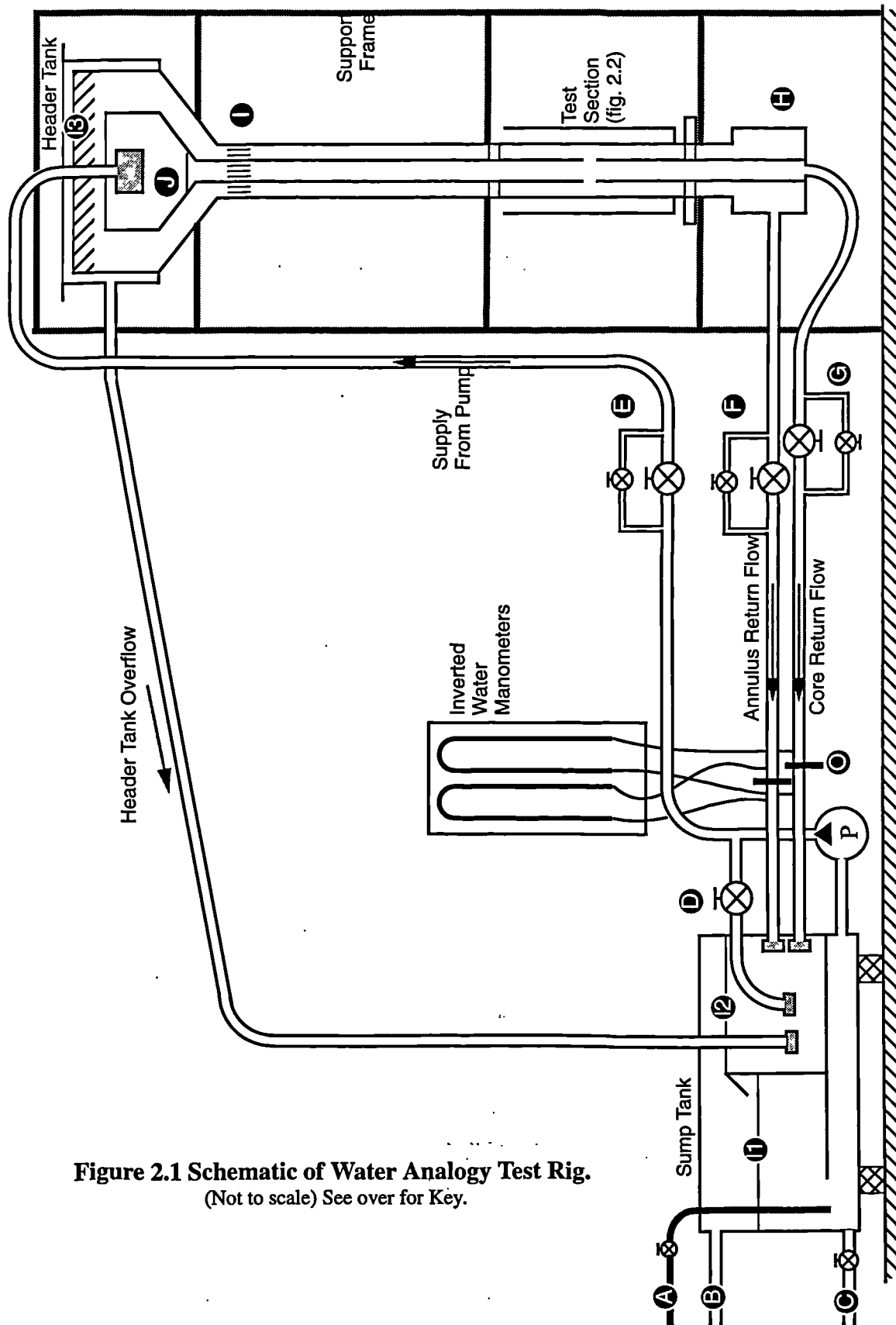
Figure 2.1 Schematic of Water Analogy Test Rig.
(Not to scale) See over for Key.

A - Mains Water Supply

B - Sump Tank Overflow

C - Drain

D - Bypass Valve

E - Supply Valve (coarse & fine control)

F - Annulus Return Valve (coarse & fine control)

G - Core Return Valve (coarse & fine control)

H - Splitter Manifold

I - Flow Straightener Bundle (3mm$\varnothing$ × 25mm long)

J - Upper Core Control Valve

I1 - Variable Sump Tank Level

I2 - Fixed Sump Tank Level

I3 - Fixed Header Tank Level

O - BS1042 Orifice Plates·

P - 1.7kW Pump

- Fine Mesh Filter Bag (at Pipe Exits)

Key to figure 2.1

6 NACA 0015
STRUTS

Split Line

Flow

A

Water
Jacket

Ports

Detail at A:-
Upper Brass Bearing

Rotating
Struts
Connecting
Ring Gear
and Core

Worm and
Ring Gear
in Sealed
Housing

Manifold
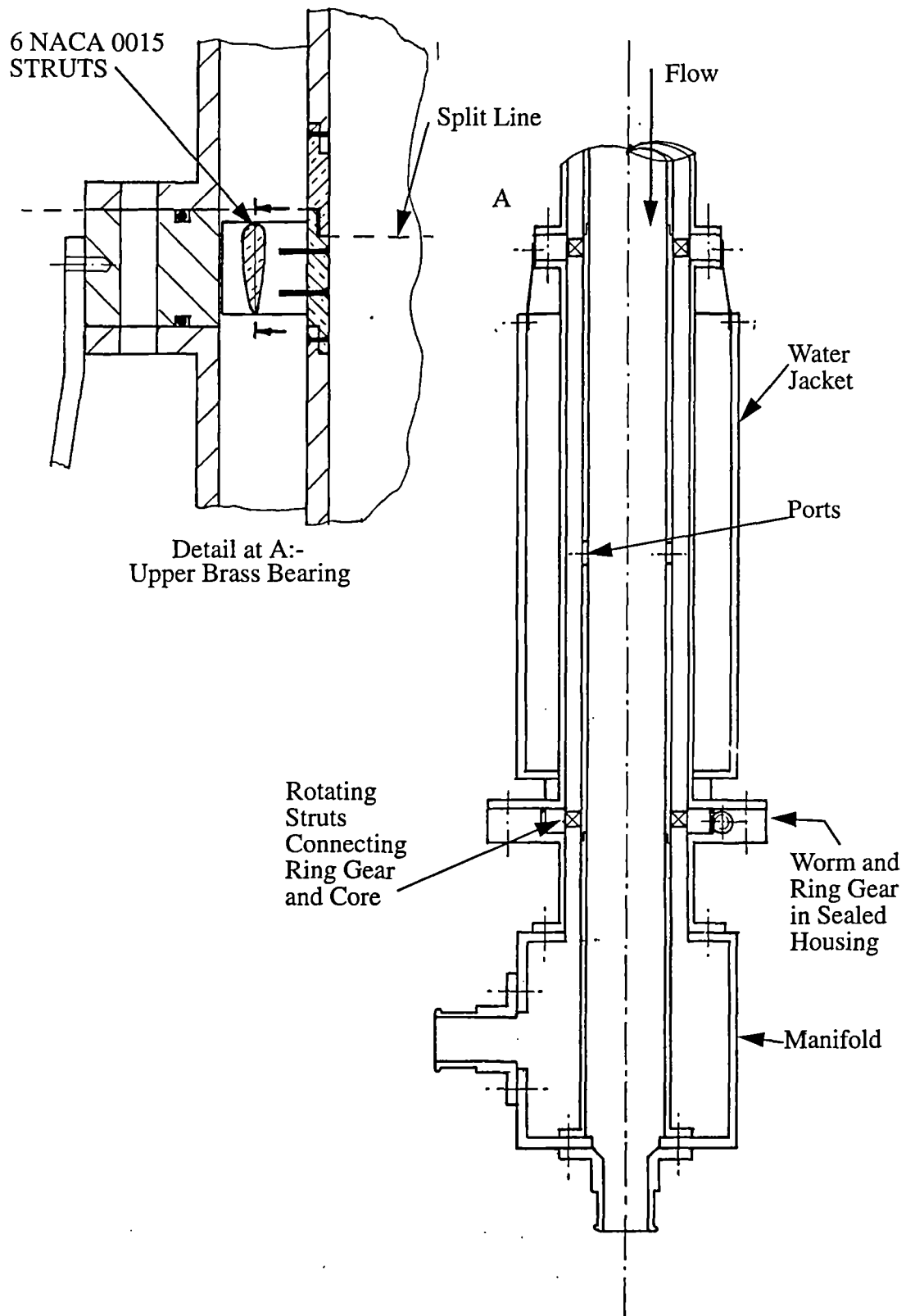
Figure 2.2 Cross Sectional View of Test Section
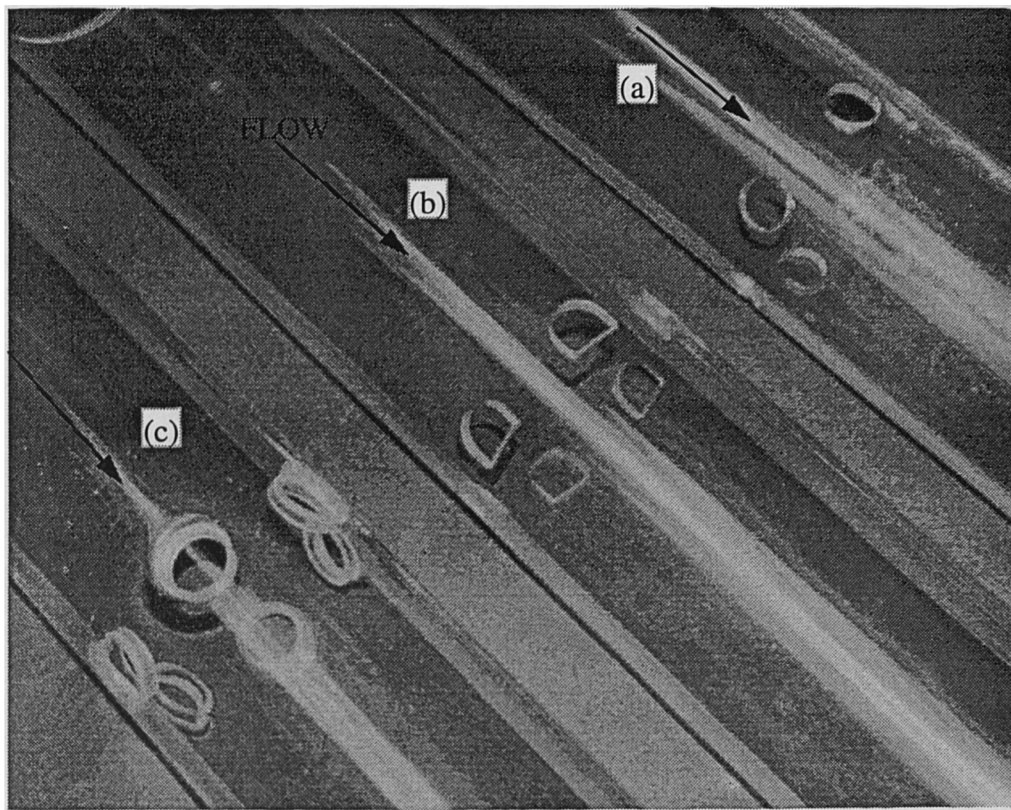
(a) Plain Port
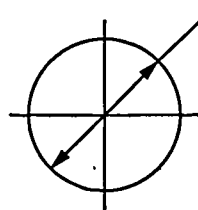
D = 20mm

(b) 'D' Shaped Port
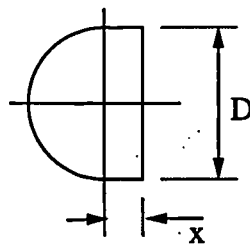
D = 20mm
x = 7.85mm

(c) Chuted Port
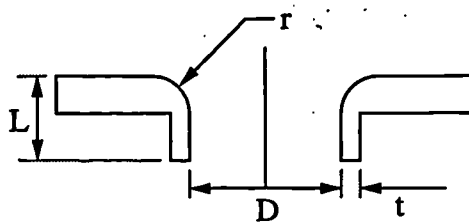
D = 19mm
L = 10mm
r = 5mm
t = 3mm

Figure 2.3 Test Section Geometries
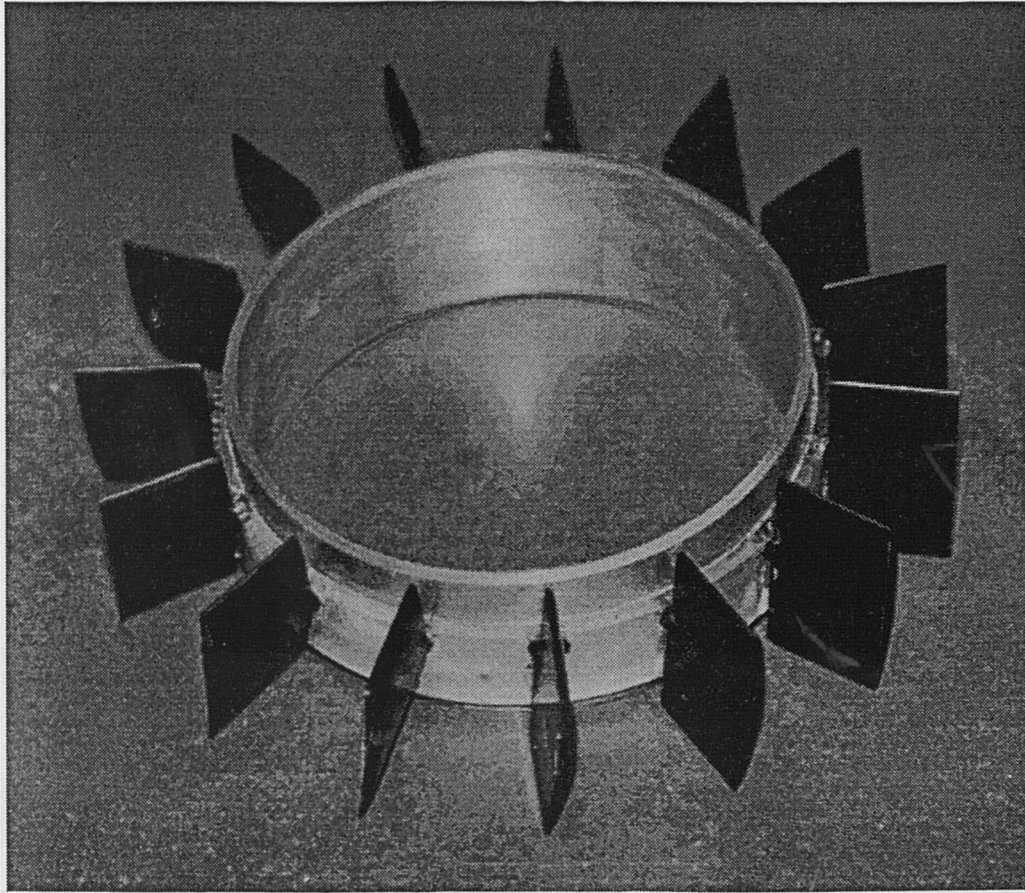
$C_L = 8.0$, Camber $= 20.1°$, Chord $= 35$mm

Figure 2.4 NACA 65-8 10 Swirl Vanes Mounted on Brass Bearing Ring
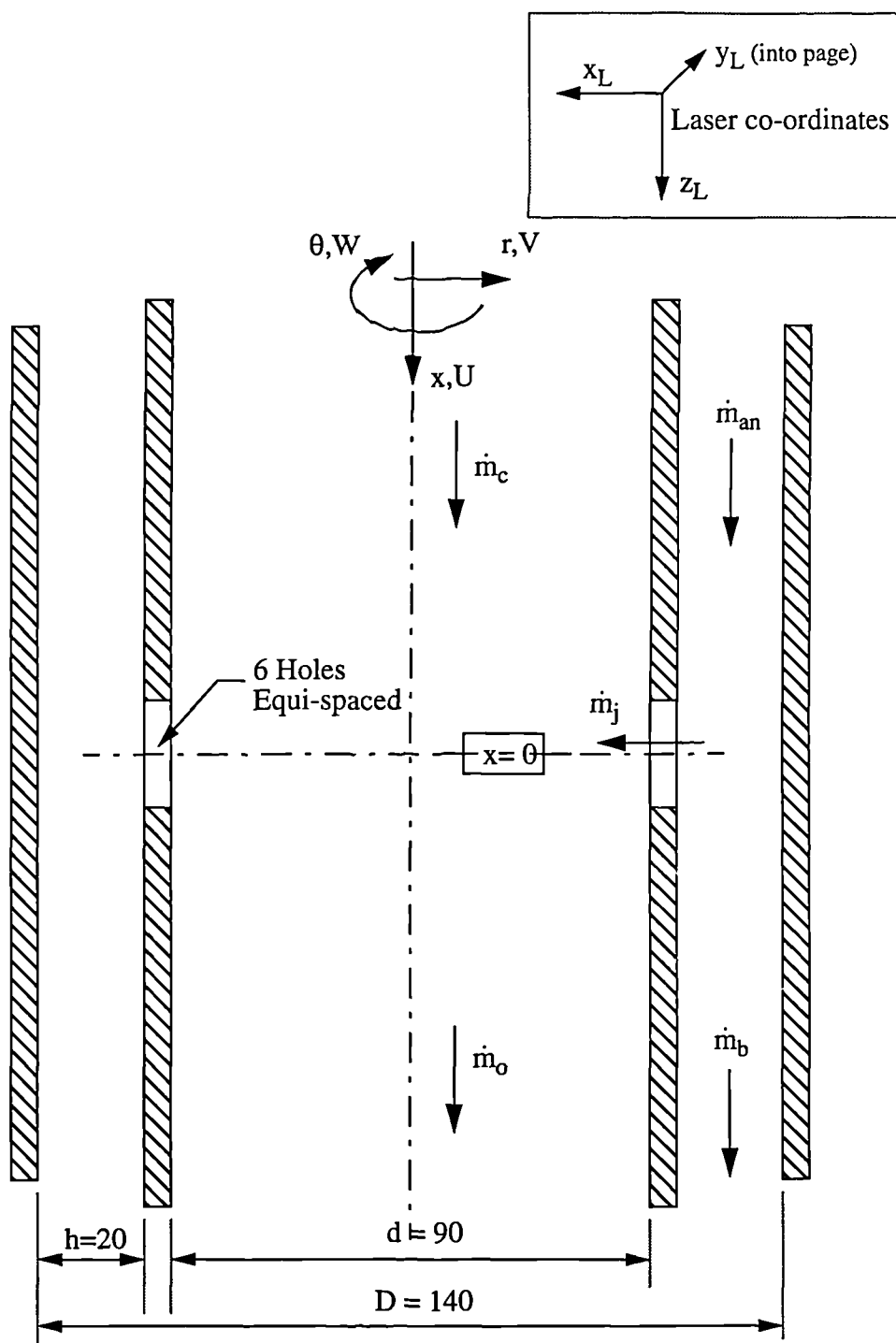
Figure 2.5 Test Section Co-ordinate System
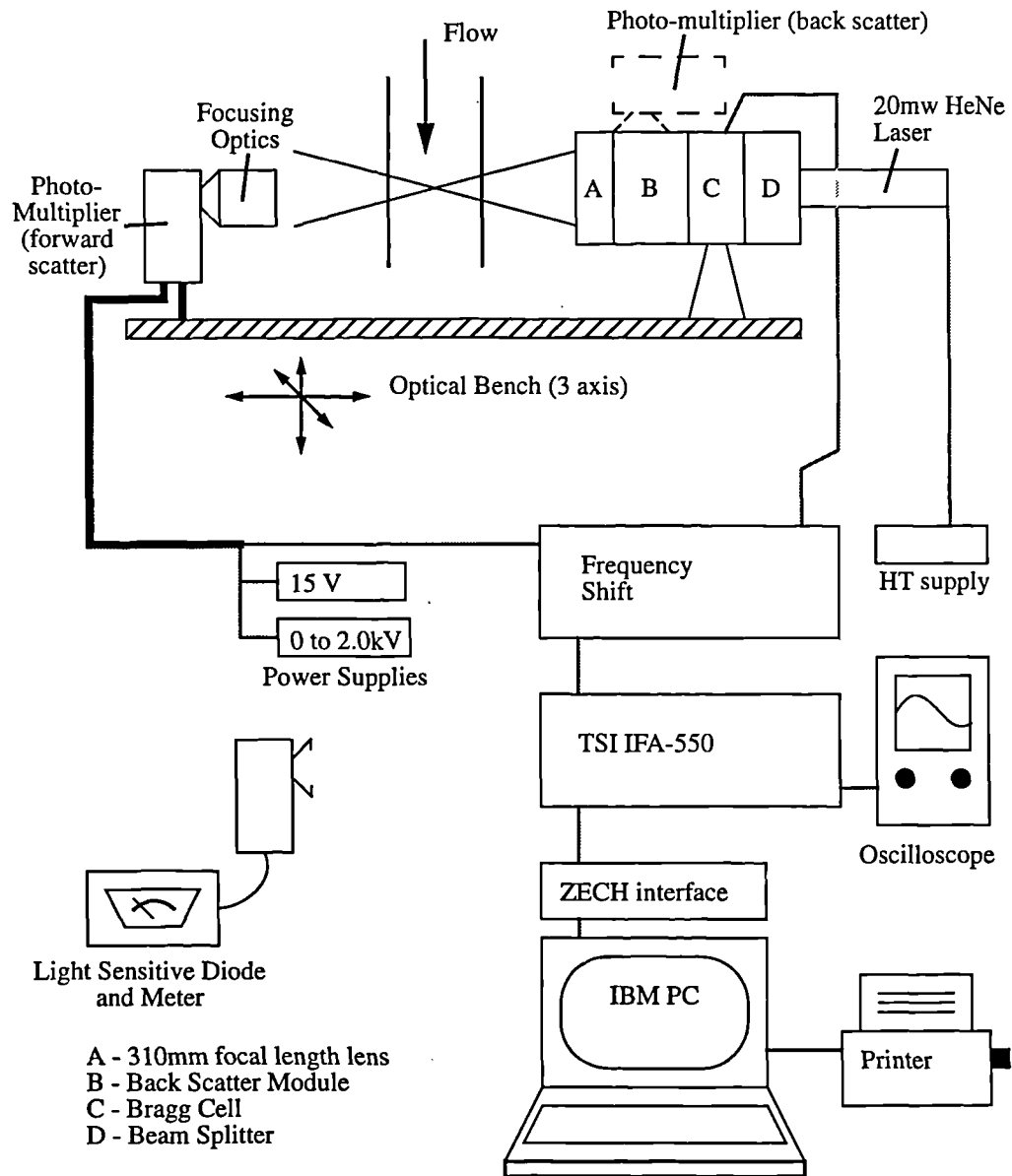
Figure 2.6 Instrumentation Setup

(a) Measuring U along optical axis

(b) Measuring U on axis perpendicular to optical axis

(c) Measuring W along optical axis

(d) Measuring V on axis perpendicular to optical axis

⊕　　- Movement of laser normal to paper

◄─────► - Direction of laser travel

╳　　- Laser beams

▬▬●▬▬ - Traversed region and control volume
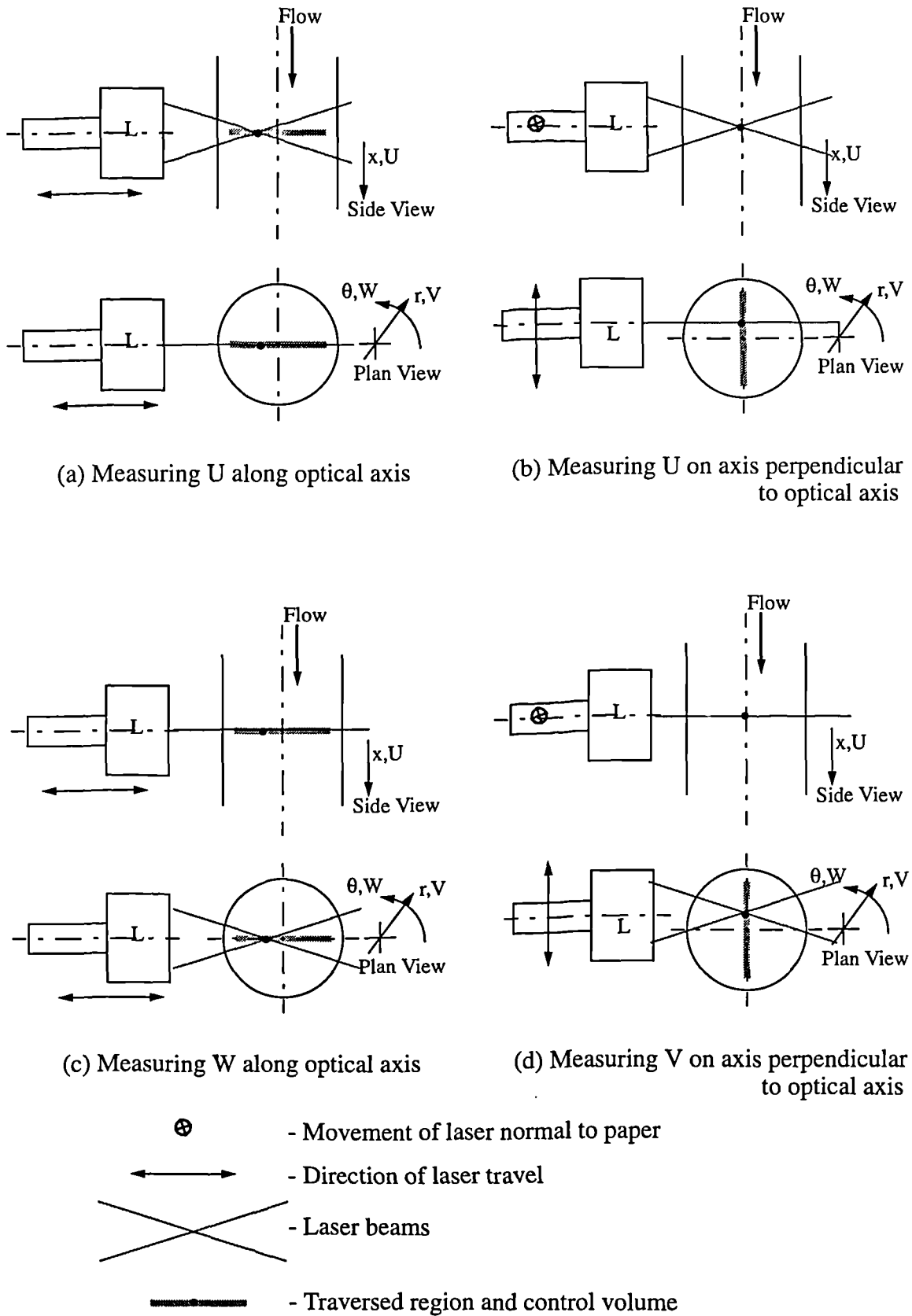
Figure 2.7 Recommended Laser Orientations and Traversing Directions (Bicen(1981))

n = refractive index of;
a = air
w = wall
f = fluid

(Orientation as figure 2.7(d))
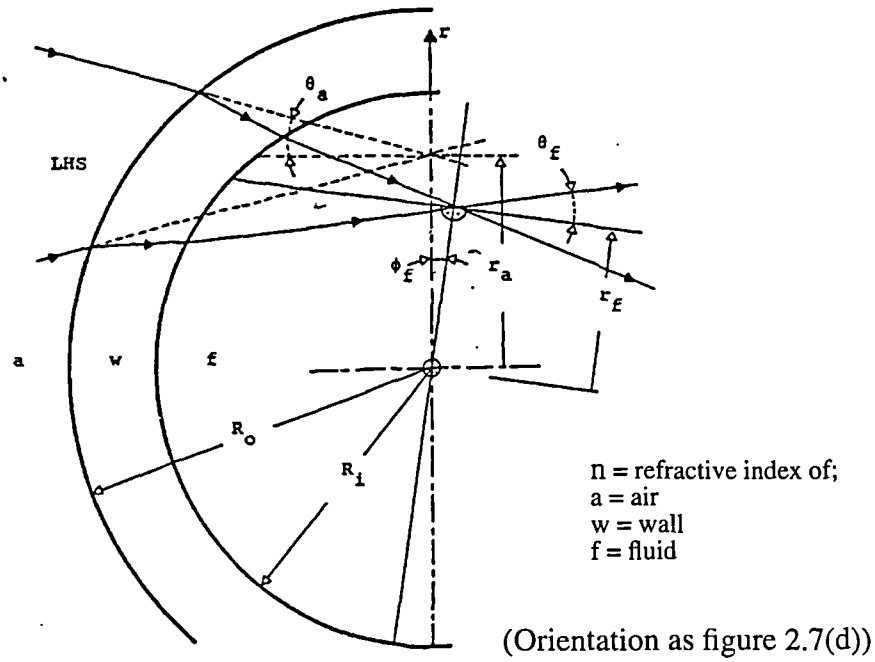
Refraction of Laser Beams During Radial Velocity Measurements, from Bicen (1981)

$$r_f = C_f \cdot r_a, \quad \text{where} \quad C_f = \frac{n_a}{n_f}$$

$$\phi_f = \text{asin}\left(\frac{n_a r_a}{n_w R_i}\cos\theta_a\right) - \text{asin}\left(\frac{n_a r_a}{n_w R_o}\cos\theta_a\right) - \text{asin}\left(\frac{n_a r_a}{n_f R_i}\cos\theta_a\right) + \text{asin}\left(\frac{r_a}{R_o}\cos\theta_a\right)$$

n_a=1.00 n_f=1.33 n_w=1.49 R_o=49.5mm R_i=45.0mm
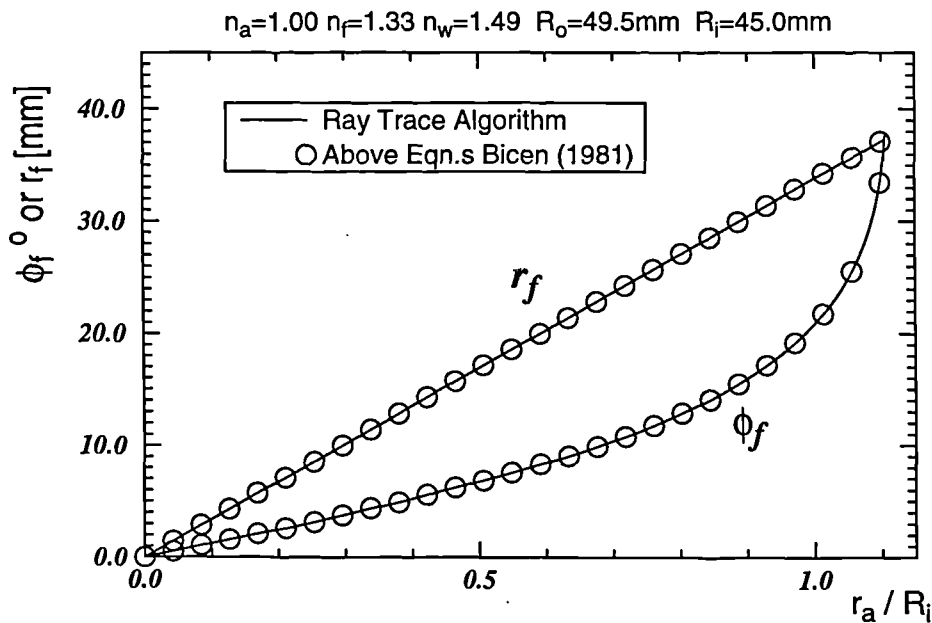
**Figure 2.8 Comparison of Correction Factors For Positional Shift Using
Bicen (1981) and Ray Tracing Algorithm**

Figure 2.9 Example Results From Ray Tracing Algorithm For The Test Rig Geometry
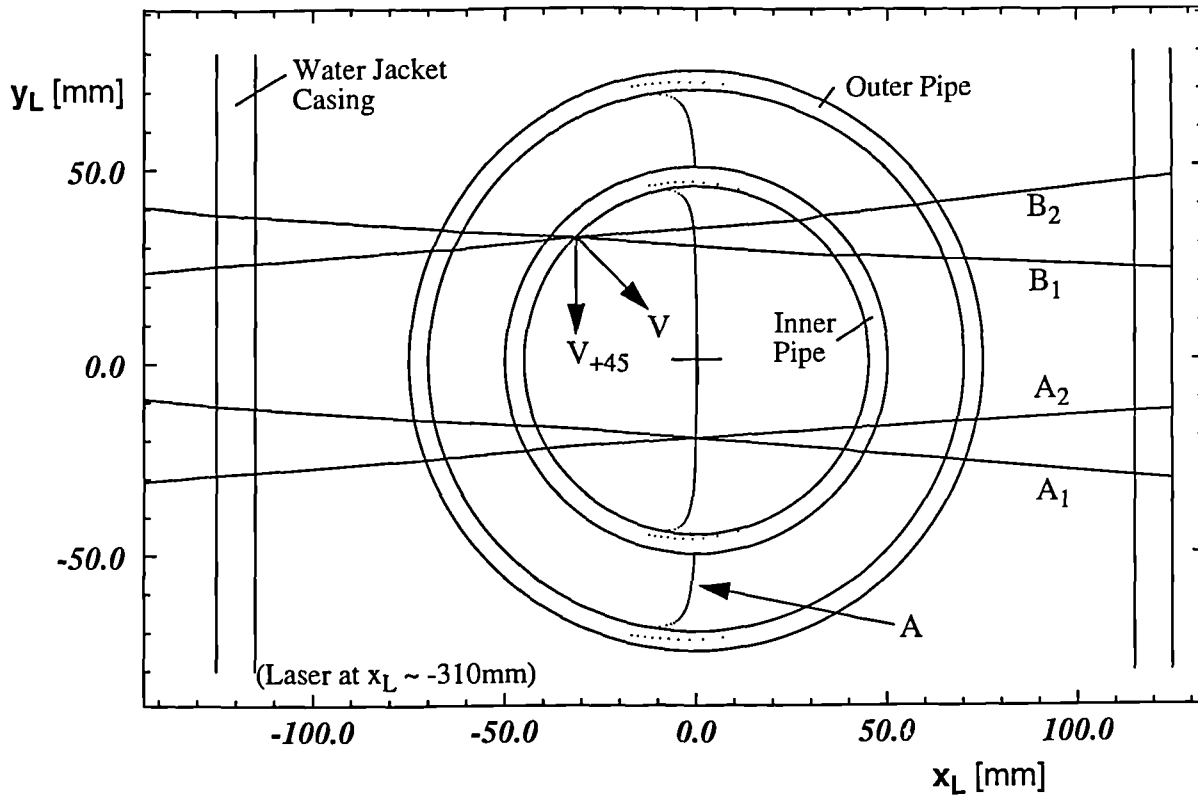
A - Loci of beam intersection for;

$x_L = 0.0$

$y_L = -70.0$ to 70.0 in 0.5mm increments

$z_L = 30.0$ (Below interference from ports)

A_1 and A_2 are example laser beams plotted for one of above positions, when;

$y_L = -20.0$

B_1 and B_2 are the computed laser beam paths when the control volume is located at;

$x = 0.0$

$r = 45$mm

$\theta = 45°$

Mass flow = 4.162 kg/s, U_{an}= 0.552 m/s
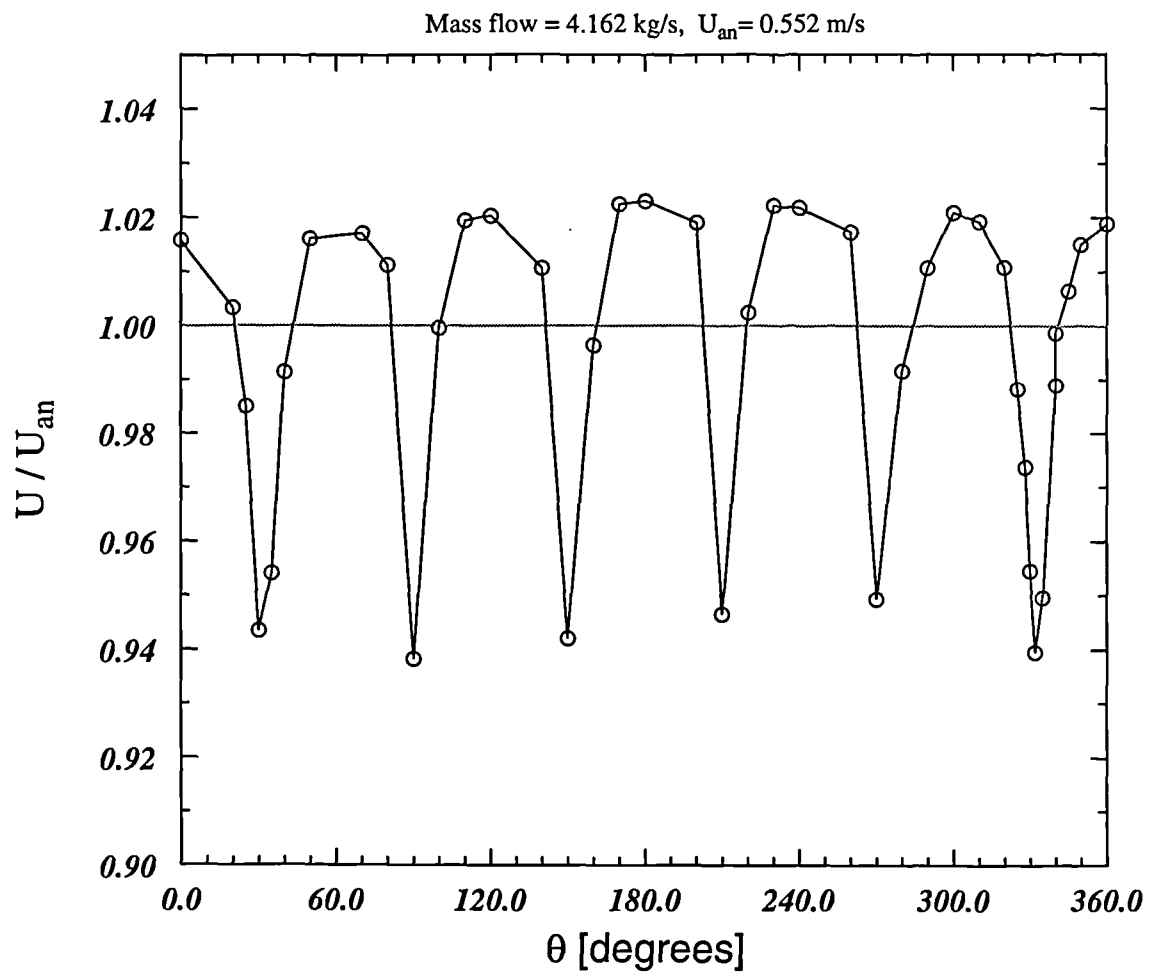
Figure 2.10 Circumferential Variation of Axial Velocity In Annulus
$x=z_L=150mm$, r=60mm
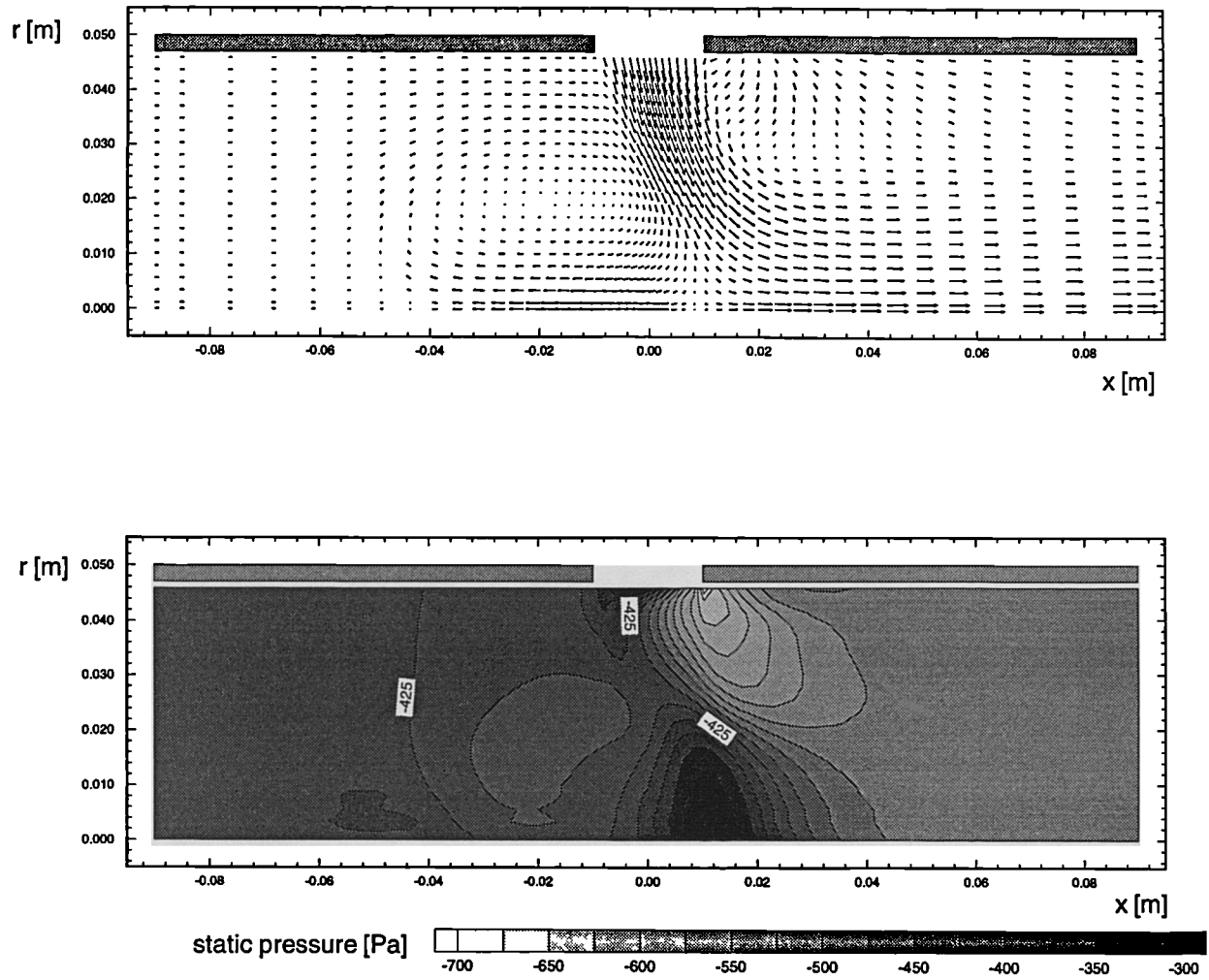
Figure 2.11 Predicted Pressure Distribution in Core for V_j/U_c=5.0
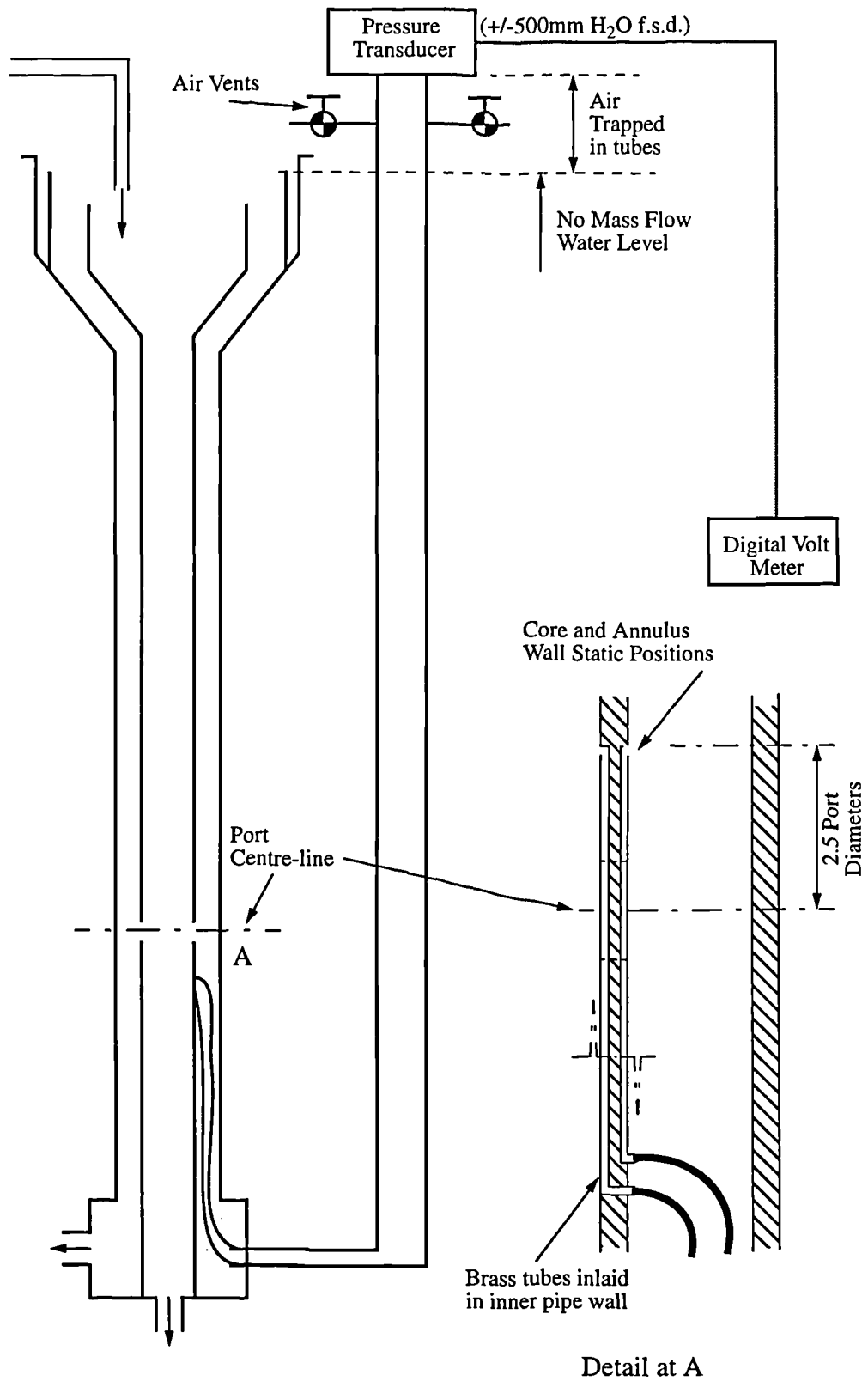
Figure 2.12 Arrangement For Measuring the Pressure Drop Across the Liner
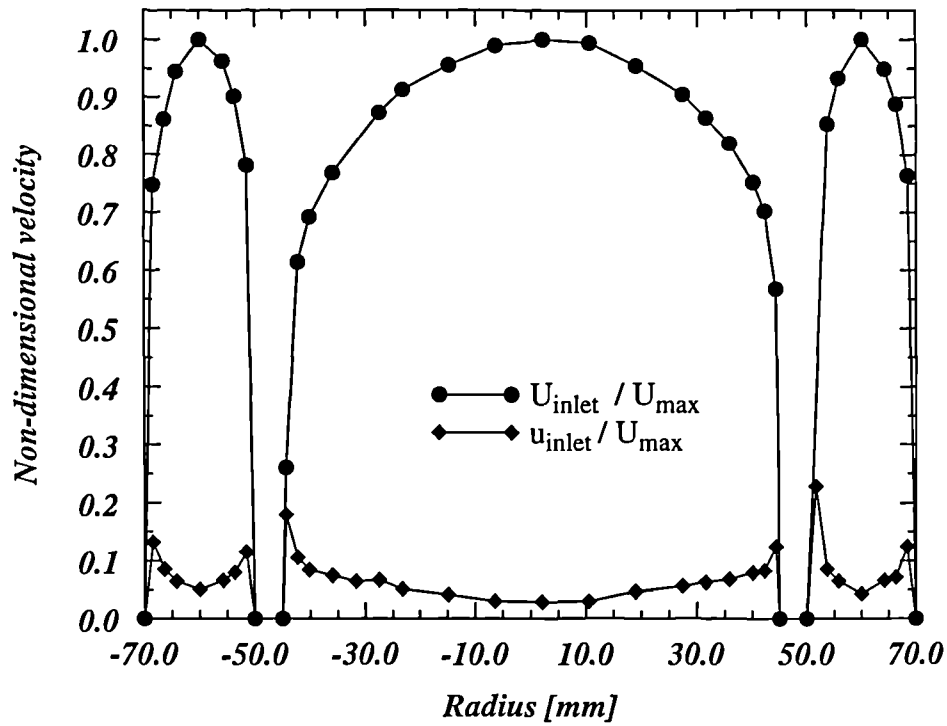
Figure 2.13 Annulus and Core Inlet Axial Velocity Profiles
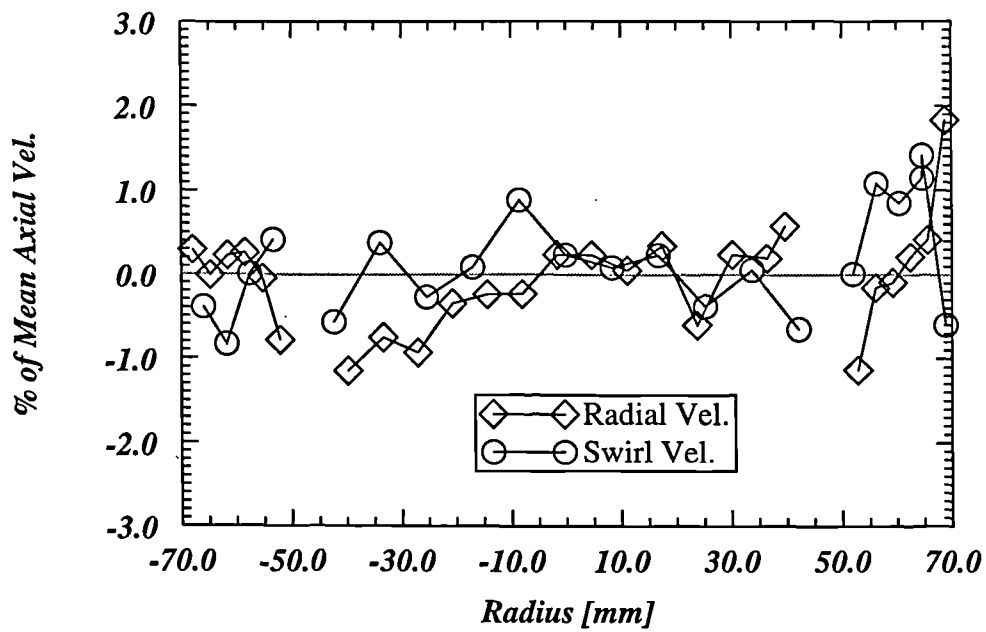
Figure 2.14 Annulus and Core Inlet Swirl and Radial Velocity Components
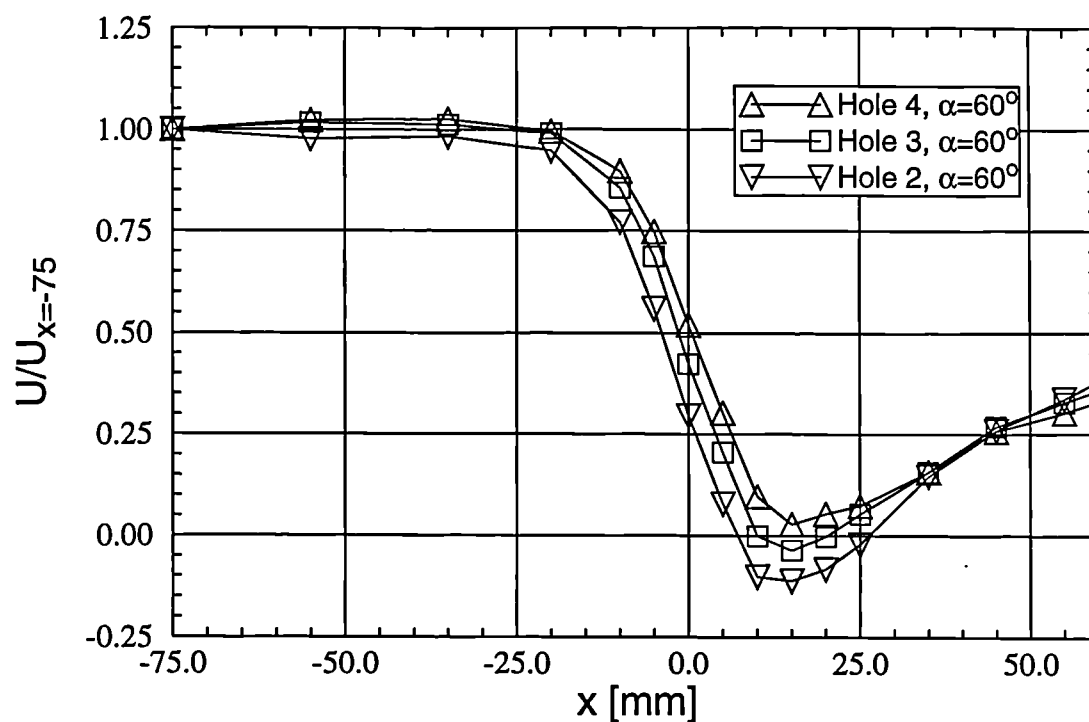
Figure 2.15 (a) Axial Velocity Distribution Over Holes 3,4 & 5
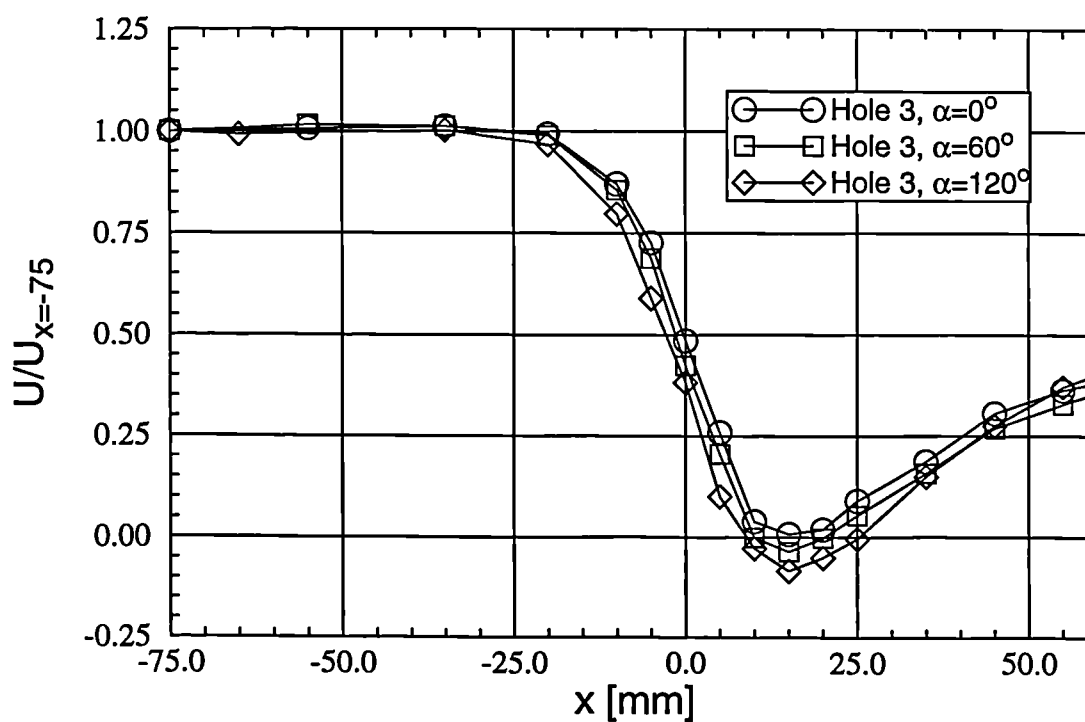
Figure 2.15 (b) Axial Velocity Distribution Over Hole 3 at Three Angles of Core Rotation

$$V_j / U_c = 4.8$$
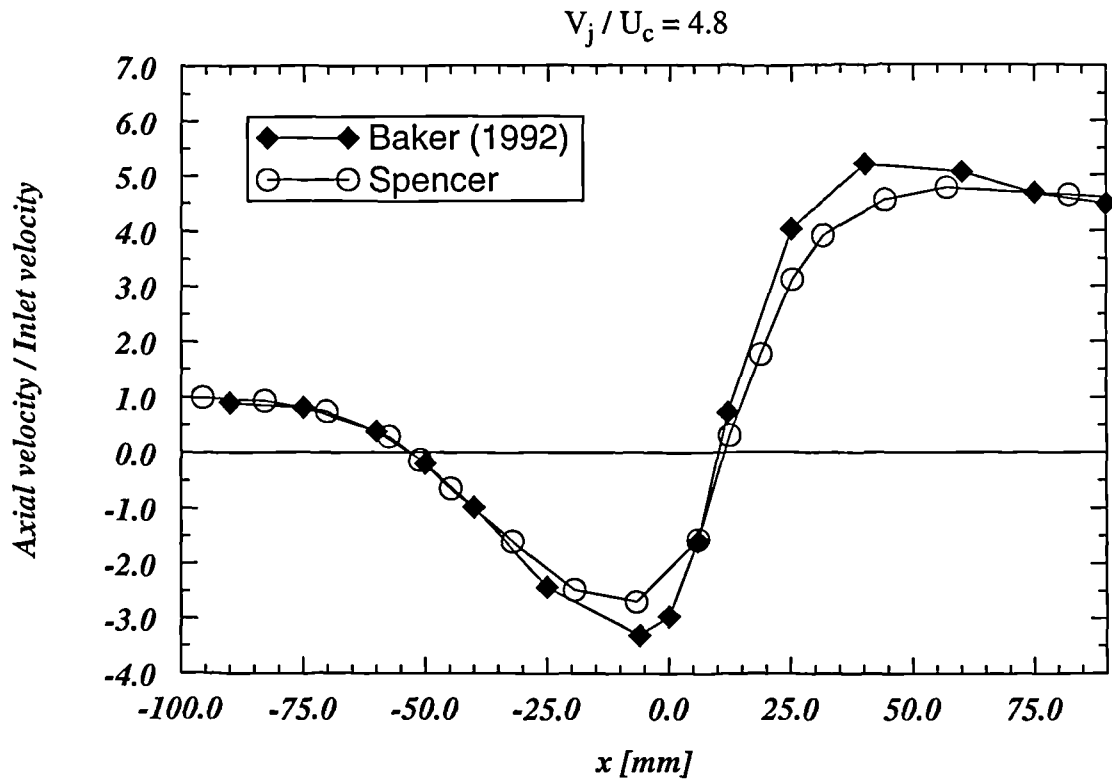
Figure 2.16 Comparison of Results With Those of Baker (1992):
Axial Velocity Profile Along Core Centre Line

Chapter 3

Experimental Results

3.1 Introduction

The majority of the results described in this chapter are from measurements taken from the test configurations summarised in table 3.1. In this matrix, the column headings describe the geometry and flow configuration, whereas the row headings indicate the type of measurements made.

Table 3.1 Main Test Matrix

		No Swirl						Swirl					
	Annulus Flow	Plain		Chuted		"D"		Plain		Chuted		"D"	
	Port Shape	P	D	P	D	P	D	P	D	P	D	P	D
	Measurements Primary / Dilution												
1	U,V & W map of core - constant θ plane	✔	✔	✔	-	✔	-	✔	-	-	-	✔	-
2	U,V & W map of annulus - constant θ plane	✔	✔	✔	✔	-	-	-	✔	-	-	-	✔
3	U,V & W along centre-line	✔	✔	✔	✔	✔	✔	✔	-	-	-	✔	-
4	Port exit U,V,W profiles	✔	✔	✔	-	✔	✔	✔	✔	-	-	✔	✔
5	U&W on plane of constant r above port	-	✔	-	✔	-	✔	-	✔	-	-	-	✔
6	U on plane of constant x at port edges	✔	✔	-	✔	-	✔	-	✔	-	-	-	✔
7	U & W at exit from core - residual swirl	✔	-	-	-	-	-	✔	✔	-	-	✔	-
	Cd Measurements	✔	✔	✔	✔	✔	✔	✔	✔	✔	✔	✔	✔

The brief measurement descriptions in the table will become clearer as results from each type are presented, but figure 3.1 shows the measurement plane for each type. As can be seen in table 3.1, the main variables in each test configuration were, (i) port shape, (ii) the presence of annulus swirl and (iii) the mass flow splits through the test section (to give primary or dilution port velocity ratios). Removing the three port shapes (described in chapter 2) from the 12 test permutations shown above identifies the four main flow configurations to be reported here. The flow conditions for these four configurations are given in table 3.2.

Table 3.2 Flow Conditions

	Annulus Flow	No Swirl		Swirl	
Variable	Primary / Dilution	P (Datum)	D	P	D
$R\ (V_j/U_c)$		5.0	2.0	5.0	2.0
$B\ (Q_b/Q_a)$		50%	20%	50%	20%
Re_j		$>2.4 \times 10^4$	$>2.4 \times 10^4$	$>2.4 \times 10^4$	$>2.4 \times 10^4$
W_a/U_a (Swirl)		0.0	0.0	0.215 (12°)	0.215 (12°)

The mass flow splits through the test section are dependent on only the jet to core velocity ratio, R, and the proportion of annulus bleed flow, B. The values of R and B for the primary and dilution port configurations were chosen to be representative of a typical combustor, and values close to those found in a combustor similar to that shown in figure 1.3 were used, Boyce (1995).

The results presented in this chapter will be separated into 6 main sections. Firstly, the reader will be introduced to the flow field and characteristics found in what was chosen to be the datum configuration, namely a plain circular port with primary port-like flow conditions and zero annulus swirl. This will be performed in detail to illustrate clearly how composite velocity vectors and contour plots have been created. For comparison, results will then be presented which are representative of a dilution port flow condition. A fourth section will look at the effect of varying the proportion of annulus bleed on the core, annulus and jet flow fields. In this section a more detailed interrogation of the annulus flow has been conducted than in previous investigations. With an insight into the effects of each main flow variable considered, the effects of changing the port shape are then presented for various flow configurations. The sixth section describes the effects of introducing swirl into the annulus flow, a feature which has not been studied previously in the context of annulus port flows, but which is demonstrated to have considerable effect. Finally, a summary of the findings is given, in which measured and derived global parameters are discussed in the context of the detailed flow field.

3.2 Datum Configuration: Primary Port Flow

3.2.1 Measured Velocity Profiles

Figure 3.2 shows the velocity profiles obtained by traversing the LDA measuring volume in the radial direction on the $\theta=0^\circ$ plane (or 90° for the radial velocity) at eight axial locations for the three velocity components. By referring back to figure 2.5 the location of each traverse can be seen, for example; x=0 refers to the traverse location coincident with the port centre line. The profiles of U,V and W in figure 3.2(a),(b) and (c) respectively have been non-dimensionalised by U_c, the bulk average axial velocity at inlet to the core at x=-150mm, which for this test was 0.201m/s. It is also standard

practice to non-dimensionalise the chosen co-ordinate system in a study of this nature. However, other than changing the details of the port geometry, no dimensional changes were made to the test section. Despite these detailed changes, the area of each port was equivalent to a plain circular port of diameter 20mm. Rather than use this port diameter to provide a basis for non-dimensionalisation, none was used to remind the reader that this is not the only characteristic dimension of importance. Equal weight may be placed upon the core diameter or annulus height in their influence on the scale of the flow. It is then trivial to create a non-dimensional scale of length based upon the chosen characteristic dimension from the absolute dimensions given. The sequence of axial locations shown in figure 3.2, for example, range from -5.0 to 3.75 jet diameters.

For the axial and circumferential velocities, U and W, the profiles are given across a whole diameter to indicate the level of symmetry achieved in this test. Only one profile of the radial velocity, V, is given across a full diameter (at x=0) in order to confirm symmetry. This was due to the additional complications in setting up the laser in this orientation; as the measuring volume crossed the rig centre-line both the direction of the frequency shift required reversal, and the photo multiplier position required re-optimising. Hence to save a significant period of time over the course of several traverses only one full diametral profile of V was taken. It can be seen that the level of symmetry is good, particularly in the core. However, on closer inspection of the axial velocity profiles in the annuli at x=15mm, just downstream of the ports, we see evidence of separation bubbles at both the inner and outer walls of the left hand annulus. On the right hand side it is seen from the profile shape that the flow is close to, but not quite, separated. Looking further upstream on each side of the annulus some difference can be seen between the peak value of each profile, 3.41 to 3.51. This asymmetry was not seen with the blank test section (i.e. no port flow). At 50% bleed, the presence of a recirculation behind a port in the annulus is perceived as a blockage by the upstream flow causing some flow migration from this x-r plane. These recirculations will be shown to be unstable at a bleed of around 50% later in this chapter (principally because the separation bubble is beginning to interact with the inner wall and result in a change in flow pattern). Because of the inherently unstable nature of the annulus flow at this condition it is not surprising that some asymmetry is observed. Despite these signs of asymmetry in the annulus, an uneven mass flow split

through each port does not seem to have resulted, as indicated by the level of symmetry in the core.

Looking at the U profile at the axial location furthest upstream, it is evident that a relatively flat inlet profile was achieved. By x=-50mm negative axial velocity is seen, indicating the presence of back flow along the core pipe centre line, with a significant increase in axial velocity toward the wall of the inner pipe. This is due to the recirculation along the centre of the pipe causing a blockage to the core flow, hence for mass continuity the core flow must accelerate around the central recirculation region. A similar picture is seen in the core at x=-30mm, with the recirculation growing stronger and the velocity near the wall increasing further, to nearly three times that of inlet. At this location it is possible to see a slight skew in the annulus profile compared to that at the inlet as the annulus flow begins to anticipate the presence of the port and migrates toward the inner wall. This is seen as a slight negative radial velocity in figure 3.2(b) at x=-30mm. From the same profile in the core region it is seen that the flow from the recirculation is being transported away from the centre line to mix with the core flow, and eventually pass downstream of the jets. Without this mixing the recirculation bubble, fed by the impinging jets, would continue to grow further and further upstream. Up to this axial location no significant azimuthal velocity can be seen, as may be expected on a θ=constant plane of symmetry. At x=-5 and 5mm the recirculation in the core is still evident, suggesting that the jet, issuing in this plane from -10<x<10mm, is being bent downstream as it penetrates the core flow. The reversal in direction of axial velocity between x=5 and 15mm indicates that the jets impinge between these two points. At x=40mm the jets have merged and a peak axial velocity of $8.5U_c$ is seen at the centre line. This centre line velocity then begins to decay further downstream as turbulence begins to mix out the shear layers of the jet, evident at a radius of between 10 to 15mm. In the annulus, flow from out of the measurement plane is entering the plane in the lee of the port entry location, and the axial velocity profile is re-establishing itself to approximately half of that of the inlet velocity by x=75mm.

Constructing an autocorrelation function at impingement allowed the integral length scale to be calculated at around 15mm. (Integral length scale being an estimate of the

largest eddies - see Tennekes and Lumley (1974).) This equates to a time scale, τ, of 75ms, based upon the bulk velocity in the core. However, close to the impingement point, where the local velocity is much closer to zero the integral time scale will increase dramatically, thus requiring sampling periods of the order of hours for each measurement point. Furthermore, each of the three components of the rms velocity at the impingement point (presented in figure 3.3) is large, i.e., $u/U_c=1.7$, $v/U_c=3.6$, w/ $U_c=3.0$. These two effects combine to produce a large error due to statistical uncertainty being proportional to the number of statistically independent samples (i.e. separated by 2τ) and the ratio of the local rms velocity to mean velocity. Other secondary effects may play a further role in increasing the errors associated with measurements at impingement, such as long residence times of particles in the control volume, p.d.f. broadening due to turbulence and possible low frequency unsteadiness or periodicity of the flow at this point. The combination of all these effects are thought to be responsible for the slight positive values measured for the swirl component, W, around the impingement point. This effect is quite localised, and away from the complex singularity in the mean flow field around impingement, there is no swirl component measured, as would be expected.

The rms velocity profiles corresponding to the mean velocity profiles in figure 3.2 are presented in figure 3.3. Again, a good level of symmetry is seen about the centre line for each of the profiles. The level of anisotropy of the turbulence is quite striking. At impingement the axial fluctuations are approximately half of the radial and circumferential values as mentioned above. This result is reversed in the region just upstream of the recirculation, where $u \cong 2v \cong 2w$. As may be expected the level of turbulence in the annulus is much less than in the core. One interesting feature is that at x=-5mm the higher level of turbulence is seen toward the outer radius, whereas downstream of the port the higher levels are found at the inner radius. To understand this, and other features identified from the measured array of 1D profiles it is beneficial to construct 2D field plots from them.

3.2.2 Core Flow Field

Figures 3.2 and 3.3 have shown that the flow field under investigation is very complex, containing large scale recirculations, high levels of turbulence and significant anisotropy in the turbulence field. The totality of the experimental data is much more understandable when presented in the form of velocity vectors and contour maps, given in figures 3.4 to 3.7 for the core flow.

Visualisation of the core flow field is straight forward by examining the velocity vectors of figure 3.4, which are calculated from the data given in figure 3.1. It is quite easy to identify both the jet and upstream recirculation, centred about $(x,r) = (-8,22)$mm. The jet centre-line could not be traced directly with the laser arrangement, as is often performed with intrusive probe methods, by *tracing the locus of maximum velocity*. Therefore, to establish the trajectory of the jet figure 3.5 shows "streamlines" calculated from the measured velocity field (n.b. assuming no out of plane velocity component). Both the deflection of the jet and the extent of the upstream recirculation can be clearly seen. Much of the core flow seen passing around the recirculation, then being entrained into it by the jet, actually passes around the jet and re-enters the $\theta=0^{\circ}$ plane in the lee of the jet. This explains why the fluid being entrained by the lee of the jet appears to be issuing from the wall. In reality this downwash occurs where the fluid passing around either side of the jet has met and is entrained by the jet. It is clear by considering these three figures in association figure 3.4 why this distribution in anisotropy occurs. At impingement the flow is originating from the jet and flowing radially inward (also from out of plane by the other jets) thus the radial and circumferential stresses are greatest. Upstream in the core, however, the flow is predominantly axial. In fact, the stagnation point in the mean flow at the head of the core recirculation could be considered as an impingement point where the flow deflected upstream from the jet impingement meets the core flow. In this case it is the axial stresses which are greatest in comparison to the secondary radial and azimuthal components.

Figure 3.6 shows the three normal stresses in the core, u^2, v^2, and w^2 non-dimensionalised by U_c^2. It is immediately obvious that the v^2 and w^2 fields are quite similar but strikingly different to the u^2 field. Around the impingement point in

particular there is no significant increase in the axial normal stress whereas in the circumferential and radial directions the normal stresses are over three times the magnitude found elsewhere in the flow. The most significant difference between the radial and circumferential normal stresses being in the vicinity of the jet exit. In the upstream edge of the jet the radial normal stress is greatest. Whereas in the lee of the jet the circumferential normal stress is greatest, possibly due to unsteadiness in the wake of the jet. This unsteadiness could be due to vortex shedding from the lee of the jet, (which is effectively a cylindrical blockage to the core flow) much the same as in a von Karman vortex street. The axial normal stress is greatest within the recirculation itself and extends further upstream than either the radial or circumferential normal stresses, such that u^2 is typically double v^2 or w^2.

In figure 3.7 the normal stresses have been combined to form the turbulent kinetic energy, k. It is seen that the dominating feature is the impingement point where k/U_c^2 is at a maximum of 16. In the lee of the jet, near the wall of the core pipe, a high level of turbulence is seen. At this point flow which has passed around the jet is entering the measurement plane from both sides and impinging, similar to the flow around a circular cylinder. Looking at the vectors in figure 3.4 this flow is then entrained by the jet.

Before looking at the flow field in the annulus, a more detailed look at the nature of the flow along the centre line will be taken. Figure 3.8 shows part of the axial velocity time history and the corresponding probability distribution function (pdf) measured at 10 axial locations. At each location 8192 measurements were made at 1kHz in ten blocks, such that each of the pdf's were constructed from 81920 samples, though only the first 10s of the velocity time history is shown. The pdf's at x=-150 and -125mm are seen to be very narrow, indicating a low level of turbulence, associated with the core inlet flow. However at x=-95 and more so by x=-75 occasional 'bursts' of negative velocity are seen. These are only just significant enough to be evident in the pdf, but are quite obvious in the time histories. These negative velocities have been described as bursts because flow visualisation has shown that they are due to a sudden increase in the size of the recirculation followed immediately by a collapse to its original size. Spectral analysis was carried out on the velocity histories at each axial location, but no

dominant frequency could be identified. At x=-57 the mean velocity was 0.012m/s, i.e., close to the upstream stagnation point. Here a bi-modal pdf is evident, being apparently composed of two superimposed gaussian distributions. From x=-19 to 63mm the pdf's have similar variance whilst the mean axial velocity increases along the centre-line. At impingement, (x=-19mm), several 'zero holds' have been imposed on the velocity history, because no data has been recorded. The validated data rate around the impingement point was observed to drop from 20 to 5kHz typically. Although this is on average 5 times greater than the sampling frequency, occasional periods are seen in which no measurements are validated by the IFA550 LDV signal processor.

In figure 3.9 an equation describing two gaussian distributions has been fitted to the pdf at x=-57mm. This was performed by utilising the non-linear curve fitting routine which is in essence a method of least squares fit by using a modification of the Levenberg-Marquardt algorithm, see Bevington (1992). Five variables have been obtained by using this method, the mean and variance of each distribution U_1, U_2, u_1 and u_2, and the proportion of time associated with each distribution, f_1 (noting that, $f_2=1-f_1$). The goodness of fit suggests that the flow is bi-modal, with flow associated with a mean of -0.1268m/s being present 54.05% of the time, (and with 0.1256m/s 45.95% of the time). This is strong evidence that two flow patterns occurred within the core, one with a large recirculation extending up to approximately x=-75mm and one with a significantly smaller recirculation. Data presented in this chapter from the core region therefore represent the resulting time-averaged properties of the flow field, as opposed to either of the individual flow states associated with a large or small recirculation. It is interesting to note that at this quasi-stagnation point the mean velocity of each mode is almost equal and opposite. Calculating the overall mean velocity from $U=f_1U_1+(1-f_1)U_2$, where each value is taken from the curve fitting routine, gives U=-0.011 m/s, close to the value of -0.012m/s measured directly. The non-linear curve fitting routine can be quite sensitive to the initial guesses required for each unknown, so this result gives some reassurance in the method. Moreover, it may suggest there is a better way to evaluate the five parameters required here. For example; if we obtain U_1 and U_2 from curve fitting, then use the knowledge of the measured overall mean velocity, U, to calculate f_1 from the previous equation, a

consistent set of parameters will be found. To do this some iteration would be required, but in this case, consistency has been demonstrated to a suitable level.

The turbulence levels which have been measured will also have a component due to the difference between the mean velocity of each flow field. On the initial evidence of this measurement it is the turbulence field associated with the large recirculation which will dominate. Here the normal stress calculated from the whole sample, $uu=0.0362$, is close to that of $u_1u_1=0.0372$ which dominates over $u_2u_2=0.0024$. However, if we consider an energy budget at this location, the turbulent kinetic energy in the two individual gaussian distributions is $1/2(f_1u_1u_1 + (1-f_1)u_2u_2)$ equalling $0.01060\mathrm{m}^2/\mathrm{s}^2$. This is $7.5\mathrm{x}10^{-3}$ short of that measured as a whole, $1/2(0.0362) = 0.0181\mathrm{m}^2/\mathrm{s}^2$. If we assume this is the energy associated with the switching from one mode to the other, we can also evaluate it from, $1/2u_{switch}^2 = 1/2(f_1(U-U_1)^2+(1-f_1)(U-U_2)^2) = 7.9\mathrm{x}10^{-3}\mathrm{m}^2/\mathrm{s}^2$, where u_{switch} is the rms velocity due to the changing between the two modes about the overall mean velocity. The similarity of these two figures gives added confidence to the consistency of this method, and shows that the measured rms velocity has three components:- one from each of the two gaussian distributions and one (not insignificant) from the switching between modes. From a modelling viewpoint, it is obvious that a time-averaged Navier-Stokes formulation will not be able to resolve this type of phenomenon. A more interesting question would be: would the RANS model time average the two flow modes or would it converge toward one of the two individual modes? Large Eddy Simulation would certainly be much better suited to this type of problem, but the complexity introduced by adopting such an approach might be wasted on the remaining 95% of the flow field being studied here.

To illustrate this bi-modal behaviour, the flow visualisation photographs in plate 3.1 taken approximately 3s apart show how the size of the upstream region varies considerably. The two snapshots of the core flow field support the above evidence that a bimodal flow field exists. The recirculation region evident in the mean flow field can only just be distinguished when studying the small time slice contained in each photograph. For this reason a video was taken of the flow visualisation experiments, which allows the viewer to construct an idea of the mean flow field. A video is available which records the core flow field for a sequence of R from 30 down to 2.

3.2.3 Annulus Flow Field

Repeating the same data reduction within the annulus as for the core, the resulting velocity vectors are presented in figure 3.10. This data was collected from plane 2 in figure 3.1, on the plane $\theta=0^{\circ}$, containing hole 1. In this figure a recirculation behind the port can be seen centred at around (20,65), with the flow separating from the outer wall at approximately x=10mm. The flow at x=20mm is clearly biased toward the inner wall, after being drawn into an inner radius by the presence of the port. Some of the fluid which is drawn from the outer wall appears to impinge on the inner wall behind the port and then flow downstream. The magnitude of the velocity vectors gradually increase from x=20 to 70mm due to mass flow entering the measurement plane circumferentially. This can be thought of as similar to a wake, since downstream of the ports there is a velocity deficit, thus mixing will occur with the flow passing between ports.

The peak value of turbulence in the annulus can be seen in figure 3.11 to be where the flow, separating from the outer wall reaches the back edge of the port, where it appears the flow is impinging on the inner wall. The turbulence field away from this point is dominated by the shear layer which exists around the recirculation bubble. Turning to figure 3.12 it can be seen how each individual fluctuating component contributes to the turbulent kinetic energy. The axial fluctuations are largest in the shear layer between the flow entering the port from the outer radius and the recirculation bubble, whereas the largest radial fluctuations occur between the same recirculation and the flow originating from the impingement immediately behind the port. In both cases the largest fluctuating components are normal to the local flow direction. The circumferential fluctuations are similar in distribution to the radial field, and are again largest where the flow impinges on the inner wall. The turbulence field in the annulus is thus greatest in the region downstream of the port inlet and the flow in this region is quite anisotropic.

To investigate the nature of the flow in the circumferential direction the axial velocity has been measured on r-θ planes coinciding with the most upstream and downstream points of the port, x=-10 and 10mm respectively, presented in figure 3.13. The bulk mean velocity upstream in the annulus is $2.5U_c$ consistent with a B of 50% and R of

5.0. The level of symmetry about $\theta=0^\circ$ is observed to be good at both stations. The flow has obviously accelerated into the front edge of the port at x=-10mm and the boundary layer on the outer wall is significantly thicker than the inner one. The radial distribution of axial velocity is biased towards the inner wall at all circumferential locations. These boundary layers also increase in size away from the port due to the migration of the flow from between ports to the ports. At x=10mm similarities to a wake behind blockage in the flow can be seen. The free stream flow between ports is also still biased toward the inner wall, with a peak value, $2.2U_c$, comparable to the annulus bulk inlet velocity. The bulk average velocity at this station is $1.25U_c$. Of interest here is the way in which the reverse flow feeds the port. The ratio between the integrated volume flow rates at each station is 49.7%, consistent with the 50% bleed ratio set during the test. However 1.01% of the flow passing through x=10mm returns back upstream, indicated by the unshaded regions (denoting negative axial velocity). Thus approximately 1% of the mass flowing through the ports enters the port from downstream of the port itself.

Further evidence of the growing boundary layer at the outer wall is seen in figure 3.14 in which the axial velocity fluctuations are larger at the outer wall at x=-10mm. Otherwise the turbulence levels are low upstream of the port as expected of a well-conditioned inlet flow. Behind the port the axial velocity fluctuations are dominant in the region which could be described as a wake due to the port entry flow field. The peak value of $uu/U_c{}^2$ is at the impingement point on the inner wall close to the rear edge of the port, consistent with the levels shown in figure 3.12a (which bisects this plane through $\theta=0^\circ$).

3.2.4 Jet Velocity Profile

As described in section 2.5.1 direct measurement of the radial velocity profile issuing from a port could not be performed with the LDA system. Figure 3.15 presents profiles which have been measured across a port diameter coincident with $\theta=0^\circ$ at r=45mm, thus the profile is measured over -10<x<10mm. The axial and circumferential velocities were easily obtainable, and figure 3.15(a) shows the measured U and W profiles at a port exit, labelled appropriately. Also shown are the four profiles of

velocity measured at $\pm 30°$ and $\pm 60°$ to the radial velocity component. Each of the two measured pairs could then be used to calculate the radial velocity component, and then compared to each other as an initial check of the technique. Both agreed well, though at $\pm 30°$ only the central region of the profile could be measured. The filled circles thus represent the exit radial velocity profile across this diameter calculated from the equations given in section 2.5.1 for the velocity data measured at $\pm 60°$ to the radial component. Across this port diameter it would be expected that the W component of velocity is zero due to symmetry, and it can be seen that the measurements support this. At the upstream edge of the port U is also small and V is negative, indicating that the flow from the annulus has separated from the inlet edge of the port and not reattached. This produces a small recirculation within the port itself which fluid from the core is entering.

Plane of measurement (figure 3.15)
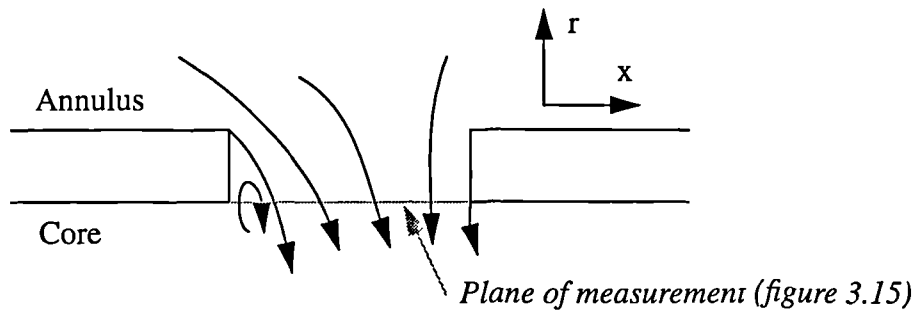
Except for the recirculation, the axial velocity is high towards the front of the port but reduces to zero at the back edge. This can be seen above to be due to the direction from which the fluid is fed to the port. Some of the annulus flow axial momentum is conserved at the front edge of the port, whereas most of the fluid entering the rear of the port has entered the port radially. The radial velocity is seen to be reasonably constant over the rear three-quarters of the port, rising slightly toward the downstream edge. It may be expected that because the velocities have been normalised by the bulk average radial velocity through the port, the radial profile would be closer to 1.0 over the plateau region. However, due to the vena contracta formed by the flow, the plan area of the port, A_p, on which the bulk velocity is based is reduced by the contraction coefficient, C_c, to the effective area A_e, thus higher through port velocities are seen. C_c, can be estimated using a mass flow balance from, $1.0A_p=1.5A_e$ and $C_c = A_e/A_p = 0.66$. Although this is a rough estimate, the discharge coefficient, C_d, measured for this configuration was 0.639 and it is expected that C_d be slightly less than C_c since $C_d =$

$C_c\ C_v$ where C_v is the ratio of actual jet velocity to the expected ideal velocity (usually close to unity). This evidence would suggest that in this case the plateau of $V/V_j = 1.5$ covers two thirds of the port.

The variation of flow angle from the port exit shows that the flow becomes increasingly perpendicular to the port towards the rear of the port. At the upstream edge the angle becomes negative, due to the recirculation at the front of the port, which is seen to occupy the first 3mm of the port. From the recirculation to the centre of the port a flow angle of 66° to 70° is observed, then rising to almost 90° at the rear edge of the port. Since the profile of radial velocity is level over this region the variation in flow angle is mainly a function of the axial velocity. Looking back to figure 3.10, we see how the history of the flow entering the port has determined the flow angle at exit of the port. The front of the port being fed by the upstream annulus, which retains much of its axial momentum. At the rear of the port the flow enters more radially, with flow entering from the outer radius of the annulus.

In figure 3.15(b) the turbulence profiles coinciding with the above velocity profile are presented across the port diameter. It is evident that the central portion of the jet contains relatively low (5%) turbulence intensity which is isotropic. At both the upstream and downstream edges the turbulence increases. The high turbulence at the upstream edge is coincident with the shear layer between the small recirculation contained in the port and the jet. The higher levels at the rear of the port are probably as a consequence of the flow history of the fluid entering this region, supported by the composite plots of the next section.

3.2.5 Composite Plots

As a summary to this section the field plots of the core and annulus have been combined along with the measured jet exit profiles to form a composite picture of the velocity vectors, figure 3.16, and turbulent kinetic energy, figure 3.17, on a diametral plane through a port centre line.

It is particularly interesting to observe the interface between the three regions. The back flow into the port from the core is evident at the upstream edge of the port shown

by two upward pointing vectors. The jet angle variation across the port can also be seen from the jet exit velocity vectors. The relative magnitude between the turbulence levels in the annulus and core is evident and it would be expected that small variations in the annulus turbulence field would have little effect on the core flow the turbulence field of which is dominated by the jet impingement.

3.3 Dilution Port Flow Configuration

3.3.1 Core Flow Field

The two jet to core velocity ratios reported in this work, R=5.0 & 2.0, are typical of primary and dilution jets respectively. The resulting flow fields differ in that the primary jets impinge and create a recirculation zone (figure 3.4), whereas the dilution jets are deflected downstream before they have chance to impinge, thus no reverse flow exists in the core. The core flow field can always be catagorised by one of these two flow scenarios. For the plain port geometry, impingement occurs when R is greater than around 2.7. However it was noticed that this depended upon whether R was gradually decreased from an impinging flow configuration or increased from a dilution jet configuration. This hysteresis effect, which was not studied in detail, should be avoided as it could result in an unstable operating point. This statement may raise some questions in the reader's mind as to whether this may have effected the results at R=2.0 and 5.0. The hysteresis could be summarised in the sketch below, with estimated values of jet to core velocity ratios (R) which are important to this process for the current configuration;
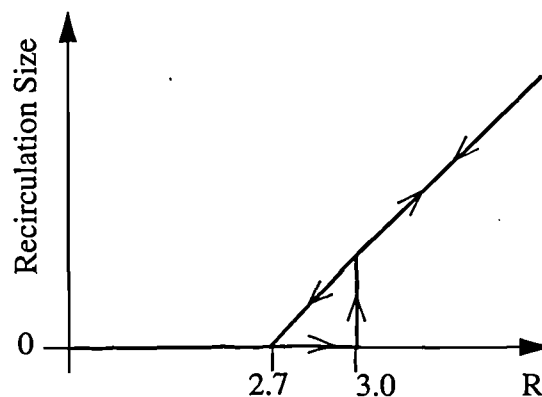
It was apparent that as it was attempted to form a recirculation from a non-impinging situation the value of R required was higher than that which would sustain a recirculation when R was decreased from an impinging situation. The hysteresis could be considered to be due to a "start-up" energy which is required to produce the recirculation. The range over which this occurred did not have any influence on the results taken for the dilution and primary flow configurations.

Figure 3.18 shows the calculated velocity vectors for the dilution flow configuration. At the rear of the port the jet enters almost perpendicularly to the cross stream flow but is rapidly deflected down stream. At x=30mm the jet core would appear to be at a radius of 17mm, however, at the exit plane the jet has clearly mixed with the core flow and the peak velocity is at the centre line suggesting the six jets have merged. This can perhaps be better seen in figure 3.18b, in which the jet core is highlighted by the concentration of "streaklines". At x=25 and 60mm the highest radial velocities are coincident with the jet core, as expected. Between x=60 and 120mm however, the fluid along the centre-line has accelerated, as the jet's momentum has mixed with that of the flow close to the centre line.

Figure 3.19 shows that the components of normal stress are distributed similarly and are of roughly equal magnitude. Circumferential velocity fluctuations are most dominant in the lee of the jet exit, possibly due to the shedding of the bound vortices. The near isotropic flow thus leads to the turbulent kinetic energy distribution being of similar distribution to that of the individual normal stress components. Figure 3.20 shows that in this plane the highest turbulence is contained within the jet entrainment region in the lee of the jet. When normalised by the jet velocity this is of similar magnitude to the value found in the lee of the jet for the primary configuration, $(0.9/2^2$ =0.225, compared with $5.0/5^2 = 0.20$ from figure 3.7). This would suggest similar mechanisms acting in this region though the effect is much less pronounced in the primary configuration due to the dominance of the impingement zone.

3.3.2 Annulus Flow Field

Looking back to figure 1.1 it is seen that primary ports are upstream of dilution ports. The consequence of this is that the primary ports have a higher bleed ratio, since any

feed air to the air admission ports further downstream has to bypass the primary ports. The difference between the annulus flow for the two types of port is thus the proportion of bleed flow. For the dilution port setup less of the annulus air bypasses the port, i.e. more passes into the port proportionally than in the primary case.

Figure 3.21 shows the velocity vectors in the annulus for a bleed ratio of 20%. Comparing this with figure 3.10 it is evident that there is significantly more reverse flow downstream of the port (shaded region), indicating much more of the flow is entering the port from downstream. The extent of the region of negative axial velocity is much greater and the separation point of the flow from the outer wall has moved upstream of the port's centre line. The result of this scenario is that the flow entering the port does so more perpendicularly in the central region. This can be clearly seen from the velocity vector directions as they enter the port. A similar recovery of the annulus flow downstream of the port is evident with the flow initially biased towards the inner wall. Properties of the annulus flow downstream of the port (such as the inwardly biased axial velocity profile) will have some effect on any air admission holes downstream of the port. It could hardly be expected that a cooling ring close to the rear of the port would be fed evenly: the amount of flow through the holes within the ring would be dependent upon whether it was in-line, or between the port.

In addition to this, all of the approach flow profiles reported here have been fully developed, but: How significant would a change in this profile be on the detailed flow properties of the port being fed? It is not possible to answer this question here, but only point to where its influence would be greatest. With lower velocities and higher turbulence levels to promote mixing in the dilution set-up, the radially inward bias of axial velocity is no longer obvious by x=70mm. In the primary configuration however (figure 3.10), the flow still exhibits significant bias towards the inner wall at x=70mm (3.5 port diameters downstream). This is unfortunate since the upstream air-admission holes of a combustor will always have the highest bleed ratios, resulting in unknown conditions for any ports downstream. If flow profiles are important to subsequent rows of holes then either some manipulation of the flow will be required or further investigations will be required to reveal any unidentified effects of non-uniform - but quite probable - annulus feed velocity profiles.

The normal stresses shown in figure 3.23 have a very similar distribution to those found in the primary case. Some care has to be taken in comparing the absolute values however. The turbulence quantities in the annulus have been non-dimensionalised by the bulk core velocity. In changing the flow conditions the ratio of annulus bulk velocity to core bulk velocity has changed significantly; U_a/U_c =2.5 in the primary setup and U_a/U_c =0.625 for the dilution case. Hence to compare turbulence quantities in the annulus based on the annulus bulk velocity for these two cases the values presented in each must be divided by the appropriate $(U_a/U_c)^2$. Alternatively the values in the dilution setup can be multiplied by 16 ($2.5^2/0.625^2$) and then compared to the primary setup values which have been non-dimensionalised by the core bulk velocity. Performing this process for the turbulent kinetic energy levels figure 3.22 (c.f. 3.11) shows that the peak level of turbulent kinetic energy within the annulus increases by threefold when reducing the bleed ratio from 50% to 20% (0.8 compared with 0.15*16=2.4). This peak value can be seen to occur at the rear of the port where the flow entering from upstream meets the flow entering from downstream. For the dilution setup this occurs within the port entrance itself, though for the primary case it occurs at the rear edge of the port. This is evidence that the increased size of the separation bubble in the dilution case has increased flow instability, raising overall turbulence levels. Because more of the fluid is entering the port from downstream in the dilution case, higher levels of turbulence will also be expected within the jet itself, particularly towards the rear. This will confirmed in the next sub-section when looking at the distribution of stresses across the exit of the port diameter.

Figure 3.24a shows the axial velocity distribution for a sector of the annulus at x=-10mm, and may be compared with figure 3.13a. By the previous non-dimensionalisation argument, to compare levels with those in figure 3.13, the values in this figure must be scaled by 4.0. The bulk average velocity upstream of the port is $0.625U_c$ which is 1/4 of that in figure 3.13. At inlet to the annulus the maximum axial velocity would be 120% of the bulk average, (see table 2.1). The area of flow accelerated to 0.75 or greater is larger for the dilution setup than for the primary flow setup, particularly in the radial direction. This would indicate that as the proportion of annulus flow entering the port is increased it is from the circumferential direction that more flow is drawn. This, in part, may be due to the presence of the outer annulus wall.

However, the annulus height is fairly typical of combustor geometry, so this effect is quite realistic.

Figure 3.24b again shows the axial velocity distribution for the same sector at x=10mm, just downstream of the port. The unshaded contours indicate the region of negative velocity, i.e. back flow into the port. By integrating to find the volume flow rates through both planes (x=-10 and x=10mm) it is possible to determine the volume flow rate through the port by calculating the difference. To find only the amount of back flow on the x=-10mm plane, the above integration is repeated but for only the region of negative velocity. Using this process it can be calculated that 16% of the flow passing through the port has entered from downstream of the port, further confirmation at the increase in flow complexity over that at higher bleed ratios.

3.3.3 Jet Velocity Profile

With a reduction in bleed from 50% to 20%, and the resulting increase in flow entering the port from downstream, a marked difference can be seen between the jet characteristics of the primary and dilution flow configurations. The radial velocity profile shown in figure 3.25a shows a distinct peak at the rear of the port, which is the most striking difference between figure 3.25a and 3.15a. The axial velocity also becomes negative at the rear of the port. Both of these features could be accounted for by the increase in flow entering from downstream of the port. It should also be noted that since the normalised radial velocity is typically between 1.4 and 2.0 a significant area of the port must contain regions of radial velocity less than the bulk mean, $V/V_j <$ 1.0, through the port. Some of this is seen to be at the front edge of the port, though this must extend around the upstream circumference of the port to account for the apparent high proportion of mass entering through this diameter.

As a result of these differences in velocity profile the distribution of flow angle across the port diameter is significantly different to the primary jet. At the rear of the port the flow is much more aligned with the port centre-line, being steeper than $90°$ for $0.5 < x/r_{port} < 0.7$. α being greater than $90°$ indicates that this flow entered the port from the down stream annulus, as supported by figures 3.24b and 3.21. The portion of the jet fed from the upstream annulus exhibits similar velocity profiles as the primary jet, from

the front through to the core of the jet. Averaging the flow angle across the diameter shows the dilution jet is around 5° steeper.

Comparing the turbulence levels across the dilution jet, figure 3.25c, with those of the primary jet, figure 3.15b, shows similar trends. Despite the relative turbulence levels in the annulus between the flows, by the time the flow has been accelerated through the port, the levels of rms velocity are seen to be quite similar. As with the mean velocity profiles, the front half of the jets contain similar distributions of rms velocities, though at the rear a larger portion of the dilution port contains high turbulence levels due to the flow history, as discussed. In practical terms these levels are quite low compared with those found in the core flow of either the dilution or primary jet, thus the small change due to differing annulus bleed ratios would not be expected to have significant impact on the core flow field, nor the level and distribution of turbulence it contains.

3.4 Effect Of Varying The Proportion of Bleed Flow

Flow visualisation was initially used to examine the effects of changing the bleed ratio, B, in the annulus whilst the jet to core velocity ratio was kept constant at R=5.0. Air bubbles were produced in the flow, as described in chapter 2, and these illuminated with a light sheet. Naturally the air bubbles experienced buoyancy effects though this was only significant in particularly stagnant regions, and on the whole a informative insight into the flow topology could be gleaned. Photographs of the flow proved useful for high bleed ratios, or in the upstream region for lower bleed ratios. High turbulence levels in the lee of the port entry for low bleed ratios made interpretation of 'snapshots' quite difficult in this area.

The photographs in plate 3.1 shows two snapshots of the 'primary' flow field, as described in section 3.2. The trace lines are longer in the first photograph as this was taken at a shutter speed of 1/15th s and the second at 1/30th. The annulus flow features described in section 3.2.3 can quite clearly be seen, such as:- the flow being swallowed by the port, the stagnant region established on the outer annulus wall, and the 'fan' of fluid reestablishing the annulus flow behind the port. Comparing the photos with figure 3.10 also shows good similarity. It is predominantly the near stagnant regions, such as on the outer annulus wall in the lee of the jet, which are hard to distinguish.

Interpretation of the flow in these regions is difficult principally due to directional ambiguity, short time traces and high turbulence levels.

The ability to watch and follow the flow allows the observer to construct an image of the flow field, thus a video camera was also used to record the flow field. Several values of bleed ratios were recorded and representations of the streamlines can be seen in figure 3.26. The bleed values were chosen to show the principle flow patterns found across the whole range of bleed ratios. The reported bleed values have been carefully estimated by examining consecutive frames of the video to determine the particle inlet velocities. This was necessary because the LDA equipment was unable to measure within aerated flow. However, R was kept at around 5.0 as the bleed was varied by observing the size of the core recirculation and keeping it constant.

At a bleed ratio of around 80%, shown in figure 3.26a, the outer annulus wall has little effect on the flow field. The flow closest to the inner wall enters the port and the remaining fluid diffuses out into the downstream annulus. When the bleed ratio was reduced to 50% (3.26b) a significant recirculation has formed on the outer annulus wall since the flow is then separating from the outer wall. Separation from the outer wall occurs when the bleed ratio is reduced to around 60% for this annulus geometry. At a bleed ratio of 40% (3.26c) this recirculation has grown in size and it begins to interact with the inner annulus wall. Flow of fluid into the region behind the port can now only enter circumferentially (out of plane), since the separation streamline from the outer annulus wall now enters the rear of the port. Previously this was drawn to the inner annulus wall behind the port, and then continued downstream. When B is reduced further to less than 20% (3.26d) this separation streamline enters the port almost perpendicularly, and close to the centre of the port. A significant proportion of fluid is now entering the rear of the port from downstream. It is apparent that the fluid takes a complex route for this to happen. Fluid which has passed between ports and also flows close to the rear of the port circulates back to the outer annulus wall before being swallowed by the port. Although this region of the flow is quite unsteady, it is the sketched flow structure which appears most dominant. Again with no bleed flow a similar, but larger recirculation is apparent (3.26e). With no mean axial flow

component in the downstream annulus this recirculation drives a series of smaller recirculating eddies further downstream in the annulus.

The above sequence has only focused on an azimuthal plane through the centre of a port, a plane which could theoretically be considered a plane of symmetry. This pseudo 2D flow picture has only hinted at the complexity of the flow topology. With the adopted experimental techniques it is only possible to estimate the mean stream tubes in 3D, and figure 3.27 shows the three principle flow patterns found as interpreted from several flow visualisation experiments. The annulus has been drawn rectangular in shape for ease. It has to be stated again that these diagrams are interpretations of the flow as averaged by the eye. The three sketches can be related back to the previous figure to understand the way in which flow enters the port in each case. The vortex structures shown behind the port at 10% bleed are drawn symmetrically about the plane of the previous figure (3.26). It was observed however, that at any one time it would be likely one of the two "hoops" at the rear of the port would be more dominant than the other. When this occurred, the axis of the dominant vortex would move from being in the azimuthal direction to being radial - a possible hint toward the origin of the through port vortex, as noted by previous workers, Carrotte (1990) and Baker (1992).

In an attempt to capture these flow patterns experimentally the velocity fields were measured in the annulus for several bleed ratios, 50, 40, 25 and 10%. Each of these tests being carried out with R=5.0. To enable evaluation of the streamlines the measured velocity profiles were superimposed onto a common grid as described in section 3.2.2. The 2D "streamlines" were then evaluated for the mean flow in this plane. Similarities in the sequence of figures 3.28a-d and 3.26 a-e can clearly be seen. The separation bubble in 3.28a is enclosed by a streamline which enters close to the outer wall, passes around and under the recirculation, nearing the inner wall then moving back out towards the outer radius. Reducing the bleed ratio by 10% has a large effect. In figure 3.28b the streamline entering close to the outer wall now enters the port at x=4mm. Thus the larger recirculation is being fed from out of plane fluid which then enters the port behind the separation streamline. As the bleed is reduced further to 25 and 10% this separation streamline moves further upstream in the port, at 10%

being close to entering at the port centre line. The random looking streamlines at x>40mm are caused by an insufficient sampling period of highly turbulent flow with near zero mean component.

Mention has been made on several occasions in the previous text about the appearance of through-port vortices at low bleed ratios. Figure 3.29 shows the first evidence of this occurring in the current arrangement. To avoid concerns raised by the effect of rotating the test section, the secondary through-port velocities have been measured here for only ports 1 and 4. This could be done easily because both lie on the optical axis when port 1 is at $\theta=0^{\circ}$ and port 4 is at 180°. Rotation was shown not to have significant effect on the mean flow field in chapter2, but it was observed that the vortices were quite unstable and test section rotation was thought to be less acceptable when considering interactions between individual ports. Flow visualisation was used in conjunction with the LDA measurements to establish the predominant vortex direction in each of the six ports. Figure 3.29 displays how the vortices appear to act in pairs. If each neighbouring port has a vortex rotation in the opposite sense the pattern of clockwise/anti-clockwise vorticies shown in the axial section would be found. With this pattern in mind, it would be expected that ports 1 and 4 would have vortices in opposite directions, and the secondary velocities across each diameter show this is the case. Care has to be given to how the sense of rotation is defined, which is always that perceived if looking radially inwards from above the port. (If we view the vortex through ports 1 and 4 both from above port 1 then they would appear to rotate in the same direction.) Looking more carefully at port 1, with the information available it may be construed that the vortex is acting in an anti-clockwise sense. The centre of the vortex will be shown to be at or downstream of the rear edge or the port, thus the positive azimuthal velocity indicates the upstream portion of the vortex rather than the downstream portion. These measurements were taken at the entry plane to the port and could not be continued further downstream.

Figure 3.30 helps convey the messages of the last paragraph by again using the results of flow visualisation. The flow sketched for the right-hand port would be similar to that of port 1 in the previous figure. The dominant vortex, affecting the through-port flow is in the clockwise sense, and it can be envisaged how this would lead to a positive

azimuthal velocity on the port centre-line over the rear half of the port. The more important message of figure 3.30 is how the vortex pairs interact. Firstly we must consider the fact that the through-port vortex is the more dominant vortex of a pair which each port has at low bleed ratios, as shown previously in figure 3.27c. What we see from the current sketch is that this other vortex does not disappear, but forms a vortex line with the minor vortex of the neighbouring port. The neighbouring port will then have its dominant vortex acting in the opposite sense. This system could quite clearly be seen, albeit intermittently, with flow visualisation. Video evidence of this was also captured, though it is not as clear as it is during first-hand observation. It is possible to see how this flow pattern is self-sustaining by looking at the streamlines between ports. The outer two streamline pass downstream of the ports, but because there is no or little bleed flow, these turn back upstream behind the ports. This flow then meets that flowing between the ports concerned, and the two flows "roll-up" and a vortex line connecting the two ports is formed. This is shown in cross-section below the main figure. This pattern encourages eddies of size comparable to the annulus height to form in the downstream annulus, in which the net mass flow is zero. These eddies may then influence the fluid motion in other neighbouring ports.

Whilst the proceeding flow visualisation has not really provided quantitative analysis of the annulus flow field, a substantial understanding of the nature of the flow has been gained. This understanding would be difficult to obtain in any other way due to the complexity of the highly 3D flow. This is true at low bleeds particularly, where complexity, turbulence and/or unsteadiness are at their highest. Experimentally the best method for examining this type of flow quantitatively would perhaps be PIV, which was not available for this study. However practical information has been acquired by flow visualisation alone. Principally the nature of the vortices, which could help design of flow control devices in the annulus, and the lessons learned from the effects of inserting blockages in the upstream feed air. Note, as described in chapter 2, the 4 thick struts were quickly replaced by 6 thinner NACA 0015 profiled struts, which were each aligned between port centres.

To close this section, it is worth noting the effect on the core flow of varying the bleed ratio. The change in the location of the impingement point and the size of the core

recirculation for the four tests shown in figure 3.28 are presented in figure 3.31. The sketch at the bottom of this figure explains how these quantities have been determined from the zero-crossings of the axial velocity, when plotted along the centreline. By considering the impingement point, it is clear that the overall jet trajectory has steepened as the bleed is reduced from 50 to 40% then little change is observed as the bleed is reduced further. This movement of the impingement point upstream is a direct consequence of the mode of supplying air into the annulus, being more vertical at a bleed of 40% and less - as previously described. This evidence supports the idea of differing modes of flow in the annulus. Consequences of this could be quite serious for the performance of a combustor, in which the jet trajectory is used to control the aerodynamic zones. If any of the ports operate close to a point where this mode change occurs, the stability of combustion may be detrimentally affected. The recirculation size decreases more gradually with decreasing bleed, rather than having an obvious step change. This is though to be due to the increasing amount of turbulence which has been shown to exist within the port as bleed ratios are decreased. As the jet's turbulence levels increase then so will its diffusion as it penetrates the core-flow, resulting in a weaker impingement. This weak impingement will then produce a smaller upstream recirculation. Another, possibly contributory explanation would be that the proportion of jet mass flow which splits upstream and downstream at impingement is dependent upon the jet angle. However, if the jets are being used to promote mixing within the core, reduced mixing will occur as the annulus bleed reduces.

Bleed ratios higher than 50% could not be obtained whilst keeping the jet Reynolds number above 2.4×10^4. This was because these bleed ratios were not considered relevant to flows typical of combustors at the onset of this work. The facility was thus not designed beyond this limit, though slight modifications would make it possible. To complete the picture, and to help design of future combustors, which may have higher bleed ratios, (due to axial staging for example) further work could be undertaken in this area which could be of substantial benefit to both combustor designers and modellers.

3.5 Port Shape Effects

Numerous port geometries have been employed for combustor air admission ports, though the majority of those used have been variations of plain, chuted or D shaped geometries, each with varying levels of inlet radiusing (plunging). The table below shows the measured C_d's for each port shape studied here, including the values predicted by the correlations of Adkins(1986) and Lefevbre(1983).

Table 3.3 Measured Discharge Coefficients

Port Shape	Plain		Chuted		D shaped	
flow condition	Primary	Dilution	Primary	Dilution	Primary	Dilution
Measurements	.639	.649	.812	.875	.647	.661
Adkins 1986 (Difference)	.593 (7.8%)	.611 (6.1%)	-	-	-	-
Lefebvre 1983 (Difference)	.604 (5.8%)	.617 (5.1%)	.783 (3.7%)	.807 (8.4%)	-	-

The discharge coefficients obtained for the plain port are around 6% greater than implied by the two empirical correlations. This difference is probably due to the significant thickness of the liner wall used in these tests, being 0.25 port diameters in thickness, whereas an actual combustor port thickness would be typically less than 0.1 port diameters. The thicker wall was required here to allow accurate construction and maintain circularity of the acrylic pipe. A small increase in C_d would thus be expected as some additional pressure recovery would occur within the port, see Hay (1992) for the effects of port length to diameter ratio on C_d. Some difference is also seen between the values obtained for the chuted port in the present experiment and those predicted by Lefebvre(1983). However, the chuted port geometry is not described in Lefebvre, and again differences in port geometry may be the cause of the discrepancy. Changing the flow configuration from primary to dilution is observed here to produce a slight increase in C_d, for all port shapes, as predicted by the Lefebvre correlation. It is seen in these six comparisons that the measured C_ds are typically 6% higher than those previously reported, but despite this the present results follow the trends well, thus it is fair to compare the results found here with each other. Repeatability of the tests was found to be within 2%, which forms a guide to what is a significant difference in values. The C_d of the D shaped port is slightly higher than that of the plain port, but the chuted port's C_d is approximately 30% higher than the plain port. This emphasises the

effect of increased port length on the C_d, which, along with the inlet radiusing, increases the size of the vena contracta, hence C_d. More will be reported on the details of the jet after the annulus flow has been considered.

3.5.1 Port Shape Effect on the Annulus Flow Field

To compare the differences in the annulus flow field due to port shape changes the dilution flow configuration has been focused upon. In the dilution scenario it has been shown that fluid enters the port from all directions, and would therefore be expected to have a larger dependence on port shape than the primary flow configuration. Figure 3.32 presents the velocity vectors on plane 2 (refer back to figure 3.1) for the chuted and D shaped port. Comparing figure 3.32 with figure 3.21 shows only one significant difference between the velocity vectors on this plane for the three port shapes. Looking closely at the vectors entering each port it can be seen the vectors at the front and rear edge of the chuted port contain a much larger radial component than the other two ports. The inlet radiusing of 5mm (not shown) has allowed the fluid to flow around the smoother periphery of the port reducing the effects of flow separation at the port edges as experienced by the plain and D ports. The result of this is the flow entering the chuted port is much better conditioned than that of the other two cases. Because each port carries the same mass flow and the chuted port has a more even radial velocity component entering the diameter shown, the magnitude of the velocity entering it is noticeably lower at the 3 centrally measured locations. The remaining flow field is quite similar on this measurement plane, each containing a similar region of reverse flow, as indicated by the shaded regions.

The turbulence fields for the chuted and D ports shown in figure 3.33 also have a similar distribution to each other and to the plain port. In considering the magnitude of the non-dimensionalised turbulent kinetic energy, k/U_c^2, a significant range is seen in the peak value found at the rear of the port. In the case of the plain port there is a peak value of 0.21 in the region where the flow from the downstream annulus enters the port. For the D shaped port this level has reduced to 0.15. This occurs because the back flow has a larger circumferential span through which to enter the rear of the D port than a circular port thus reducing flow accelerations in an unsteady region. A further

reduction is seen at the rear of the chuted port where the peak k/U_c^2=0.1. Again this could be attributed to the reduced flow acceleration over the radiused rear edge of the port. Moving away from the region of peak k/U_c^2, for each port shape the 0.05 contour line describes a similar arc around the peak of radius similar to that of the port. Outside of this level each port shape has a similar turbulence distribution and magnitude.

Moving attention to the axial velocity distribution across plane 6 (see definition in figure 3.1) significant differences arise due to changes in the port shape. On the upstream, x=-10mm plane, the differences observed for the three port geometries are small, figures 3.34, 3.35 and figure 3.24a. The 1.25 contour level is closer to the wall for the chuted port since at θ=0°, the inlet radiusing takes the port surface 5mm below the wall shown in this figure. A larger azimuthal influence can be seen of the chuted port by comparing contours at U/U_c=0.75. It would appear the inlet radiusing of this port encourages flow to enter the port from increased azimuthal directions, possibly reducing the extent of the recirculation in the annulus behind the port.

The distributions of axial velocity at x=10mm for the chuted port and x=8mm for the D port however are each significantly different. Looking at the table below shows the relative amounts of fluid entering the port from up and downstream.

Table 3.4 Flow Paths In the Annulus

Port Shape	Plain	D Shaped	Chuted
path 1	34%	32%	27%
path 2	66%	68%	73%
path 3	13%	12%	4%
path 4	79%	80%	77%
path 5	21%	20%	23%
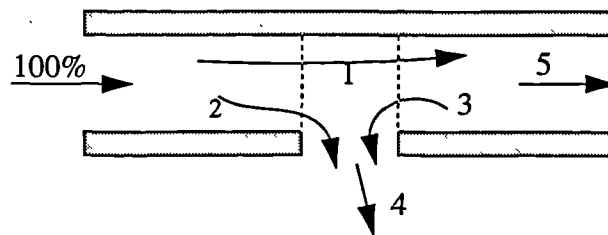
The splits for the plain and chuted port are quite similar with 12-13% of the annulus mass flow entering the port from a plane at the downstream edge of the port. It appears for the chuted port that a third less fluid enters from the rear, indicating much more fluid is able to enter the from the sides of the port. This is supported by looking at figure 3.34, it is evident that the 0.4 contour line close to the inner wall has been drawn towards the port by comparing it to both the distributions for the plain and D shaped port. With a reduced mass flow into the rear of the port the peak velocity is reduced from $1.25U_c$ to $0.6U_c$. This reduction is also seen for the D shaped port, but a much larger region is encompassed by the $0.6U_c$ contour line, since the back of the D is coincident with the measurement plane.

Figure 3.36 again shows the axial velocity distributions on the same sector for the D port with 50% bleed. Compared with the plain port this figure shows that the inner reverse flow region has disappeared and that the outer one has reduced in size. This supports the marginal reduction in back-flow into the port seen with 20% bleed in changing from a plain to circular port of 1%. At 50% bleed 1% of the port flow entered from the down stream plane for the plain port, and with the D port no back flow into the port is evident. The significance of this is that the velocity deficit is reduced in the wake of the port exit and the annulus flow is able to recover sooner downstream. Each of these downstream sector velocity distributions also indicates why it is advisable to cicumferentially stagger consecutive rows of air admission ports along a combustor. A port in line with the one measured behind would be fed with poor quality air, with high levels of turbulence and reduced dynamic pressure. Positioning downstream ports in the mid plane between ports has the advantage that the flow is already biased toward the inner wall and has high dynamic pressure.

Changing to a new perspective of the flow in the annulus, figure 3.37 describes the velocity field on a radial plane just above the entry plane of the plain and D-shaped ports. Flattening of the radial plane has been done by plotting $r\theta$ against x to maintain a 1:1 aspect ratio. The 2D stream-traces could be considered to be close to what would be seen if oil-trace flow visualisation had been carried out on the inner wall. With this in mind, and considering the flow pattern sketched for a bleed of around 10% in figure 3.27, it is possible to understand how these "stream-traces" have been formed. Clearly

the bottom of the two vortices (described as loops) can be seen sitting behind the ports, almost symmetrically, but just off to one side in both cases. The origin of the back-flow into each port, as shown in the previous figures, can also be seen. Quite narrow bands of fluid between ports then diffuse into what could be described as the wake behind the port. What is a significant change in geometry at the back of the port has not really brought about significant changes in the flow pattern. The most striking difference is the width (in this plane) of the fluid being swallowed by the ports. The widest distance between streamlines to be swallowed is 40mm for the plain port, which rises to 44mm for the D-shaped port.

3.5.2 Port Shape Effect on the Jet Characteristics

Chuted ports are used generally only for primary or intermediate ports. To compare the port exit velocity profiles of the three port shapes attention has therefore focused on the primary flow configuration, in which each port shape may be used. In figure 3.38 the radial, axial velocities and flow angle distributions across the exit diameters of the three port shapes are presented. Note that the D-shaped port data stop at $x/r_{port}=.73$ since its axial length is foreshortened to keep its area consistent with the other two ports.

The radial (through-port) velocities are quite similar for the plain and D-shaped ports, as are the axial velocities and hence flow angles. Differences between the axial velocities are seen over the rear half of these two ports, which reflects the small differences in the way fluid enters the rear of the ports, as shown earlier.

An exit velocity lower by about 12% is observed for the chuted port than for the plain or D-shaped. At first glance this could appear not to be consistent, since the port has a higher C_d. However, it is the mass flow which is being kept constant for each port, as opposed to the pressure drop. Thus a port which has a higher C_d will also have a larger effective area, and for the same mass flow, a reduced through-port velocity. In an engine configuration it would be the pressure drop which would be fixed, thus changing from a plain to chuted port would result in a higher mass flow through that port.

The magnitude of the axial velocity is also reduced at the front of the chuted port in comparison to the other two. This reflects the ability of the inlet radiusing of this port to reduce the onset of separation from the upstream lip of the port. It appears that there is some separation, but almost half of that of the other two ports. Away from the front edge the exit flow angle is quite consistent for the three port shapes. This suggests that the direction of the jet core is principally dependent on the flow conditions rather than port shape. Evidence collated by Lefebvre(1983) supports this finding. The correlations of Lefebvre used earlier in this chapter are:

$$C_d = \frac{F(K-1)}{\left[4K^2 - K(2-\alpha)^2\right]^{0.5}}$$

where, α is the hole mass flow rate divided by the annulus mass flow rate (i.e. α=1-B), F is a factor based on hole shape (1.25 for circular ports and 1.65 for chuted ports) and K is the pressure-drop coefficient:

$$K = \frac{\text{jet dynamic pressure}}{\text{annulus dynamic pressure}} = 1 + \frac{P_a - P_c}{0.5\rho U_a^2}$$

To evaluate the initial jet angle θ_j (i.e. at exit of the port) the relationship;

$$\sin^2\theta_j = \frac{C_d}{C_{d,n}}$$

is suggested by Lefebvre, in which $C_{d,n}$ is the value of C_d as K tends to infinity. The only parameter dependent on port shape, F, cancels when evaluating θ_j, and it is seen that the initial flow angle is independent of port shape. The evidence of figure 3.38 supports this, but some differences are noted in the detail between certain ports. In these tests K was about 11.5 for the primary configuration and this results in a predicted θ_j of 75°, which in turn is a reasonable estimate for the average flow angle based on the variation shown. From a modelling standpoint it is clear the above relations will give a reasonable estimate of the average jet angle but cannot capture any variation across the port.

3.5.3 Port Shape Effect on the Core Flow

Any changes in jet characteristics will have a marked effect on the flow field within the core. Velocity vectors are given in the core for the chuted and D-shaped ports in figure 3.39, these may be compared to the primary port flow through a plain port given in figure 3.4.

The core recirculation of the chuted port is much smaller than those of the plain and D-shaped ports. Looking at the velocity vectors of the chuted jet's core at x=15mm indicates that it is more deflected in the axial sense than the other two ports. These features, the reduced recirculation size and increased jet deflection are as a result of decreased jet to core flow momentum ratio. Although the mass flow has remained constant the velocity through the chuted port has reduced, by an amount similar to the increase in effective area of the port. Since the jet momentum is proportional to the square of the velocity, but only directly proportional to the effective area, the jet's momentum will be reduced by a proportion similar to the proportional increase in C_d.

Another difference between the three flow fields of note is the increased reverse flow into the lee of the D-shaped port compared to the others. This indicates a larger wake behind the jet as would be expected due to its squarer back. Daly(1994) studied the spectra of velocities in this area for both the plain and chuted ports using the current facilities. This work was initiated because Huang. et al.(1991) had observed vortex shedding behind chimneys in cross flows (comparable to long chuted ports) with a Strouhal Number of 0.21. However, Daly was unable to find distinct frequencies for either port and it is possible the chuted port was too short to have significant effect in this instance. Measurements of the power spectrum density for the azimuthal velocity just behind the D-shaped port in this study, however, showed a quite distinct frequency of 5.7Hz in the, as presented in figure 3.40. As Huang points out, the peak frequency in the spectra is at a frequency of twice that of the vortex shedding. The shedding frequency is thus 2.85Hz which relates to a Strouhal number of 0.26. Although this area of investigation has only "scratched the surface" it has been mentioned due to possible implications on the acoustic properties of a combustor. Typical flow conditions within a combustor could lead to frequencies of around a few hundred Hertz, which may create undesirable combustor noise.

Figure 3.41 presents the turbulent kinetic energy fields for the core flow of the chuted and D-shaped ports, which may be compared to that for the plain port in figure 3.7. Lower levels of turbulence have been found for both of these when compared to those of the plain port. This is not surprising for the chuted port which has been noted to have weaker penetration due to its reduced through port velocity. The D-shaped port also has lower levels, particularly around impingement, which is surprising because both jets have similar entry profiles to the core. The reason for this is not clear but a possible explanation could be that there is increased mixing due to the vortex shedding from the lee of the jet (the increased turbulence in this region is quite evident in figure 3.41(a)).

3.6 Effect of Introducing Annulus Swirl

During the course of this work Carrotte(1995) discovered in his investigation of diffuser systems for combustors that significant amounts of swirl could be present in the annulus of an annular combustor, due to residual swirl after the compressor outlet guide vanes. In the inner annulus, where circumferential velocities increase, due to conservation of angular momentum, swirl components of up to 15° were observed. Naturally questions were raised as to the consequences of this on the downstream aerodynamics. No work has been reported which focuses on the effects of annulus swirl on combustor air-admission ports.

The table below shows that a noteworthy change in C_d is measurable when swirl is introduced into the annulus.

Table 3.5 Effect of Annulus Swirl on Discharge Coefficients

Port Shape	Plain		Chuted		D shaped	
flow condition	Primary	Dilution	Primary	Dilution	Primary	Dilution
No Swirl	.639	.649	.812	.875	.647	.661
12° Swirl change	.631 (-1.3%)	.644 (-0.7%)	.751 (-7.5%)	.797 (-8.9%)	.612 (-5.4%)	.629 (-4.8%)

Table 3.5 shows that the effect on C_d is dependent upon the port shape. Swirl reduces the C_d of each type, but the reduction of 8% for the chuted port and 5% for the D-shaped port were most marked - the plain port's C_d reducing by only 1%. The detail

behind these reductions will be described later, but since a typical combustor will contain a mixture of port shapes, the critical balance of flow split between each may be adversely effected. In addition to this, because the inner annulus contains most of the swirl, the mass flow split may become biased toward the outer annulus, resulting in a displacement of the impingement point.

3.6.1 Annulus Flow Field

The sequence of figures 3.42 to 3.47 present results comparable to those for the annulus of the dilution port, section 3.3.2, with the only difference being the addition of annulus swirl in the current figures. Figures 3.42 and 3.43 define the velocity field for this condition; figure 3.42 shows the in-plane velocity vectors and in figure 3.43 contours of the velocity normal to this plane are given. Comparing the velocity vectors with those in figure 3.21 it is evident that swirl has not significantly changed the flow pattern upstream of the ports. Downstream of the ports, however is quite different, in particular the region of reverse flow (shaded) has greatly reduced. The reason for this can be understood by considering the flow topology at low bleeds, as in figure 3.27. By introducing swirl the flow pattern as sketched will skew about the port's centreline, rotating the plane of symmetry, contained in the mean flow-field, by the angle of swirl. This symmetry plane through the idealised flow which contains the highest levels of negative axial velocity is thus twisted out of the measurement plane. Further clarification of this concept is given later when results from a radial plane are given. Swirl velocities are greatly increased in the lee of the port, where the annulus flow curves into this plane from between ports, again becoming clearer from later plots. The unshaded region over the rear half of the port indicates negative swirl velocity (into page using right-hand screw rule) suggesting the presence of a strong through-port vortex with its axis coincident with the most downstream $W/U_c=0$ contour line. Quite high levels of swirl persist in the downstream annulus (exiting at around double that at inlet), particularly considering the axial velocity has reduced on average by a factor of 5. This implies much higher local flow angles in the x-θ plane than that at inlet of 12°. On this evidence, should swirl be present in a feed annulus then each subsequent row of ports will see increased swirl angles.

The normal stresses in figure 3.44 contain similar anisotropy to the non-swirling case in figure 3.23. Levels of radial stress in each are considerably lower than those in the axial and azimuthal directions, evidence that the vortex identified in the previous two figures is unstable and moves relative to the port. This large scale motion would thus result in artificially high levels of turbulence in the axial and azimuthal directions. The results for the non-swirling flow-field could be interpreted similarly, due to the similar variation in anisotropy. Naturally, time-averaged modelling of this scenario could not resolve these types of features. The distributions of higher normal stresses are more localised around the port with the introduction of annulus swirl. Again, this could be attributed to the skewing of the symmetry plane defined by the flow topology from the measurement plane. This is echoed in figure 3.45, in which similar levels of turbulent kinetic energy are found around the port as with no swirl, but it is much more localised.

Skew in the flow can be seen to be occurring not only in the azimuthal sense, but also the radial sense in figure 3.46. Upstream of the port, the flow has accelerated more from the left of the port, indicated by the non-symmetric $U/U_c=0.75$ contour line. Downstream of the port the region of reverse flow is then skewed over to the right, more so with increasing radius. The proportion of back-flow on this plane appears to have reduced, and this is echoed in the table below, in which the flow paths are explained earlier in section 3.5.1.

Table 3.6 Flow Paths In the Annulus

Port Shape	Plain no-swirl	Plain with swirl
path 1 (by-passes port)	34%	30%
path 2 (direct into port)	66%	70%
path 3 (back-flow)	13%	9%
path 4 (jet)	79%	79%
path 5 (bleed)	21%	21%

The skewness brought about in the flow topology by the annulus swirl can clearly be seen in figure 3.47 for both the plain and D-shaped ports. The reduction in the proportion of back-flow (from 13 to 9% of the total annulus inlet flow) can be attributed to the fact annulus swirl has brought the saddle point further upstream. By comparing figures 3.47 and 3.37 this saddle point has moved from an $(x,(r\theta))$ of about

(18,0) to (13,10) for the plain port. This demonstrates quite graphically how the flow is skewed in the azimuthal sense behind the port when upstream annulus swirl is introduced. The through-port vortex is also evident in figure 3.47, and is seen to be a feature of the mean flow field, rather than an unsteady phenomenon as observed for the non-swirl annulus condition. The mechanism which gives rise to this vortex appears similar to that presented in figure 3.27, in which one of the two symmetric vortices becomes dominant and its axis rotates through $90°$ to become predominantly radial in direction. It could thus be considered that a component of swirl in the annulus will act to stabilise the flow pattern in the annulus behind the port. However, the downside to this is that the flow angle will be amplified by the presence of the port. What may also be suggested by this comparison is that, without the presence of annulus swirl, if a stable through-port vortex is formed the flow downstream of the port will contain a component of swirl. In this case the negative radial (through-port) swirl is balanced by positive axial swirl created in the downstream annulus, and angular momentum is conserved.

The secondary velocity components have been compared in figure 3.47 for a plain and D-shaped port because of the symmetry of the port shapes. The plain port has an infinite number of lines of symmetry (diameters) and appears the same to flow approaching from any angle (excluding the effects of curvature of the liner wall). The D-shaped port however has only one line of symmetry ($r\theta=0$ in figure 2.47b) and with increasing swirl in the approach flow the port will offer an asymmetrical profile to the flow. Despite this difference the through port vortex does not move from its location within the port with $12°$ of upstream swirl. It could be imagined for example that this vortex may move toward the most lee-ward corner of the port at higher swirl levels.

3.6.2 Jet Characteristics

Swirl in the annulus results in little change in the through-port velocity distribution at exit of the port, as indicated in figure 3.48. In this figure the velocity profiles for the datum configuration are compared with the same flow scenario, but with the inclusion of annulus swirl. Secondary velocity components are clearly affected however. A more even distribution of axial velocity, particularly in the jet's core region, and significant

levels of azimuthal velocity are evident with the presence of swirl. At the rear edge of the port the azimuthal velocity is 30% of the average through-port velocity. The origin of this high component is illustrated in the previous figure (3.47a) in which the approach flow to the rear of the port has quite high levels of azimuthal velocity.

Perhaps of greater interest is the flow direction at exit from the port. Figure 3.49 shows these angles calculated from the measured profiles of the previous figure. As a result of the more even distribution in axial velocity, the jet direction in the x-r plane, α, is more even when swirl is present in the annulus. Without swirl the jet enters the core aligned with the port's centre line in the r-θ plane, i.e. a β of 90°. With swirl this angle has reduced, indicating that the jet is no longer travelling radially. Away from the separation at the upstream edge deflections of around 4-9° are present.

The trends in shown in these two figures are echoed when comparing swirl with no swirl situations for a dilution set-up and also D-shaped ports. This demonstrates that the effects on the jet's characteristics are intuitive: as annulus flow enters the port, conservation of angular momentum results in the jet being deflected sideways. Also, the increased dynamic pressure due to the swirl component is not significant enough compared with the port pressure drop to affect the through port velocity. On the other hand it is less obvious how this modified port exit profile will affect the core flow field.

3.6.3 Core Flow Field

An astonishing effect is noted in the core flow field when ports are fed with annulus flow containing swirl. The flow conditions presented in figure 3.50 are identical to those of the datum, except with the inclusion of annulus swirl. It is obvious, when comparing the velocity vectors in this graph with those in figure 3.4, that the reduction in size of the core recirculation suggests a major change to the structure of the core flow field. This change occurs because the jets have been deflected by an angle, β (figure 3.49), which creates a mis-alignment and jet impingement does not occur at the centreline. Instead the jets create a strong vortex about the core centreline as indicated in figure 3.51 where levels of azimuthal velocities reach $2.25U_c$. This rotation is also seen to occur within the upstream recirculation. What is considered to be happening is that the jet flow entering this recirculation is taken out of the measurement plane and

can pass between jets, reducing the blockage effect of the recirculation. The strong vortex along the core centreline also reduces the mixing. At the exit plane in figure 3.50 the peak axial velocity occurs at a radius of 10mm, whereas without swirl mixing results in the merging of the jets and the peak axial velocity is at the centreline by x=40mm (figure 3.4).

The angular momentum budget was considered for the plain, primary port flow with annulus swirl, the velocity field of which is shown for the core in figure 3.50. Annulus inlet and core exit angular momentum about the rig centre-line were calculated from measured axial and azimuthal velocity profiles at x=-100 and 100mm via;

$$M_x = \int_A \rho UWr dA = 2\pi\rho \int_r UWr^2 dr$$

Because the annulus exit velocity distribution was complex and contained high levels of unsteadiness, the momentum was not evaluated due to time limitations. Naturally the core contained no swirl at inlet. The values calculated were M_{xa}=0.0302 and M_{xo}=0.0127 kgm^2/s^2. The core exit angular momentum is thus 42% of that at annulus inlet. With 50% of the annulus flow entering the core a proportion of angular momentum closer to 50% of the annulus inlet would be expected to exit the core. What is clear though, is a significant proportion of angular momentum is conveyed through the port, 84% in this case. The mechanism outlined here for misaligned jets creating swirl in the core could also occur in annular combustors. If each jet entering the combustor was deflected in the same sense then an axial angular momentum could be created about the engine centreline. The annular combustor would be more susceptible to annulus swirl than can-combustors due to their layout, and it is probable each annulus would have different levels of swirl. Considering how pre-diffuser exit swirl could affect combustor aerodynamic performance is therefore worthy of further investigation, particularly in realistic geometry.

The magnitudes and distribution of normal stresses in the core are also effected by annulus swirl. Comparing figure 3.52 with 3.6 reinforces the evidence of the reduced recirculation size, since the upstream extent of high stress levels is greatly reduced. The maxima of radial and azimuthal normal stresses occur at the same location, but

levels are reduced by 20% because the jets are not fully impinging due to their mis-alignment in this case. This is echoed in figure 3.53 which presents the turbulent kinetic energy in the core. Compared to figure 3.7 the turbulence field has been compressed into a much smaller region upstream of impingement due to the reduced size of the recirculation. The maximum levels have also reduced, again because of weakened jet impingement. Excluding these two main features the distribution and levels of turbulence are quite similar. However, it has already been seen that less mixing has occurred with swirl in that the jet cores are still identifiable at x=45mm.

3.7 Closure

The generic annulus/port geometry described in chapter 2 has been examined using LDA and flow-visualisation techniques. The purpose of these measurements was to increase the database of experimental data suitable for validation of computational methods whilst increasing the understanding of the physical processes involved in the complex nature of annulus/core interactions. Rather than embarking on a parametric study, taking each possible variable through its range of likely values, a more detailed look has been taken at conditions considered typical of a combustor. Thus, port shapes have been varied along with the flow configuration to mimic conditions representative of those found around air admission ports of actual combustors.

A datum case was chosen for two reasons; to demonstrate the methods of data reduction used and to provide a benchmark against which subsequent flow/geometry configurations could be compared. The datum chosen was a plain circular port with primary port-like flow conditions; jet to core velocity ratio of 5.0, annulus bleed ratio of 50% and no swirl velocity in the annulus. Measurements on planes in the annulus, jet and core regions allowed a picture of the flow field to be created and its associated turbulence field. The principle characteristics were identified such as the large-scale core recirculation, jet impingement and a small, but noticeable flow separation from the outer annulus wall. High levels of anisotropy were noted in the core region, and the complexity was further demonstrated with evidence of bi-modal flow behaviour where the core flow impinges on the jet recirculation.

A less complex core flow was produced with dilution port-like conditions in which the jets did not impinge. However, with reduced bleed flow the annulus flow was found to contain large scale recirculation and higher levels of turbulence. The annulus was found to have some effect on the jet exit profiles, producing more initially radial jets containing higher turbulence levels.

Flow visualisation was used extensively to understand the effects of variation in bleed ratio. Several modes of flow pattern were observed with various bleed ratio ranges. Each pattern was principally dependent upon the magnitude of the separation of flow from the outer annulus wall above the port and how the resultant recirculation interacted with the inner wall and the flow feeding the jet. The interpretation of the flow visualisation was confirmed with LDA measurements at a range of bleed ratios. Substantial flow unsteadiness was observed at low bleed ratios due to occasional formation of through-port vortices. The highly 3-D nature and interactions of these unsteady features were observed but quantitative measurements could not be made with the available instrumentation. The change in annulus flow pattern was also seen to have a measurable effect on the location of the core jet impingement point and recirculation size.

Port shape was not seen to have a substantial effect on the annulus flow, though differences in jet characteristics, discharge coefficient and the core flow field were measured. The plain and D-shaped ports behaved similarly in many respects, but as expected the chuted port significantly increased the port discharge coefficient. Surprisingly though this did not result in a stronger jet impingement, but this was because the chuted port had a much more uniform exit velocity than the plain port hence lower maximum velocity for a given mass flow rate.

Introducing swirl to the annulus produced large changes in all areas of the flow field. Discharge coefficients were reduced by differing amounts, depending on port shape, plain ports being least affected, but chuted ports seeing a reduction of 8%. The most marked effect of annulus-swirl was a significant reduction in the size of the core recirculation size. This was seen to be due to jet mis-alignment reducing the strength of impingement and thus the proportion of jet fluid flowing against the core flow direction. Moreover, the jet mis-alignment ensured that most of the angular momentum of the annulus flow was conserved.
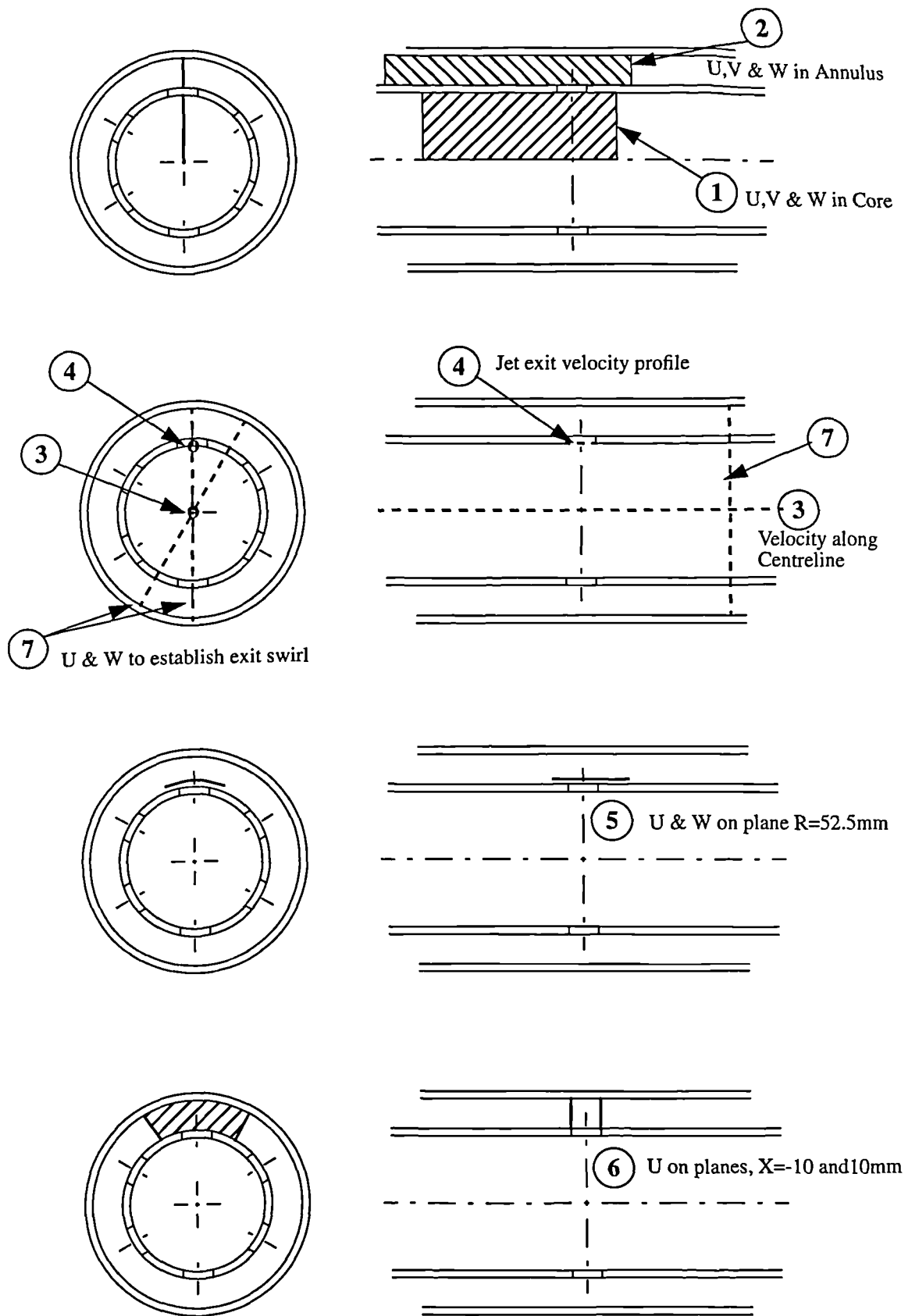
Figure 3.1 Principle Measurement Planes
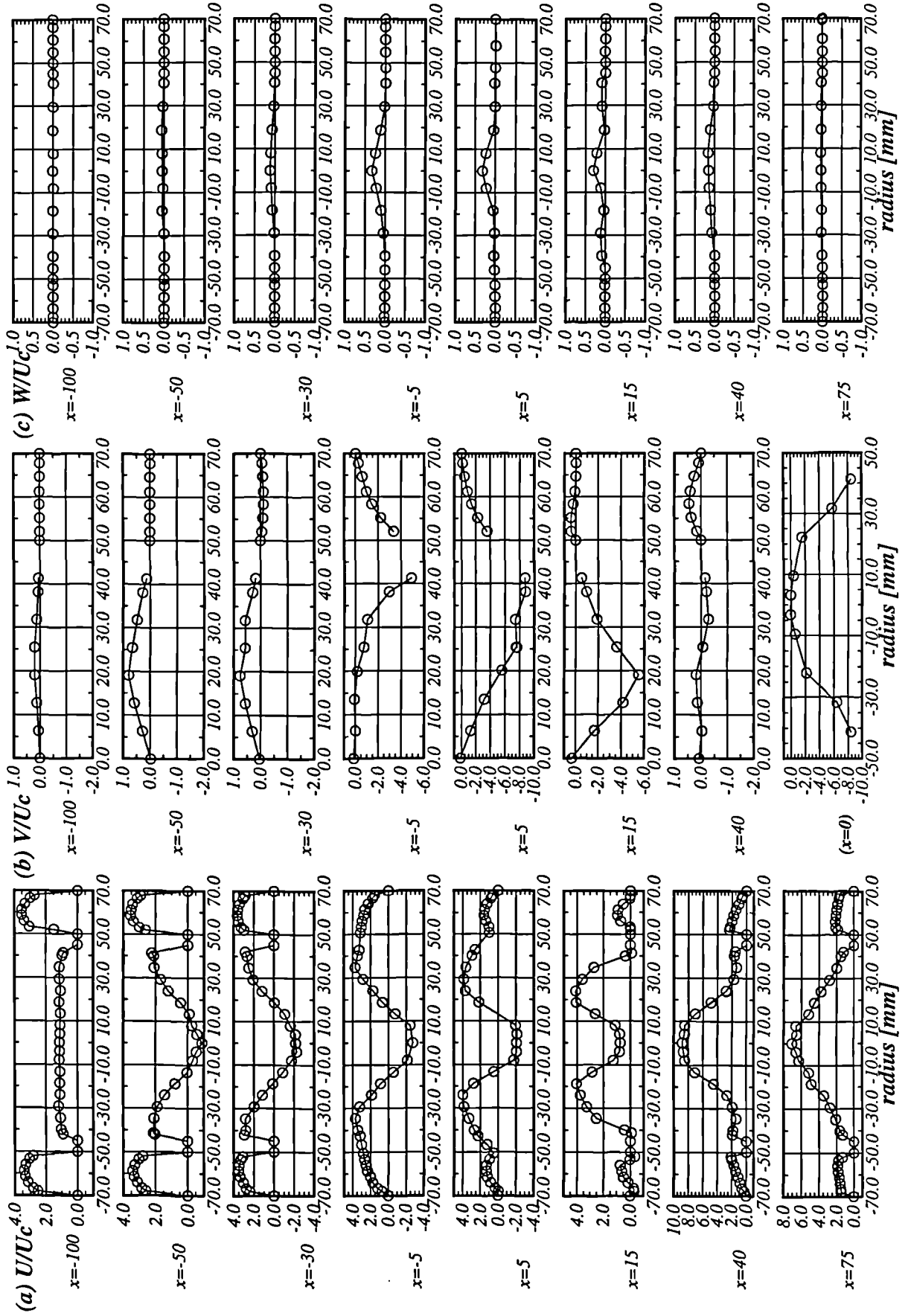
Figure 3.2 Normalised Velocity Profiles At Eight Axial Locations.
Plain Port, R=5.0 Bleed=50%, W_a/U_a=0.0
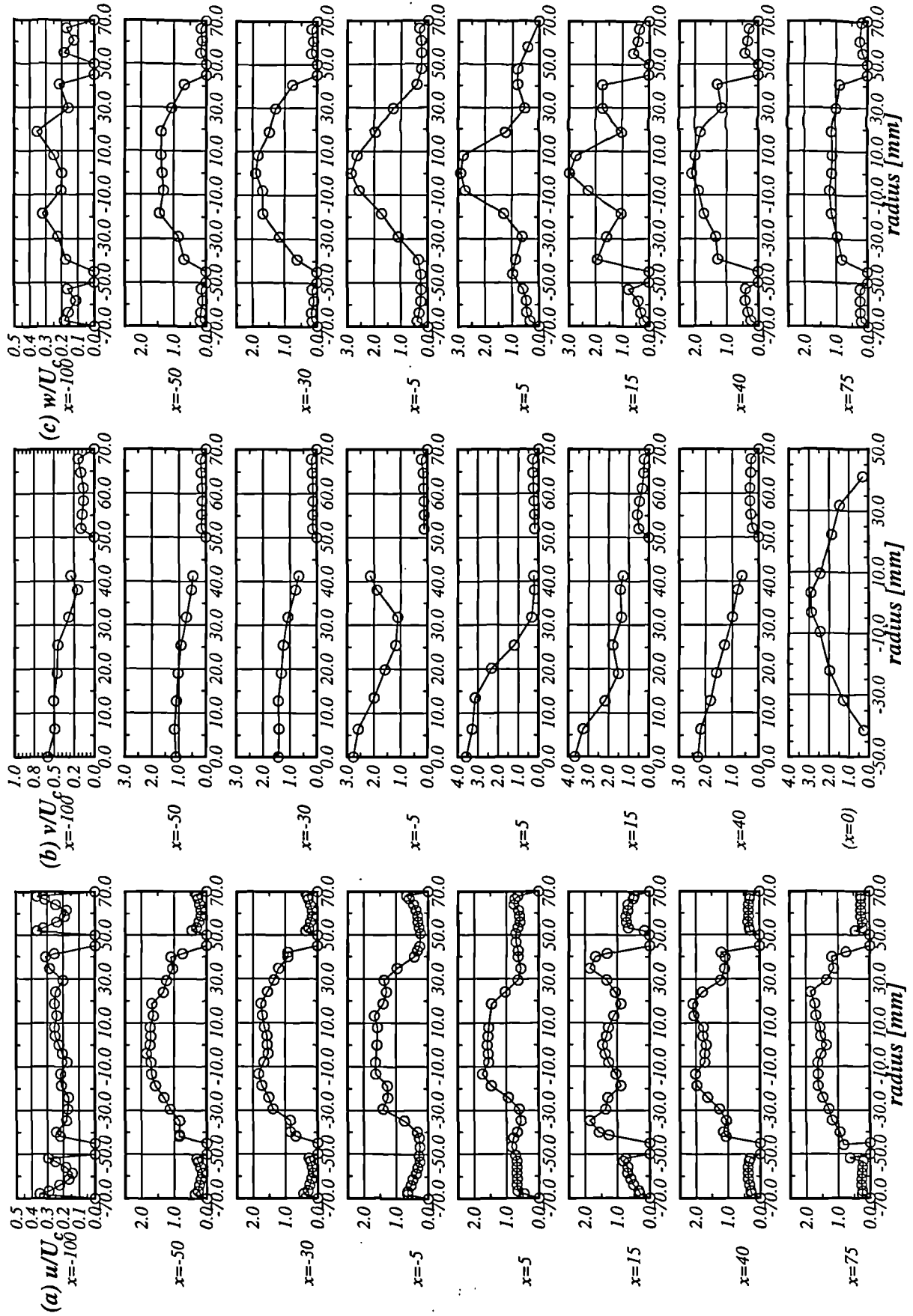
Figure 3.3 Normalised R.M.S. Velocity Profiles At Eight Axial Locations.
Plain Port, R=5.0 Bleed=50%, W_a/U_a=0.0
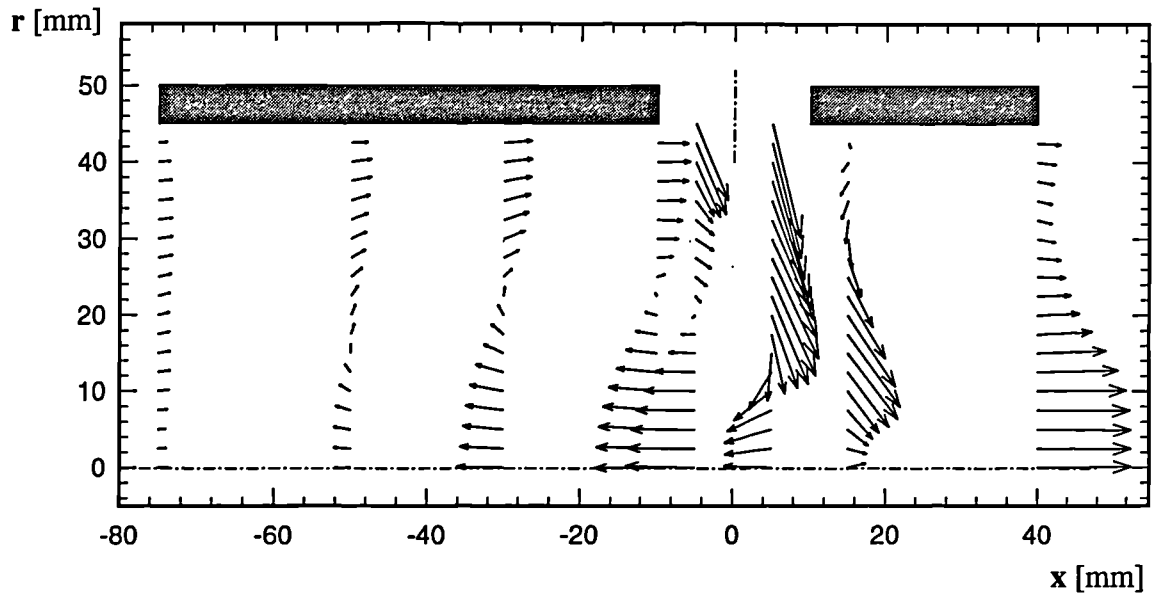
Figure 3.4 Velocity Vectors In Core
Plain Port, R=5.0 Bleed=50%, W_a/U_a=0.0
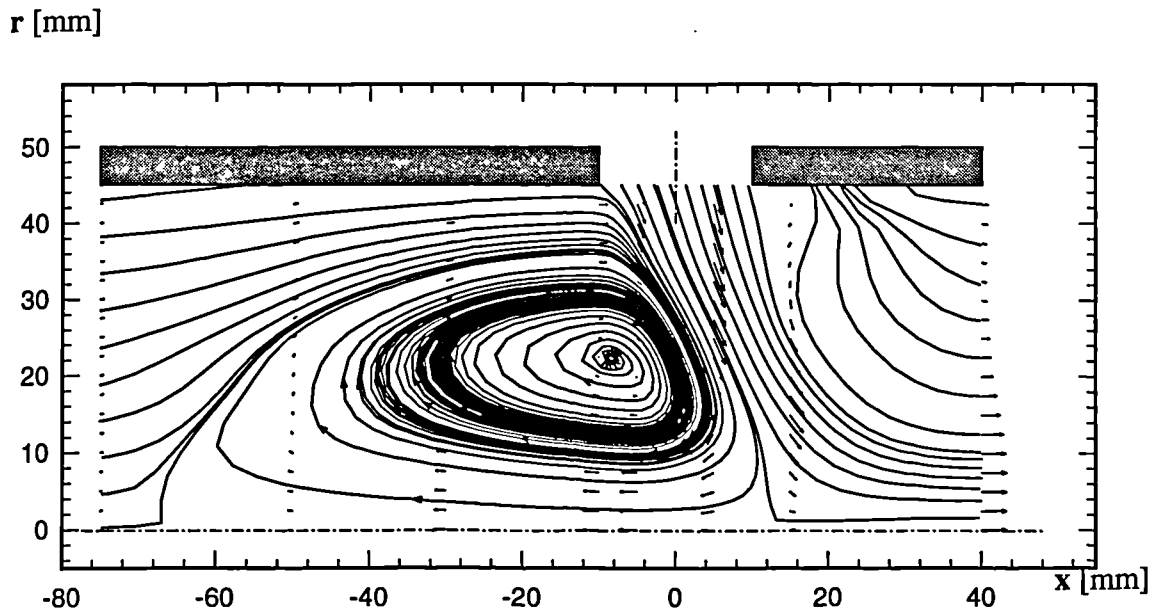
Figure 3.5 2-Dimensional Particle Tracks In Core
Plain Port, R=5.0 Bleed=50%, W_a/U_a=0.0
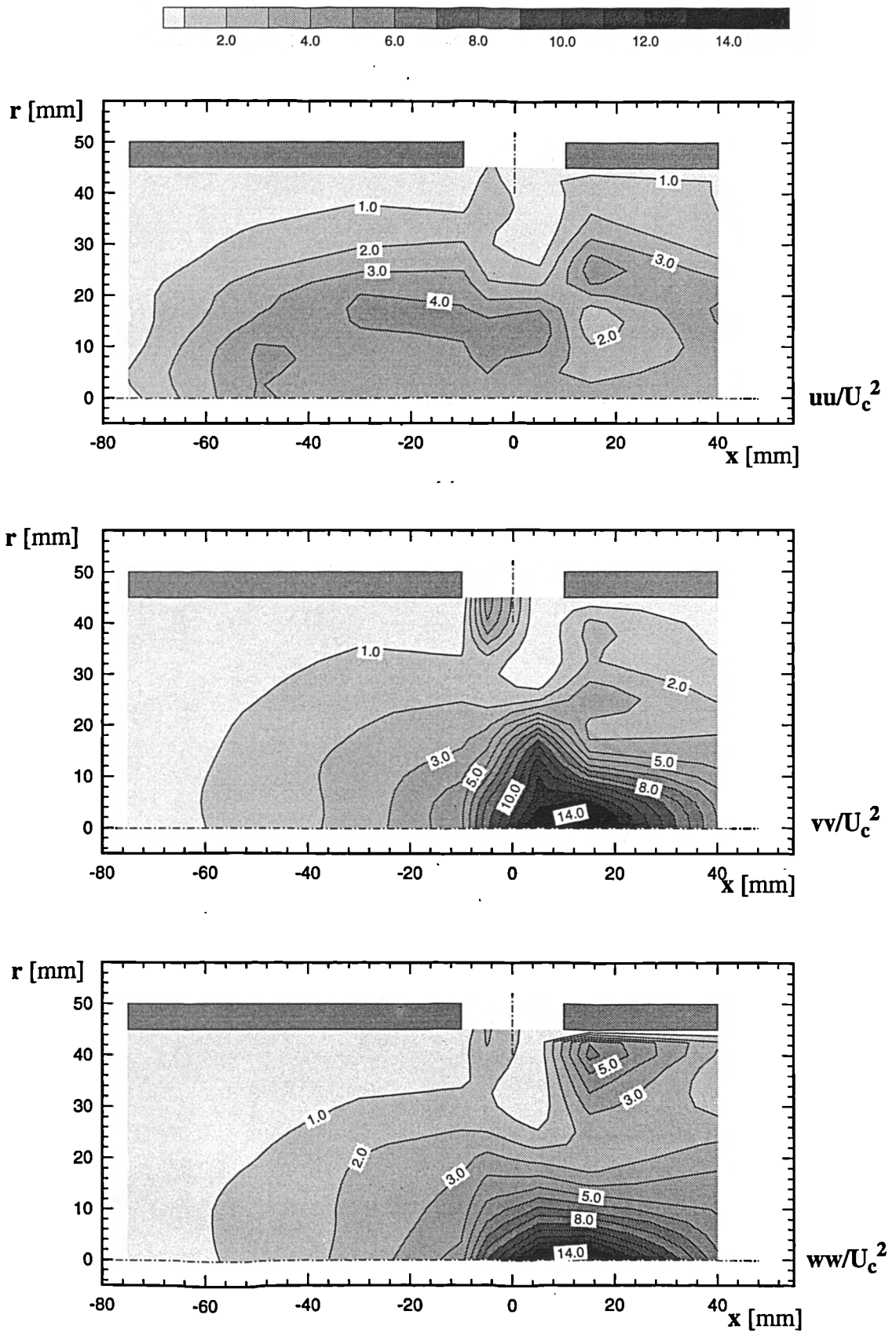
Figure 3.6 Non-Dimensional Normal Stresses In Core
Plain Port, R=5.0 Bleed=50%, W_a/U_a=0.0
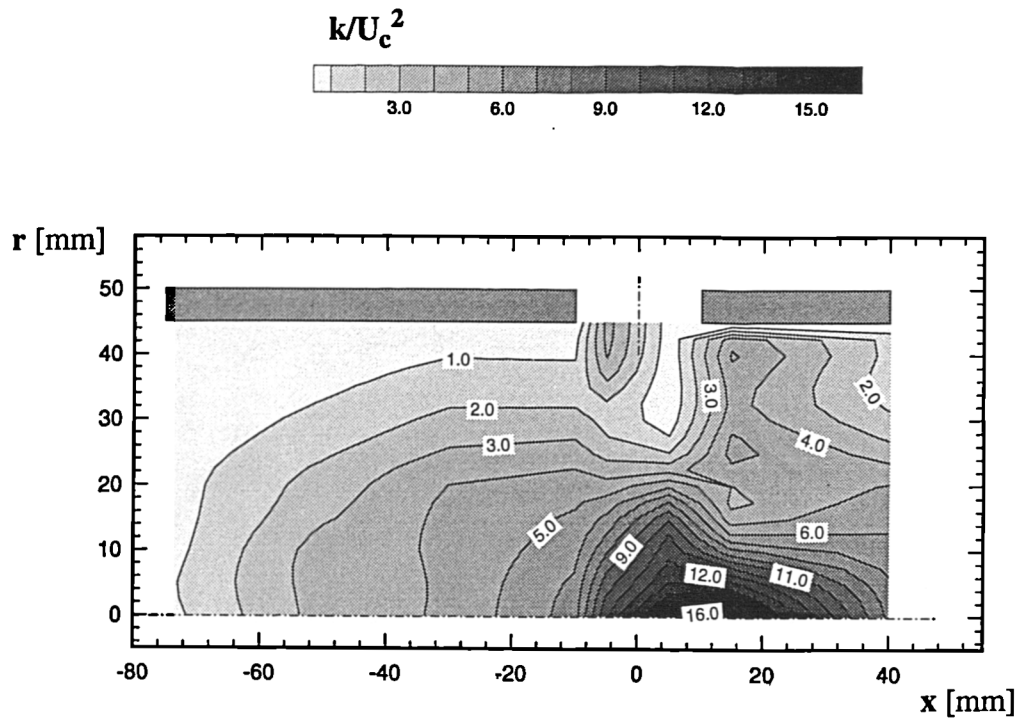
Figure 3.7 Non-Dimensional Turbulent Kinetic Energy In Core
Plain Port, R=5.0 Bleed=50%, W_a/U_a=0.0
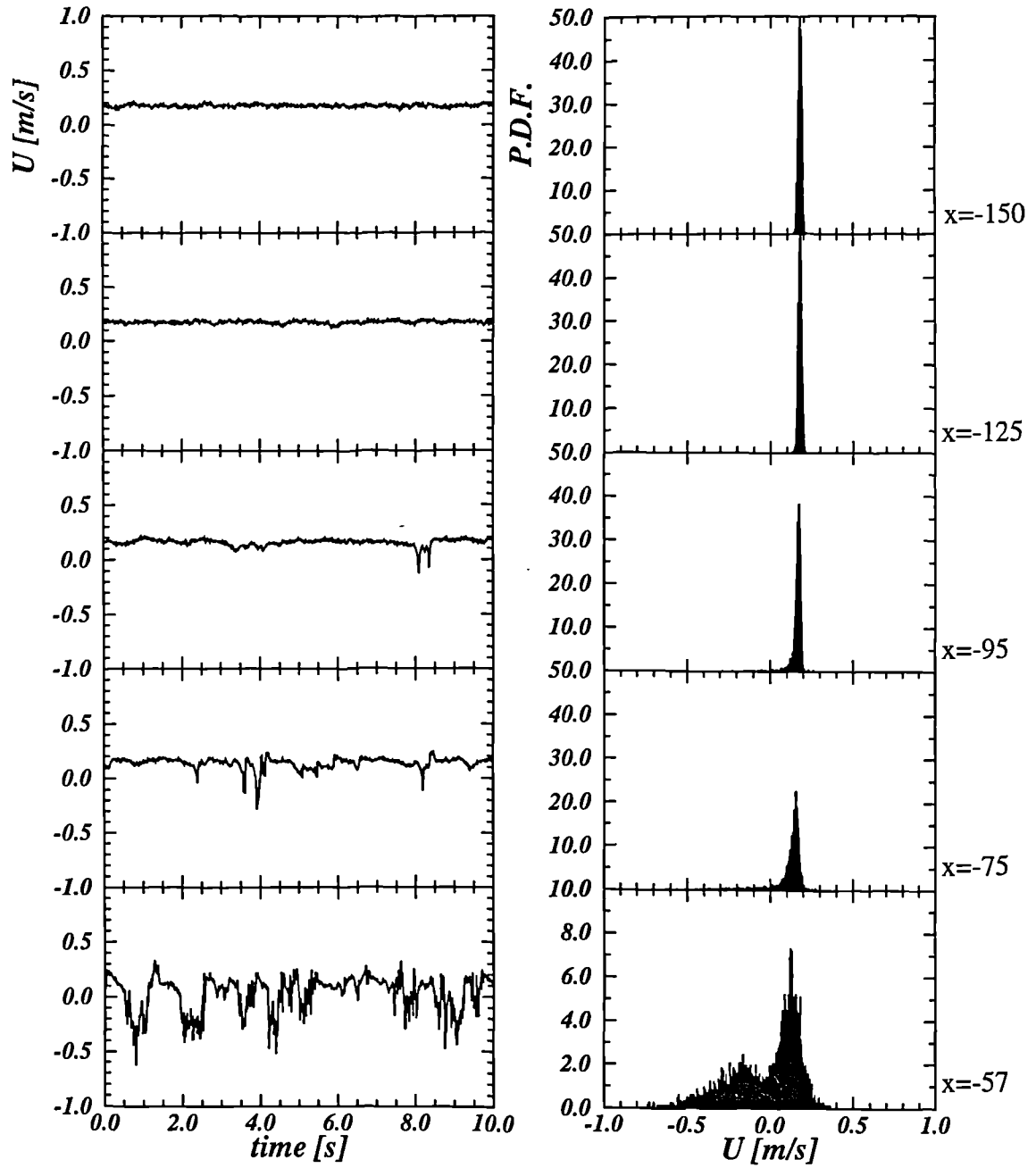
**Figure 3.8 Axial Velocity Time Series and P.D.F. on Core Centre-line at 10 Axial Locations** Plain Port, R=5.0 Bleed=50%, W_a/U_a=0.0 (full sample 82s at 1kHz)
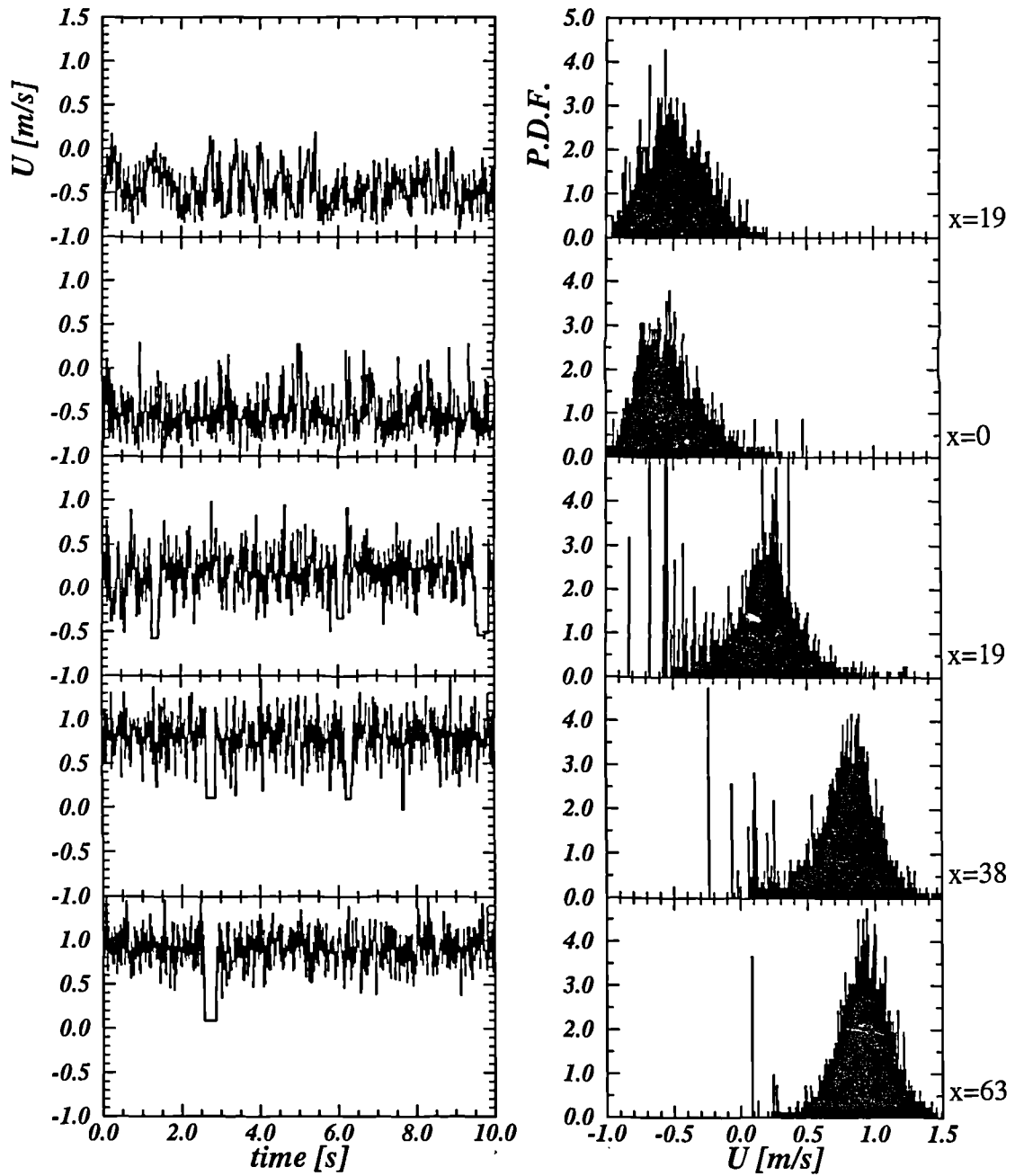
Figure 3.8(continued) Axial Velocity Time Series and P.D.F. on Core Centre-line at 10 Axial Locations. Plain Port, R=5.0 Bleed=50%, W_a/U_a=0.0 (82s at 1kHz)

Assuming probability distribution function is bi-modal with two gaussian distributions;

$$PDF = \frac{f_1}{\sqrt{2\pi u_1 u_1}} \exp\left\{\frac{(U'-U_1)^2}{2u_1 u_1}\right\} + \frac{1-f_1}{\sqrt{2\pi u_2 u_2}} \exp\left\{\frac{(U'-U_2)^2}{2u_2 u_2}\right\}$$

U' = Instantaneous velocity.

U_1 & U_2 = time averaged mean velocity of each mode.

u_1 & u_2 = r.m.s. velocity of each mode.

f_1= proportion of time velocity associated with first gaussian distribution.
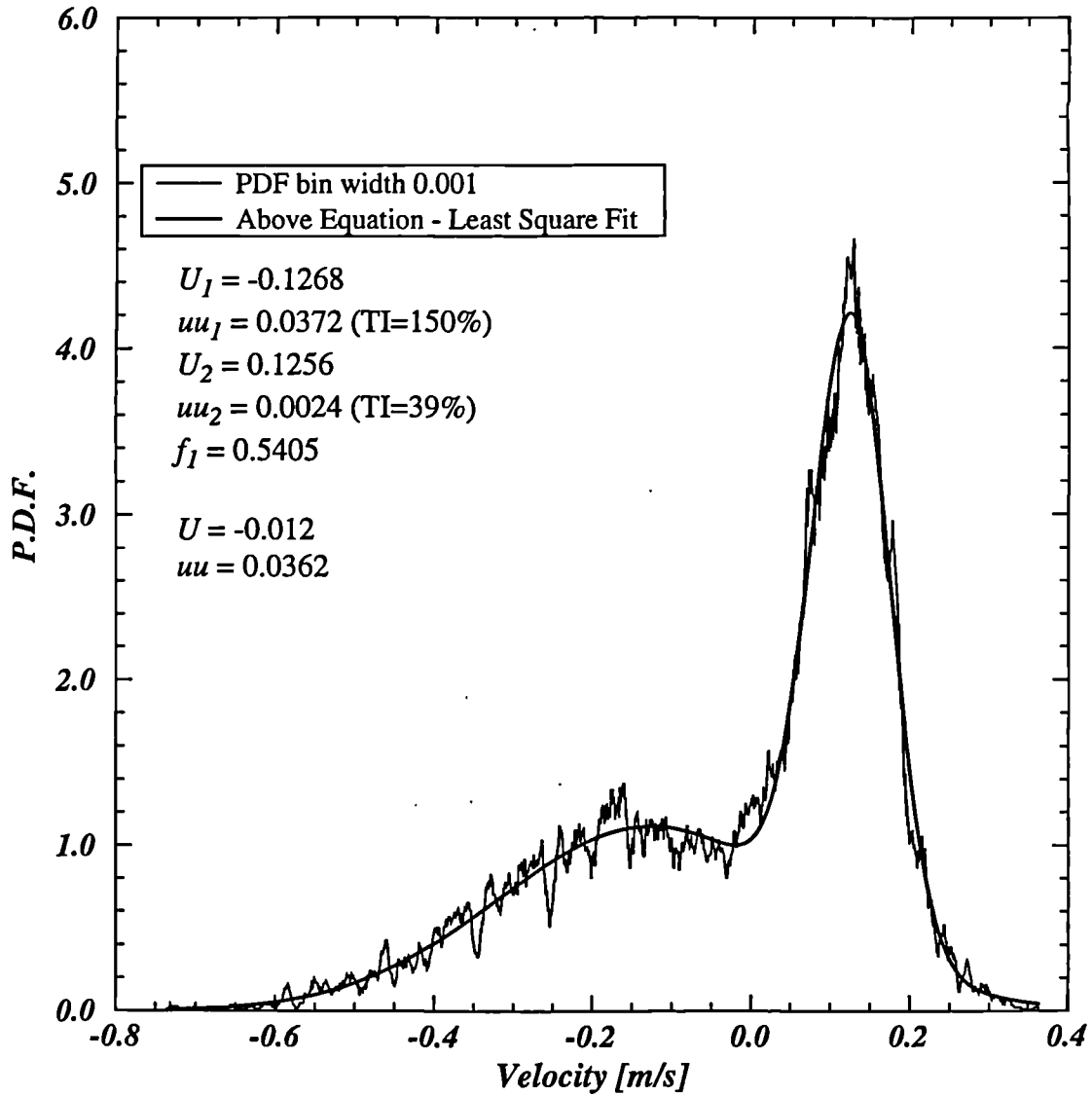
Figure 3.9 P.D.F. at Upstream Extent of Core Recirculation, x=-57mm
Plain Port, R=5.0 Bleed=50%, W_a/U_a=0.0 (82s at 1kHz)
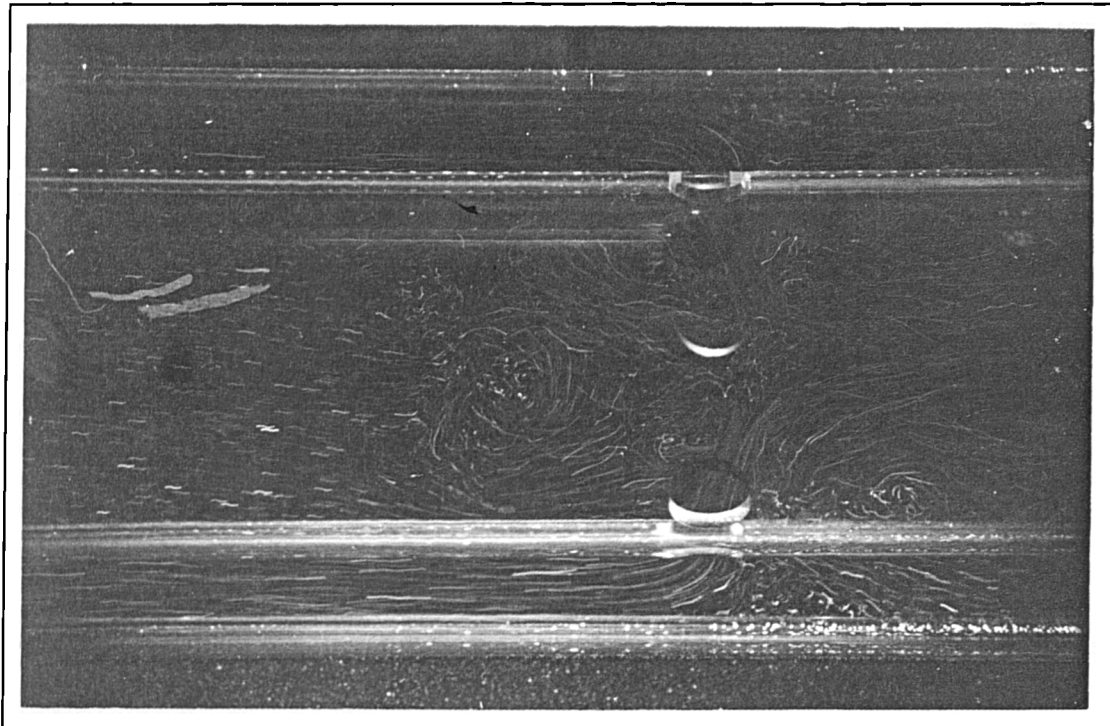
t=0s (f11, 1/30s)
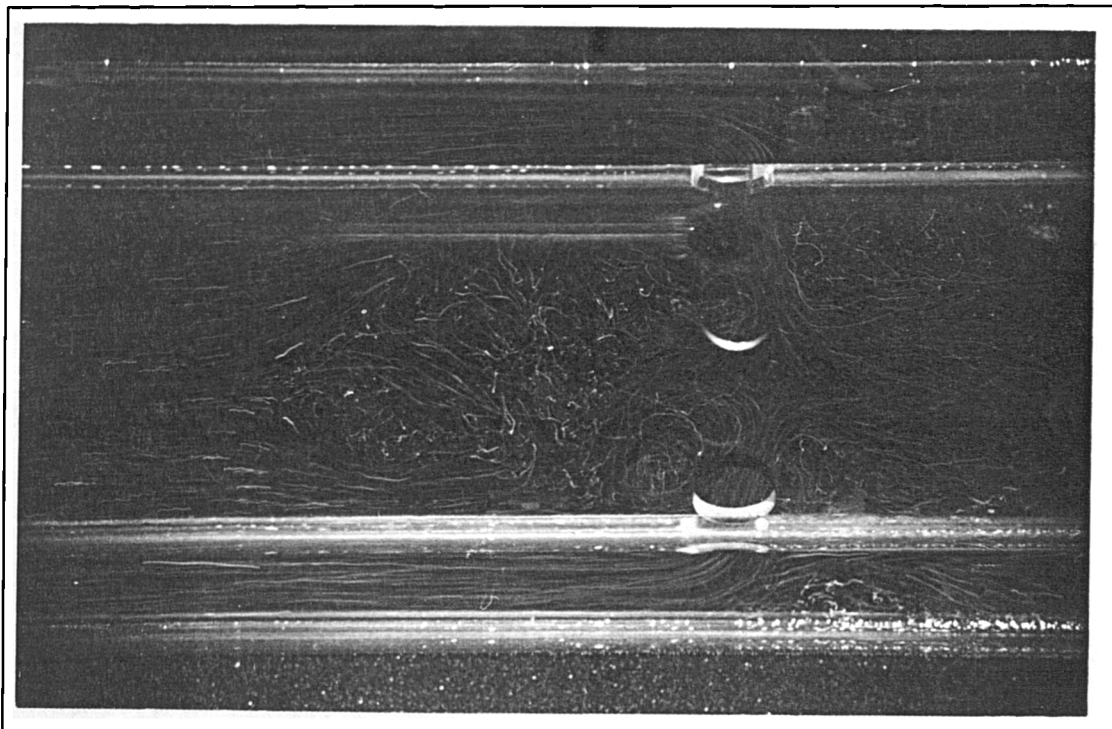
t=3s (f11, 1/15s)

Plate 3.1 Primary Flow Field - Flow Visualisation, R~5.0, B~50%.
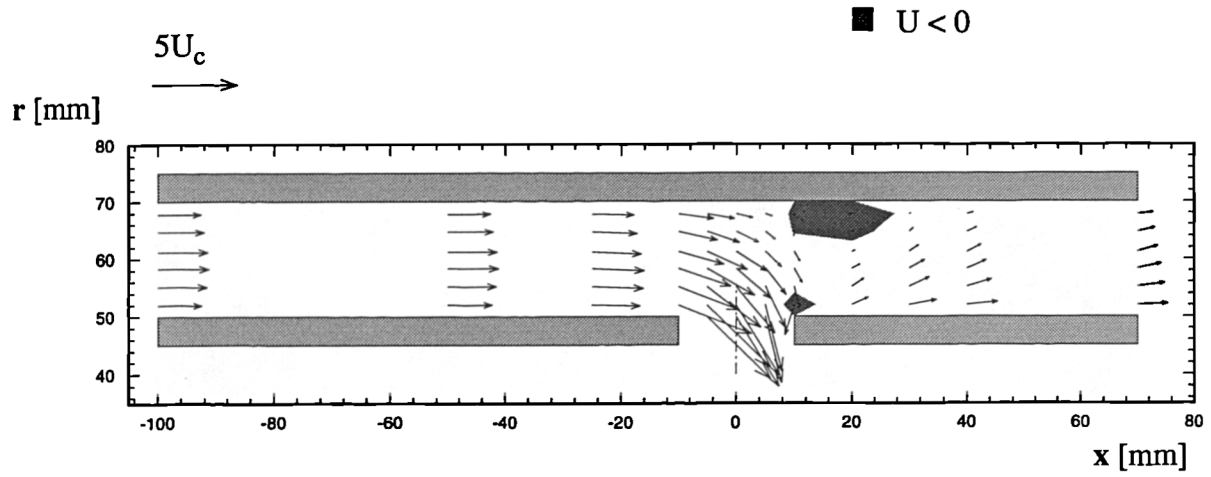
Figure 3.10 Velocity Vectors in Annulus
Plain Port, R=5.0 Bleed=50%, W_a/U_a=0.0
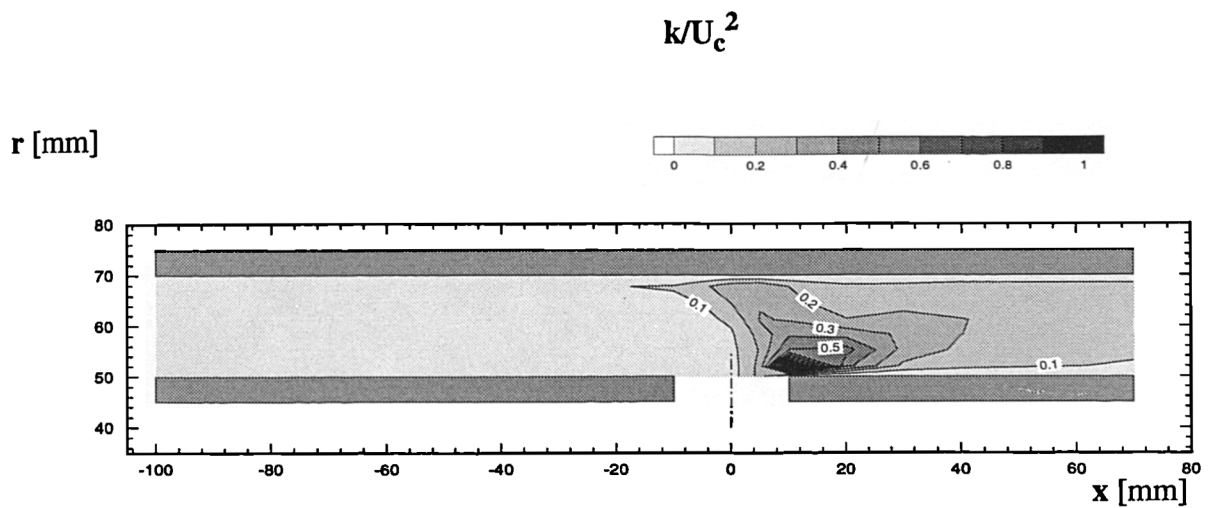
Figure 3.11 Non-Dimensional Turbulent Kinetic Energy in Annulus
Plain Port, R=5.0 Bleed=50%, W_a/U_a=0.0
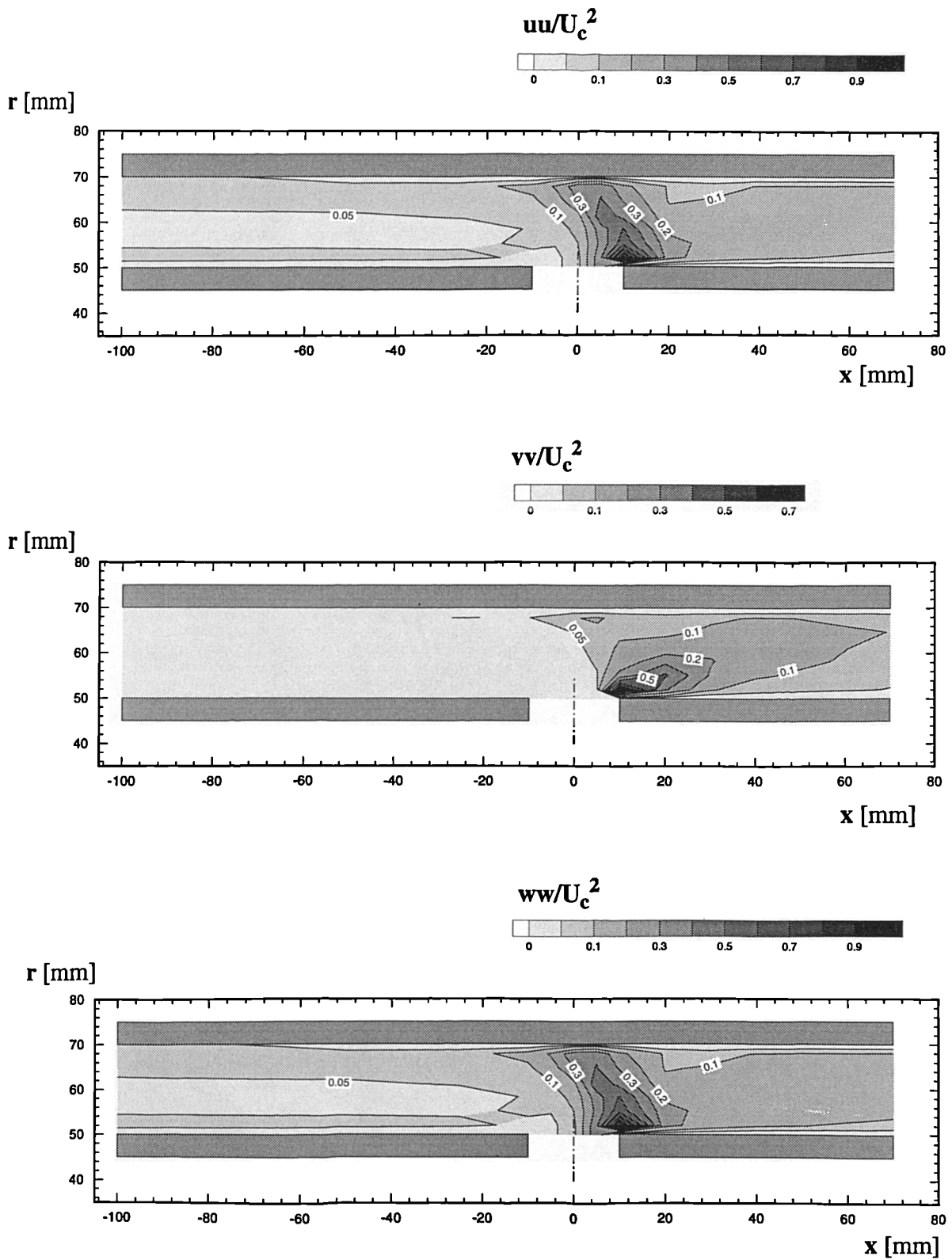
Figure 3.12 Non-Dimensional Normal Stresses in Annulus
Plain Port, R=5.0 Bleed=50%, W_a/U_a=0.0
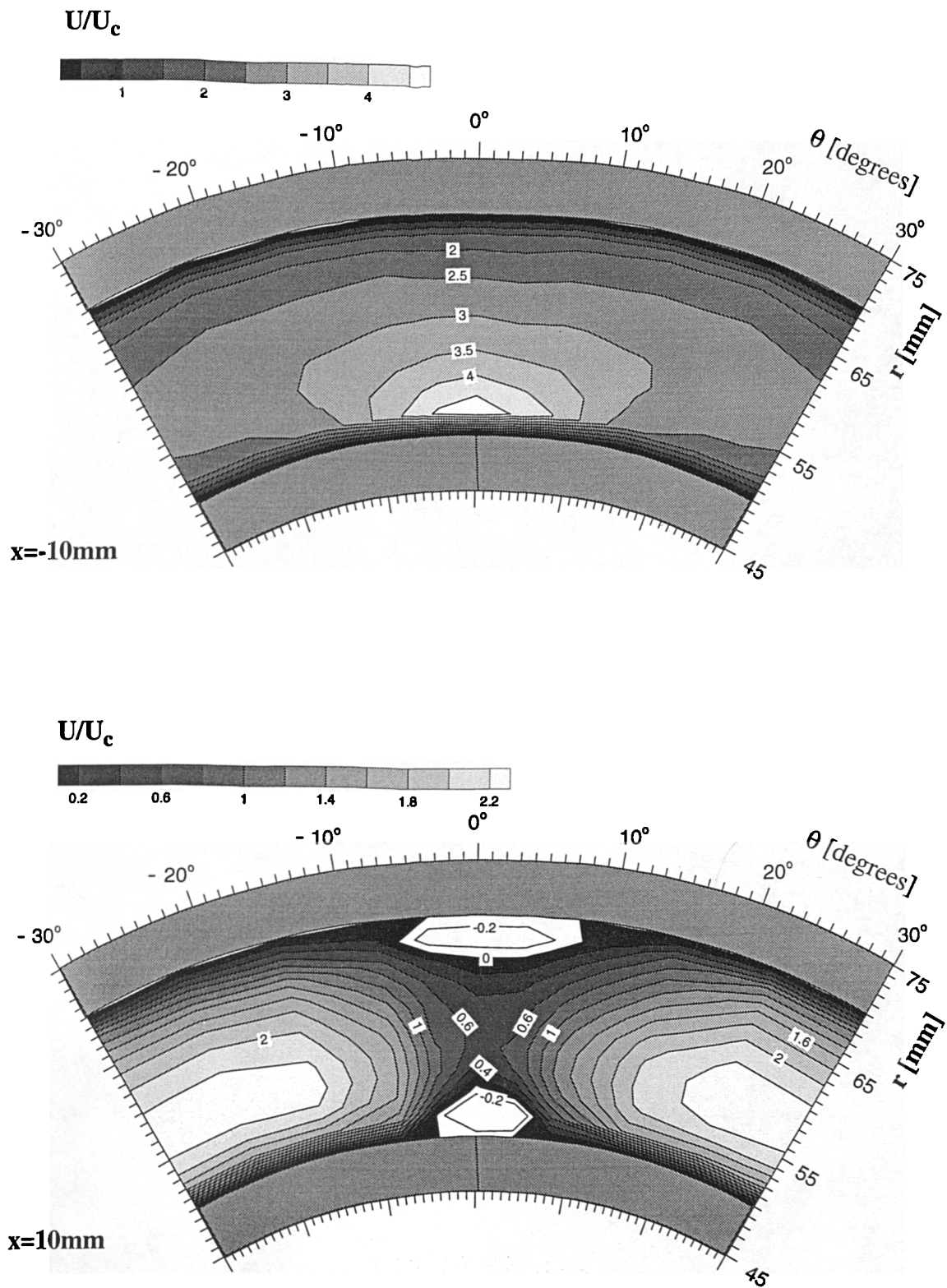
Figure 3.13 Axial Velocity Distribution in Annulus on x=-10 and x=10 Planes
Plain Port, R=5.0 Bleed=50%, W_a/U_a=0.0
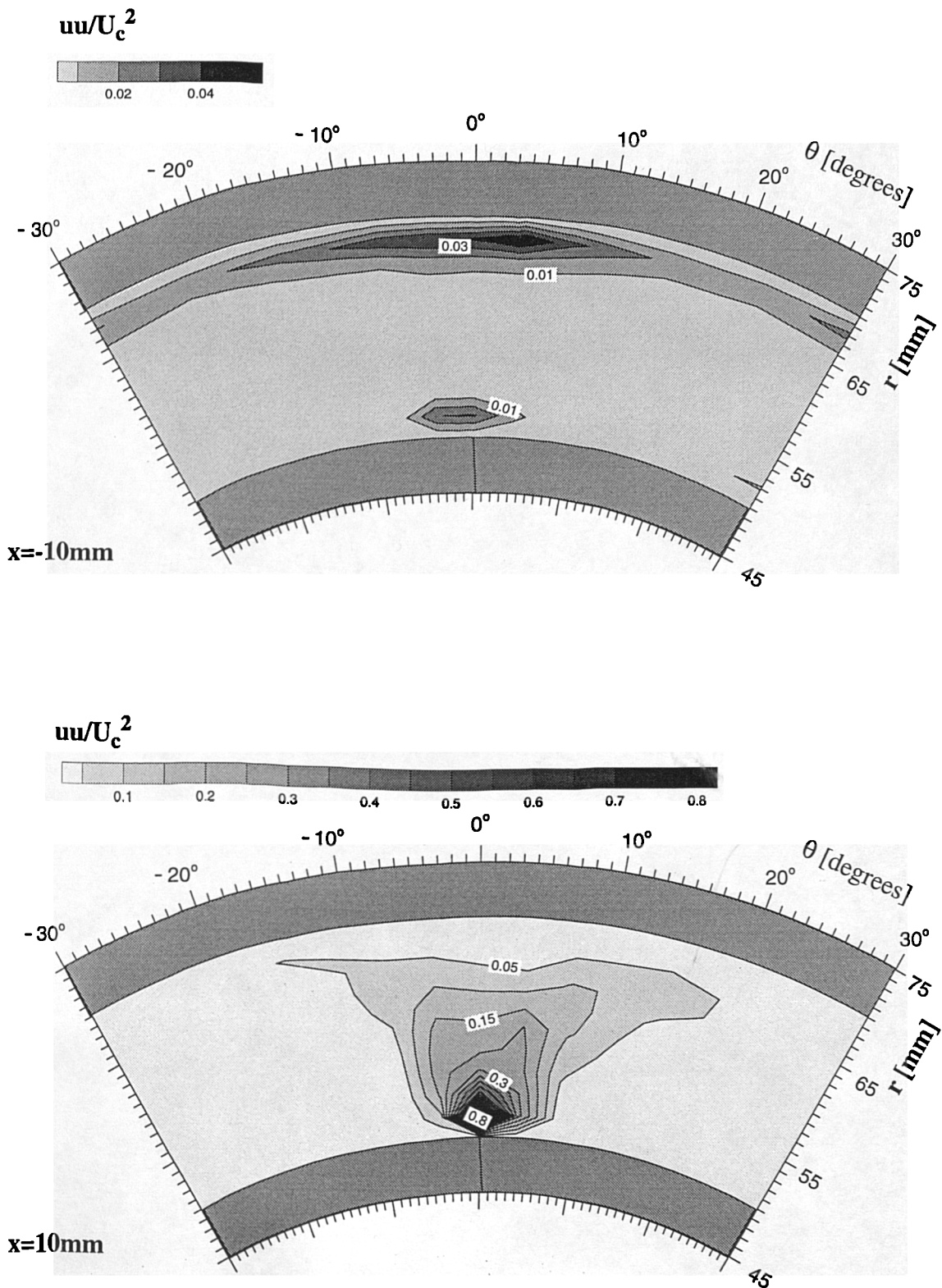
Figure 3.14 Normal Stress Distribution in Annulus on x=-10 and x=10 Planes
Plain Port, R=5.0 Bleed=50%, W_a/U_a=0.0

U - Axial Velocity
● - Radial Velocity (from 1,2,3&4)
W - Azimuthal Velocity

1 - $V_{\theta=30}{}^{\circ}$
2 - $V_{\theta=-30}{}^{\circ}$
3 - $V_{\theta=60}{}^{\circ}$
4 - $V_{\theta=-60}{}^{\circ}$
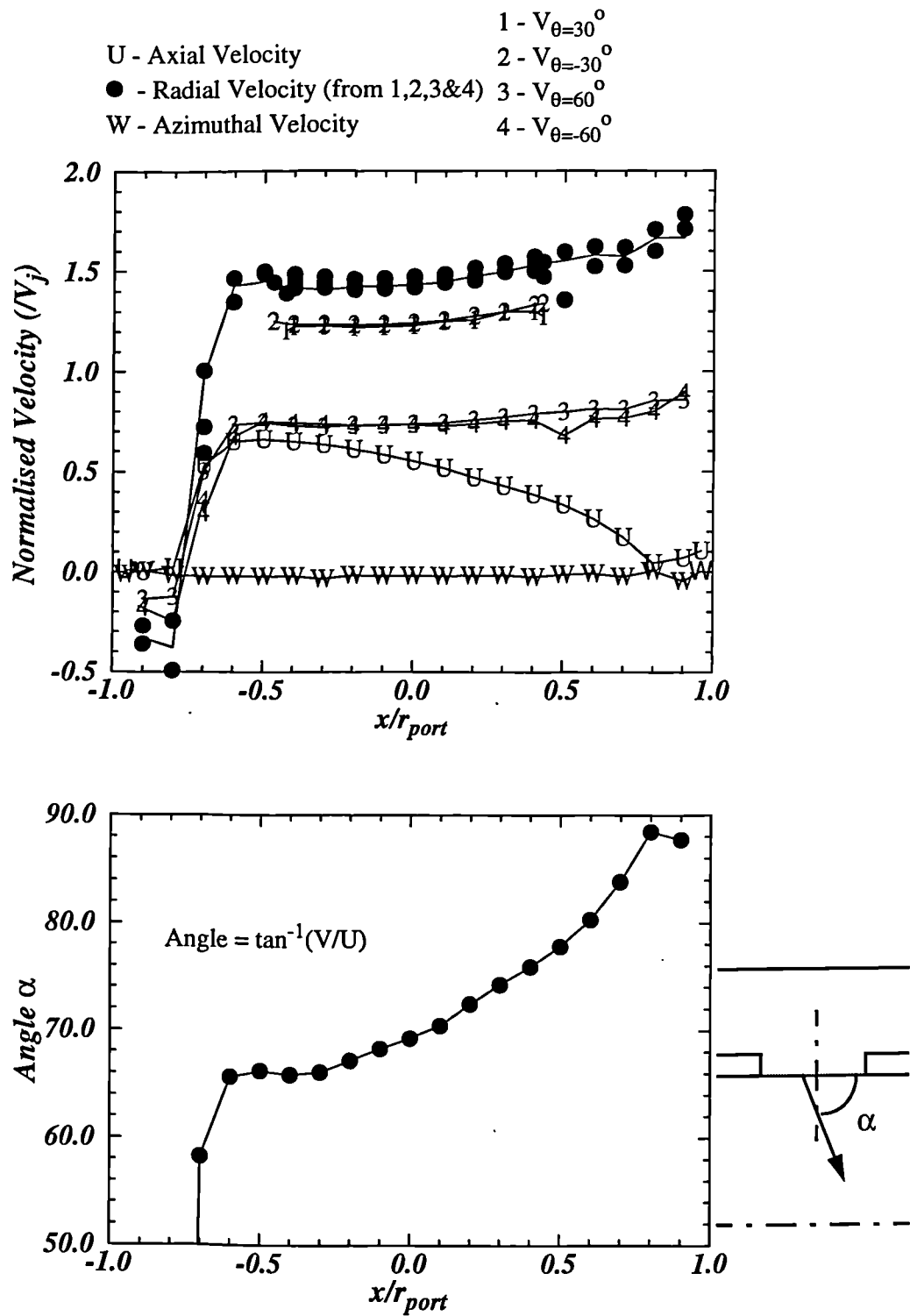
Figure 3.15 (a) Port Exit Velocity Profiles and Flow Angle
Plain port, R=5.0, Bleed = 50%, W_a/U_a = 0.0

Individual rms components measured to evaluate v.
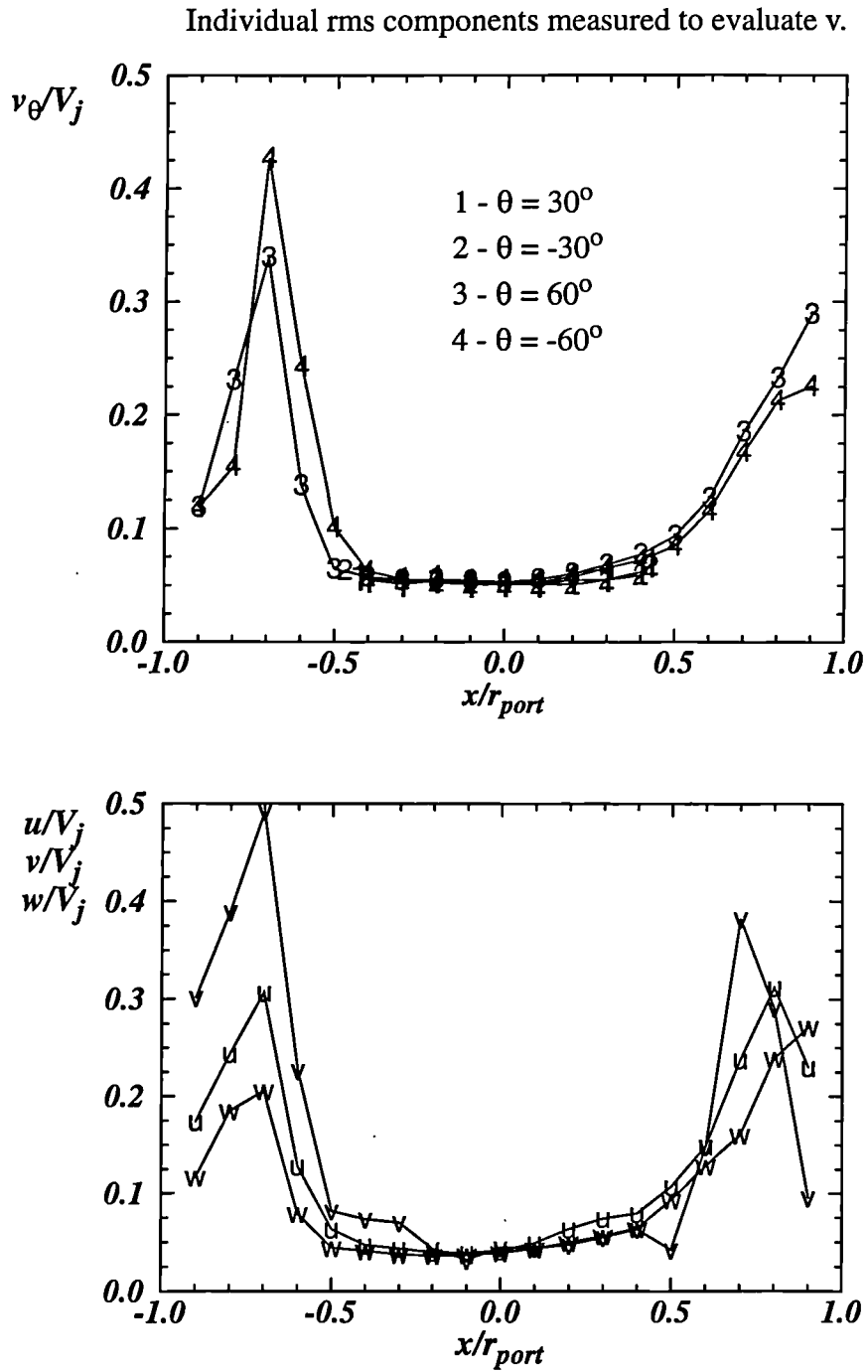
Figure 3.15(b) Port Exit Turbulence Profiles
Plain port, R=5.0, Bleed = 50%, W_a/U_a = 0.0
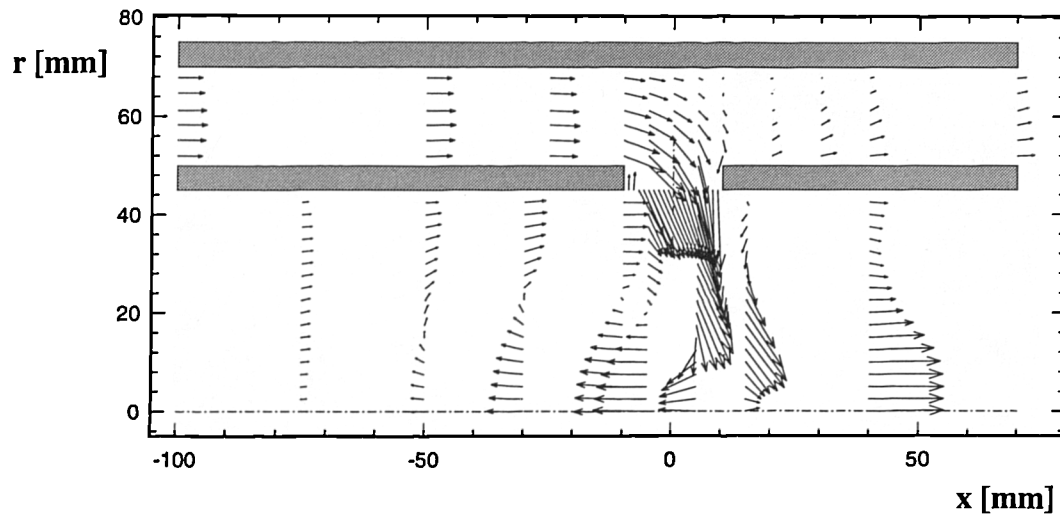
Figure 3.16 Combined Core, Annulus and Jet Velocity Vectors
Plain Port, R=5.0 Bleed=50%, W_a/U_a=0.0
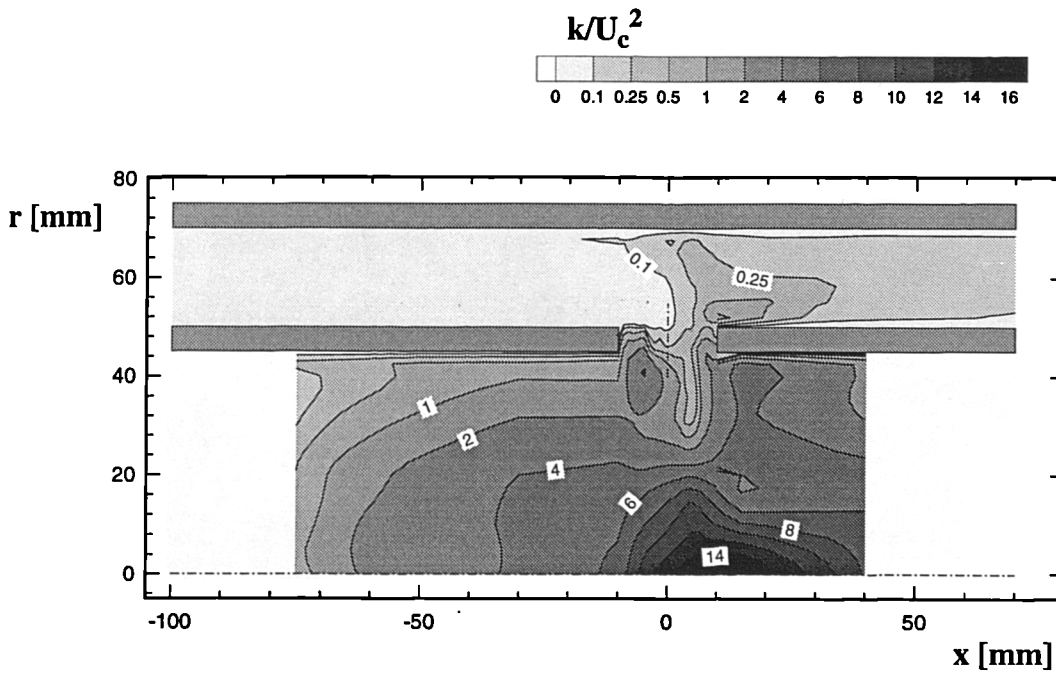
Figure 3.17 Combined Core, Annulus and Jet Turbulent Kinetic Energy
Plain Port, R=5.0 Bleed=50%, W_a/U_a=0.0
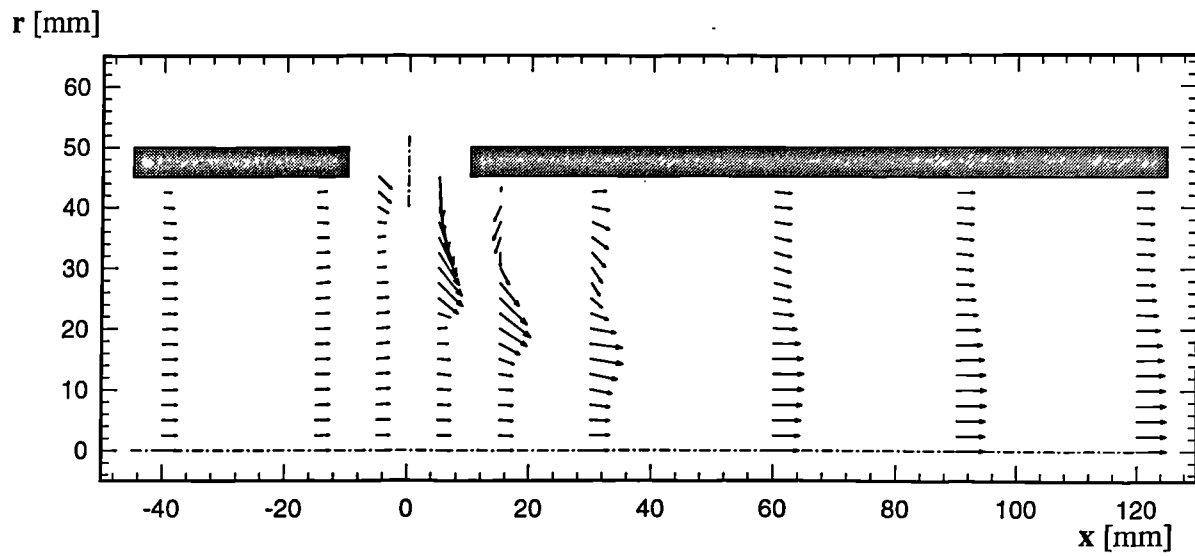
Figure 3.18(a) Velocity Vectors in Core
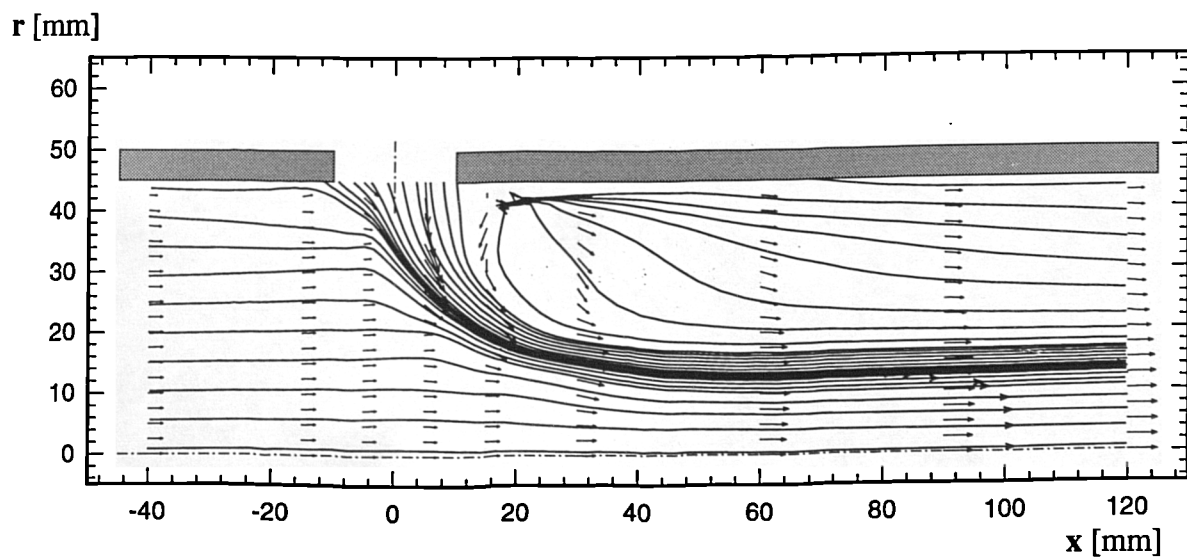Plain Port, R=2.0 Bleed=20%, W_a/U_a=0.0

Figure 3.18(b) 2-Dimensional Particle Tracks in Core
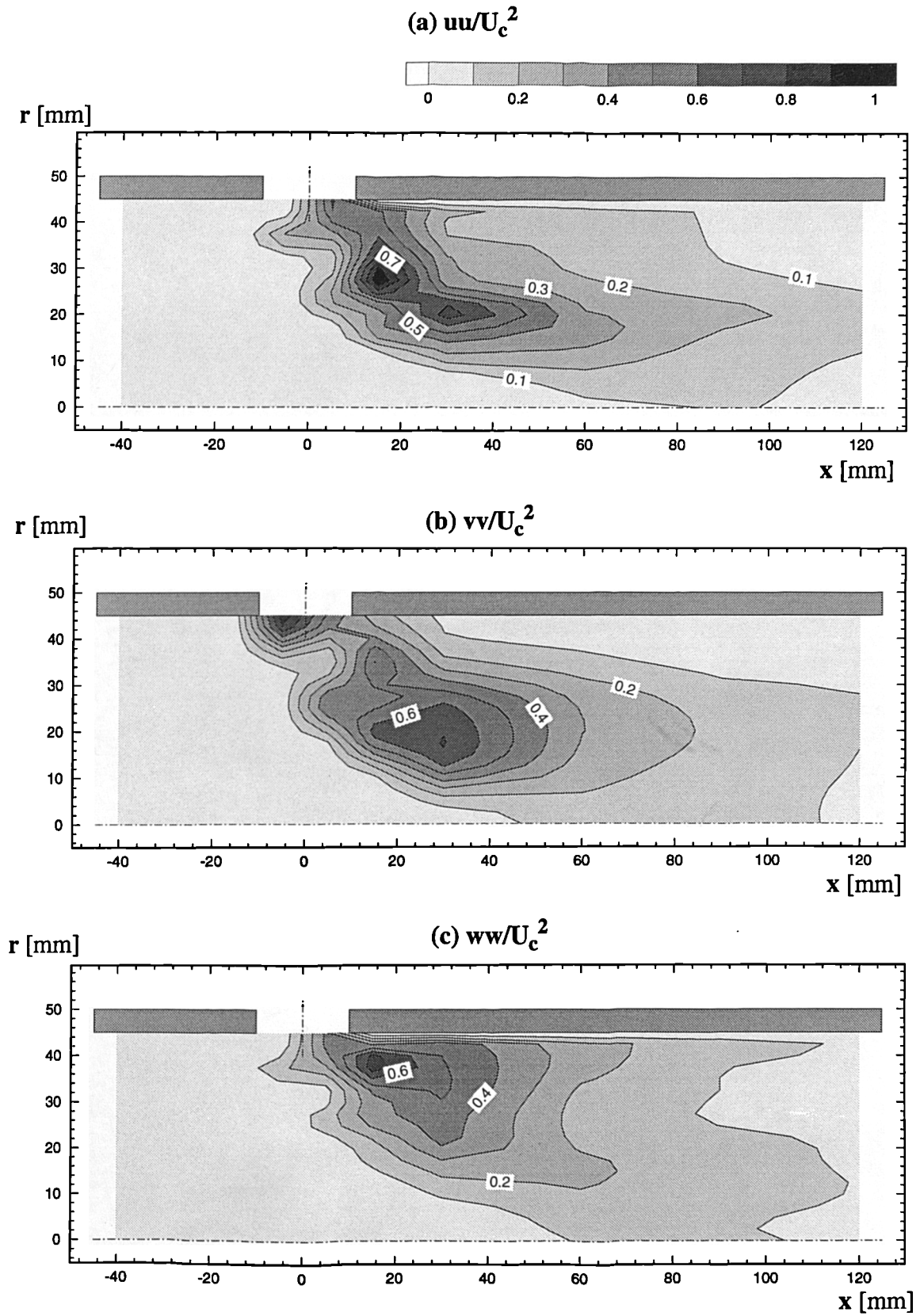Plain Port, R=2.0 Bleed=20%, W_a/U_a=0.0

(a) uu/U$_c$^{2}

(b) vv/U$_c$^{2}

(c) ww/U$_c$^{2}

Figure 3.19 Non-Dimensional Normal Stresses in Core
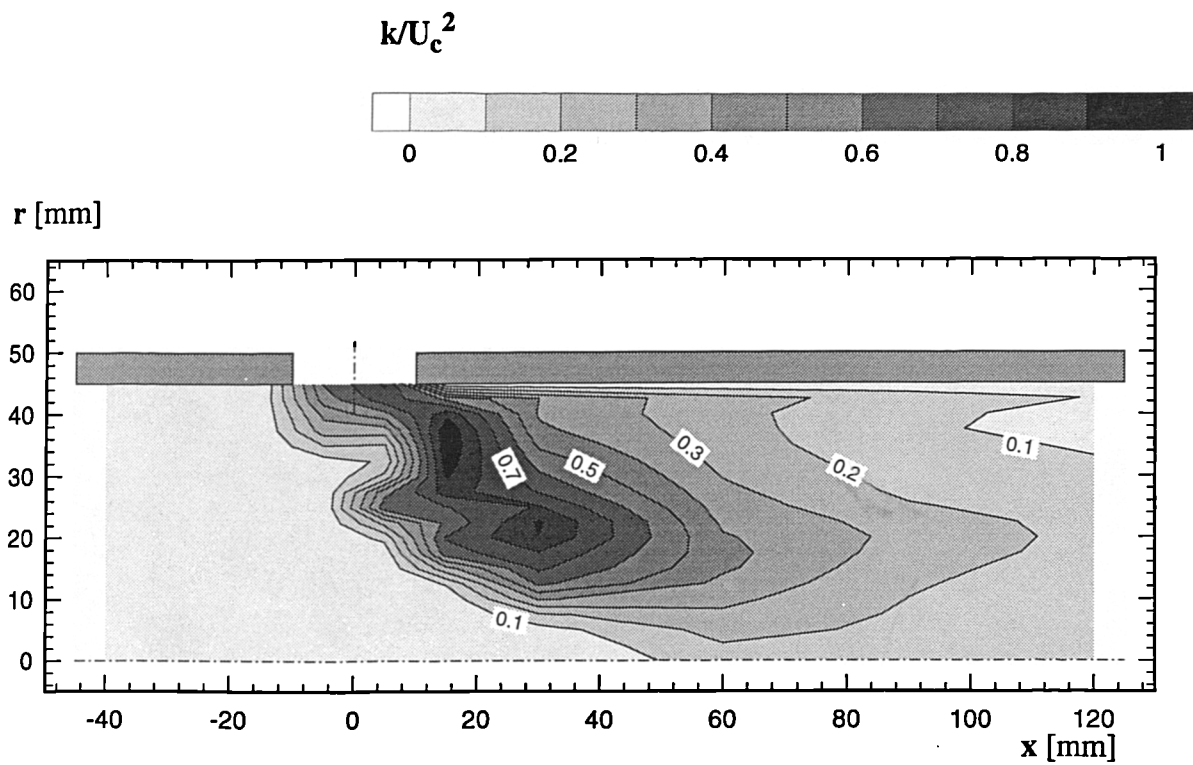Plain Port, R=2.0 Bleed=20%, W$_a$/U$_a$=0.0

$$k/U_c^2$$

Figure 3.20 Non-Dimensional Turbulent Kinetic Energy In Core
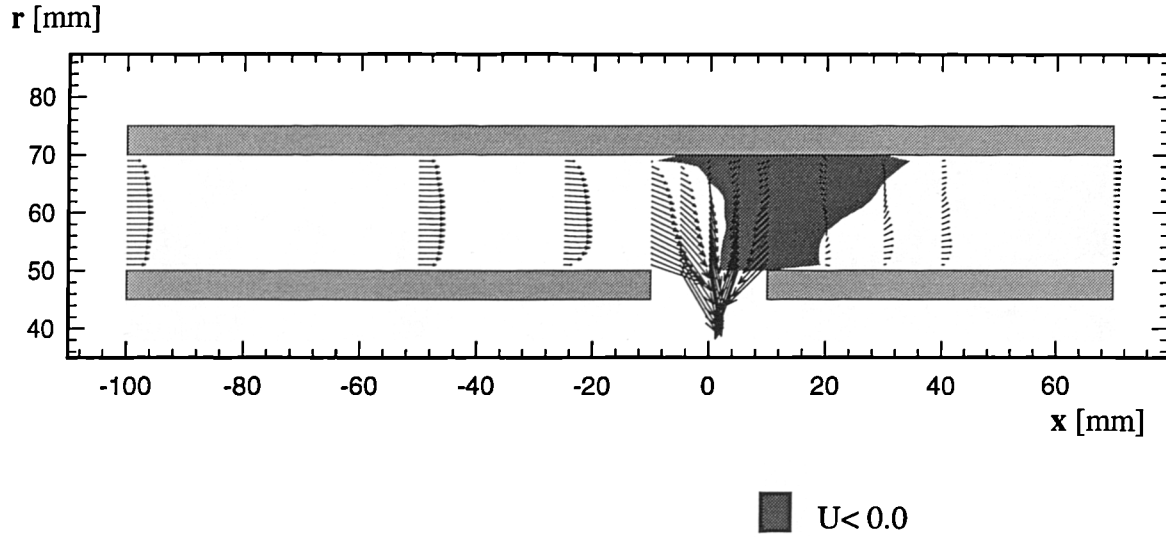Plain Port, R=2.0 Bleed=20%, W_a/U_a=0.0

Figure 3.21 Velocity Vectors in Annulus
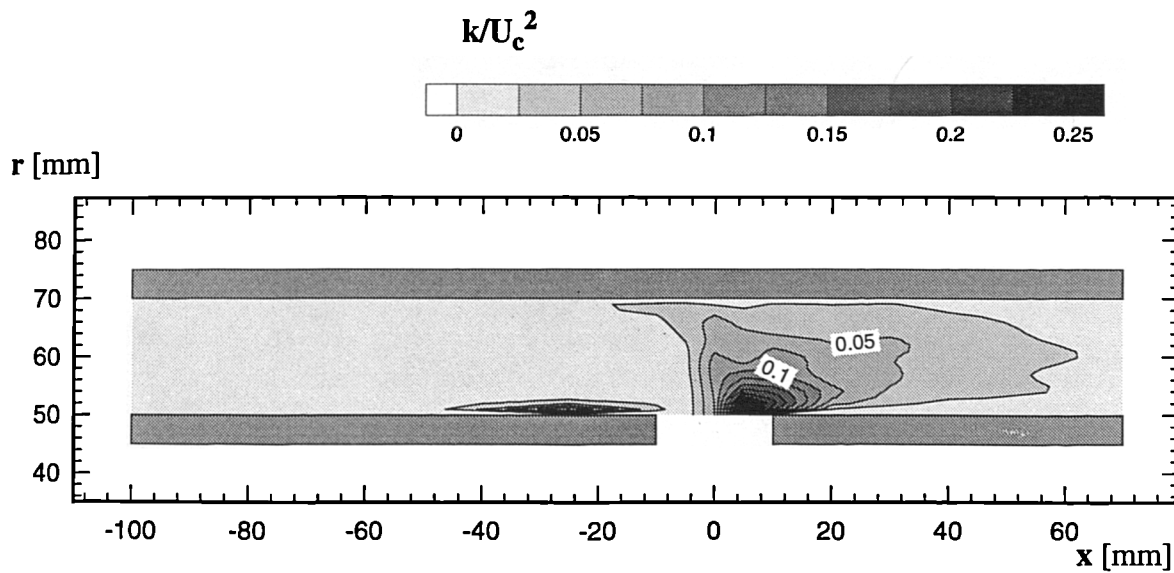Plain Port, R=2.0 Bleed=20%, W_a/U_a=0.0

Figure 3.22 Non-Dimensional Turbulent Kinetic Energy in Annulus
Plain Port, R=2.0 Bleed=20%, W_a/U_a=0.0

(a) uu/U_c^2
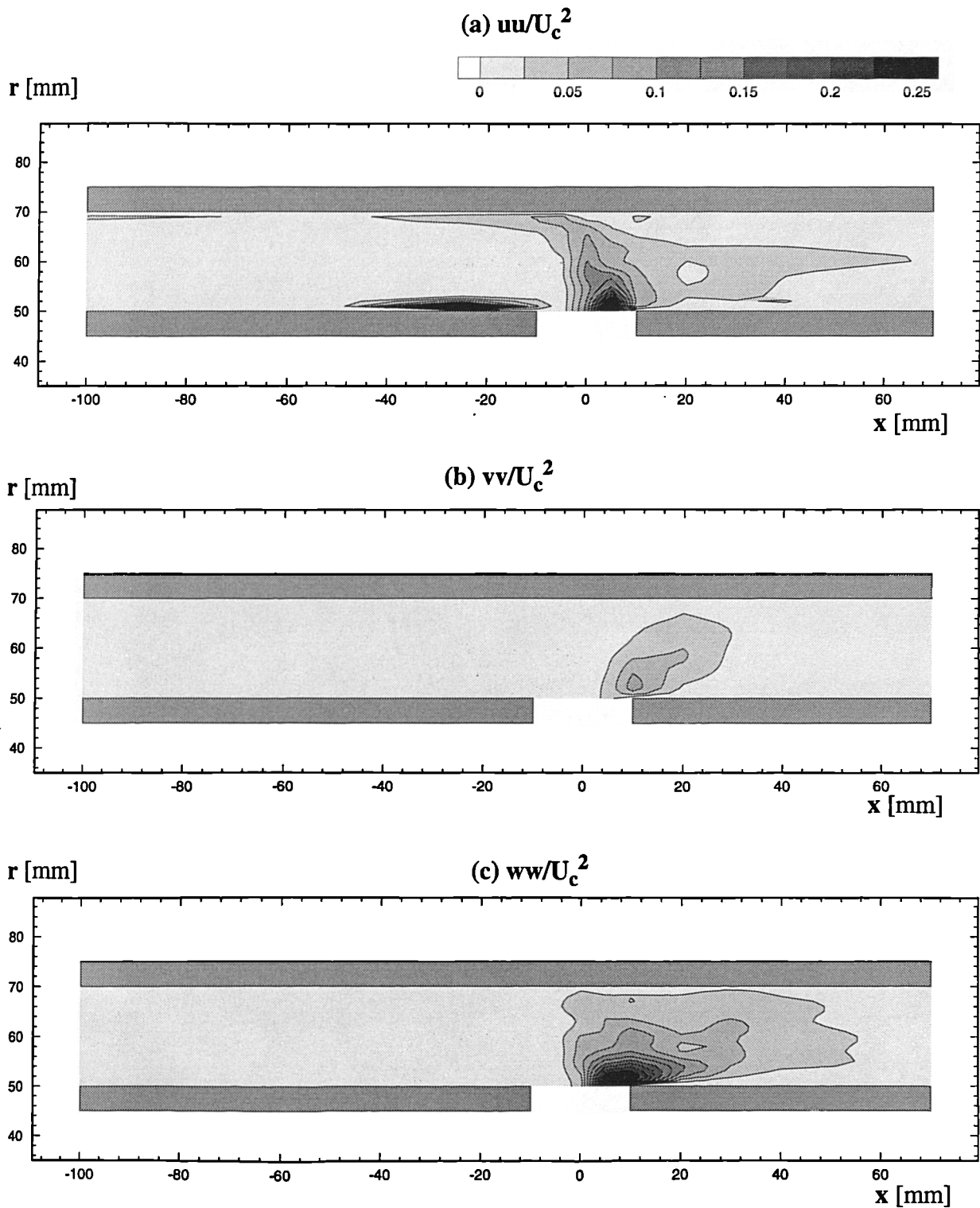

(b) vv/U_c^2

(c) ww/U_c^2

Figure 3.23 Non-Dimensional Normal Stresses in Annulus
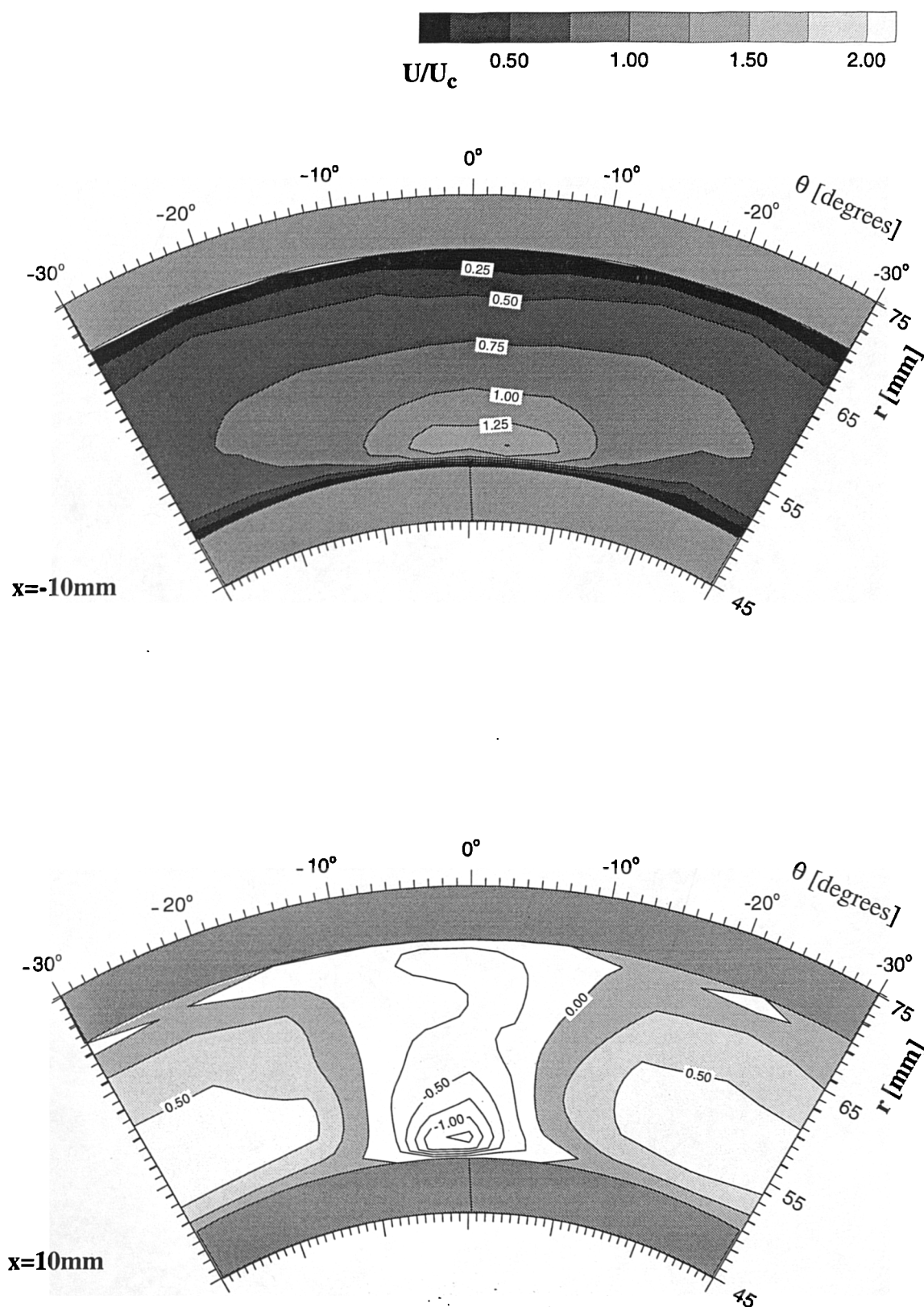Plain Port, R=2.0 Bleed=20%, W$_a$/U$_a$=0.0

Figure 3.24 Axial Velocity Distribution in Annulus on x=-10 and x=10 Planes
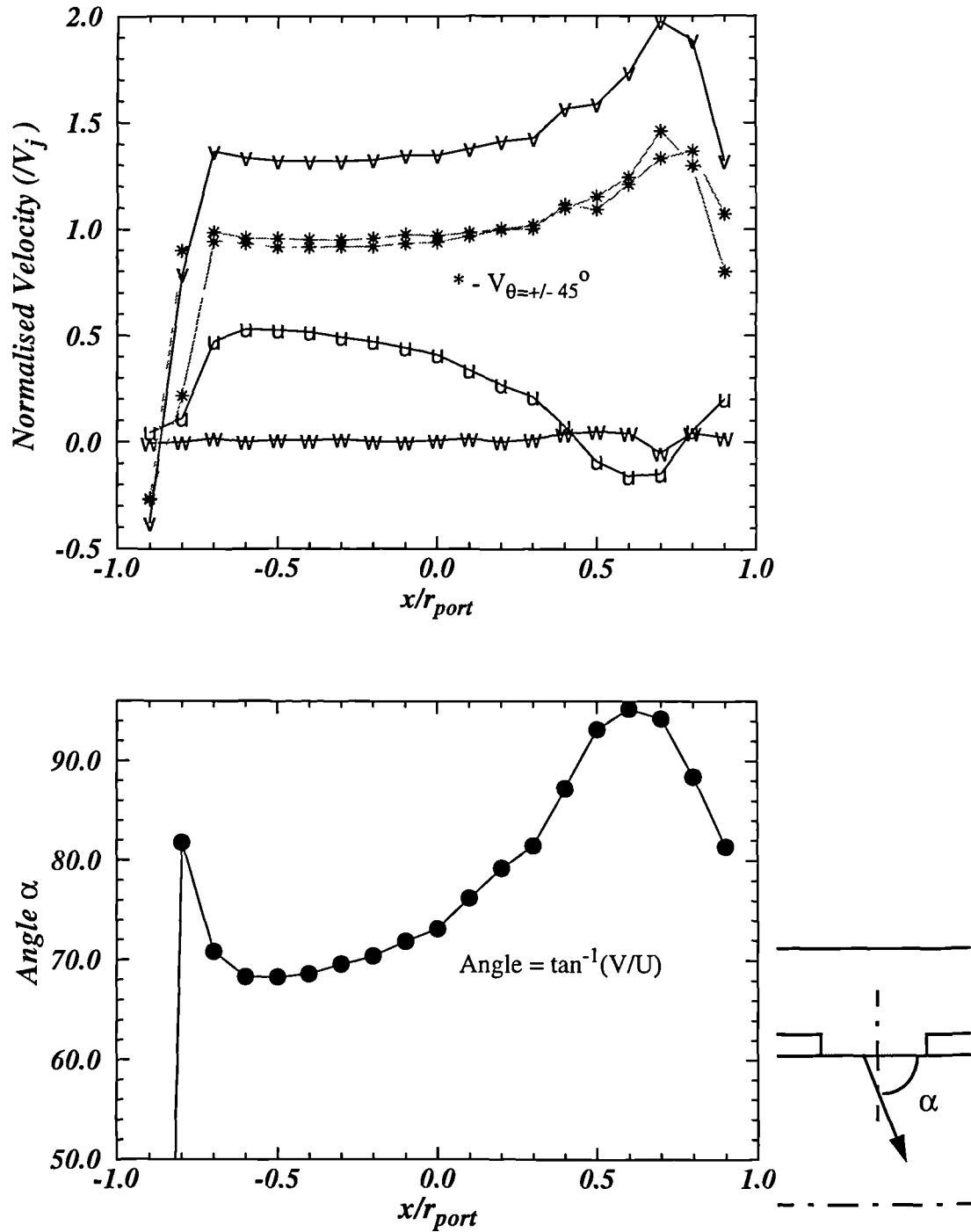Plain Port, R=2.0 Bleed=20%, W_a/U_a=0.0

Figure 3.25 (a) Port Exit Velocity Profiles and Flow Angle
Plain port, R=2.0, Bleed = 20%, $W_a/U_a = 0.0$

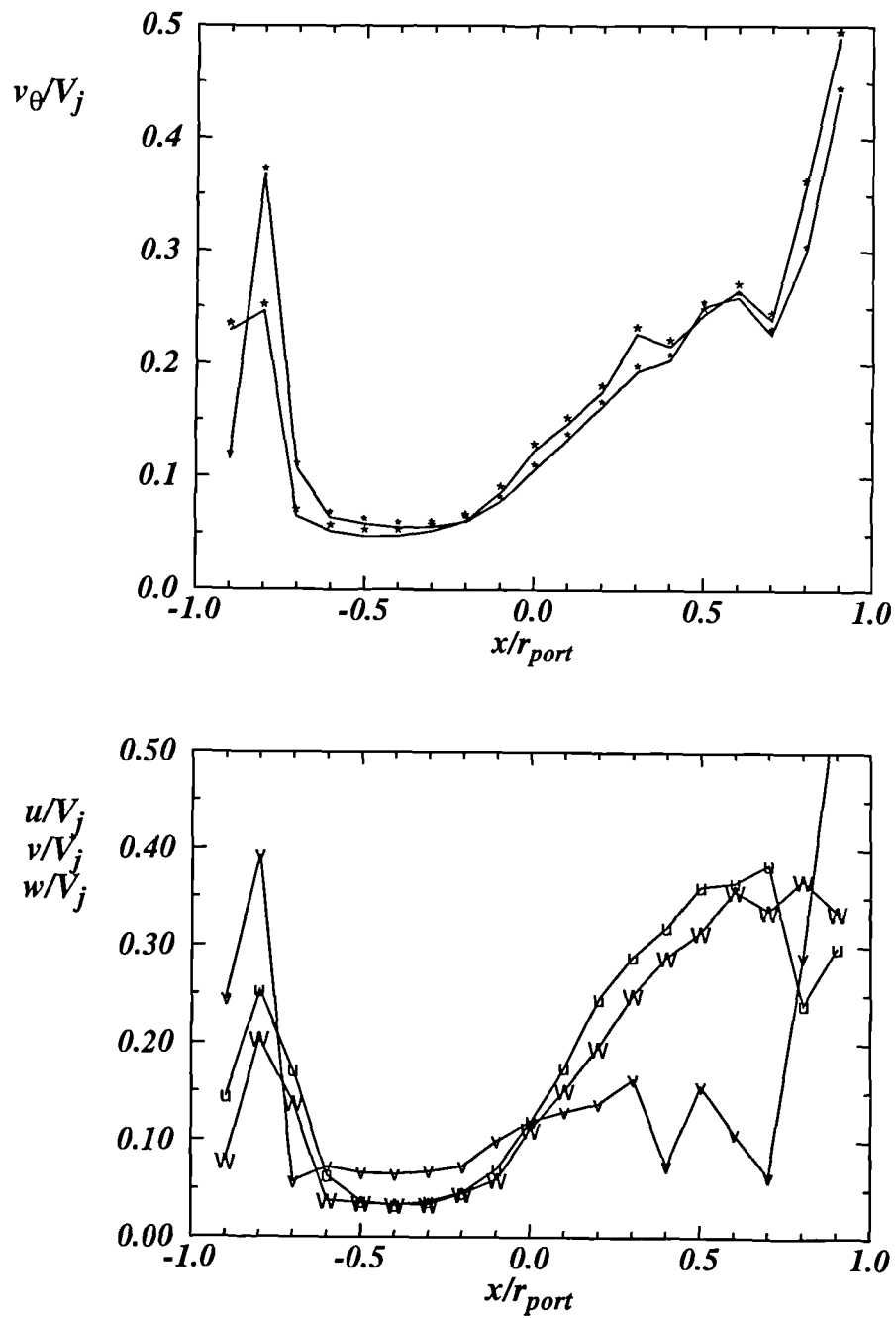**Figure 3.25(b) Port Exit Turbulence Profiles**
Plain port, R=2.0, Bleed = 20%, W_a/U_a = 0.0
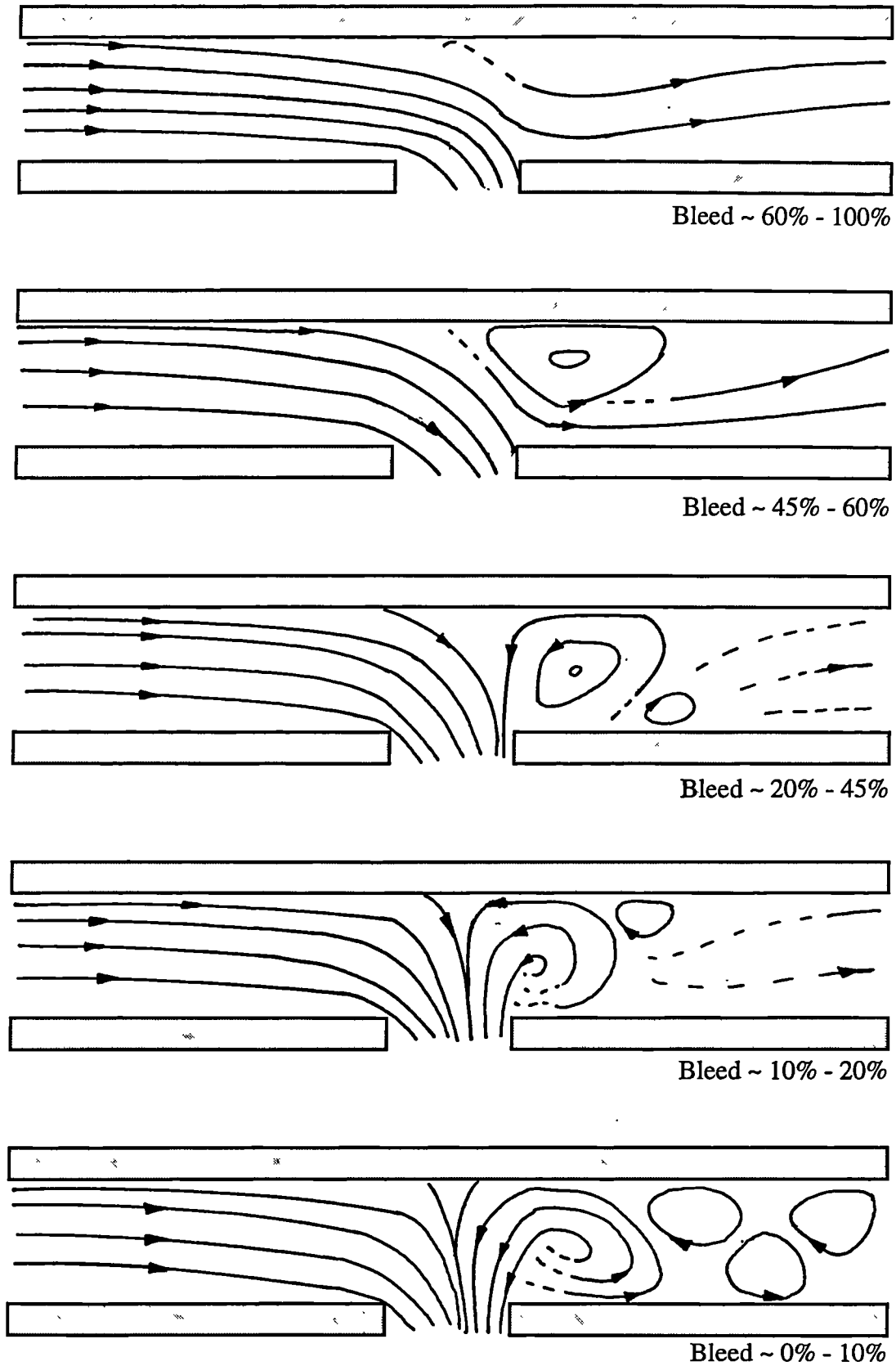
Figure 3.26 Flow Visualisation - Schematic of Annulus Flow Patterns
Plain Port, R≈5.0 Bleed 0% to 100%, W_a/U_a=0.0

Bleed ~ 80%

Bleed ~ 50%

Bleed ~ 10%

Symmetric

Asymmetric
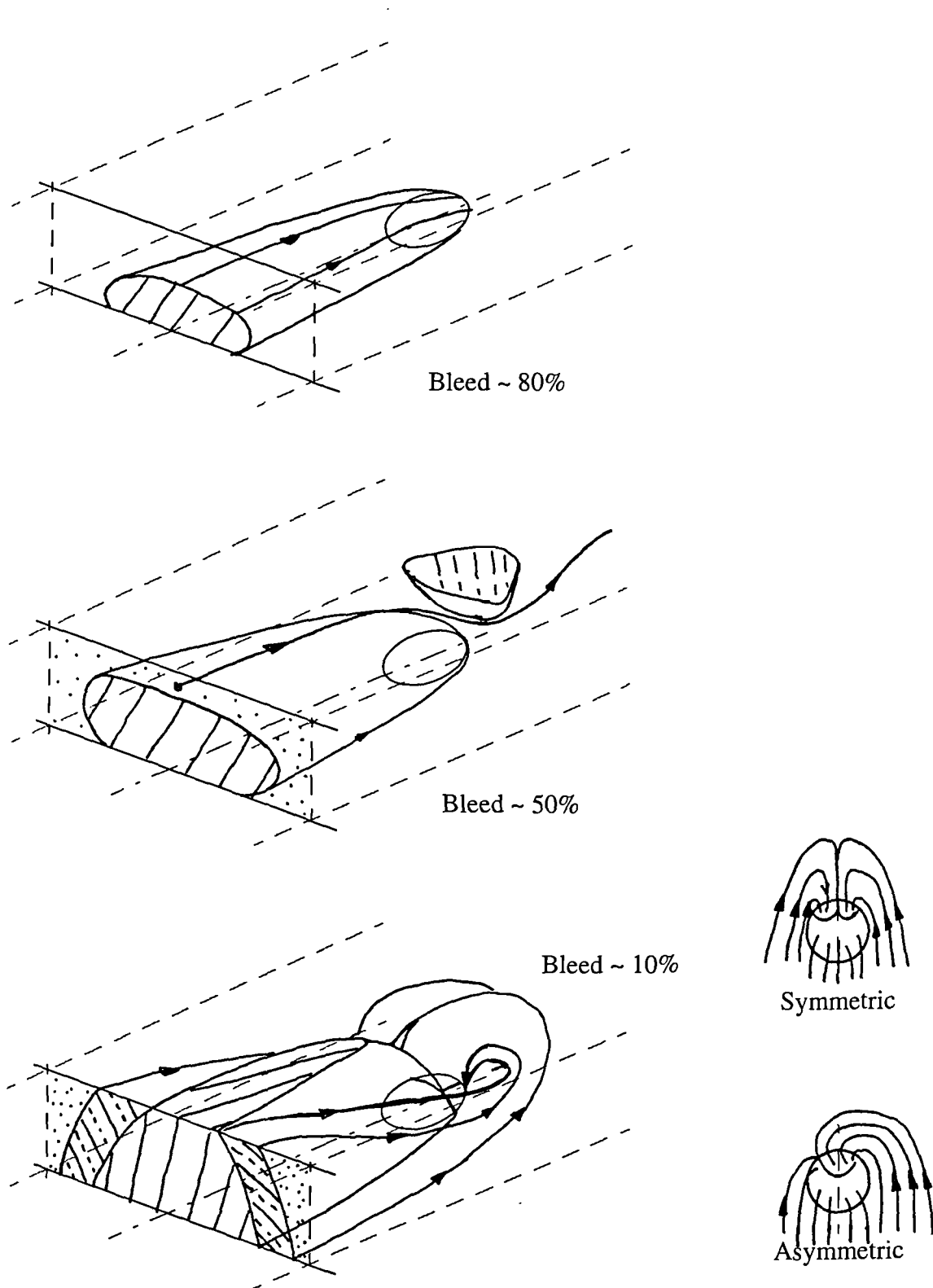
Figure 3.27 Flow Visualisation - 3D Topology of Time Averaged Flow
Plain Port, R≈5.0 Bleed ~ 10% to 80%, W_a/U_a=0.0
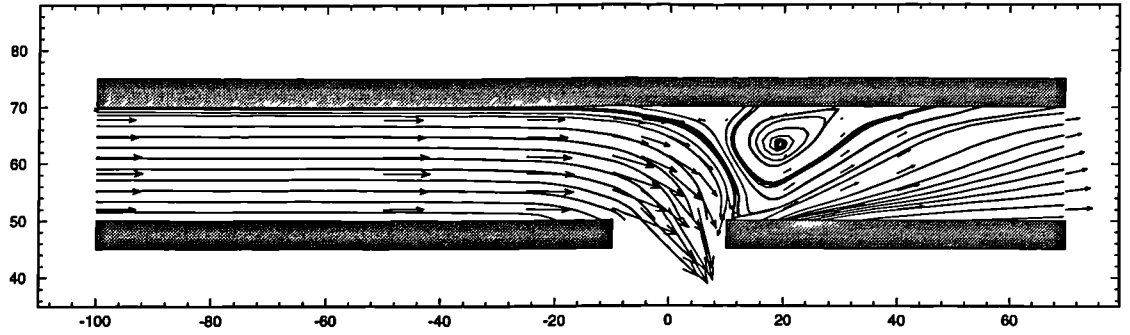
(a) Bleed 50%
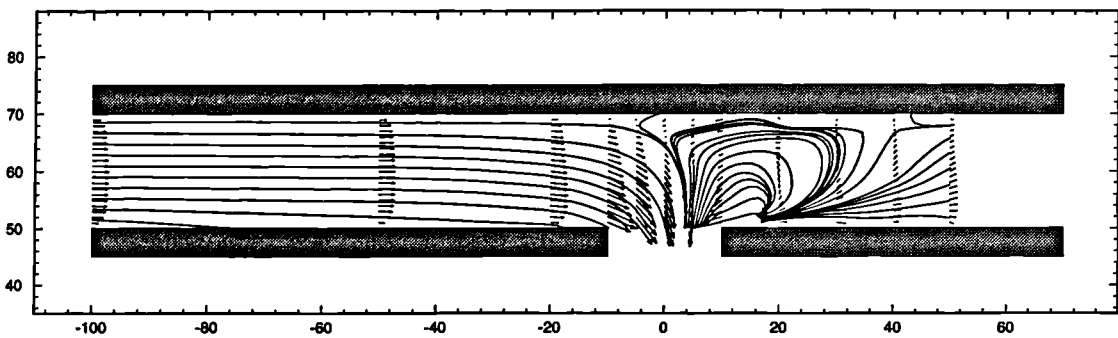
(b) Bleed 40%
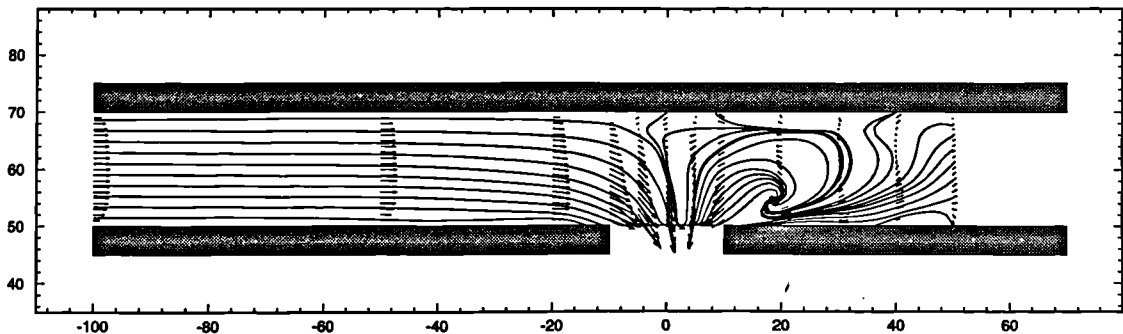
(c) Bleed 25%
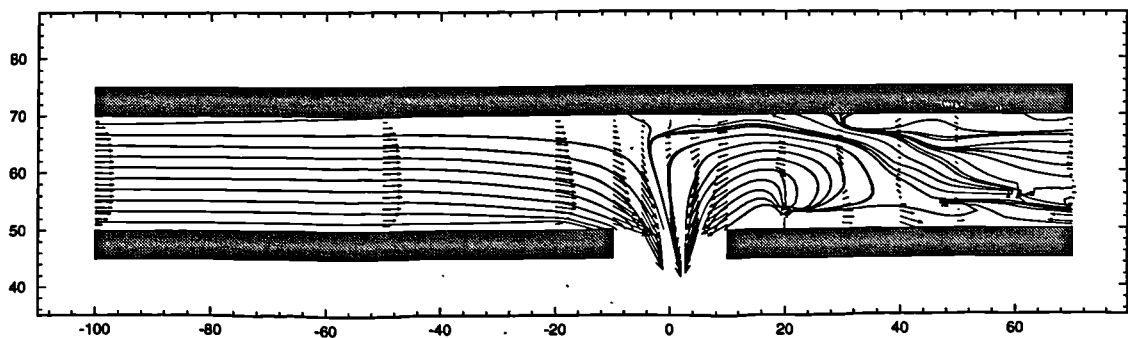
(d) Bleed 10%

Figure 3.28 Measured Annulus Flow Patterns
Plain Port, R=5.0 Bleed 10% to 50%, W_a/U_a=0.0

Secondary Velocity Components Across Two Port Diameters:
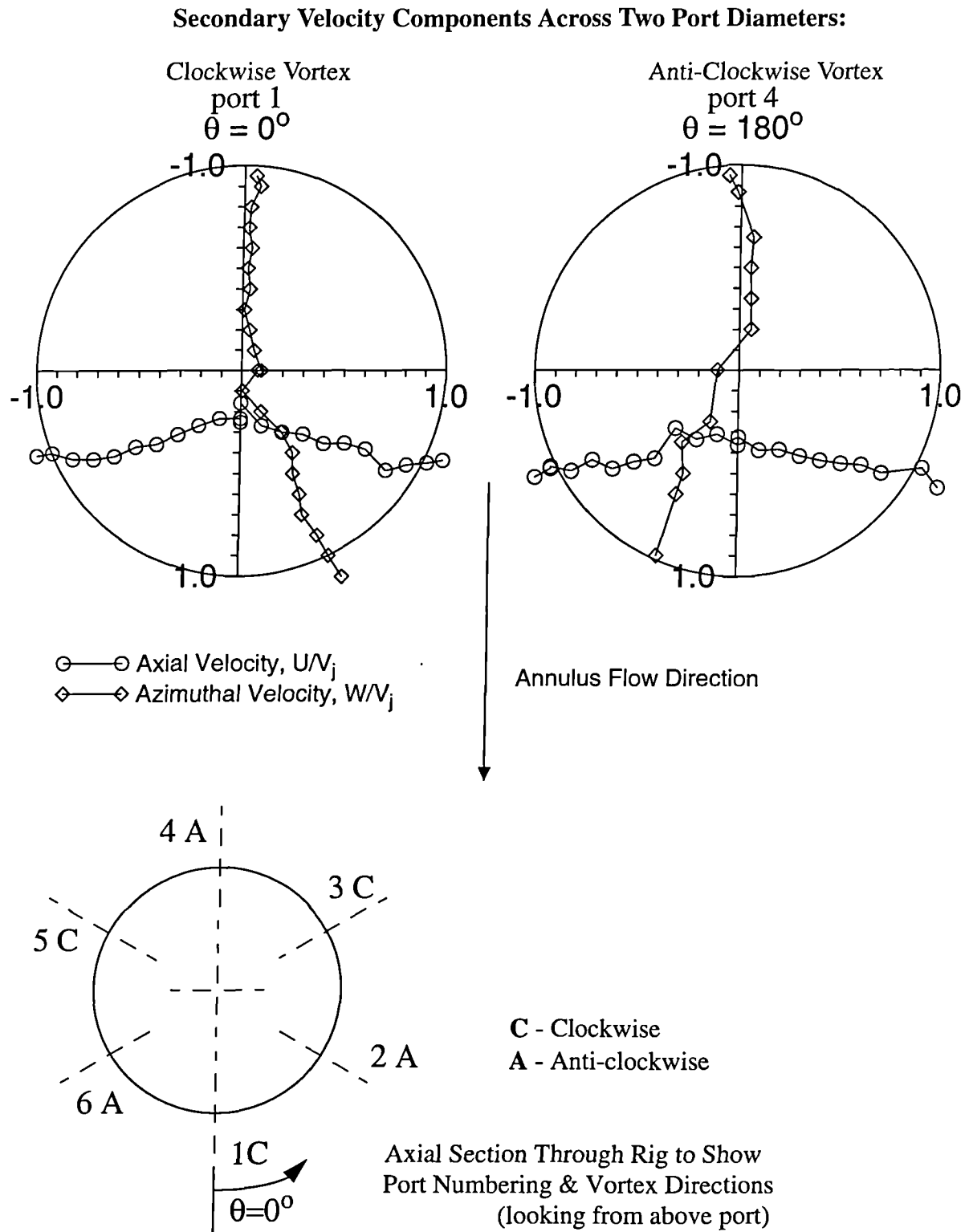
Figure 3.29 Evidence Of Contra-Rotating Vortices in Port Pairs
Plain Port, R=5.0 Bleed 0%, W_a/U_a=0.0

Section A-A
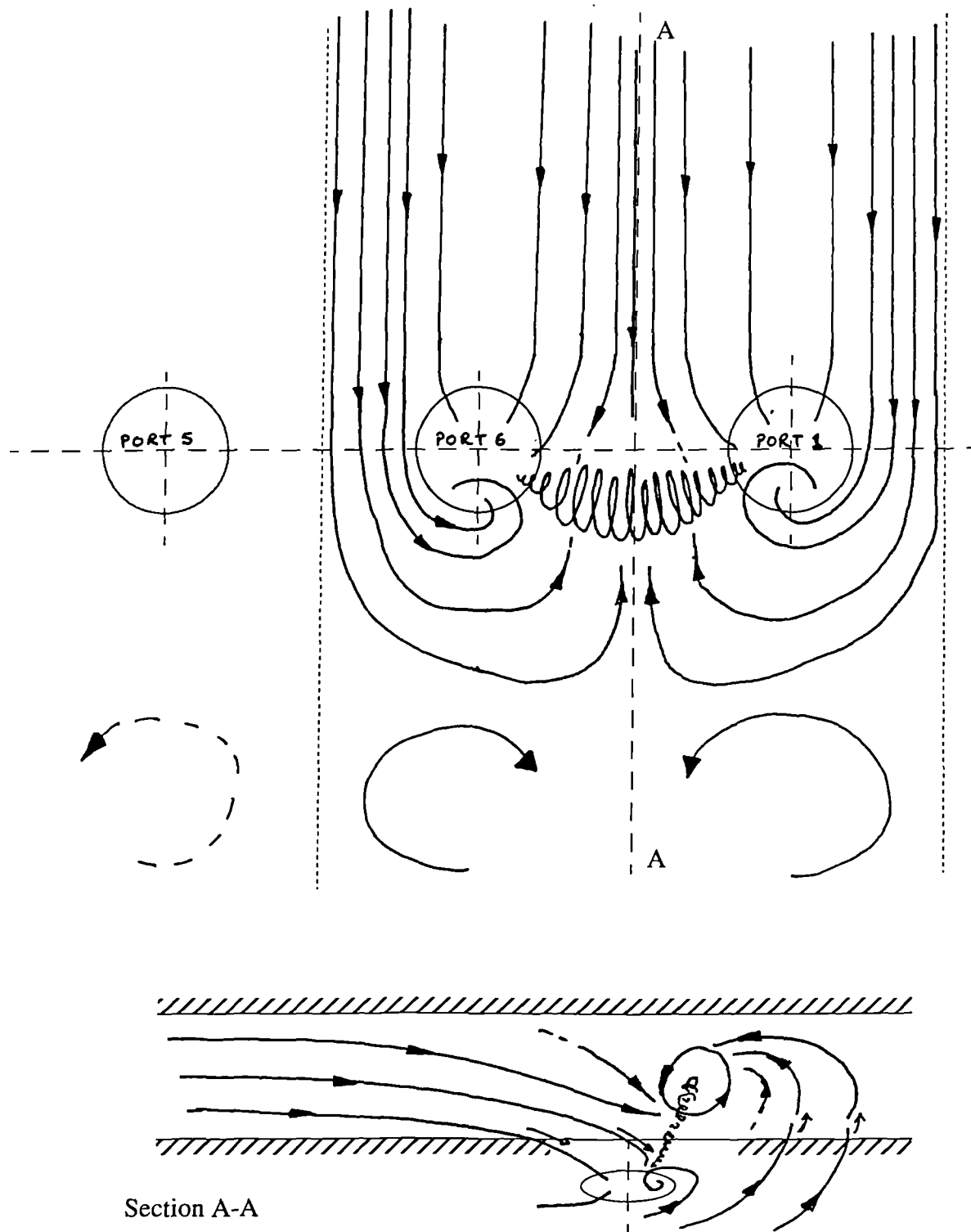
Figure 3.30 Flow Visualisation: Port Vortex Interactions
Plain Port, R≈5.0 Bleed 0%, $W_a/U_a=0.0$
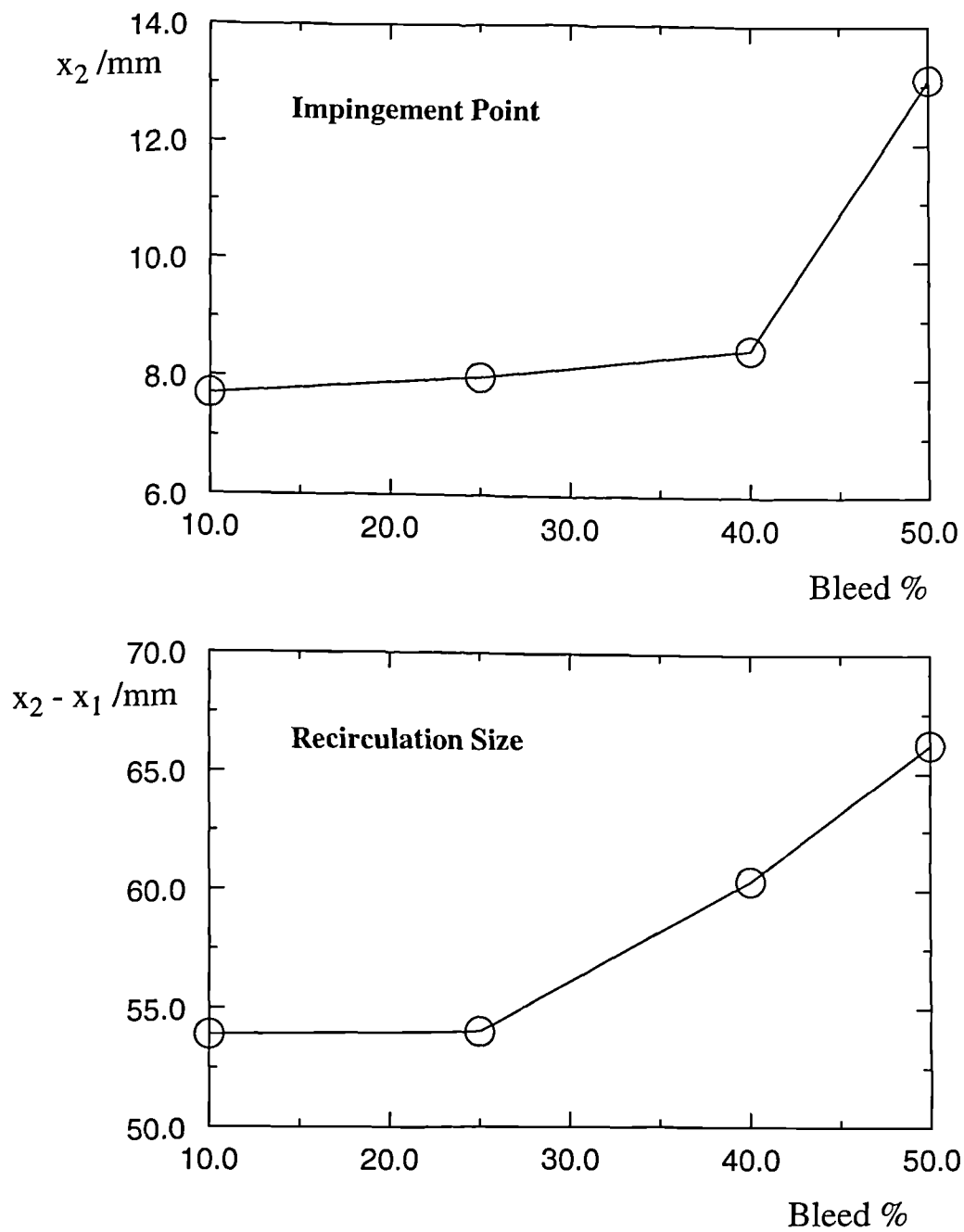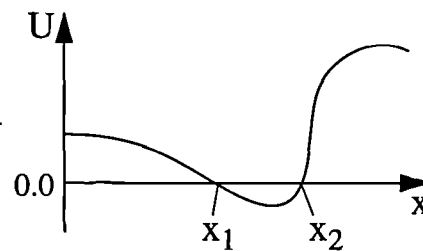
Figure 3.31 Effect of Varying Bleed on Core Flow
Plain Port, R=5.0, Bleed 10%-50%, W_a/U_a=0.0

r [mm]

(a) Chuted Port

r [mm]
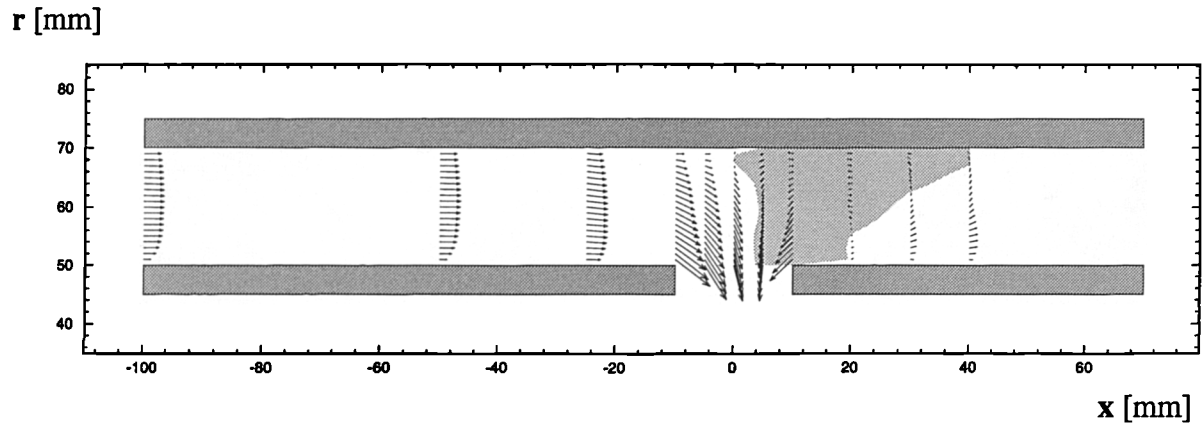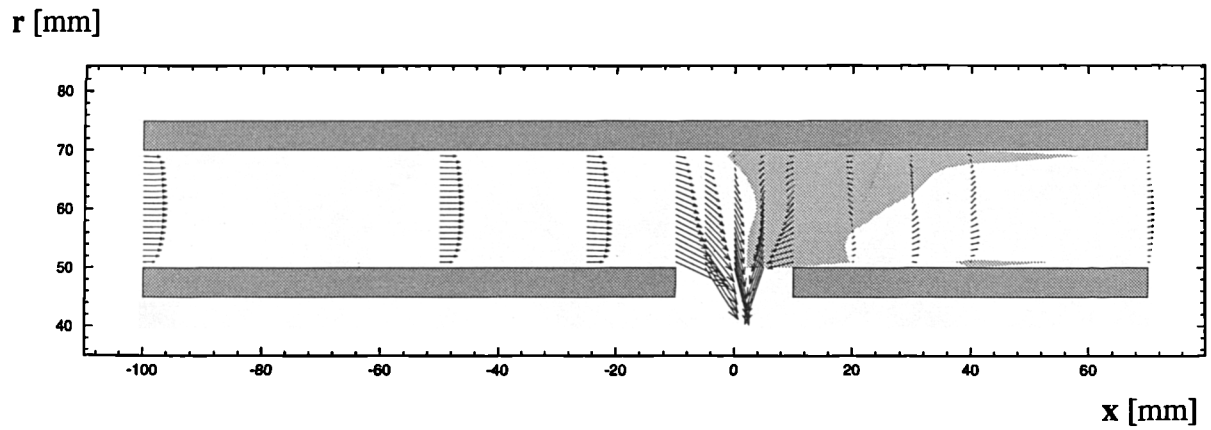
(b) D-shaped Port

▨ U < 0.0

Figure 3.32 Comparison of Annulus Flow For Chuted and D-Shaped Ports.
R=2.0 Bleed=20%, W_a/U_a=0.0

(a) Chuted Port
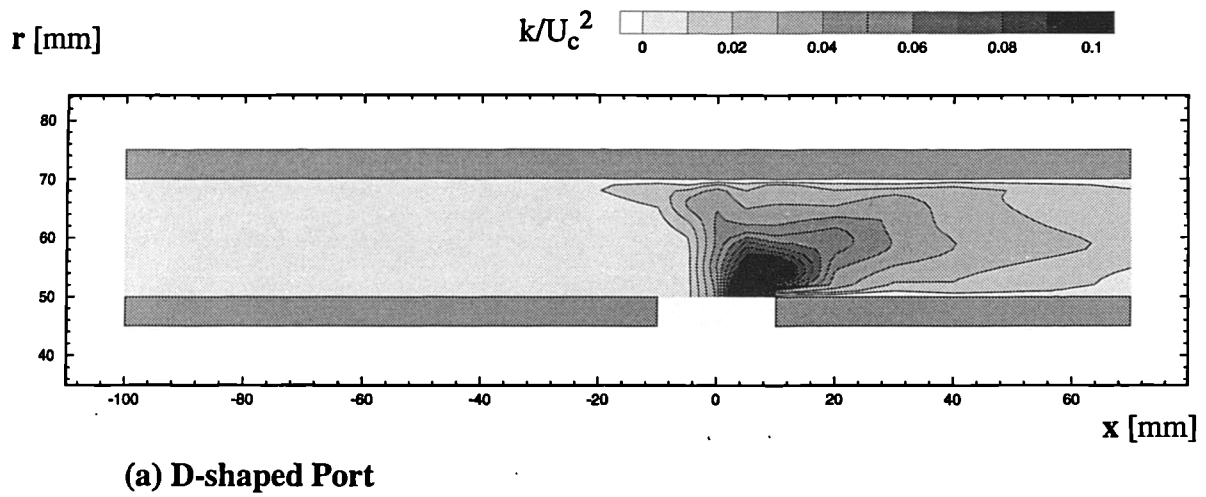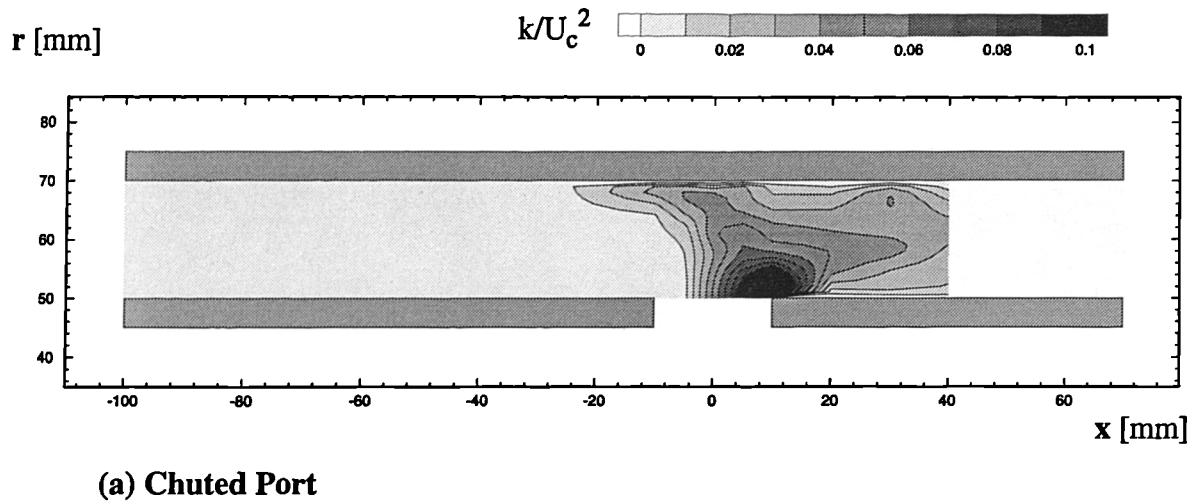
(a) D-shaped Port

Figure 3.33 Annulus Turbulent Kinetic Energy For Chuted and D-Shaped Ports.
R=2.0 Bleed=20%, W_a/U_a=0.0
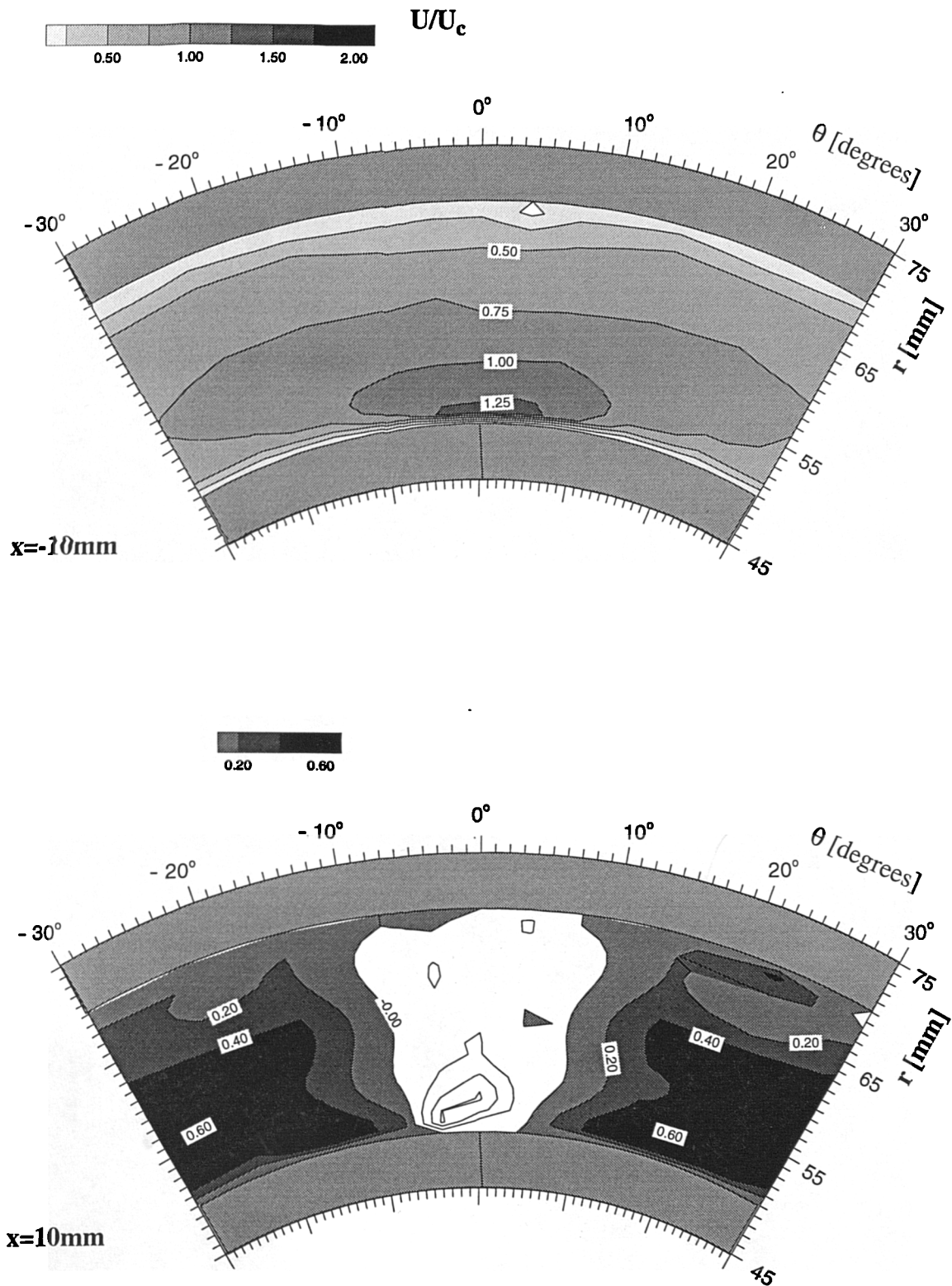
Figure 3.34 Axial Velocity Distribution in Annulus on x=-10 and x=10 Planes
Chuted Port, R=2.0 Bleed=20%, W_a/U_a=0.0
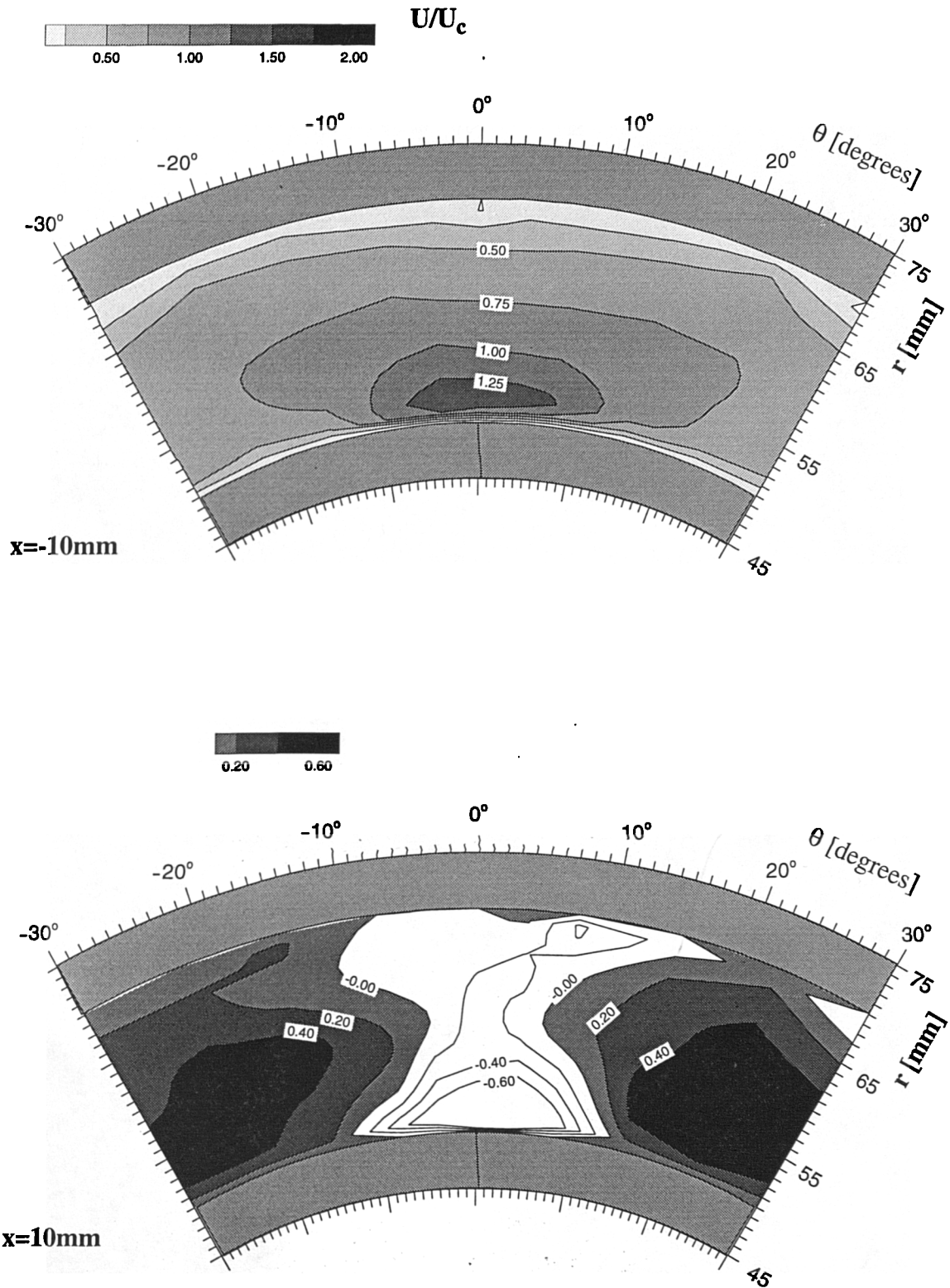
**Figure 3.35 Axial Velocity Distribution in Annulus on x=-10 and x=10 Planes
D-Shaped Port, R=2.0, Bleed=20%, W_a/U_a=0.0**
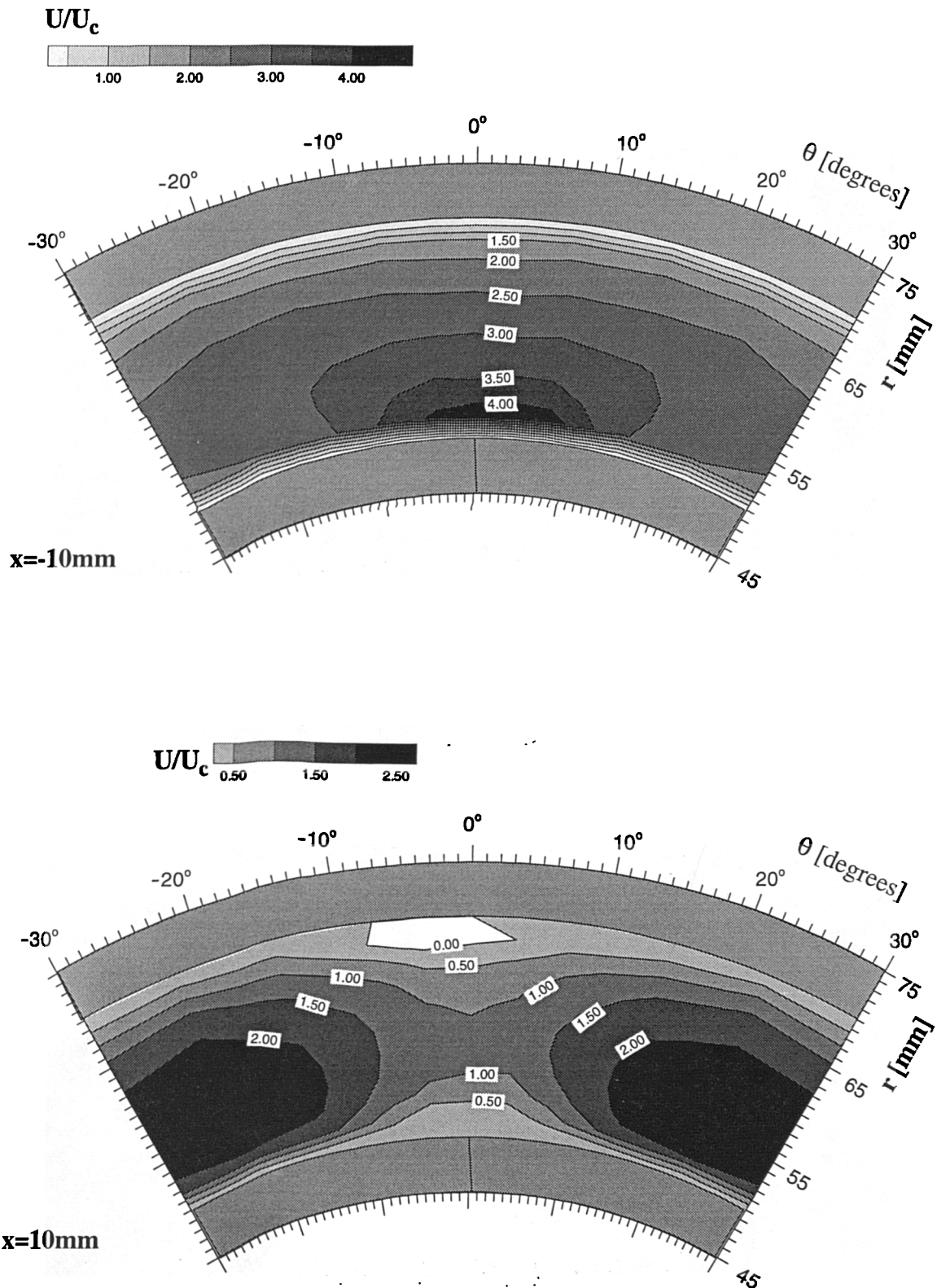
Figure 3.36 Axial Velocity Distribution in Annulus on x=-10 and x=10 Planes
D-Shaped Port, R=5.0 Bleed=50%, W_a/U_a=0.0

(a) Plain Port
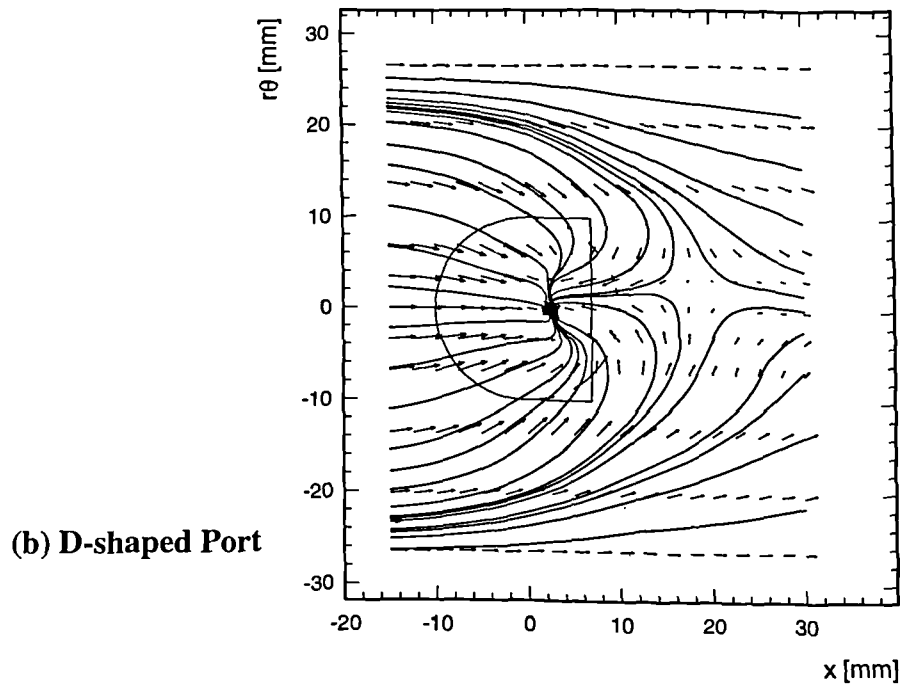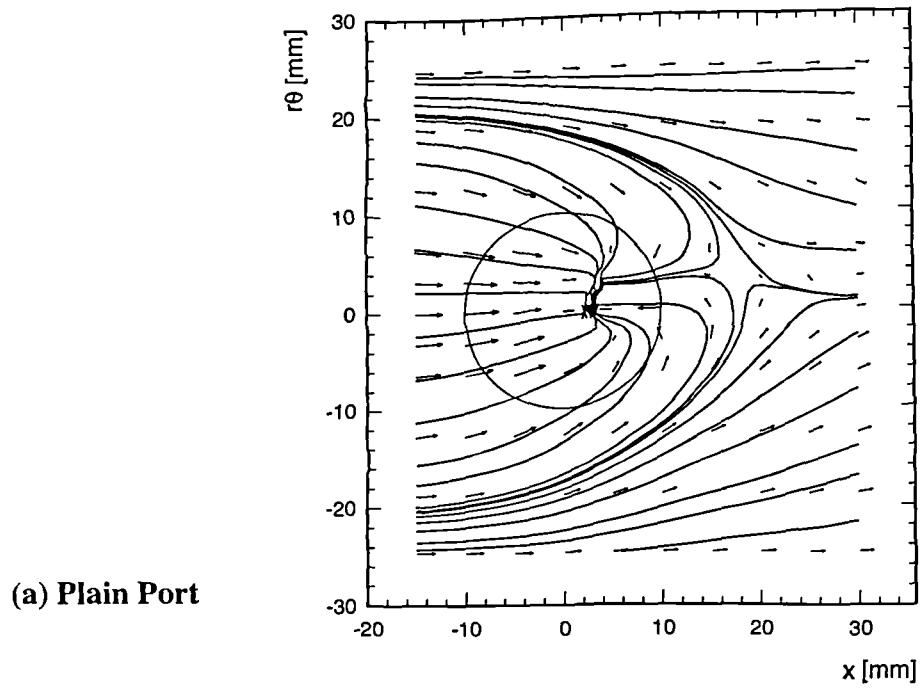
(b) D-shaped Port

(plane r=52.5mm)

Figure 3.37 Secondary Velocity Vectors Near Inner Annulus Wall
R=2.0 Bleed=20%, W_a/U_a=0.0
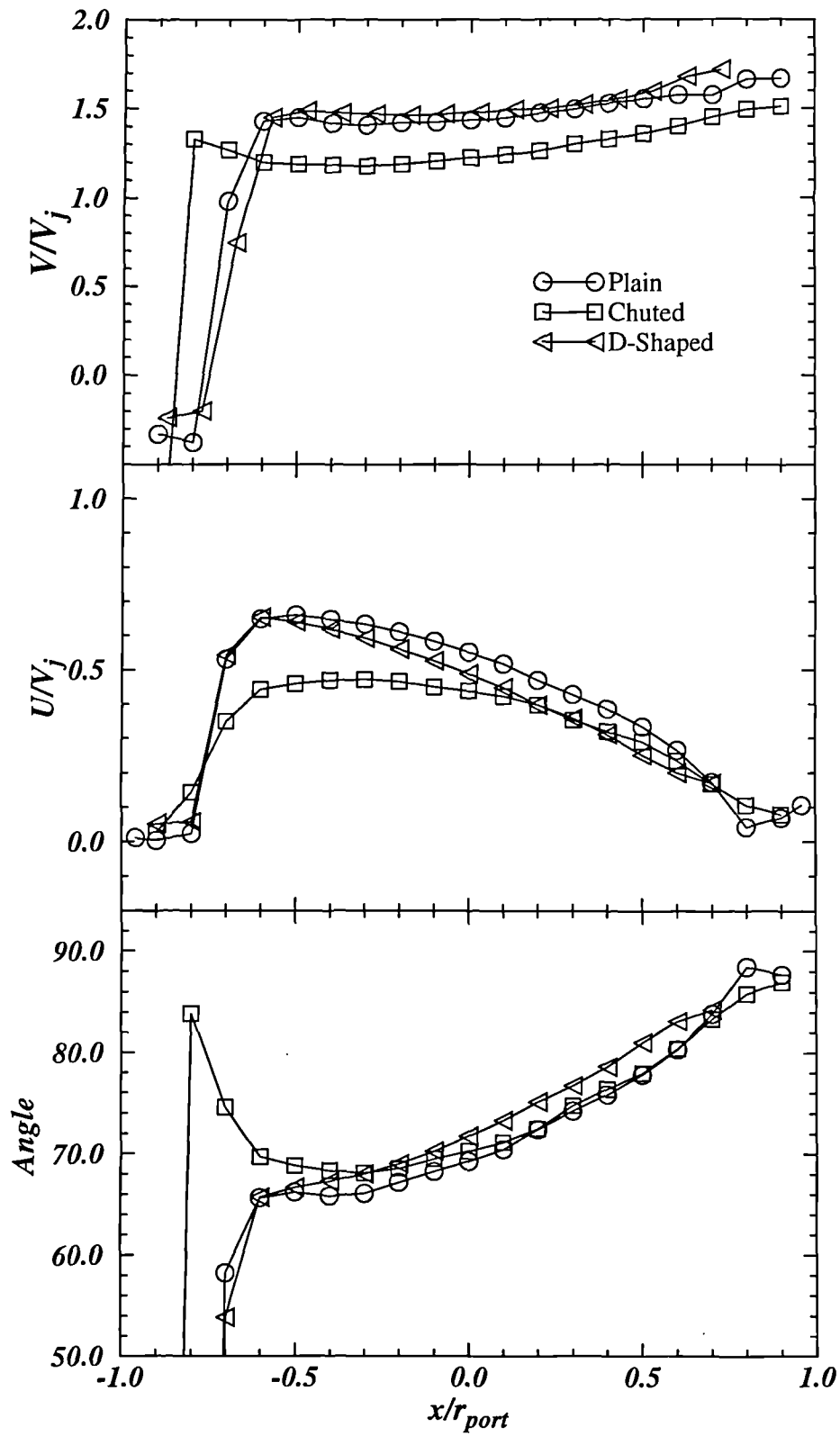
Figure 3.38 Jet Exit Velocity Profiles For Three Port Shapes
R=5.0 Bleed=50%, W_a/U_a=0.0
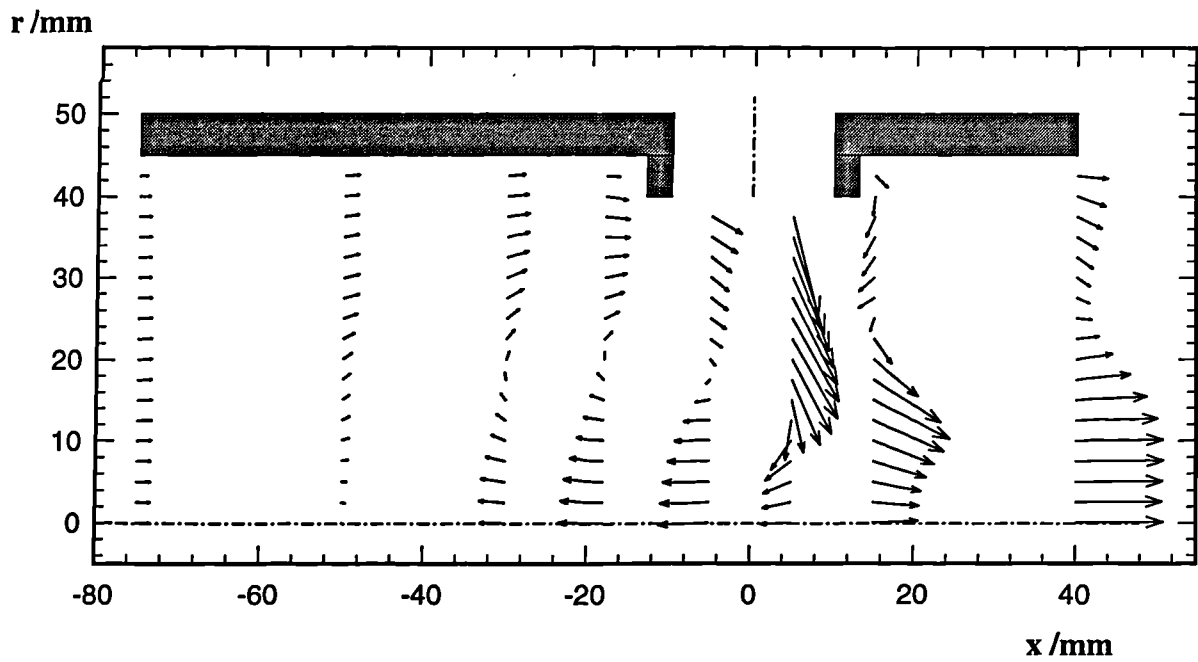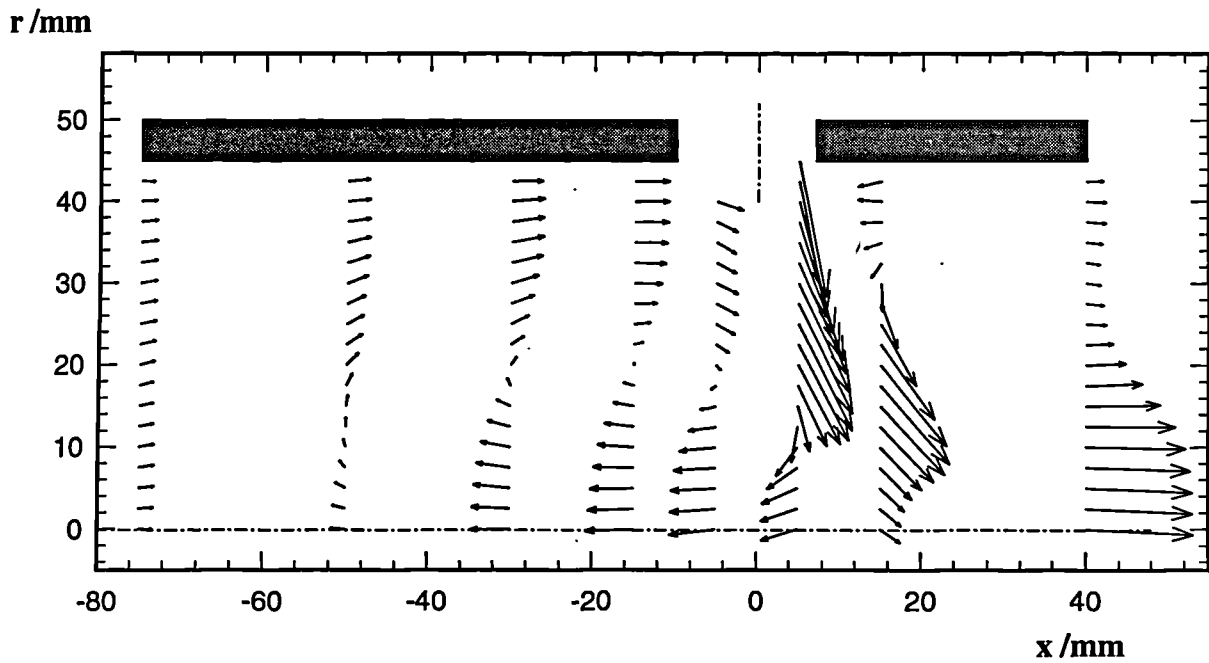
(a) Chuted Port

(b) D-Shaped Port

Figure 3.39 Comparison of Core Flow For Chuted and D-Shaped Ports
R=5.0 Bleed=50%, W_a/U_a=0.0
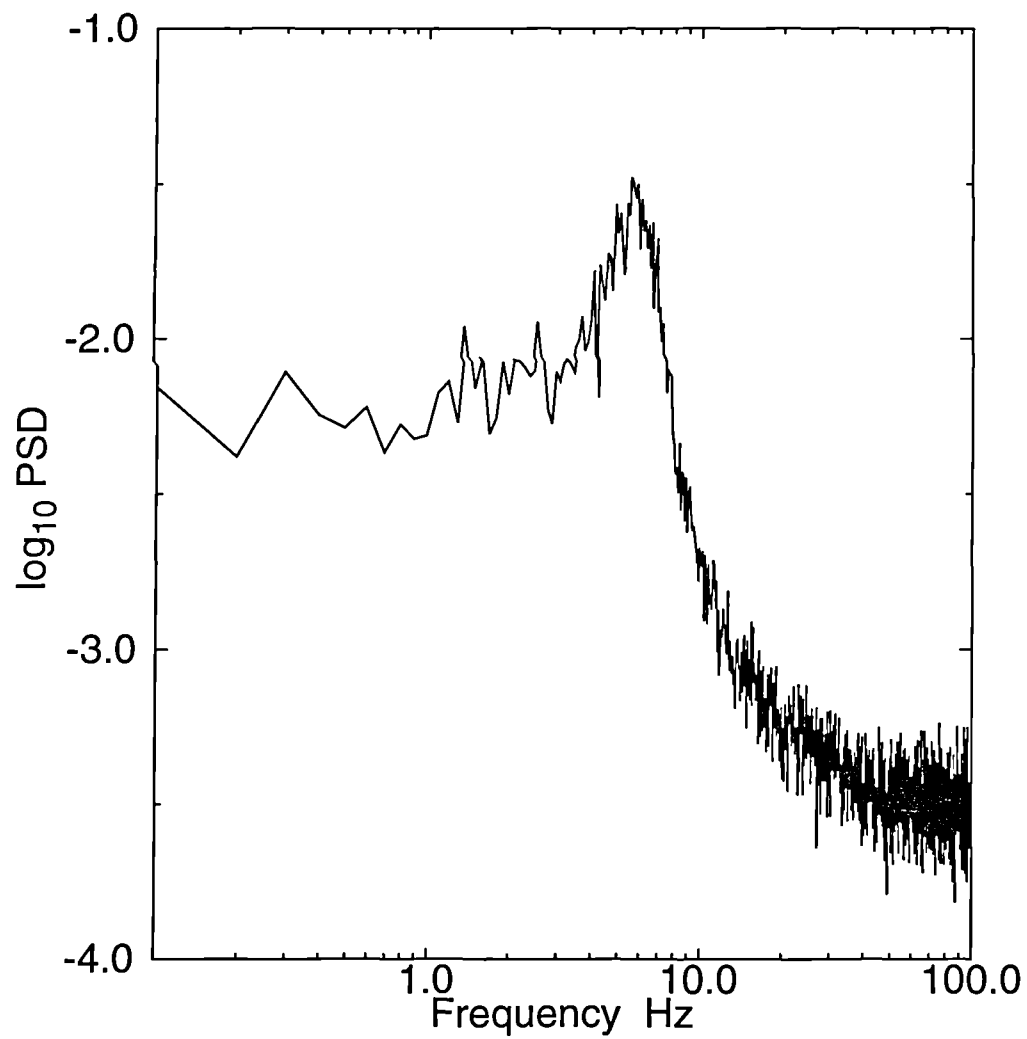
Figure 3.40 Spectra in the Wake of a D-Shaped Port
R=5.0 Bleed=50%, W_a/U_a=0.0
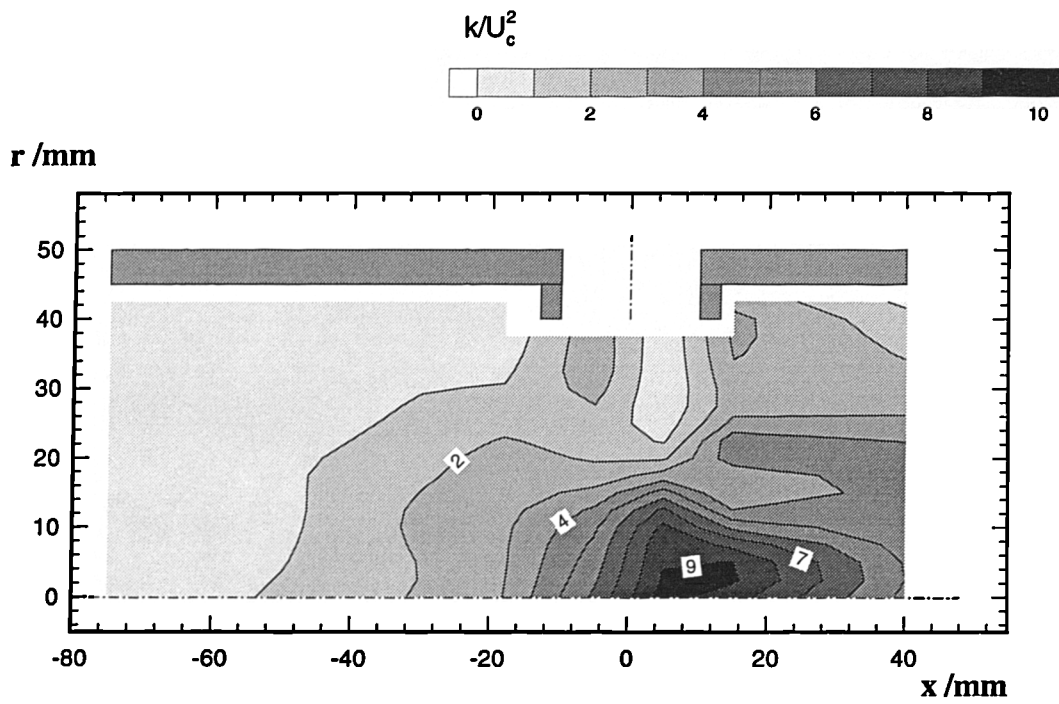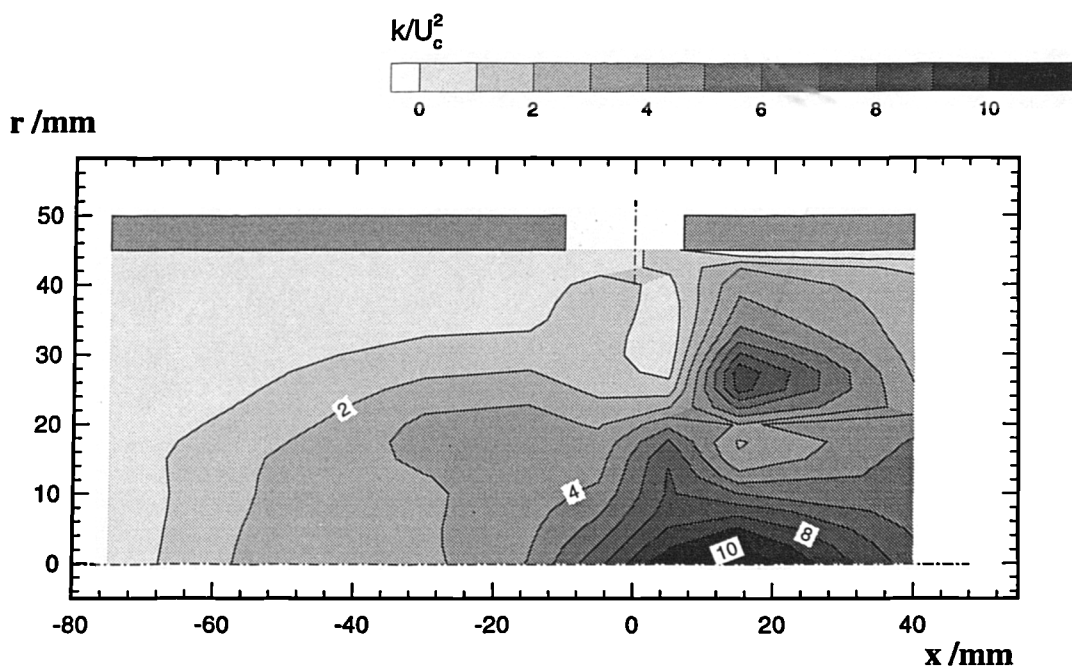
(a) Chuted Port

(b) D-Shaped Port

Figure 3.41 Comparison of Core Turbulent Kinetic Energy for Chuted and D-Shaped Ports
R=5.0 Bleed=50%, W_a/U_a=0.0

■ U < 0
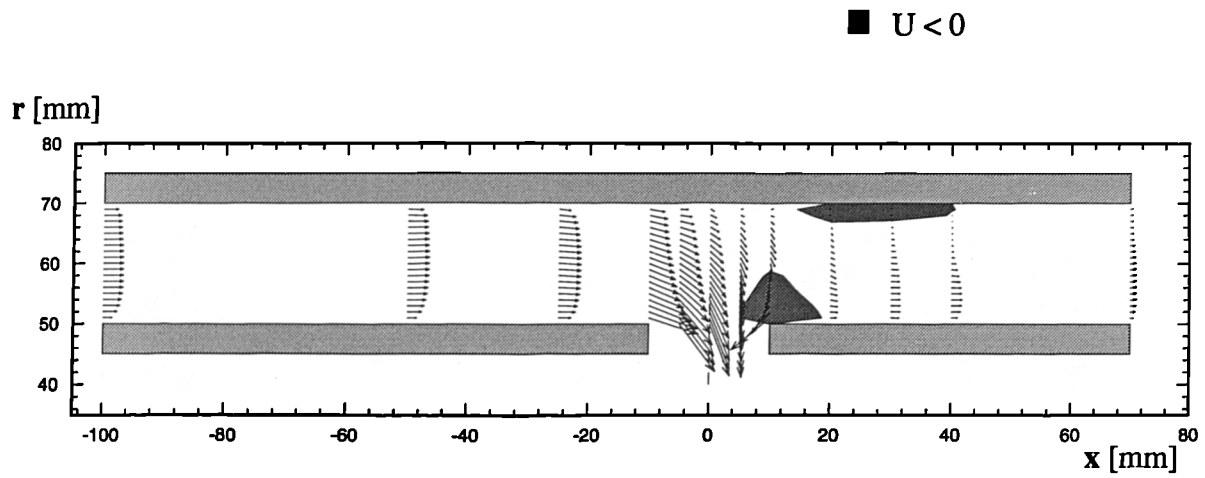
Figure 3.42 Velocity Vectors in Annulus
Plain Port, R=2.0 Bleed=20%, W_a/U_a=0.215

W/U_c

0.2   0.4
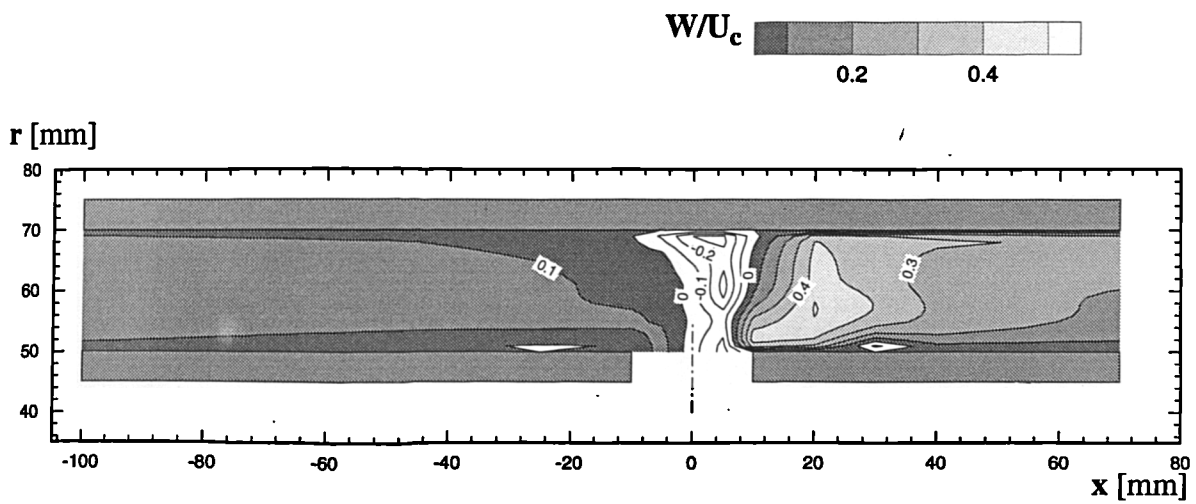
Figure 3.43 Non-Dimensional Swirl Contours in Annulus
Plain Port, R=2.0 Bleed=20%, W_a/U_a=0.215
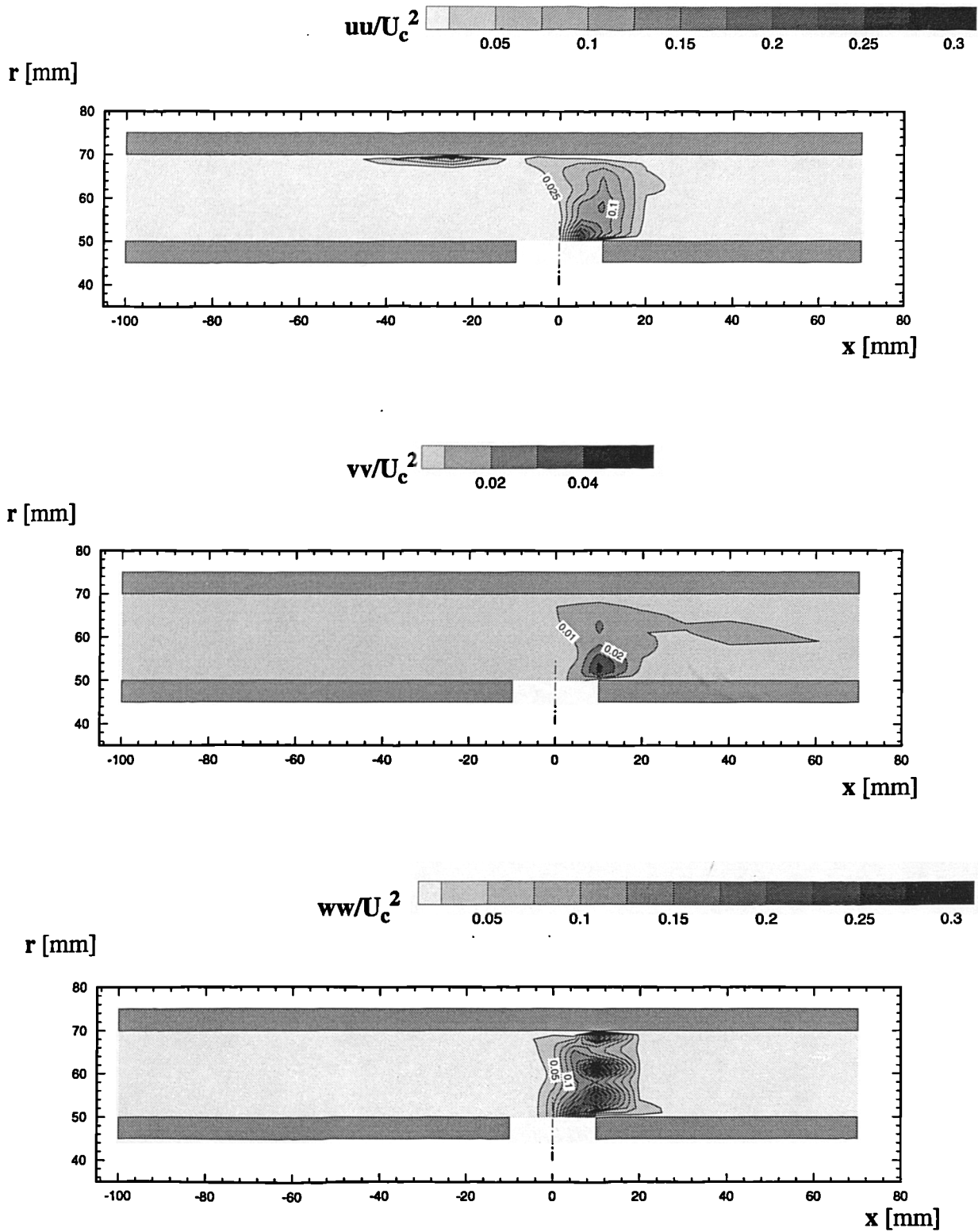
Figure 3.44 Non-Dimensional Normal Stresses in Annulus
Plain Port, R=2.0 Bleed=20%, W_a/U_a=0.125
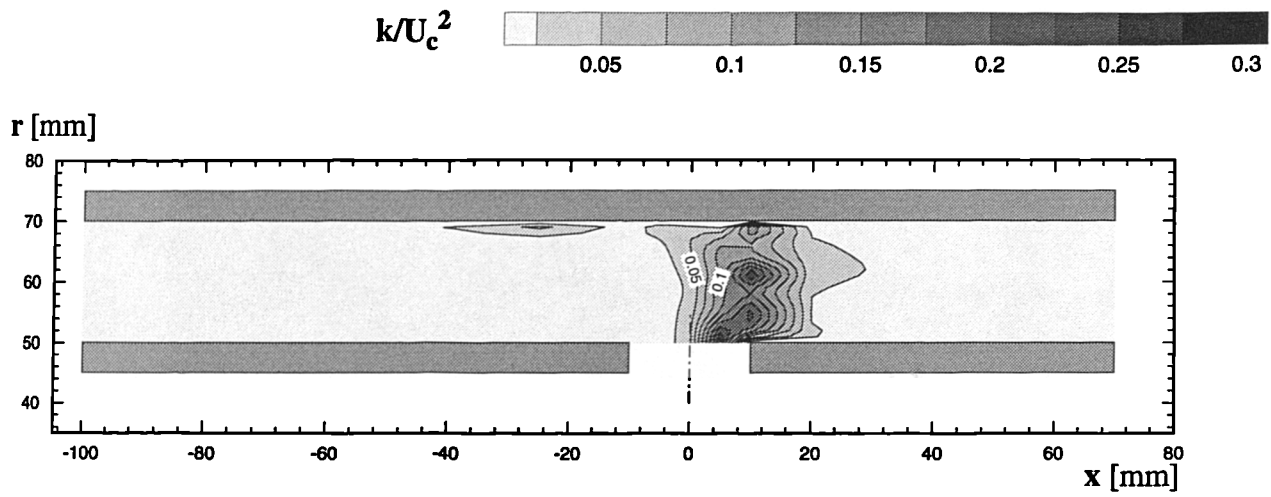
Figure 3.45 Turbulent Kinetic Energy in the Annulus
Plain Port, R=2.0 Bleed=20%, W_a/U_a=0.215
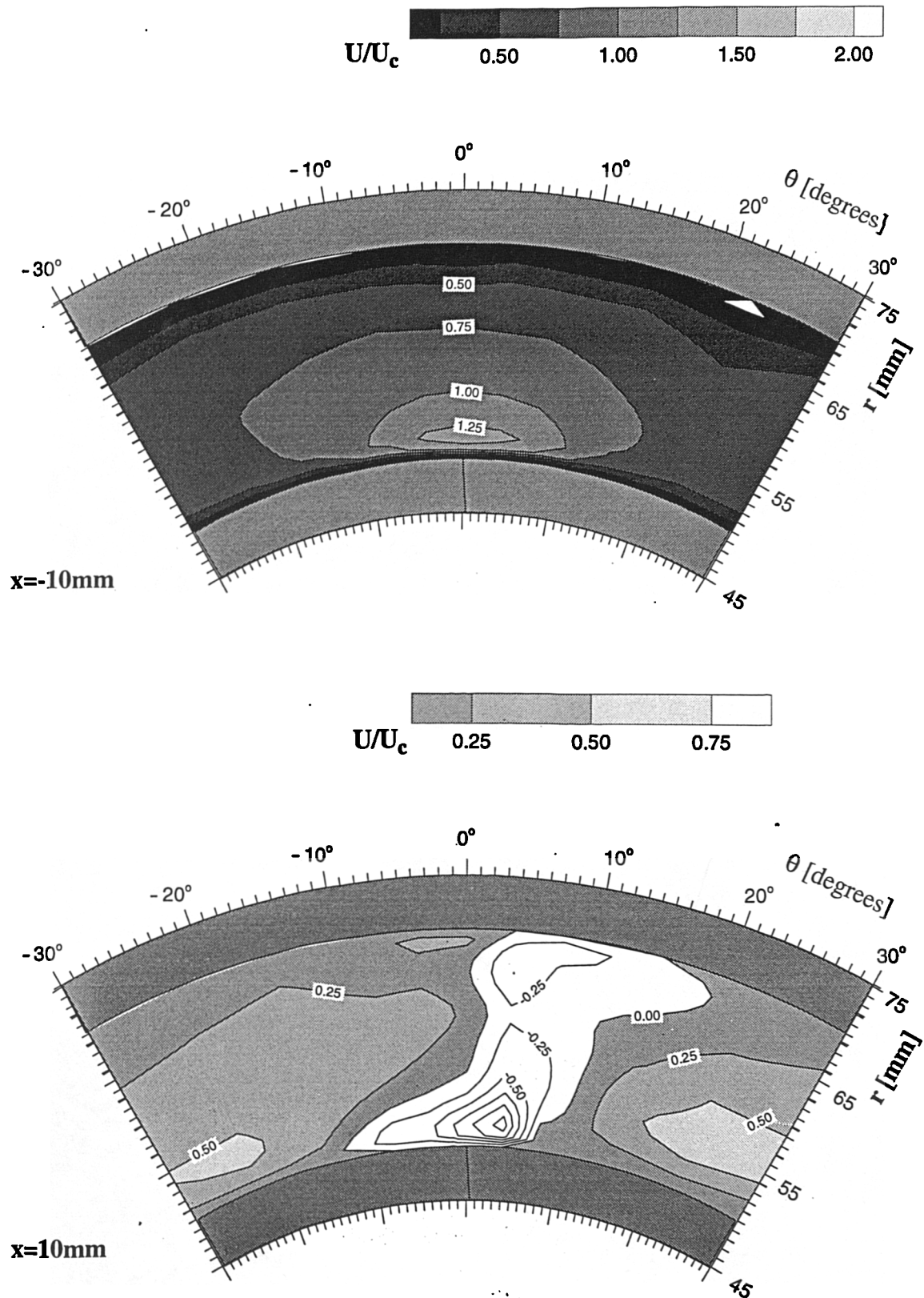
Figure 3.46 Axial Velocity Distribution in Annulus on x=-10 and x=10 Planes
Plain Port, R=2.0 Bleed=20%, W_a/U_a=0.215

(a) Plain Port

(b) D-shaped Port

(plane r=52.5mm)
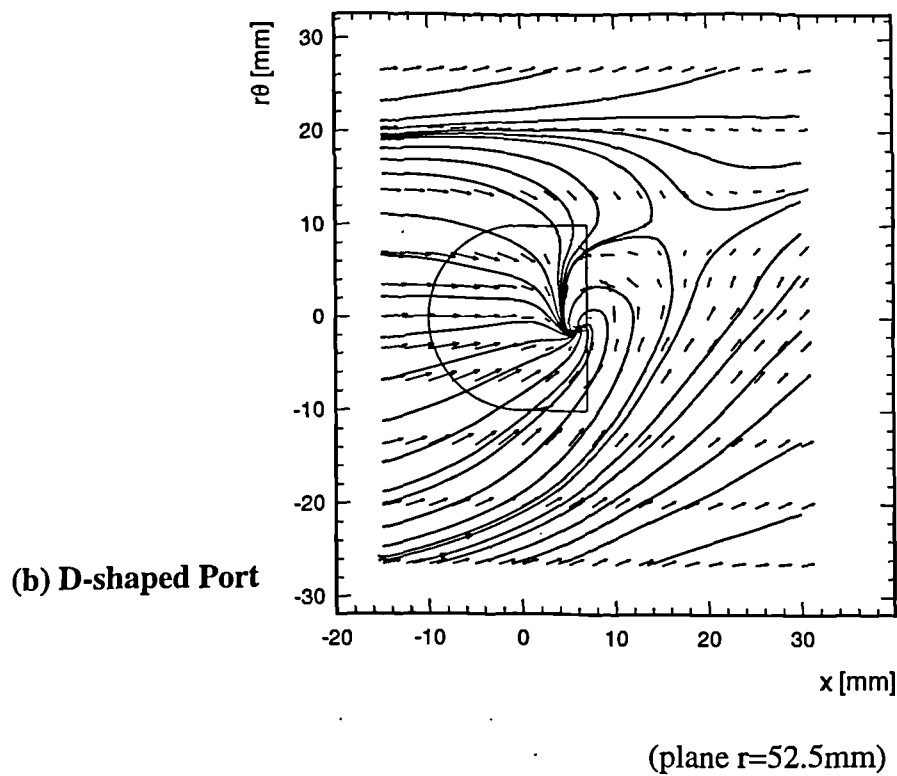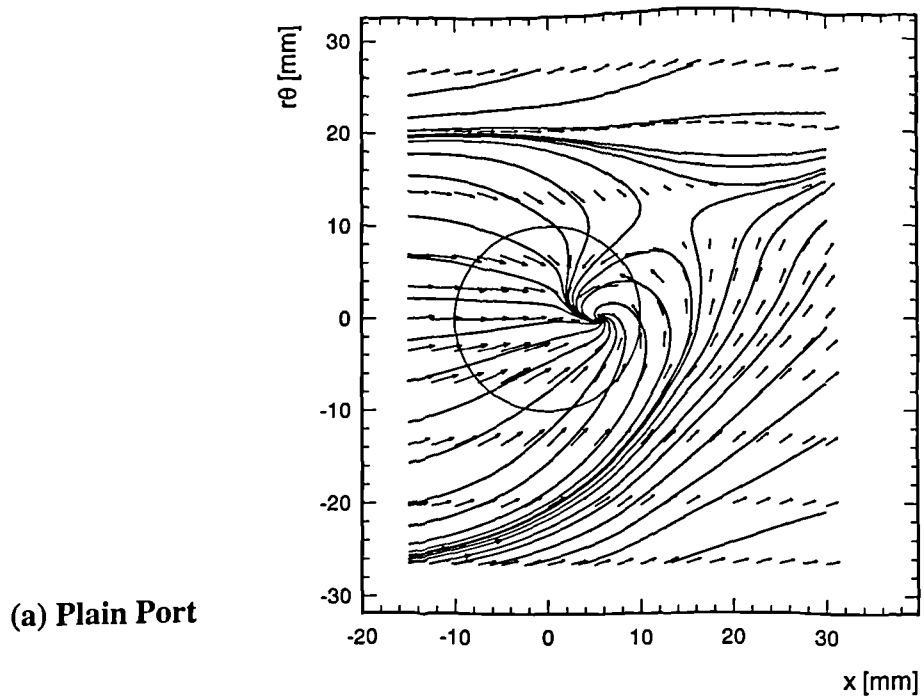
Figure 3.47 Secondary Velocity Vectors Near Inner Annulus Wall
R=2.0 Bleed=20%, W_a/U_a=0.215
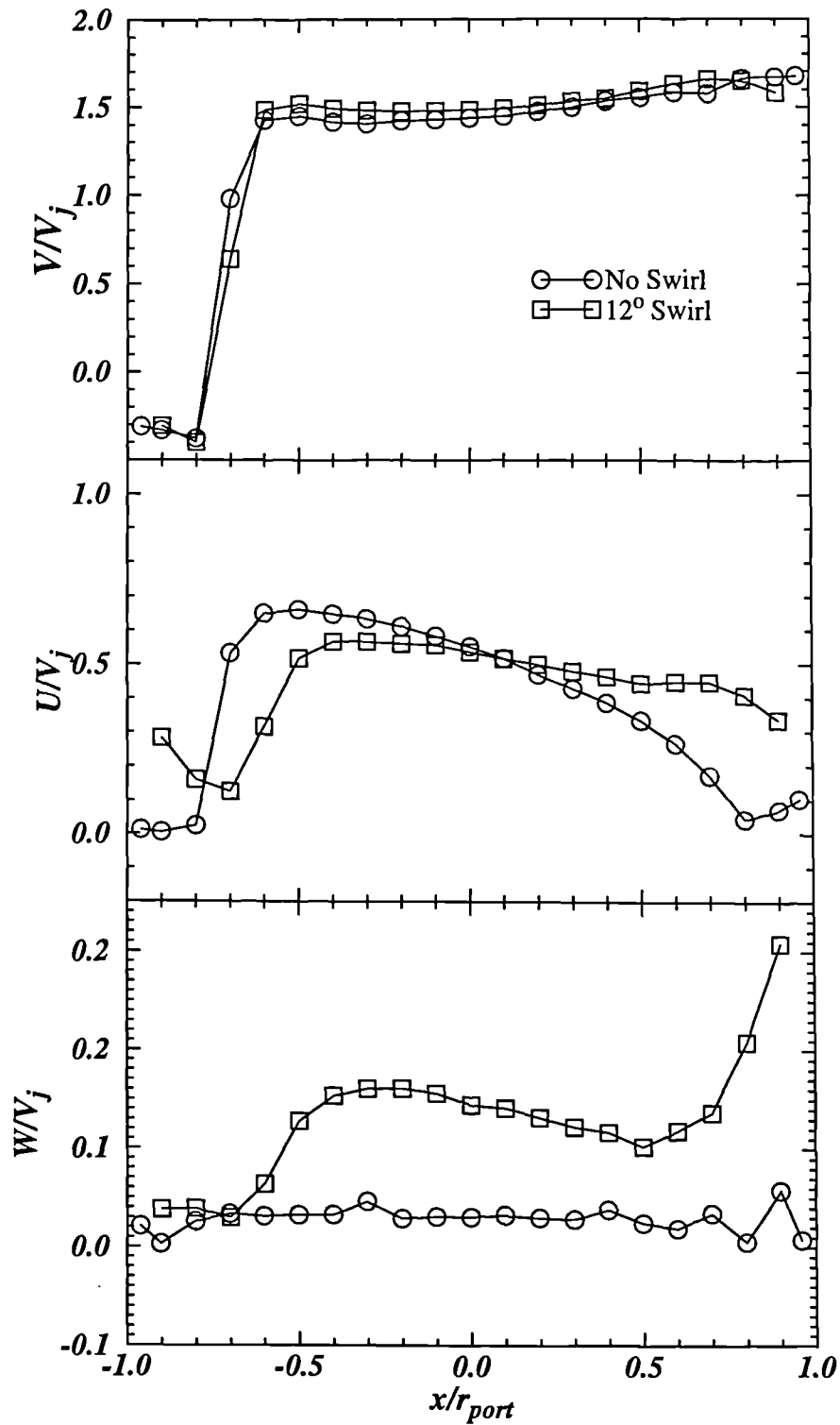
Figure 3.48 Jet Exit Velocity Profiles With and Without Annulus Swirl
Plain Port, R=5.0, Bleed=50%, W_a/U_a=0.0 & 0.215
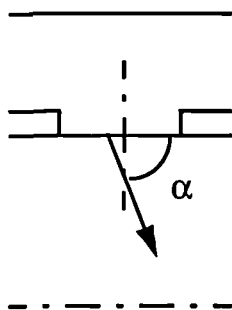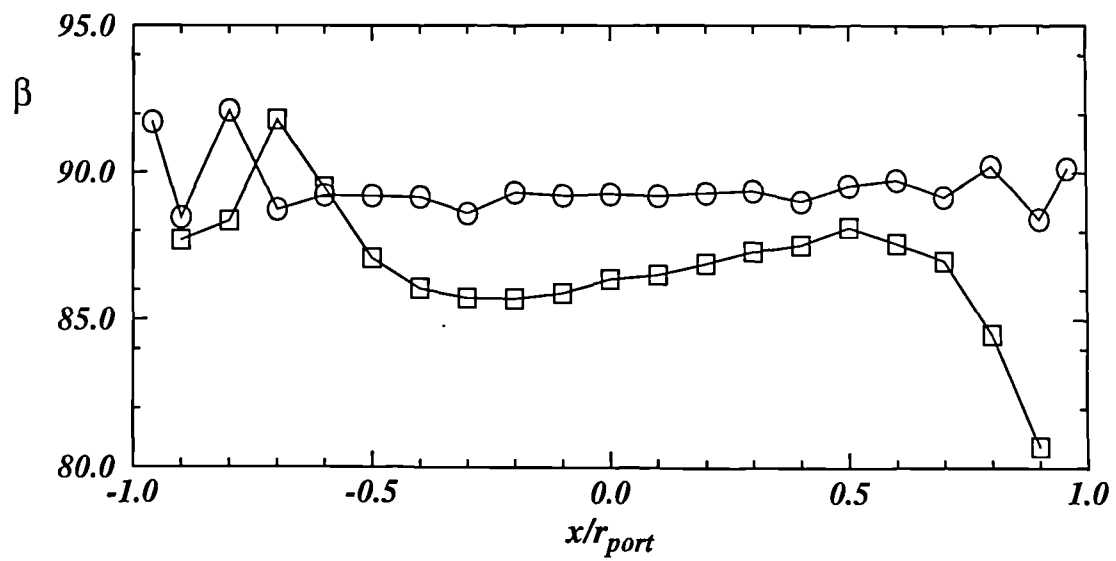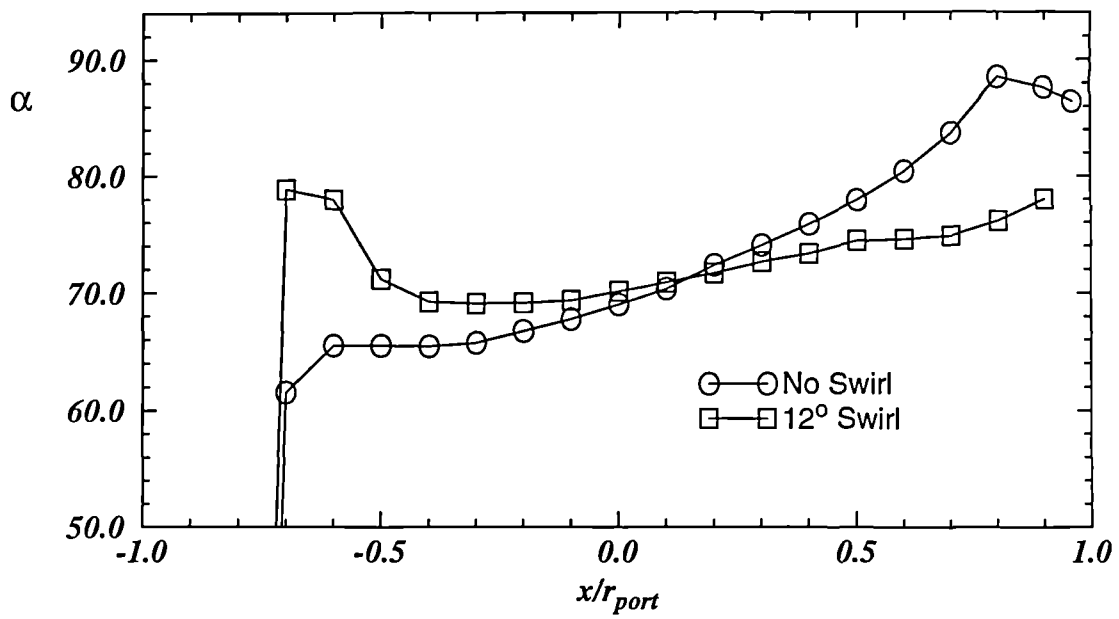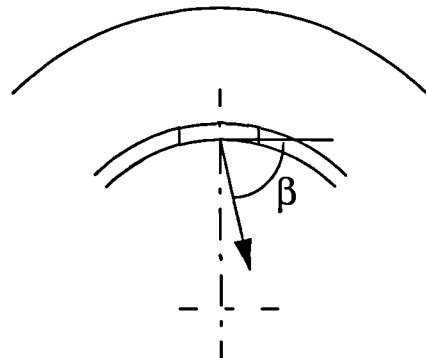
Figure 3.49 Jet Exit Flow Angles With and Without Annulus Swirl
Plain Port, R=5.0, Bleed=50%, W_a/U_a=0.0 & 0.215
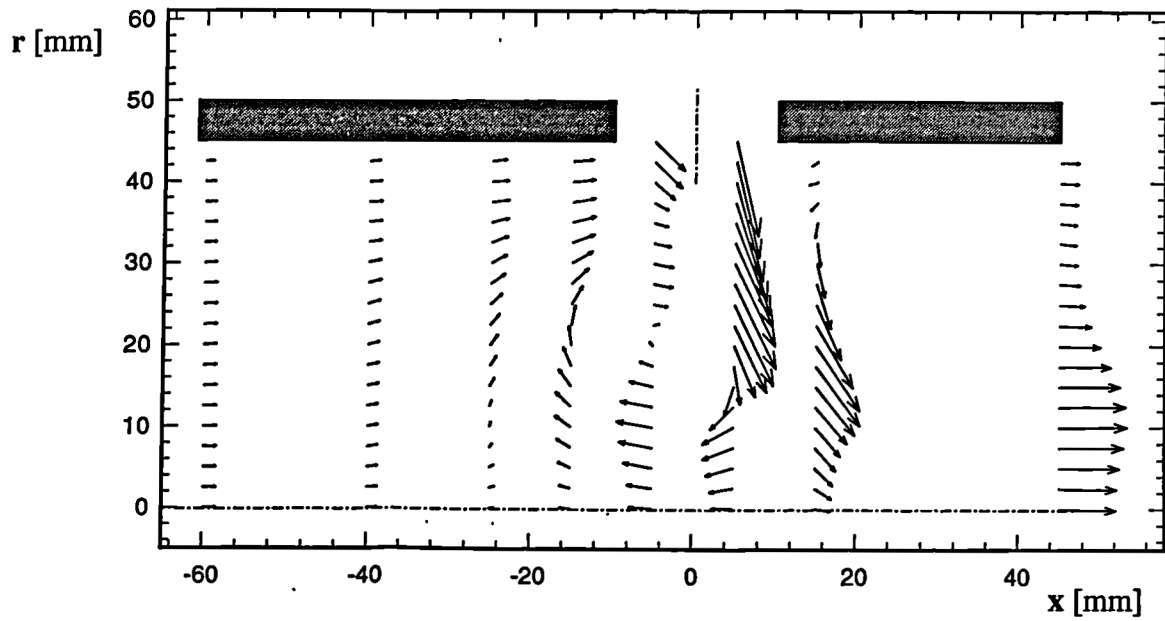
Figure 3.50 Velocity Vectors In Core
Plain Port, R=5.0 Bleed=50%, W_a/U_a=0.215
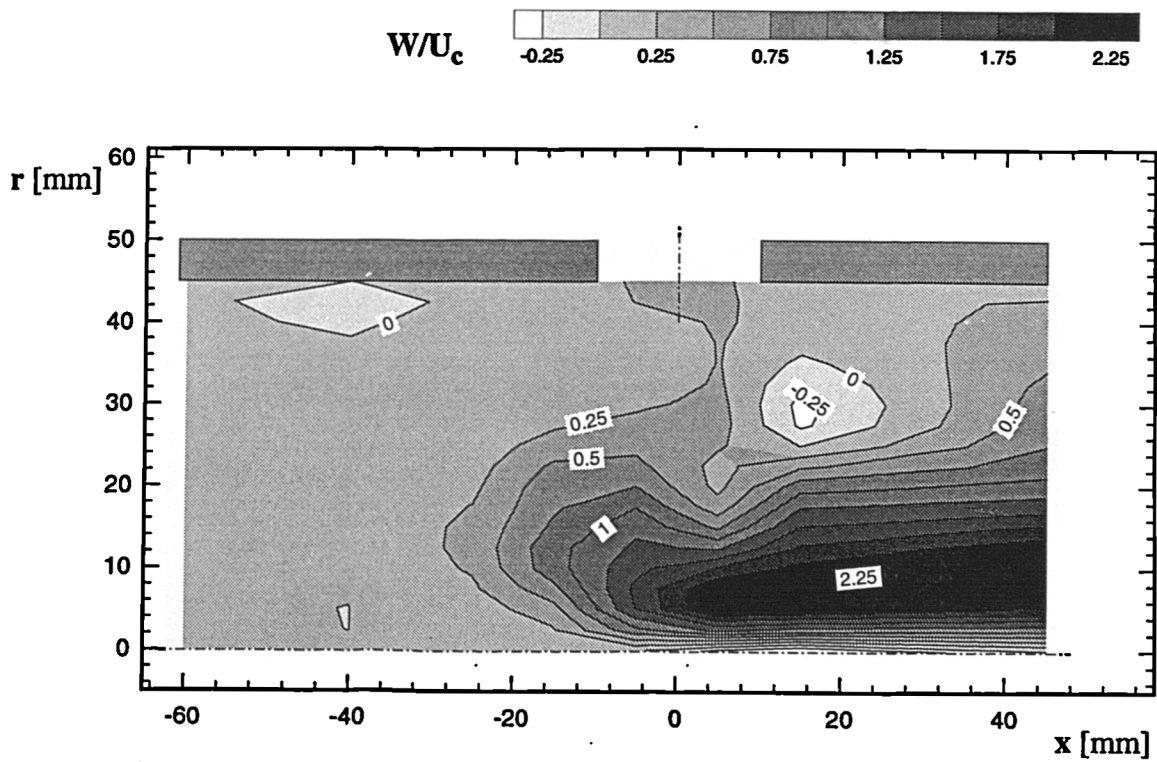
Figure 3.51 Swirl Velocity In Core
Plain Port, R=5.0 Bleed=50%, W_a/U_a=0.215
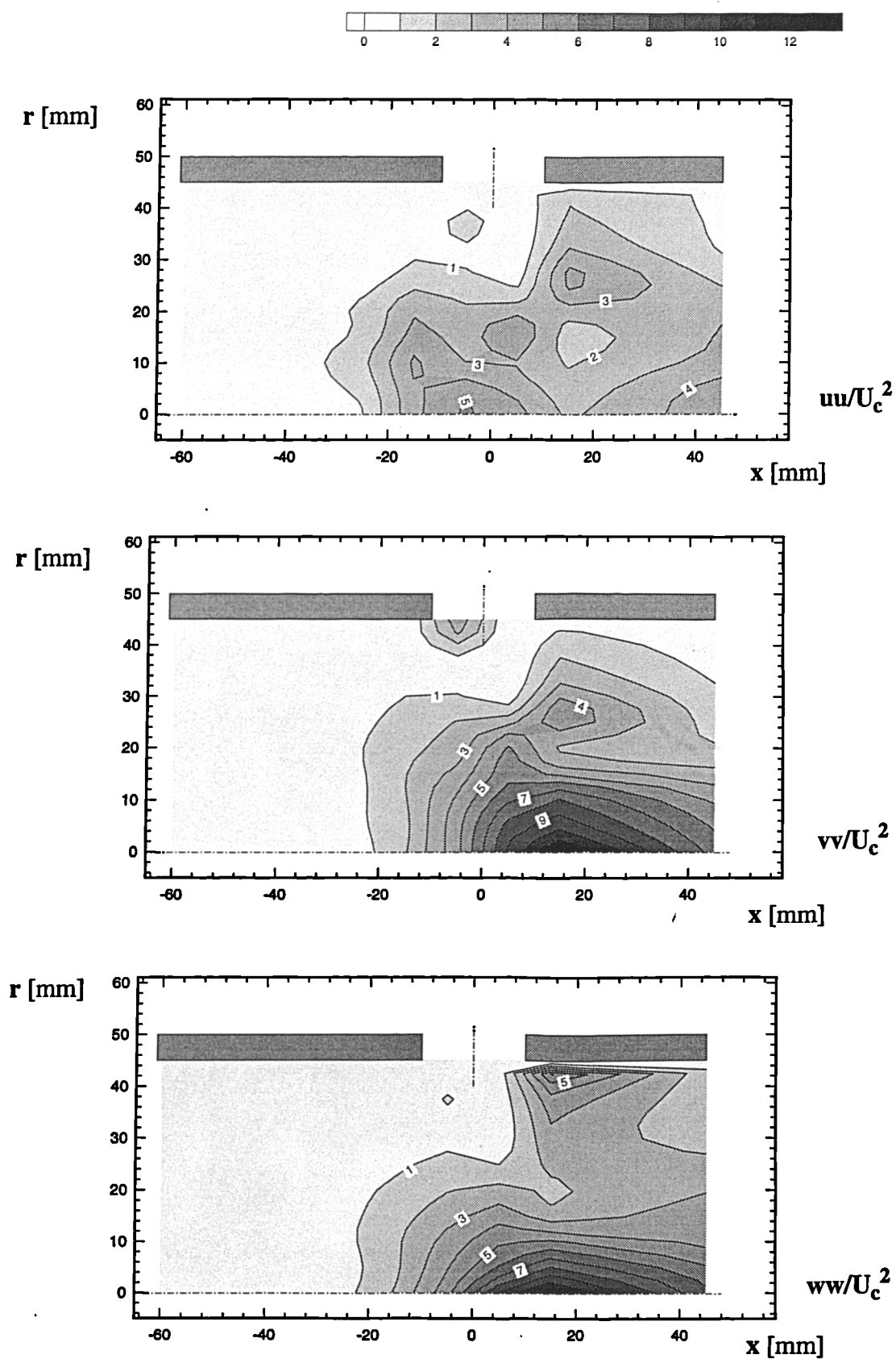
Figure 3.52 Non-Dimensional Normal Stresses In Core
Plain Port, R=5.0 Bleed=50%, W_a/U_a=0.0
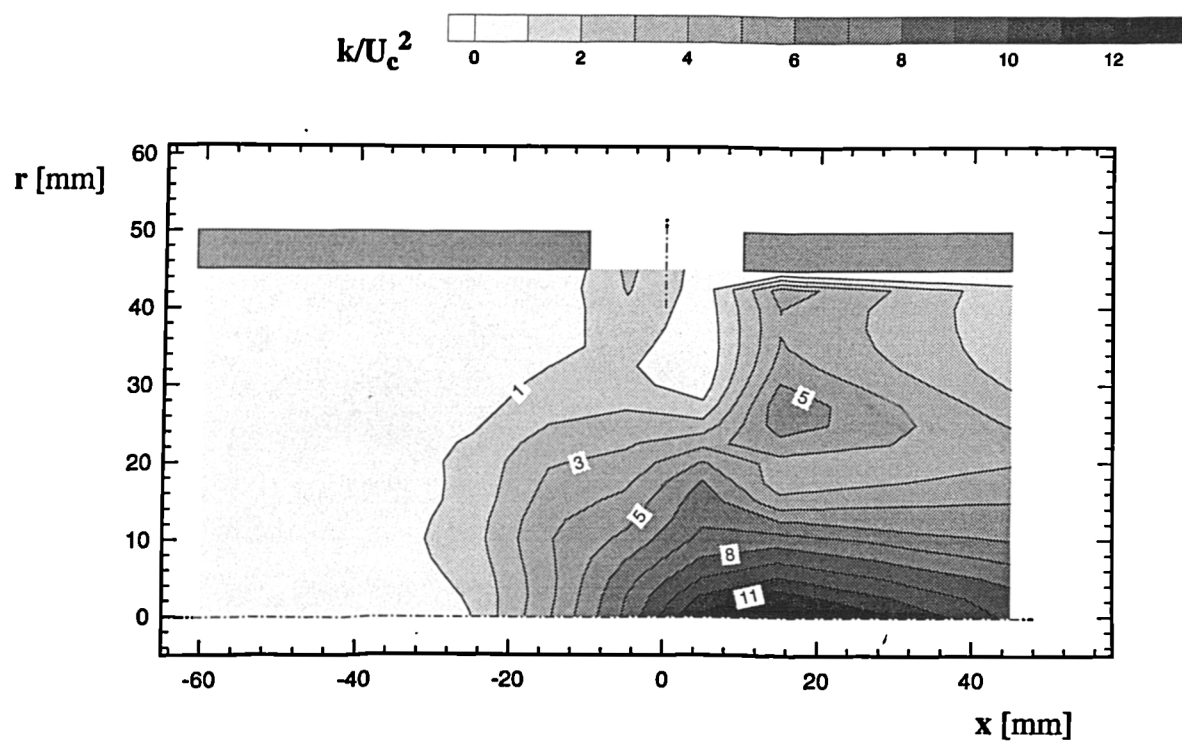
Figure 3.53 Non-Dimensional Turbulent Kinetic Energy In Core
Plain Port, R=5.0 Bleed=50%, W_a/U_a=0.215

Chapter 4

Mathematical Modelling

4.1 Introduction

The purpose of this chapter is to describe the equations governing fluid motion, what simplifications have been made to them for the calculations carried out in this thesis and how the resulting equation set has been numerically solved. This description is important due to the plethora of methods now developed to solve flow problems governed by a set of elliptic partial differential equations. The widely used Reynolds Averaged Navier-Stokes (RANS) equations have been used here in conjunction with an eddy-viscosity turbulence model. Solution of these equations is essentially a boundary value problem, thus the final sections will discuss the types and implementation of boundary constraints employed in the model.

4.2 Governing Equations

4.2.1 Equations of Motion

The continuity equation for single-phase, single species fluid flow in cartesian tensor notation is:-

$$\frac{\partial \tilde{\rho}}{\partial t} + \frac{\partial \tilde{\rho} \tilde{U}_i}{\partial x_i} = 0 \qquad 4.1$$

where ~ indicates an instantaneous (time-dependent) value. Also in cartesian tensor notation, the corresponding momentum equations can be written as:-

$$\frac{\partial \tilde{\rho} \tilde{U}_i}{\partial t} + \frac{\partial \tilde{\rho} \tilde{U}_i \tilde{U}_j}{\partial x_j} = -\frac{\partial \tilde{P}}{\partial x_i} + \frac{\partial \tilde{\tau}_{ij}}{\partial x_j} \qquad 4.2$$

the instantaneous viscous stress tensor, $\tilde{\tau}_{ij}$, for a Newtonian fluid is given by;

$$\tilde{\tau}_{ij} = \mu \left[\frac{\partial \tilde{U}_i}{\partial x_j} + \frac{\partial \tilde{U}_j}{\partial x_i} \right] - \frac{2}{3} \mu \frac{\partial \tilde{U}_i}{\partial x_i} \qquad 4.3$$

where μ is the molecular fluid viscosity (here assumed constant). Restricting interest in this study to constant density flow the continuity equation (4.1) reduces to:-

$$\frac{\partial \tilde{U}_i}{\partial x_i} = 0 \qquad\qquad 4.4$$

Decomposition of all instantaneous quantities into mean and fluctuating components, (e.g. $\tilde{U}_i = U_i + u_i$), is carried out, followed by long time-averaging of the equations to obtain a statistical description of the average properties of the flow; this leads to the Reynolds Averaged form of the Navier Stokes equations (assuming steady state conditions):-

$$\frac{\partial U_i}{\partial x_i} = 0$$

$$\frac{\partial \rho U_i U_j}{\partial x_j} = -\frac{\partial P}{\partial x_i} + \frac{\partial \tau_{ij}}{\partial x_j} - \frac{\partial \rho \overline{u_i u_j}}{\partial x_j} \qquad\qquad 4.5$$

$$\tau_{ij} = \mu \left[\frac{\partial U_i}{\partial x_j} + \frac{\partial U_j}{\partial x_i} \right]$$

where τ_{ij} is the time-averaged viscous stress tensor and the additional final term on the right hand side is the fluctuating stress tensor. Equation 4.5 can now be solved for pressure, P, and velocity U_i, providing the fluid properties, ρ and μ are known and the Reynolds Stresses $\overline{u_i u_j}$ can be related to the mean flow field.

4.2.2 Turbulence Closure

The standard high Reynolds number two-equation model of Launder and Spalding (1974) has been used for the calculations performed in this study. In this turbulence model the Reynolds stresses are related to the mean flow field via two scalar quantities, the turbulent kinetic energy, k,

$$k = \frac{1}{2} \left(\overline{u_i u_i} \right) \qquad\qquad 4.6$$

and the dissipation rate of turbulence energy, ε,

$$\varepsilon = \frac{\mu}{\rho} \left(\frac{\partial u_i}{\partial x_j} \right) \left(\frac{\partial u_i}{\partial x_j} \right). \qquad\qquad 4.7$$

Since these quantities are defined by relations involving the fluctuating velocities exact transport equations may be derived for each of these quantities from the unsteady Navier Stokes Equations. After considerable modelling (see Launder 1992), the resulting governing model equations for k and ε are:-

$$\frac{\partial(\rho U_j k)}{\partial x_j} = \frac{\partial}{\partial x_j}\left(\frac{\mu_t}{\sigma_k}\frac{\partial k}{\partial x_j}\right) - \rho\overline{u_i u_j}\frac{\partial U_i}{\partial x_j} - \rho\varepsilon \qquad\qquad 4.8$$

$$\frac{\partial(\rho U_j \varepsilon)}{\partial x_j} = \frac{\partial}{\partial x_j}\left(\frac{\mu_t}{\sigma_\varepsilon}\frac{\partial \varepsilon}{\partial x_j}\right) + \frac{C_{\varepsilon 1}\varepsilon}{k}\left(-\rho\overline{u_i u_j}\frac{\partial U_i}{\partial x_j}\right) - \frac{\rho C_{\varepsilon 2}\varepsilon^2}{k} \qquad 4.9$$

In equations 4.8 and 4.9 the three terms on the right hand side represent turbulent diffusion, production and dissipation respectively of each quantity. The Reynolds stresses are evaluated from the eddy-viscosity relationship of Boussinesq (1877);

$$-\rho\overline{u_i u_j} = \mu_t\left(\frac{\partial U_i}{\partial x_j} + \frac{\partial U_j}{\partial x_i}\right) - \frac{2}{3}\delta_{ij}\rho k \qquad\qquad 4.10$$

where the local turbulent viscosity is given by;

$$\mu_t = C_\mu \frac{\rho k^2}{\varepsilon} \qquad\qquad 4.11$$

The modelled transport equations for both k and ε contain a number of empirically found constants, and the values which have been used in this study are the original optimised set reported in Launder and Spalding (1974) and are given in the table below.

C_μ	$C_{\varepsilon 1}$	$C_{\varepsilon 2}$	σ_k	σ_ε
0.09	1.44	1.92	1.0	1.3

Table 4.1 Empirical Constants Used in the k-ε Model

4.2.3 Generic Transport Equation

To simplify computation it is desirable to reduce each transport equation into a common form. This can be done by treating each velocity component as a scalar

quantity, ϕ, along with turbulent kinetic energy and the dissipation rate of turbulent kinetic energy. The transport equation for each may then be written as;

$$\frac{\partial}{\partial x_j}\left(\rho U_j \phi - \Gamma_\phi \frac{\partial \phi}{\partial x_j}\right) = S_\phi \qquad 4.12$$

where to recover each transport equation in the set, the scalar variable, ϕ, the diffusion coefficient, Γ_ϕ, and source term, S_ϕ, are given in table 4.2 below.

Equation	Scalar ϕ	Diffusion Coefficient Γ_ϕ	Source Term S_ϕ
Continuity	1	0	0
Momentum	U_i	$\mu_{eff}\ (=\mu+\mu_t)$	$\frac{\partial}{\partial x_j}\left[\mu_{eff}\frac{\partial U_j}{\partial x_i}\right] - \frac{\partial P}{\partial x_i}$
Turbulent kinetic energy	k	μ_t/σ_k	$\mu_t\left(\frac{\partial U_i}{\partial x_j} + \frac{\partial U_j}{\partial x_i}\right)\frac{\partial U_i}{\partial x_j} - \rho\varepsilon$
Dissipation of k	ε	μ_t/σ_ε	$\frac{C_{\varepsilon 1}\mu_t\varepsilon}{k}\left(\frac{\partial U_i}{\partial x_j} + \frac{\partial U_j}{\partial x_i}\right)\frac{\partial U_i}{\partial x_j} - \frac{C_{\varepsilon 2}\rho\varepsilon^2}{k}$

Table 4.2 Diffusion Coefficients and Source Terms for the Transport Equations

4.3 Numerical Implementation

The code employed for this study to solve the governing equations described in the previous section is that written by Manners (1988). An overview of the strategy of this code is described in the remainder of this chapter, though more detail may be found in Manners (1992).

4.3.1 Discretisation

Discretisation has been accomplished with a finite volume approach, which requires appropriate differencing of the convective and diffusive fluxes at each face of the control volume. A co-located solver was used here such that all solution variables were stored at the cell centres enabling easy determination of the cell face fluxes. Diffusive fluxes were always evaluated using central differencing, whereas the convective terms were either evaluated using HYBRID (Patankar 1980) or QUICK differencing (Leonard 1979).

HYBRID differencing is based upon the exact solution of a linear one-dimensional steady convection-diffusion equation between two adjoining grid nodes. In this scheme, if the magnitude of the cell face Peclet number is less than 2.0 then central differencing is used, otherwise first order upwind differencing is used, i.e.;

$$Pe = \frac{\rho U \Delta x}{\Gamma} \qquad\qquad 4.13$$

where Δx is the node separation and Γ is the diffusion coefficient.

$$\phi_{i+\frac{1}{2}} = \frac{1}{2}(\phi_i + \phi_{i+1}) \qquad |Pe|<2 \qquad\qquad 4.14$$

$$\phi_{i+\frac{1}{2}} = \phi_i \qquad\qquad Pe>2 \qquad\qquad 4.15$$

$$\phi_{i+\frac{1}{2}} = \phi_{i+1} \qquad\qquad Pe<-2 \qquad\qquad 4.16$$

This scheme improves stability by ensuring diagonal dominance of the coefficient matrix at the cost of formal accuracy, when $|Pe|<2$ the scheme is $O(\Delta x^2)$ accurate, but when $|Pe|>2$ the accuracy is reduced to $O(\Delta x)$.

QUICK or quadratic upwind differencing assumes a quadratic variable distribution such that;

$$\phi_{i+\frac{1}{2}} = \frac{1}{2}(\phi_i - \phi_{i+1}) - \frac{1}{8}(\phi_{i-1} + \phi_{i+1} - 2\phi_i) \qquad U_{i+\frac{1}{2}}>0 \qquad 4.17$$

or

$$\phi_{i+\frac{1}{2}} = \frac{1}{2}(\phi_{i+1} - \phi_i) - \frac{1}{8}(\phi_{i+2} + \phi_i - 2\phi_{i+1}) \qquad U_{i+\frac{1}{2}}<0. \qquad 4.18$$

The error due to truncation of this scheme is $O(\Delta x^3)$ on a uniform grid, and is thus seen to reduce the error over that of HYBRID differencing. However, when Pe>3 this scheme can exhibit unphysical spatial oscillations due to the introduction of the downstream node (Castro and Jones (1987)). This often makes it difficult to obtain a

converged solution in comparison to the more robust HYBRID scheme. HYBRID has thus been used for most of the computational predictions presented in this thesis, with some predictions being repeated with QUICK differencing to indicate the level of numerical accuracy in the resulting solutions. Good agreement between the solutions obtained by using the two schemes on the same mesh would thus indicate that numerical error was minimal.

Once differenced and simplified the transport equation for each scalar can be posed as a matrix problem of the form;

$$\left[A\right] (\phi) = (S) \qquad\qquad 4.19$$

(ϕ) is the solution vector for the current iteration level, [A] is a coefficient matrix constructed from convective and diffusive terms for the previous iteration and (S) is the source vector from the previous iteration. (ϕ) and (S) will have one value per grid node whereas [A] will be a square matrix which for a structured grid will have a regular diagonally banded structure.

4.3.2 Pressure Equation

In calculating incompressible flow the usual relation for determining pressure, the equation of state, is unable to resolve the pressure variations accurately since the variations in temperature and density are infinitesimal. The natural equation for determining density is the continuity equation, but pressure does not appear in this, and pressure is only introduced into the equation set in each component of the momentum equation, used in this case to determine each velocity component. Indeed, the assumption of incompressibility allows density to be removed from the continuity equation also, thus the problem which arises is how to determine the pressure field from the continuity equation.

The approach adopted in the algorithm employed in this study was to use either the SIMPLE scheme of Patankar(1980) or the time dependent pressure correction method described in Manners(1988). The pressure-smoothing approach of Rhie and Chow (1982) was used to avoid pressure velocity decoupling.

Using suitable values of time step in the time dependent scheme provided a robust scheme, particularly when starting a calculation, however better convergence was achieved using the SIMPLE method. Therefore the calculations presented in this thesis have been performed using both schemes. Time dependent pressure correction was used to start the calculations though once the residuals stopped reducing for each iteration the SIMPLE scheme was used to increase the convergence rate.

4.3.3 Generalised Coordinate Implementation

A general boundary conforming structured mesh can only be generated if a transformation is performed from physical space, x_i, to a generalised coordinate space, ξ_i. This has to be done such that certain generalised coordinate lines or surfaces follow edges or surfaces in physical space respectively, thus allowing boundary conditions to be easily specified and implemented in the generalised coordinate space. A unique relationship between the two coordinate sets is required, such that in vector notation;

$$\xi = \xi(x, y, z) \quad \eta = \eta(x, y, z) \quad \& \quad \zeta = \zeta(x, y, z) . \qquad 4.20$$

The generalised coordinate space can be thought of (in two dimensions) as a rectangular domain of square cells, which via the transformation 4.20, can be distorted to fit snugly into a curved duct for example in physical space. A unique solution is required as this implies none of the grid lines of the same coordinate direction cross each other, leading to an unambiguous mapping between the coordinate systems.

Equations 4.12 can thus be transformed into corresponding equations containing partial derivatives with respect to ξ, η and ζ. This is done by introducing a Jacobian matrix which describes the transformation, for example consider first derivatives of the velocity components;

$$\begin{bmatrix} \dfrac{\partial u}{\partial x} & \dfrac{\partial u}{\partial y} & \dfrac{\partial u}{\partial z} \\[2mm] \dfrac{\partial v}{\partial x} & \dfrac{\partial v}{\partial y} & \dfrac{\partial v}{\partial z} \\[2mm] \dfrac{\partial w}{\partial x} & \dfrac{\partial w}{\partial y} & \dfrac{\partial w}{\partial z} \end{bmatrix} = \begin{bmatrix} \dfrac{\partial u}{\partial \xi} & \dfrac{\partial u}{\partial \eta} & \dfrac{\partial u}{\partial \zeta} \\[2mm] \dfrac{\partial v}{\partial \xi} & \dfrac{\partial v}{\partial \eta} & \dfrac{\partial v}{\partial \zeta} \\[2mm] \dfrac{\partial w}{\partial \xi} & \dfrac{\partial w}{\partial \eta} & \dfrac{\partial w}{\partial \zeta} \end{bmatrix} J \qquad 4.21$$

where the Jacobian matrix $\underline{J}$ is given by

$$\underline{J} = \begin{bmatrix} \dfrac{\partial \xi}{\partial x} & \dfrac{\partial \xi}{\partial y} & \dfrac{\partial \xi}{\partial z} \\[2mm] \dfrac{\partial \eta}{\partial x} & \dfrac{\partial \eta}{\partial y} & \dfrac{\partial \eta}{\partial z} \\[2mm] \dfrac{\partial \zeta}{\partial x} & \dfrac{\partial \zeta}{\partial y} & \dfrac{\partial \zeta}{\partial z} \end{bmatrix} . \qquad \qquad 4.22$$

Unless analytic relations are available for equations 4.20, which in general are not, the elements of 4.22 can not be directly calculated. It is therefore more usual to use the inverse Jacobian matrix ;

$$\underline{J}^{-1} = \begin{bmatrix} \dfrac{\partial x}{\partial \xi} & \dfrac{\partial x}{\partial \eta} & \dfrac{\partial x}{\partial \zeta} \\[2mm] \dfrac{\partial y}{\partial \xi} & \dfrac{\partial y}{\partial \eta} & \dfrac{\partial y}{\partial \zeta} \\[2mm] \dfrac{\partial z}{\partial \xi} & \dfrac{\partial z}{\partial \eta} & \dfrac{\partial z}{\partial \zeta} \end{bmatrix} . \qquad \qquad 4.23$$

in which the derivatives can be directly evaluated by using central differencing. By noting that

$$\underline{J} = \frac{\left[\text{Cofactor}\left(\underline{J}^{-1} \right) \right]^{T}}{\left| \underline{J}^{-1} \right|} \qquad \qquad 4.24$$

the elements of the Jacobian matrix can be evaluated from the inverse matrix, the first element of the Jacobian for example is;

$$\frac{\partial \xi}{\partial x} = \frac{\dfrac{\partial y}{\partial \eta}\dfrac{\partial z}{\partial \zeta} - \dfrac{\partial y}{\partial \zeta}\dfrac{\partial z}{\partial \eta}}{\left| \underline{J}^{-1} \right|} \qquad \qquad 4.25$$

hence construction of the Jacobian matrix allows the evaluation of derivatives with respect to physical coordinates, as required in equation 4.12, from the curvilinear derivatives via the chain rule.

4.3.4 Boundary Conditions

Several boundary constraints were used to specify the problems solved in this work, "fixed value", "zero gradient", mirror symmetry, wall and centre-line. "Fixed value" is as stated; the values of variables are specified at the boundary and remain fixed. This Dirichlet condition was used to fix inlet velocity and turbulence quantity profiles.

The zero gradient boundary condition was used for outflow planes, in which it was important to allow exit profiles to develop. For a scalar quantity, ϕ, this can be written;

$$\frac{\partial \phi}{\partial n} = 0$$

where n is normal to the exit plane. With multiple exit planes from a solution domain this condition does not fully specify the problem. Either a flow split between planes, or pressure difference is required. In all of the calculations reported subsequently, the annulus exit flow has been specified via a fixed exit velocity. This indirectly provides the flow split between the core and annulus exits, with the core exit being the only zero gradient condition.

Mirror symmetry allows the size of the computational domain to be reduced by assuming the flow is symmetrical about certain planes. For scalar quantities the zero gradient condition applies since the gradient of the variable must be zero normal to the plane of symmetry to avoid flow discontinuity. For the velocity vector, V;

$$V_n = 0 \quad \text{and} \quad \frac{\partial V_i}{\partial n} = 0 \qquad (i \neq n)$$

Centre-line boundary conditions had to be incorporated into the flow solver for this work, but this is a relatively trivial matter. For a scalar quantity the zero gradient condition is again satisfied, with the normal, n, being normal to the centre line - i.e. radial. For the velocity, the radial and swirl components are zero and the axial component again satisfies the zero gradient condition to prevent flow discontinuity;

$$V_r = 0 \quad \text{and} \quad V_\theta = 0 \ , \quad \frac{\partial V_x}{\partial n} = 0 \qquad (i \neq n)$$

4.3.5 Wall Functions

Naturally, non-slip wall conditions were used, such that each velocity component is zero on the wall. Standard log-law relations were used such that the boundary layer did not require fully resolving. To do this the velocity distribution is assumed to be;

$$U = \frac{\tau_w^{\frac{1}{2}}}{0.4} \left\{ \ln\left(\frac{y\tau_w^{\frac{1}{2}}}{\upsilon}\right) + 2.05 \right\}$$
4.28

where τ_w is the wall shear stress divided by the density and y is the distance from the wall. To implement this in the momentum equation the diffusion coefficient at the wall is set such that the wall shear stress is consistent with the log-law, i.e;

$$\Gamma_w = \frac{0.4 C_\mu k_1 y}{\ln\left(\frac{e^{2.05} C_\mu k_1^{0.5} y}{\upsilon}\right)}$$
4.29

where k_1 is the turbulent kinetic energy at the first cell away from the wall at a distance y. In addition to this, both the dissipation rate at the first cell away from the wall (ε_1) and the production term in the k equation (P_1) require setting to be consistent with equations 4.28 and 4.29 thus,

$$\varepsilon_1 = \frac{C_\mu^{0.75} k_1^{1.5}}{2.05y}$$
4.30

and

$$-\rho\overline{uv}\frac{\partial U}{\partial y} = P_1 = \frac{C_\mu^{0.5} k_1 U_1}{y\ln\left(\frac{e^{2.05} C_\mu^{0.5} k_1^{0.5} y}{\upsilon}\right)}.$$
4.31

4.3.6 Initial Conditions

All calculations were typically started with variables at all internal points set to zero. However turbulent kinetic energy and its dissipation rate (k and ε) were set to small

positive values ($1.0*10^{-10}$) to avoid problems with zero division during the initial iterations. It is clear where zero divide problems arise with zero values of these quantities by looking at equations 4.9 and 4.11, in which k and ε appear as denominators.

4.3.7 Solution Procedure

The structure of the "ASA" flow solver written by Manners (1988) can be summarised as below.

```
READ Input Data for calculation setup and constants
READ Initial Values of Variables
DO until converged;
        DO for each variable φ;
                Calculate the diffusion Coefficient, Γ
                Set Dirichlet boundary conditions
                Assemble sources, S
                Assemble influence coefficients, A
                Approximately solve [A](φ)=(S) for φ
                IF φ=pressure then
                        Update velocity field from dp
                        Update pressure field from dp
                END IF
                Set Neumann boundary conditions
        END DO
        PRINT iteration's residual errors
END DO
Calculate derived variables
File Variables
```

Chapter 5

Port Modelling

5.1 Introduction

Fundamental to any CFD study is the generation of the grid system representative of the geometry being modelled, on which the discretised equations can be solved. Much effort has been put into automating this task by the CFD community, but, despite this effort, generating a structured grid for complex geometries is still a demanding and time consuming process, Eccles (1997). This chapter will describe a computational technique which has been developed to allow the detailed geometry of the air admission ports to be modelled. This was required to complete the computational study of gas turbine combustors.

The aerodynamics of gas turbine combustors have, in the past, been studied as two separate flow problems, as discussed in chapter 1. The prohibitive number of grid nodes to describe both the internal and external aerodynamics would have been the first reason of keeping the domains separate. However this is less of a concern since the size of on board RAM in modern computers is larger than that of the first hard drives. Moreover, with the development of massively parallel computer architectures, the cost and speed of the hardware necessary to perform large calculations is reducing to realisable levels.

Although combustion modelling is not a facet of this study, this is another reason that internal and external modelling have remained separate. The internal combusting flow field has always been seen as the more challenging to model, and perhaps least understood region of the whole gas turbine cycle. On the other hand the external (annulus) combustor aerodynamics has been given little respect. The annulus is often treated as a 1D pipe network problem, (at best 2D CFD methods have occasionally been employed, Kharki(1990)) in order to determine the pressure losses and flow splits in to the combustion chamber. The experimental results of chapter 3 have shown how the flow in only a very simplified feed annulus is far from 1 or 2 dimensional. With low bleed ratios and the proximity of the outer annulus wall to a port it is apparent that complex 3D flow features are present affecting the nature of the flow entering the ports to the combustion chamber. From an aerodynamic aspect it is therefore important to understand the implications of performing coupled internal and external calculations.

This is preferable to attempt to provide over-simplified boundary conditions at the port exit to drive the internal flow calculation.

Often square or castellated ports have been used which have the same open area as the port being modelled, (i.e. Baker(1992), Manners(1987)). Castellated port approximations are required when flow solvers are used which can only cope with orthogonal meshes. Again, with the increase in available computing power, the overhead of increased storage and computation time due to moving to an non-orthogonal mesh is rarely a concern of the types of calculations performed here. Occasionally work is reported in which a curvilinear grid is used to represent the circular nature of the port opening, an example of which is given in figure 5.1, from Shyy (1987). All of the port representations in published work however could be described as low resolution and always on the computational domain boundary. Since this study is interested in the detailed effects of bringing together the internal and external flows it was considered important to understand what influence accurately representing the port shape within the solution domain would have. Thus a method of producing a more physically representative description of the port was required. In bringing the two domains together a new problem is posed of describing the 3D nature of a typical air admission port using a structured computational mesh. A typical port is shown in cross-section in figure 5.2 which indicates the level of geometrical complexity the design and fabrication processes introduce.

At the outset of this work the solid modelling capability available was unable to resolve even the simplest ports. This was due to problems with the intersection algorithms of the CAD/grid-generation package written by Manners(1988) as an input generator to the flow solver described in chapter 4. The principle problem was found when the line of intersection passed between separate surfaces of the same body which were not connected through the line of intersection. This happens when a cylinder (representing the port opening) is intersected with a plate (representing the liner). The lines of intersection are circles lying on the top and bottom faces of the plate - which are not connected. Further difficulties were envisaged even if this problem was overcome. When producing simple ports a large number of NURBS surface patches were required to describe it. For each of these patches the grid points to be assigned to

each corner had to be specified. This process was acceptable if it had to be done once or twice, but being time consuming and detailed, mistakes could easily be made. Thus to describe several ports, (each of which requiring a number of trial mesh permutations before a suitable grid was generated), it was decided easier to develop a stand-alone routine which could introduce a port into an existing mesh.

5.2 Port Modelling Module

The basic concept which has been adopted in developing an air-admission port modelling facility is that a designer is likely to want to explore several modifications of port shape within the same basic combustor geometry. Accordingly, the present work has developed along the lines of providing a facility to include (and modify) the port geometry description within a given body-fitted mesh which characterises the internal and external space surrounding a given combustor liner. A module is provided to allow the user to re-mesh a portion of the original grid to form a boundary-conforming mesh which fits the locally distorted liner shape after inclusion of the port geometry. By storing the initial mesh it is possible to re-mesh port details and quickly generate a different port shape, thus providing a useful design tool. The methodology reported in this chapter is summarised in paper form, McGuirk and Spencer (1995).

In what follows the various steps involved in the port modelling module are outlined, using a typical combustor liner and port geometry as an example.

- *Step 1*

  Generate or read a boundary conforming mesh which fits the combustor liner and outer casing shape, excluding all air-admission ports.

Any desired method can be used to create an initial mesh which is fitted to the liner/ casing geometry, but the method adopted in the present work has been to use the elliptic-p.d.e. method described by Thompson (1985), which involves solving a set of Poisson equations for the curvilinear co-ordinates:

$$\nabla^2 \xi^i = P^i$$

where $\xi^i = (\xi, \eta, \zeta)$ are the body-fitted curvilinear non-orthogonal co-ordinates. The actual problem solved is the inverse problem where the cartesian co-ordinates

r^i = (x, y, z) are solved for as dependent variables in the computational space defined by the curvilinear co-ordinates ξ^i as independent variables. The so-called control functions, P^i = (P, Q, R) , are used to control the spacing and orientation of the co-ordinate lines; for example these can be used to cluster grid lines near to the liner walls or in the region where the port is to be inserted to prevent too large distortions of the original mesh. This initial grid generation strategy is not described in any further detail here since the method is well developed and reported in open literature. As an illustrative example, figure 5.3 shows a portion of a combustor liner (currently free of any primary air ports) and the mesh generated to fit to it using the above method.

In subsequent stages, when the grid nodes are re-meshed using the Poisson equation, it is important to retain the original mesh node spacing. Evaluation of the control functions is therefore necessary to ensure that the mesh not only blends in with the new port feature but also the surrounding, undisturbed mesh. Typically on reading the initial mesh no information is available on the control functions used to generate it. A method of evaluating P^i is therefore required. This is done by using the definitions developed by Thomas and Middlecoff (1982) and given in Soni(1986) where;

$$P^i = \frac{X_{\xi^i \xi^i} \cdot X_{\xi^i}}{X_{\xi^i} \cdot X_{\xi^i}} \qquad \text{where: } X_{\xi^i} = \frac{\partial x}{\partial \xi} + \frac{\partial y}{\partial \xi} + \frac{\partial z}{\partial \xi} \text{ etc.}$$

thus calculating the grid derivatives and second derivatives allows the control functions to be quickly reconstructed from the discrete mesh node information.

- *Step 2*
  Provide a complete geometrical description of port.

Clearly there are limits to the amount of information which can be resolved with the finite number of mesh nodes likely to be available to model each port. However, figure 5.4 indicates the type and range of information which can be resolved in the current module. The extent to which this can model complete port geometries may be judged by comparing figure 5.2 and figure 5.4. For example the cooling hole at the rear of the port has been omitted since this will be sub-grid size for any practical model of a combustor. Ten dimensions and two vectors fully define the geometrical details of the air-admission port, e.g.; position vector of centre of port (O), direction vector of the

port axis($\overline{o}$), hole diameter (or other cross-sectional shape details) (d), chute thickness (t), chute height (h), exit plane angle (α) and internal and external fillet radii and platform heights and diameters ($r_1, r_2, s_1, s_2, D_1, D_2$). In addition to geometrical definition, this step also requires the user to specify a volume (defined by pairs of constant ξ, constant η and constant ζ planes) in the original mesh within which the re-meshing procedure will operate, leaving all other points of the original mesh unaltered. It is further necessary to specify the constant co-ordinate surfaces (i.e. two constant ξ, η or ζ planes) which define the inner and outer liner surfaces in the original mesh, and a third co-ordinate surface from the same family which will eventually be fitted to the exit plane of the chute. Finally, the number of mesh lines in the two spatial co-ordinate directions which lie in the liner surface which define the resolution of the port are specified, (e.g. m×n cells which will cover the hole area).

- *Step 3*
  Move appropriate mesh nodes to resolve chute details fully.

The appropriate mesh nodes are identified in several ways. Initially those nodes describing the liner surfaces are predefined in the body fitted grid, which for the present example are the two planes of constant η enclosing the shaded region, as depicted in figure 5.3. A subset of these nodes must now be identified which define the port's inner and outer perimeter. In computational space these nodes describe two rectangles within the η planes defining the liner surface as shown in figure 5.5. The dimensions of these rectangles is specified by the user in order to set the required port resolution (m×n). In this example the port opening is resolved by 7ξ nodes by 7ζ nodes, and the chute wall has a thickness of two nodes. A two node thickness was the minimum required by the flow solver adopted because any cell which represents solid material (i.e. blockage) can only have one face acting as a wall. Thus to describe a wall with two sides within the flow domain, a two cell thickness is required, one to describe each side. A final computational plane has to be specified which will be fitted to the chute exit plane, this will be of the same family of computational planes which define the liner surfaces, e.g. η_1 in figure 5.5.

The cross-sectional profiles defining the inner and outer shapes of the chute (e.g. two concentric circles for a round chuted hole) are calculated, using the geometrical details

specified in step 2. These are then projected onto the upper (inner shape) and lower (outer shape) mesh surfaces defining the liner with projection taking place along the port axis direction vector as shown in figure 5.6.

One such point, **p**, on the chute cross-sectional shape is depicted in figure 5.6 to illustrate the method of finding its projection onto the mesh surface. Firstly, each mesh cell is divided into two triangles, since the four nodes of a cell may, in general, not lie on a plane. The intersection point of the line passing through **p** with direction $\overline{o}$ and the plane in which the triangle lies is then found. Successive triangles on the mesh surface are chosen until the intersection point found lies on the face bounded by the current triangle. Two examples of this are shown; firstly the point **p"** is found where the line intersects the plane defined by the triangle lightly shaded, also point **p'** is found where the line intersects the plane of the triangle darkly shaded. To determine whether these intersection points fall within the plane defining triangle, a simple test can be performed. The angles α, β, γ are calculated such that $\alpha = \angle$**ap'b** etc., (where **a**, **b** and **c** are the vertices of the respective triangle) and their sum compared to 2π. For a point within the triangle, **p'**, the sum $\alpha + \beta + \gamma$ must be equal to 2π, and for **p"**, lying outside of the plane defining triangle, the sum is less than 2π. Because of surface curvature **p"** does not fall on the mesh surface but **p'** does, thus by performing this check, each projected point is forced to lie on the mesh surface. Calculation of the angles α, β and γ can cause problems if **p'** is very close to one of the triangle's vertices. If the point **p'** lies within a given radius of **a**, **b**, or **c** then the intersection point is considered to lie within the triangle. By setting this radius to a suitable tolerance, machine round off problems are avoided. This piece-wise method of finding the projection of the port shape on the mesh surface had to be adopted since a mathematical description of the surface is not available, only the discrete coordinate information supplied by the grid node definition. This process can be made quite efficient by remembering the location in computational space of the preceding point of intersection, which can be used for the initial guess of the next point. If this guess is incorrect then a spiral search pattern is adopted, centred around the cell which the neighbouring point to **p** intersected with. With such a search pattern and with a high resolution of the profile (compared to that of the mesh) it would be unlikely that more than eight neighbouring cells would have to be examined before a valid intersection is found.

The number of points defining each projected profile has to be reduced to the same number of mesh nodes which will be fitted around them. This is done so that the distance between points is the same all the way around the closed profile. This could not have been achieved had the original profile been defined only by the finally required number of points. For example, in the current example of a circular port, the distance between nodes would change if the circle were obliquely projected on to a flat liner surface, and this uneven distribution could be exaggerated further if the liner were not flat.

The two shapes are also projected onto the chute exit plane, such that the inner and outer surfaces of the chute are now defined by the two cylinders joining the inlet and exit shapes. Four profiles in physical space have now been identified, which require the grid nodes, identified as above, to fit to them. At this stage the absolute location of the port in computational space has not been set. In plan view only the relative port opening has been set to a given resolution. The user can thus either specify the central node of the opening or, because the profiles have been projected onto the surfaces a good guess at the optimum location can be made. This optimum location is calculated by averaging each of the computational coordinates of the cells with which the projected profiles intersected, i.e., the centroid in computational space of the port opening.

Interpolation between the mesh nodes defining the inlet and exit profiles of the chute, for both inner and outer shapes, allows all points on intermediate mesh surfaces to be located on the chute's cylindrical boundaries. At the end of this step the inside and outside chute surfaces (cylindrical in this example) have been defined with the required mesh resolution specified at step 2. Figure 5.7(a) shows the distortions introduced to define the port perimeter in the upper liner surface at the end of this step.

• *Step 4*

Re-mesh liner surfaces to blend in changes to mesh made above.

The 2 mesh planes defining the liner surfaces in the original mesh are now re-meshed so that points within these surfaces (and internal to the re-meshing volume defined in step 2) are moved into new positions to blend in the modifications in these mesh surfaces made in step 2. This re-meshing process consists of solving 3D elliptic p.d.e.'s

as specified above, but after each iteration the points are projected back onto the mesh surface as defined by the original grid. The projection is necessary since the mesh nodes will tend to move toward the centre of curvature with each iteration hence tending to flatten out the surface. Liner surface mesh points are thus allowed to move around, but only within the original surface. Projection is performed in the same way as the port cross-section is projected onto the surface, but now projection takes place normal to the triangulated cell face shown previously in figure 5.6. Figures 5.7 (b) and (c) show the upper surface re-meshed to blend in the distortions shown in 5.7(a). The need for "flagging" of cells to prevent them being moved is indicated by comparing the two resultant meshes. In the first the edges of the cooling ring have not been flagged, in the second they have. This flag prevents the re-meshing procedure moving the nodes - which in this case define an edge of the surface in which the port has been included. The geometry of the cooling ring remains intact in (c), whereas the corner has been rounded off in (b).

The overall surface re-meshing approach described is simple and has been found to work well, but mesh nodes move within the flat cell faces describing curved surfaces. Another approach would be to replace the Laplacian operator with the Beltramian operator in the Poisson equation, as described by Warsi (1986). The Beltramian allows the parametric 2D surface coordinates to be solved for in 3D space. By fitting curved surface patches through the discrete nodes, (required to obtain continuous values of the surface curvature), a more accurate representation of the original surface could then be reproduced. Time was not available to incorporate this approach but its development may help to retain a more accurate representation of the initial surface definition. However, for combustor liners, which typically have only slight curvature, the current method is sufficiently adequate.

- *Step 5*

  Create fillet radii and platforms around chute as required.

Small details of port geometry (e.g. inlet radiusing or a raised step on the outer liner wall) may be created by shifting discrete grid points in a direction parallel to the port-axis vector by specified amounts as given from the geometry information in step 2. Also at this penultimate stage some tidying up is necessary, e.g. for the points lying

between the inner and outer diameters of the exit plane of the chute (for the case where several mesh lines are internal to the liner wall to resolve film-cooling flows or liner heat conduction processes). These are moved to lie within the surface defined by the chute exit plane, which is simply a matter of interpolation. At the end of this step all of the port geometrical features have been located with the selected resolution by moving all necessary points in the original mesh to lie on appropriate surfaces defining port inlet, exit and bounding planes. Figure 5.8 indicates an example of the mesh at the end of this stage.

- *Step 6*
  Blend in all internal mesh nodes to fit the new surface and port definition.

The final step is to re-solve the 3D Poisson equations within the selected volume to move the internal field mesh points to blend in with the changes made to the original mesh in steps 3-5. The control functions, P^i, calculated from the original mesh are used such that the original node clustering is retained. Remeshing can then be restricted to a sub-domain of the full grid since the grid distortion will typically be localised. Care needs to be taken that any grid nodes which describe geometrical features are not moved in this process. This is achieved by flagging nodes which describe a solid surface. As steps 3-5 are performed flags are attached to nodes which have been moved in each process such that subsequent processes do not redefine the nodes. In addition to this a boundary condition file allows the user to indicate any additional cells which should not be moved during the process.

Figures 5.8 and 5.9 indicate the final liner and port-fitted mesh which results from the above procedure for a representative combustor geometry. The upper liner surface, and any mesh planes internal to the liner, are described by η mesh planes similar to that in figure 5.8(a), where the mesh plane contains a description of only the inner diameter of the chute. The lower liner surface, and any mesh planes used to describe the cross-section of the chute, are described by mesh planes similar to that shown in figure 5.8(b) which contains a description of both inner and outer perimeters of the chute. It is by a stacking of these two styles of mesh planes (2 of 8(a) and 3 of 8(b) in this example) which makes up the third dimension of depth of the port, shown in cross-section in figure 5.b(b).

Any number of ports may be introduced into a combustor liner or other solid surfaces by repeating steps 2-6. This is illustrated in figure 5.10 which shows a flow diagram of the main procedures within the program. The program was written to be none interactive thus the required input files are indicated. Beside the initial grid definition files (either x,y,z data or a body cross section profile) a global definition file and one further file to define each port is required. The '*setgrid*' file defines such parameters as the number and order of ports to be included and the convergence criteria for iterative processes. Each '*hole.01*', etc. file defines the parametric sizes and location of the port in physical and computational space. It is the *bc_grid* file which specifies any regions which require flagging, as described earlier, to prevent loss of geometrical information. The *hole_ijk* file lists the ports location in computational space such that the information may be included in a boundary definition file required by the solver to indicate the presence of a port.

5.3 Port Grid Generation Examples

To show the abilities of the port modelling module a few illustrations of resultant grids are given. The scope of these three examples has been chosen to show the versatility of the module. Firstly a high resolution mesh fitted to a single primary-like port is shown, followed by an example of a combustor sector with several ports included at a low resolution.

Figure 5.11(a) shows a mesh fitted to part of an actual combustor liner, through which is to be included a primary port. Using this mesh as the initial mesh for the module along with the actual port parameters produces the grid shown in 5.11(b). The port can be seen in cross section in this figure since the illustrated mesh plane passes though the axial diameter of the port. To illustrate this port further figure 5.12 shows top and bottom views of the resultant solid surfaces. All of the features in the parametric model of figure 5.4 can be seen, such as; the raised platform and matching recess on the underside, the inlet radius and the oblique exit plane. The level of resolution of this first example would prove impracticable for current coupled calculations, since to model this small region around a single port has taken 1/4 million grid nodes. For a full

sector of this combustor with 10 individual ports and a burner feature this number of nodes per port would not be possible with available computing resources.

The final example thus shows a full sector of the same combustor with all of the ports modelled at a practical resolution. In figure 5.12 the resultant mesh is shown with plain ports, and in figure 5.13 with chuted ports. The geometrical resolution of the final two examples is quite good (e.g. compare figure 5.14 to figure 5.1) and are representative of mesh sizes employed currently for combustor predictions. However in the light of work which will be reported in the next chapter, it is unlikely that the mesh density is sufficient to eliminate all numerical error when performing flow prediction on a mesh of this type. However, CFD calculations have been performed for this example combustor sector with and without chutes on the ports. This has been done to see if changes in the flow field are noticed, despite probable numerical error at this resolution. These calculations will be discussed at the end of the next chapter.
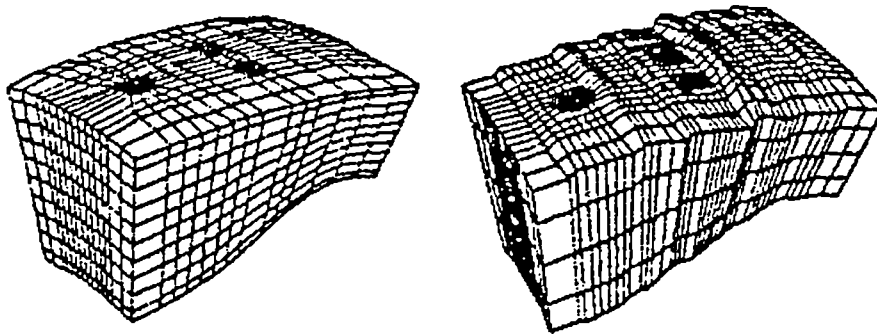
Three-dimensional view of typical combustor geometries
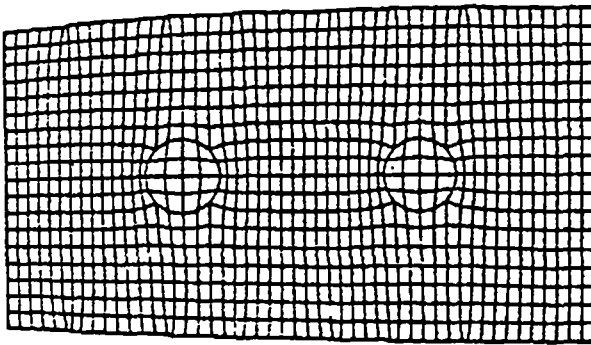
Typical top mesh surface

Typical bottom mesh surface
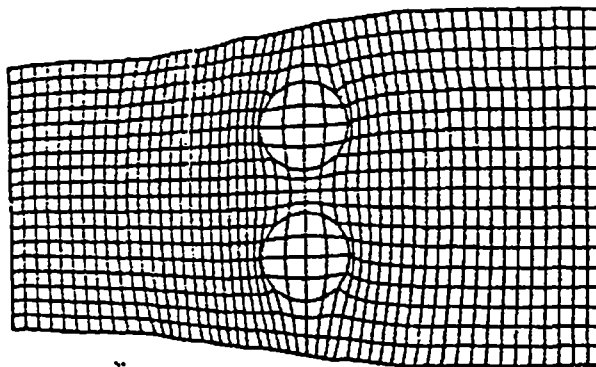
Figure 5.1 Port Fitted Mesh of Shyy (1987).
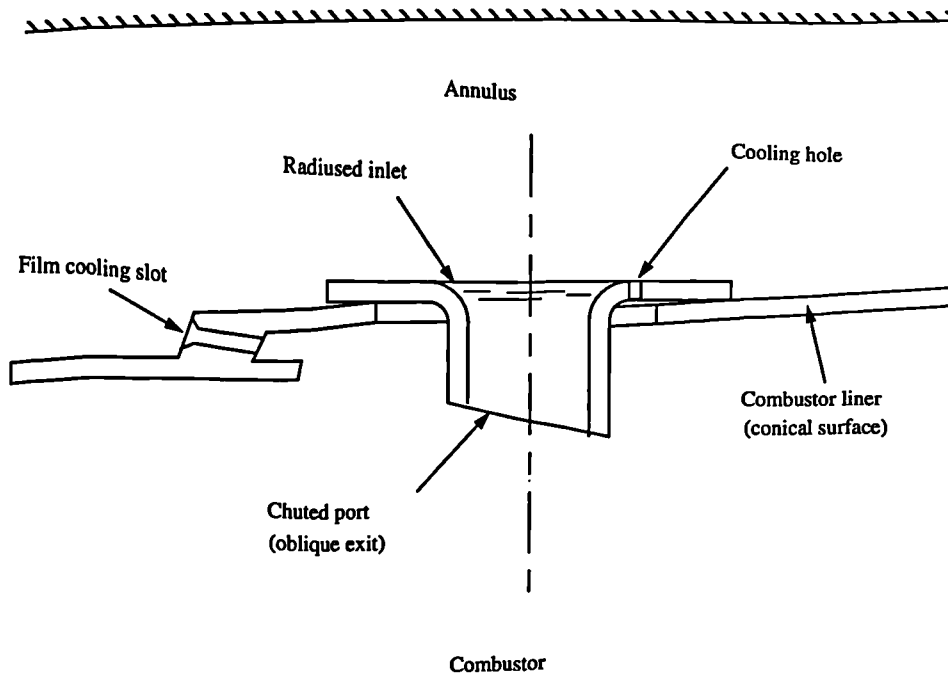
Figure 5.2 Typical Port Geometry
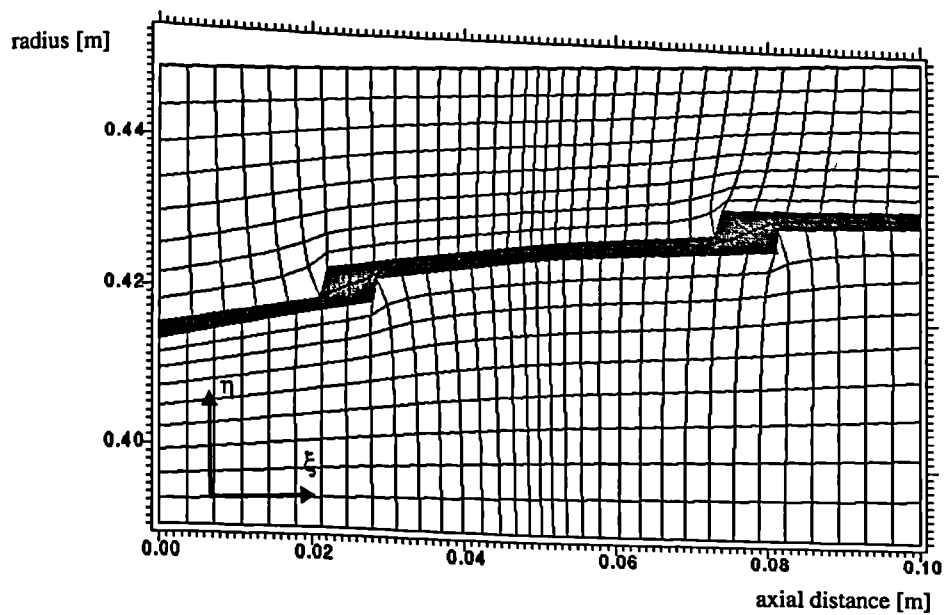
Figure 5.3 Mesh Fitted to Part of a Combustor Liner
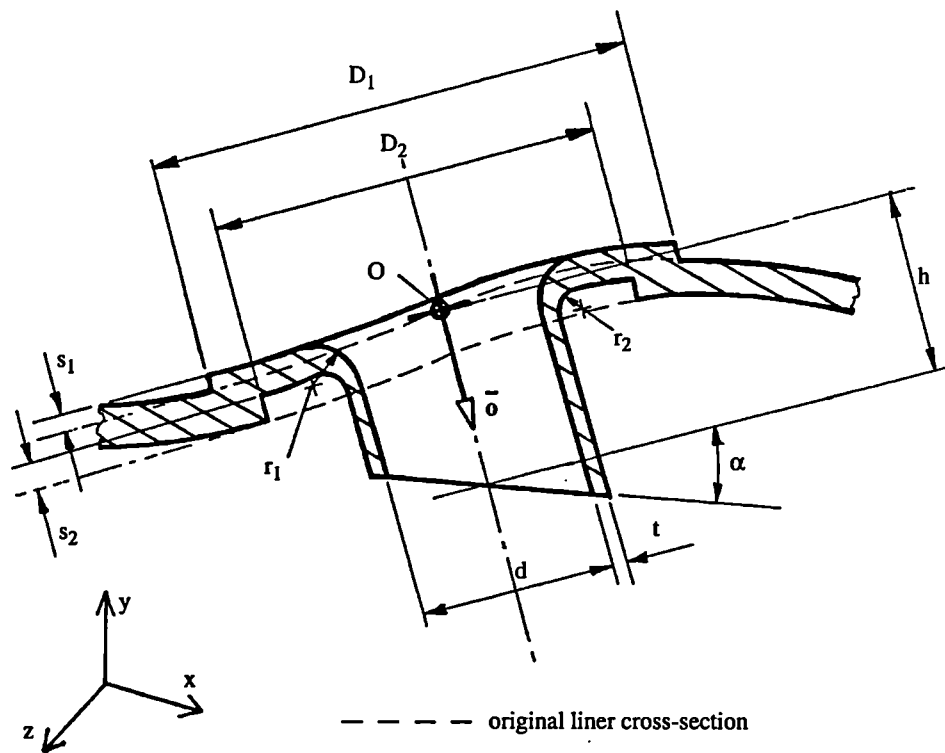
Figure 5.4 Generic Port Geometery Definitions

Plane $\zeta=\zeta_1$

Plane $\eta=\eta_1$
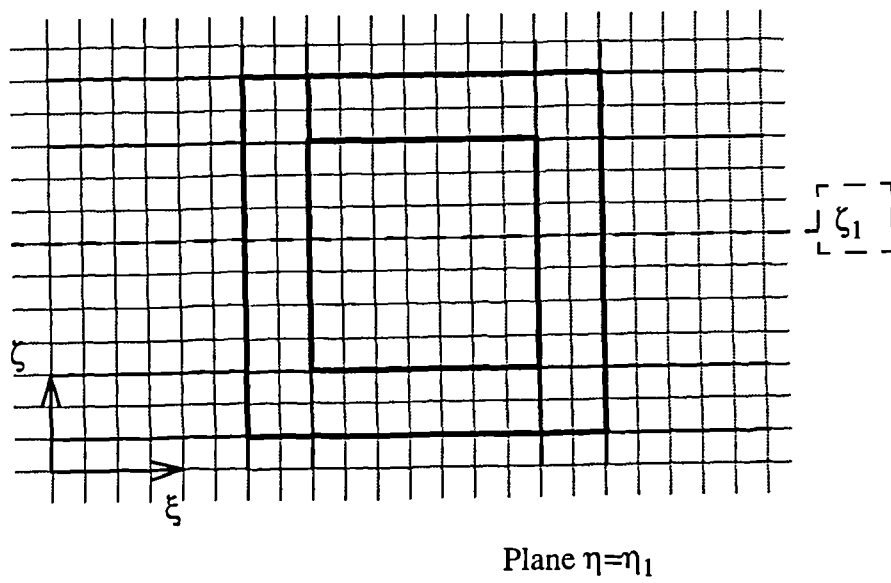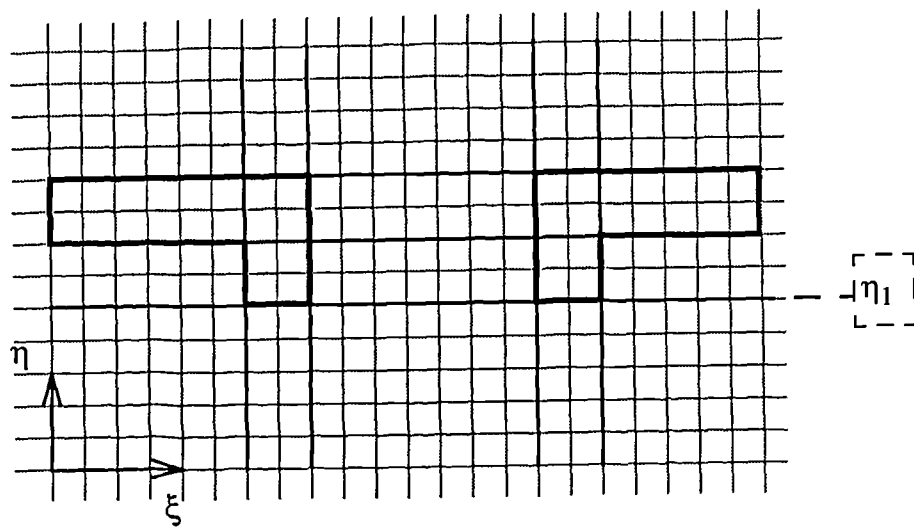
Figure 5.5 Port Topology in Computational Space
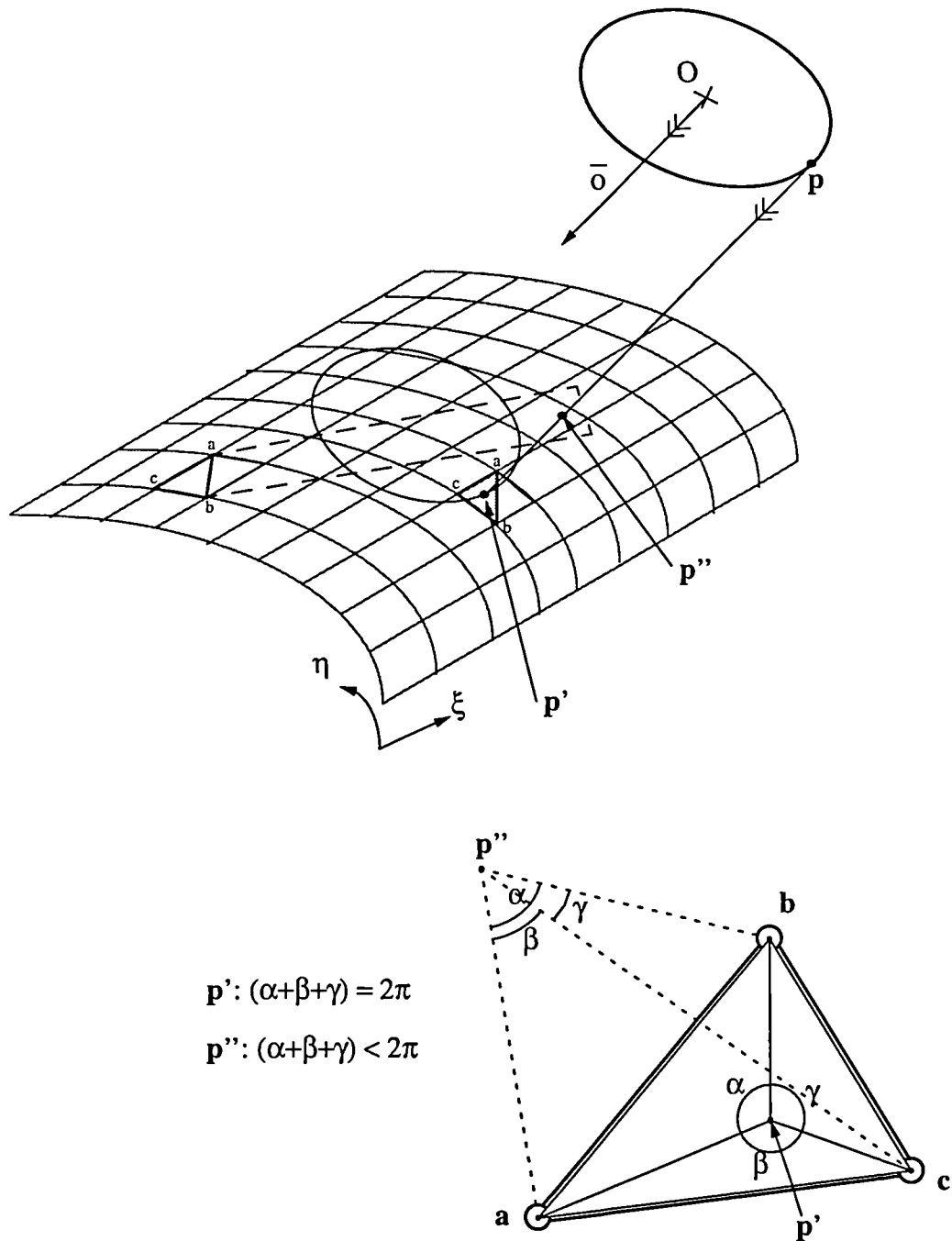
Figure 5.6 Finding Projection of Port Profile on Mesh Surface
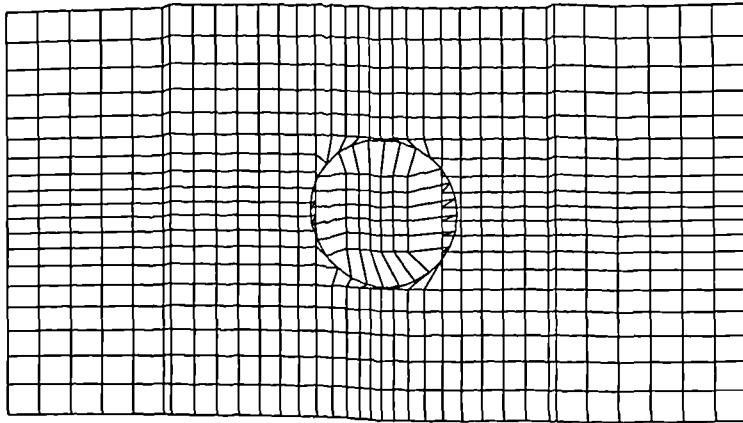
(a) After intersection - before surface meshing
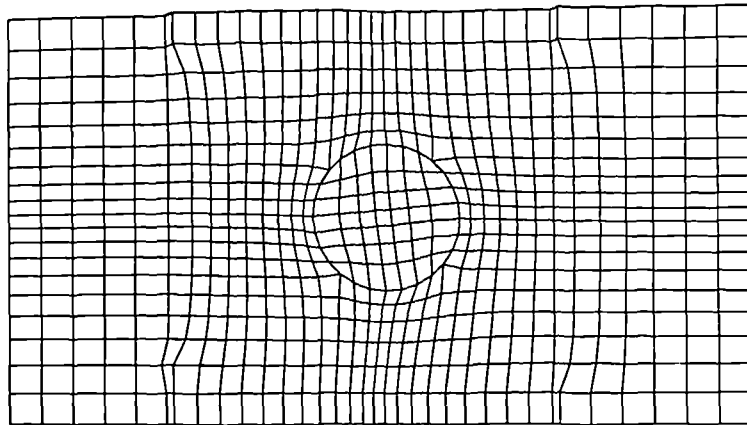
(b) After surface re-meshing - without cooling rings flagged
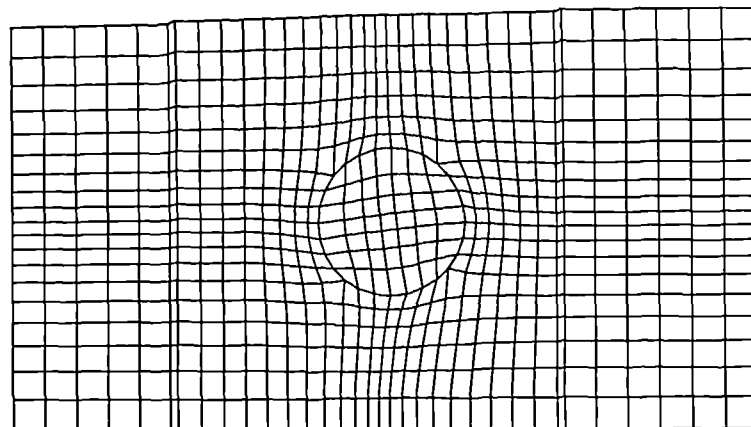
(c) After surface re-meshing retaining liner features

Figure 5.7 Liner Surface Re-meshing - "Before and After"
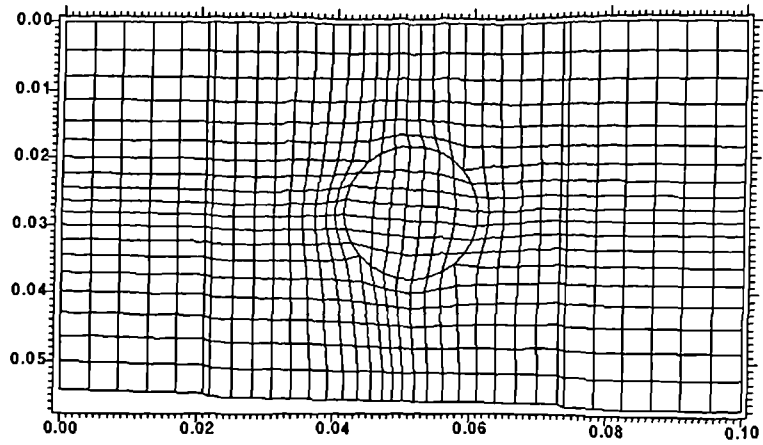
(a) Upper Liner Surface
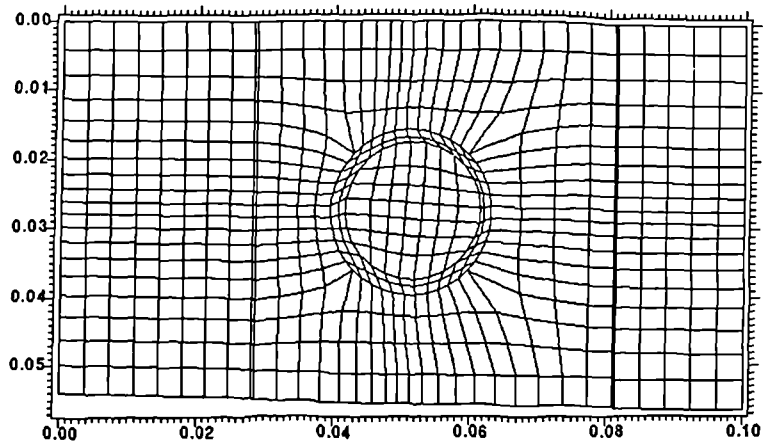
(b) Lower Liner Surface

Figure 5.8 Mesh Fitted to upper and lower liner surfaces
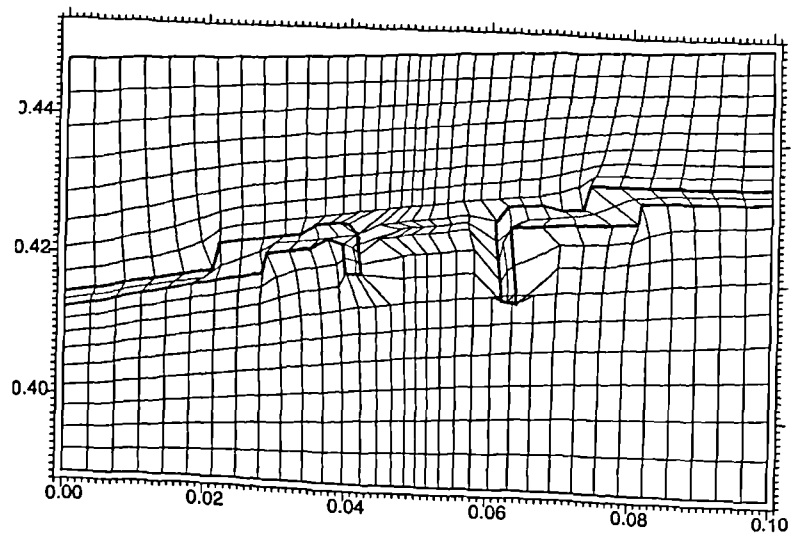
(a) All solid surfaces resolved
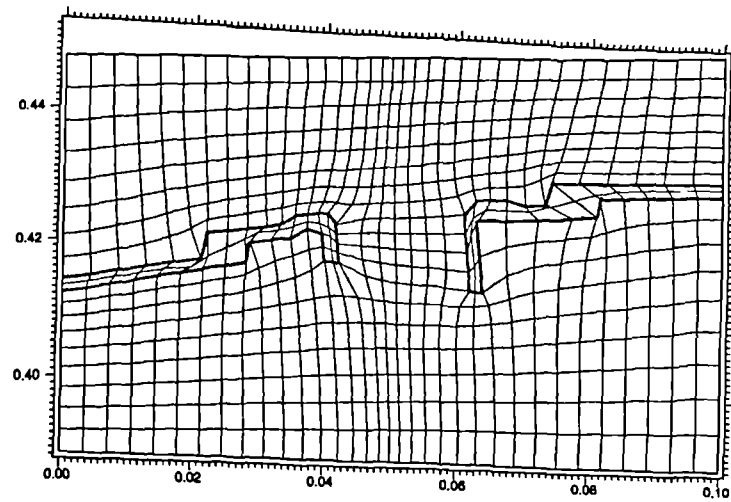
(b) Final liner and port fitted mesh

Figure 5.9 Local Remeshing to Blend in Port Feature
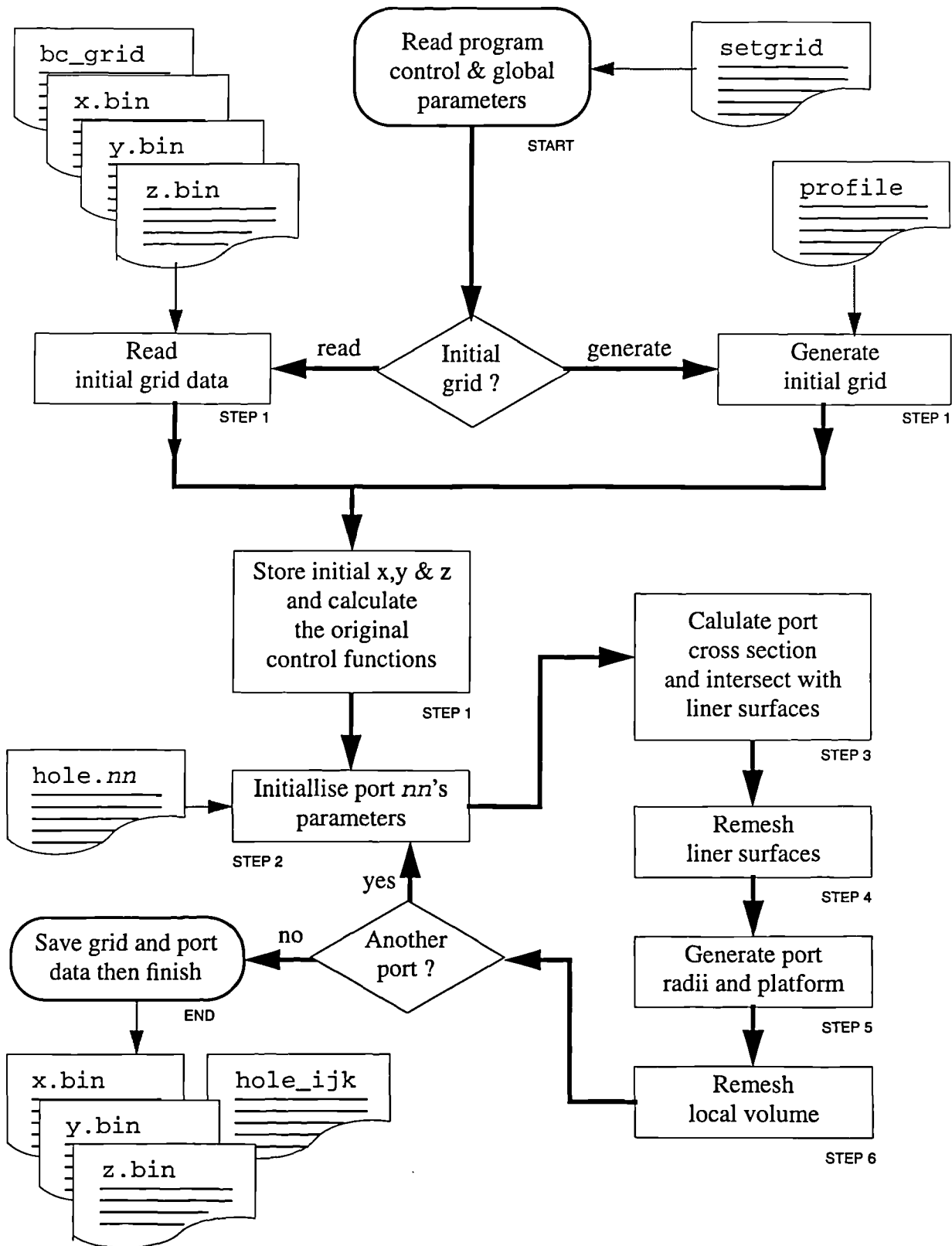
Figure 5.10 Port grid generation module - flow diagram
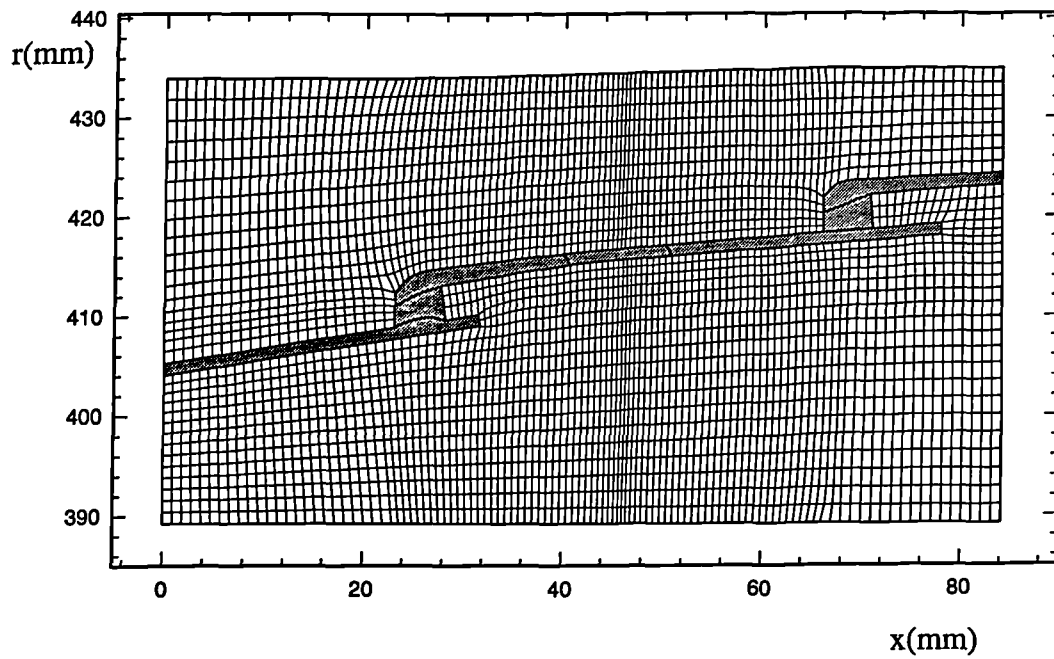
(a) Initial, pre-port module, mesh
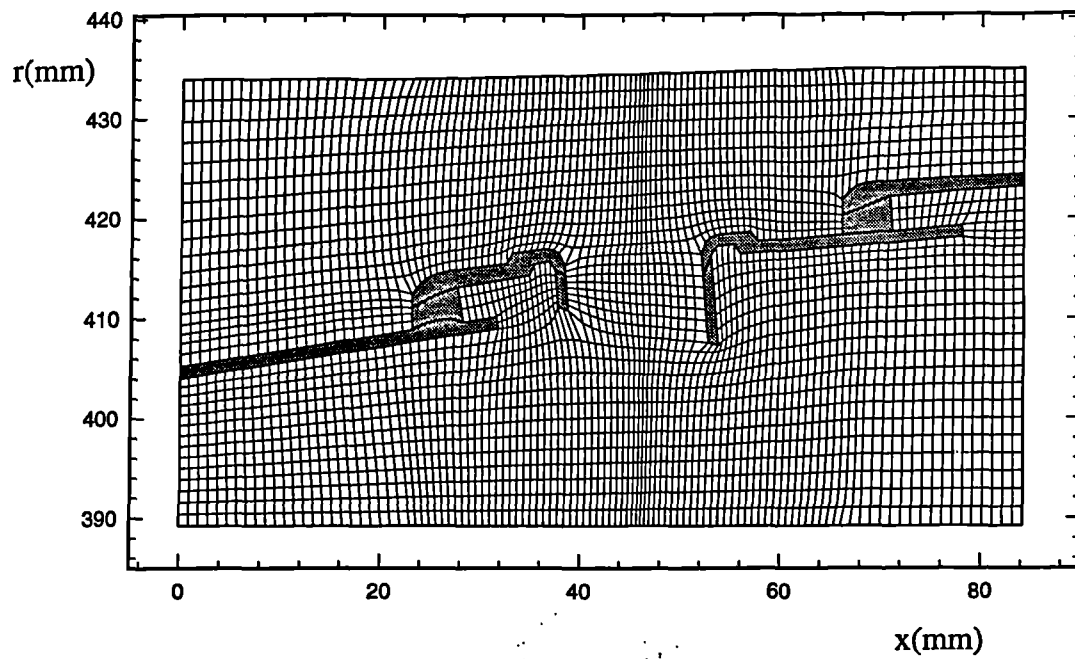
(b) Final, post-port module mesh

Figure 5.11 Example of Mesh Fitted to Realistic Primary Port

Suface mesh lines

Port detail
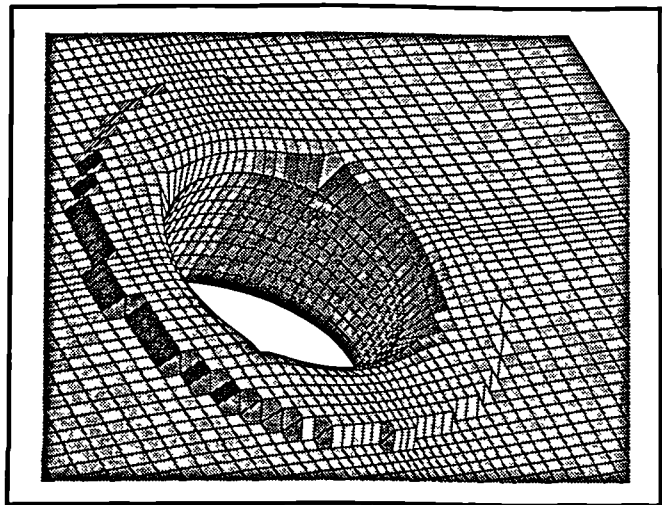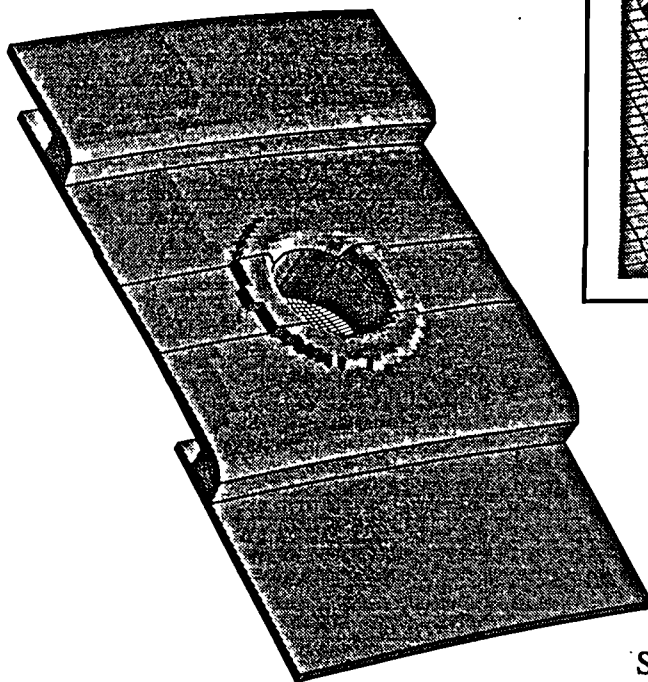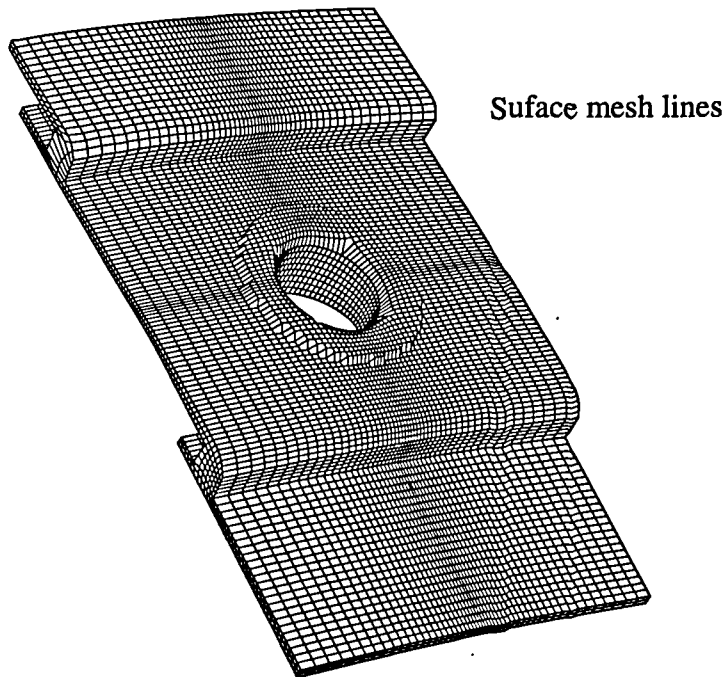
Shaded solid model

Figure 5.12(a) Primary Port Region of a CombustorLiner -Top View

Suface mesh lines
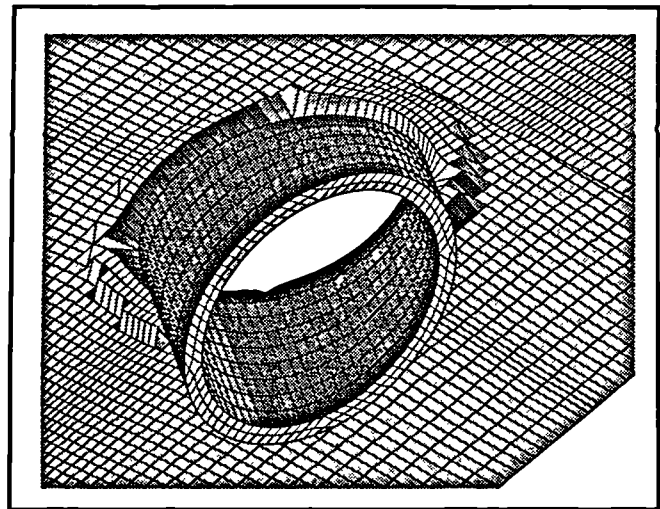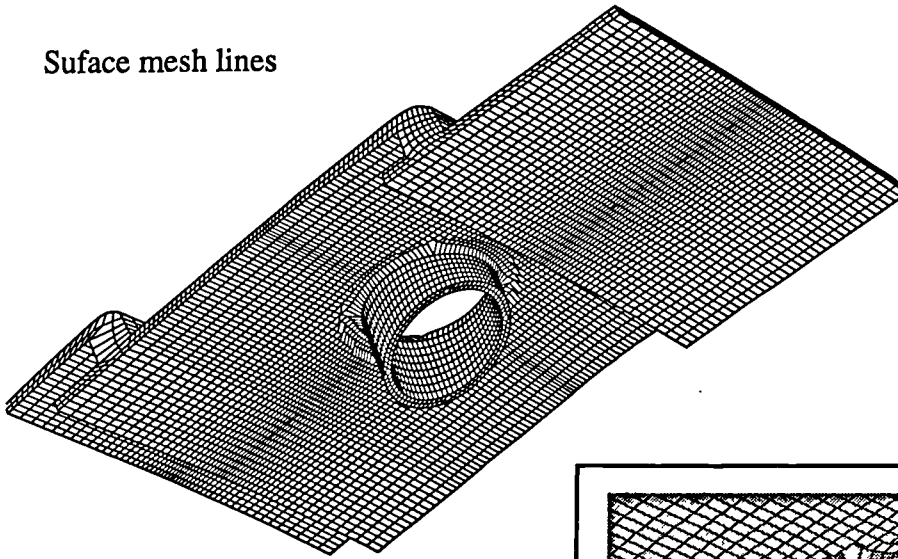
Port detail
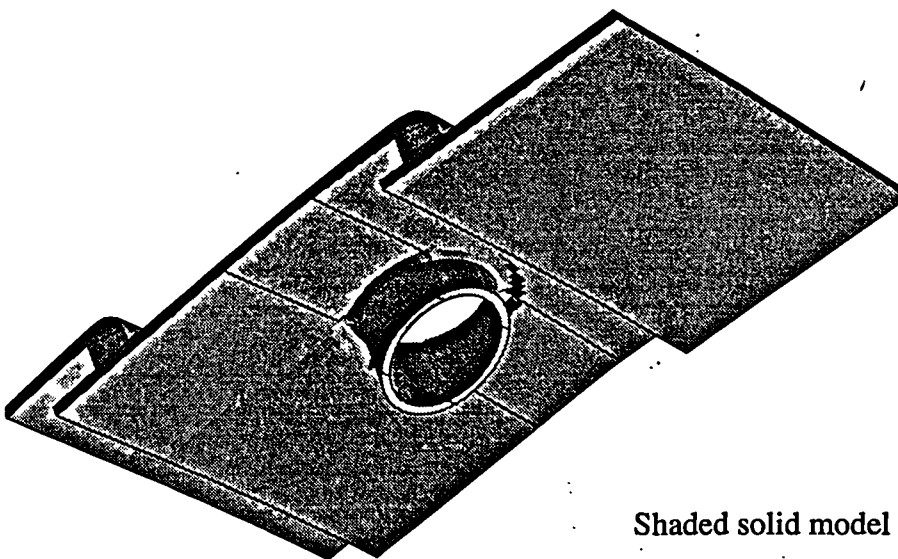
Shaded solid model

Figure 5.12(b) Primary Port Region of a CombustorLiner - Bottom View
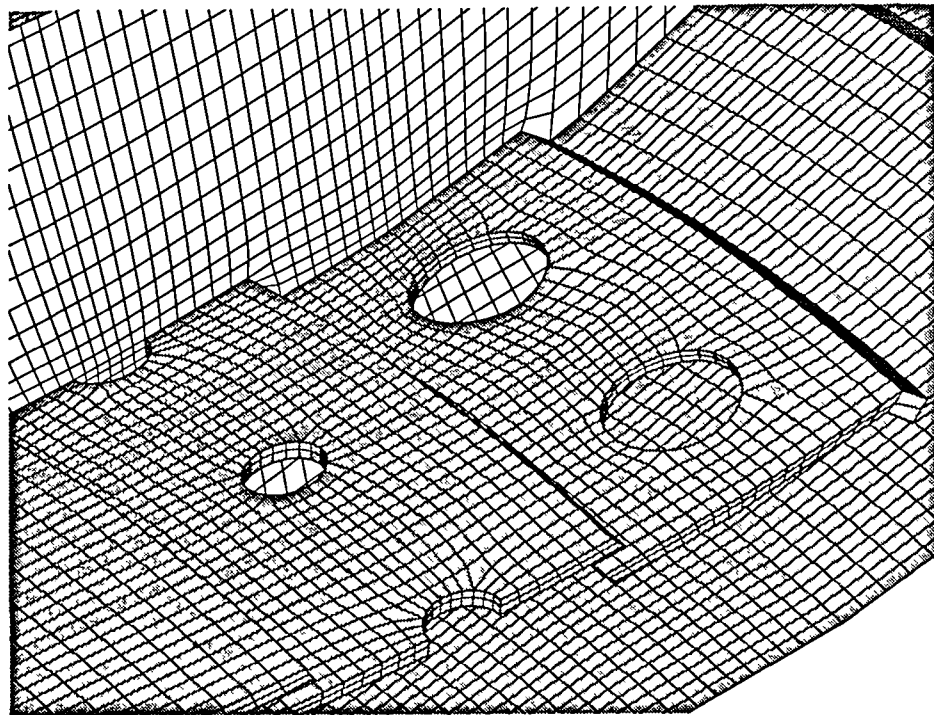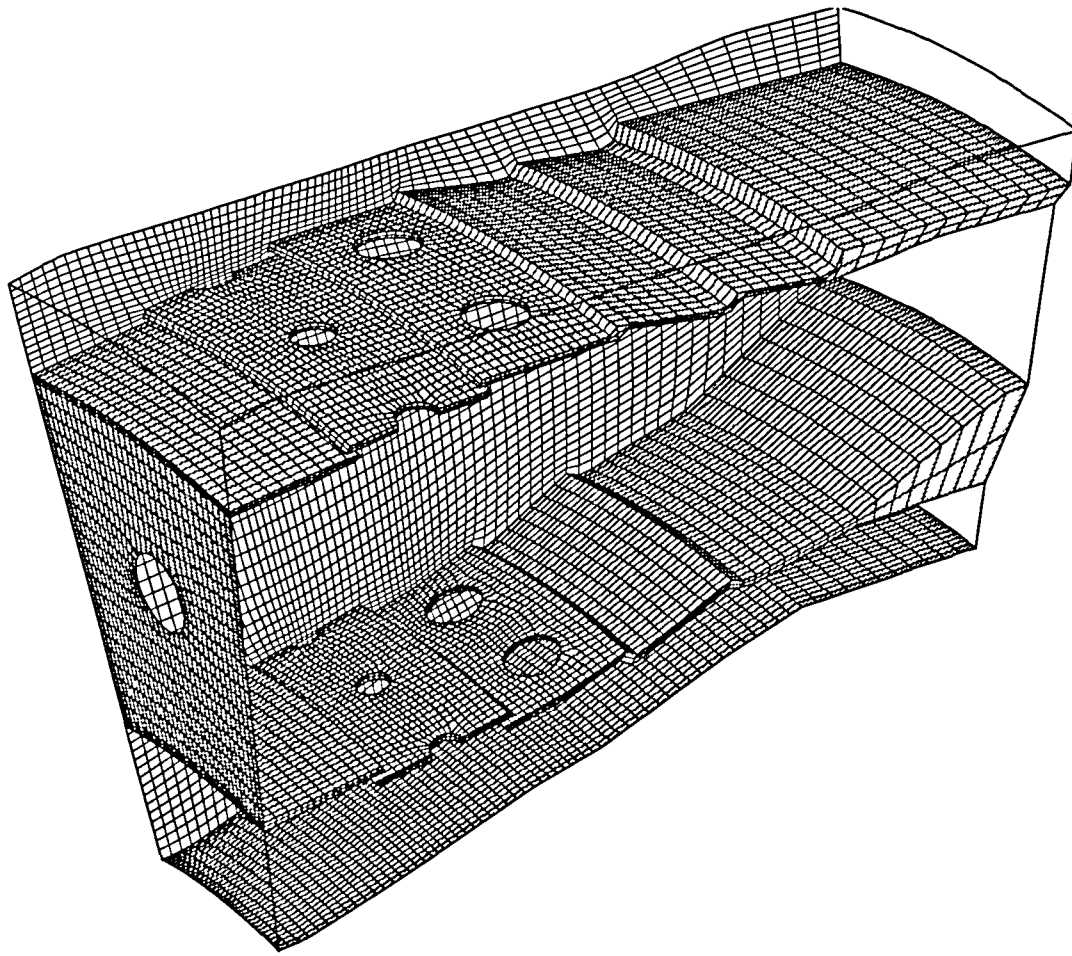
Figure 5.13 Full Model of an Annular Combustor Sector - Plain Ports
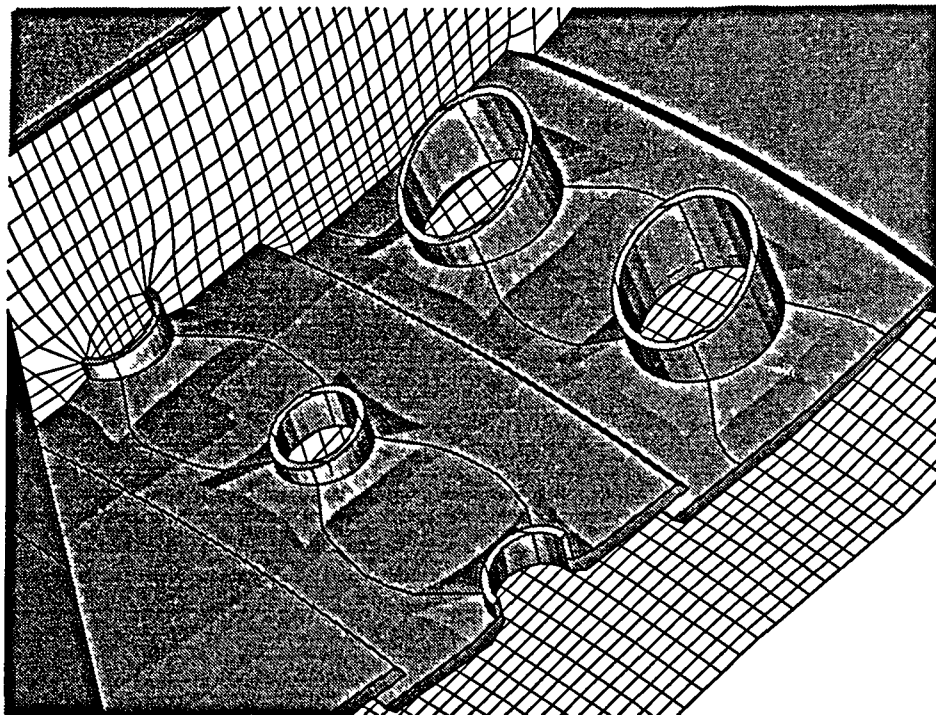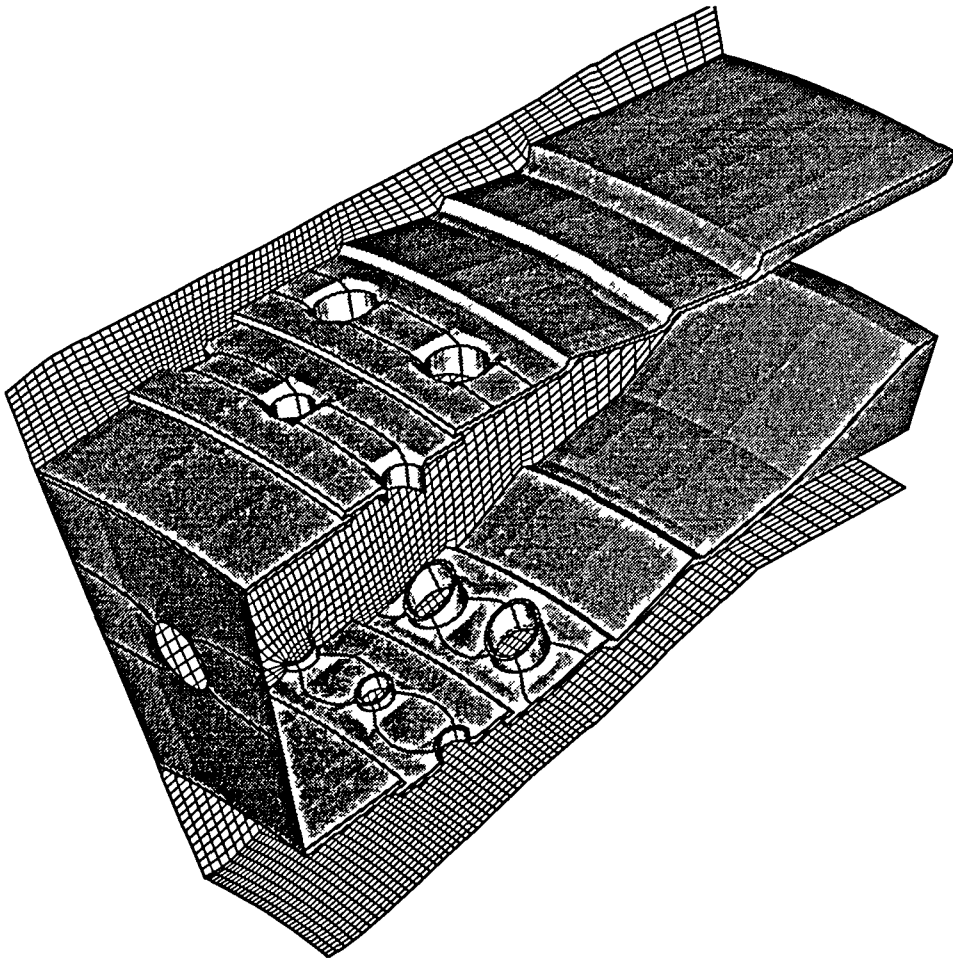
Figure 5.14 Full Model of an Annular Combustor Sector - Chuted Ports

Chapter 6

Computational Results

6.1 Introduction

One of the main advantages of CFD is its ability to predict the results of various flow scenarios quickly. Thus, whilst the time-consuming process of rig design, manufacture and commissioning was under way, the opportunity was taken to concentrate on the numerical predictions. The geometry of the rig was decided upon after the commencement of the initial predictions, and much of the preliminary computational work was performed prior to the experimental program. As a result, early calculations have been done on a slightly different geometry to that described in chapter3. Computational predictions of the rig representative geometry were performed after the experimental measurements to allow direct comparison. By adopting this procedure, the two approaches complemented each other in a number of ways. The preliminary calculations indicated the important flow regions, thus helping make decisions on rig design and instrumentation, and giving a general insight into what to expect. The experimental data then allowed precise boundary conditions to be determined for the later, matching calculations.

In any CFD study where the performance of the turbulence model is to be assessed by comparison with experimental data, it is important to establish that numerical aspects are not influencing the results. The next section of this chapter therefore describes the effects of increasing both the mesh density and the precision of the port shape representation to assess the numerical accuracy of the computational method adopted. The third section illustrates how discharge coefficients have been evaluated from the CFD results, a subject which is often omitted from published work. Sections 4 through 7 follow the same order as those in the experimental chapter 3, moving from consideration of the datum flow to the effects of introducing annulus swirl. Up to this point, the geometry of the flow problem considered has been the simplified cylindrical/ single port row studied in the experiments. To extend application of the methods developed in this thesis to more complex cases section 8 discusses the application to a sector of a realistic combustor geometry. This demonstrates the ability of the port modelling module and allows an assessment of the effects of port representation upon the flow field within calculations typical of those likely to be used in industry.

6.2 Grid Refinement Study

Before embarking upon a detailed computational modelling exercise, it is important to assess the numerical accuracy of the predictions. Errors will arise from many aspects of the modelling procedure, e.g. shortfalls in areas of the actual model (such as turbulence closure as a particular example), neglecting higher order or cross-derivatives when implementing the governing differential equations. Parameters which are easily altered and have an understandable and direct effect on the numerical accuracy should be examined first. For example, increasing the spatial resolution of a grid will help reduce those errors associated with truncation of the discretised equations. Once a solution which is independent of grid density has been reached it would be expected that the truncation error introduced by discretisation has been eliminated. An alternative method is to use a higher order accuracy discretisation scheme (smaller truncation errors) on a fixed grid; both methods have been used in the present study.

One of the flow geometries previously studied by Baker(1992) was chosen for the grid refinement study: the six port geometry and symmetry assumptions are shown in figure 6.1. The annulus height is equivalent to 1.57 port diameters and the liner is 0.16 port diameters thick. Uniform annulus and core inlet and bleed velocity profiles were used to produce a bleed ratio of 28% and jet to core flow velocity ratio of 5.0, to match exactly one of the scenarios examined by Baker both experimentally and computationally. The annulus height of the test rig used elsewhere in this thesis is 1.0 hole diameter, the bleed ratio for the primary port is 50% and the liner thickness is 0.25 hole diameters. Despite differences however, for the purposes of a grid refinement exercise, the geometry and flow conditions considered present all of the flow features which would be encountered in subsequent calculations, albeit with slightly different geometry.

Much of the previous work in this field has been performed upon cylindrical polar orthogonal grids (Baker(1992), Koutmos(1989), or boundary-fitted (but not port-fitted) meshes, (Coupland(1986), Karki(1990)) which both result in the port being represented by a castellated approximation. A possible refinement is to adopt a port fitted mesh, as generated by the methods described in chapter 5, in which case the

perimeter representation is geometrically more accurate. It is of interest to study the effect of a better port-shape representation on the accuracy of flow predictions and this was the focus of the initial predictions. Three levels of grid refinement were chosen for both castellated and fitted meshes as shown in the table below.

Grid:	castellated mesh			port-fitted mesh		
No:	C1	C2	C3	F1	F2	F3
ni (x)	48	72	100	48	72	100
nj (r)	40	40	40	40	40	40
nk (θ)	16	24	30	16	24	30
nijk	30720	69120	120000	30720	69120	120000
np	90	235	373	88	260	480
area	$1.376*10^{-4}$	$1.418*10^{-4}$	$1.424*10^{-4}$	$1.421*10^{-4}$	$1.424*10^{-4}$	$1.424*10^{-4}$
area error	-3.45%	-0.44%	-0.10%	-0.25%	-0.08%	-0.04%

Table 6.1 Mesh Resolution for Grid Refinement

Grid C1 has 48 grid nodes in the axial direction, indicated by the row ni(x). The total number of grid points is indicated by nijk, and the number of mesh nodes defining the plan of the port is indicated by np. The sum of the np cell face areas which define the port is then given in the final row as the numerical representation of the port geometrical area (compared with the exact area of half a 19.25mm diameter port: $A_h = \pi(0.01925)^2/8 \cong 1.425*10^{-4} m^2$).

A pictorial view of the mesh used in calculations C1 and F1 can be seen in figure 6.2. The global view shows the cylindrical polar mesh of C1. Port fitted meshes, F1-3, have been generated by manipulating the meshes, C1-3, using the port module described in chapter 5. Thus mesh F1 is identical to C1 except in the vicinity of the port. This is illustrated by the two enlarged views. Detailed plan views of the mesh describing each port can then be seen in figure 6.3. It is worth noting that even the coarse mesh is significantly more resolved than many typical combustor calculations, in which (typically) only 16-25 points would be used in the plane of the port. Because of the approximated port shape of C1, the area of the port is 3.45% less than a 19.25mm diameter port - the subsequent, more accurately defined ports, all match the required

area to within 0.5%. At the finest resolution the modelled area for the castellated approach has double the error of that of the fitted approach. With decreasing port resolution the error associated with the castellated port open area increases at a greater rate than does the fitted representation error (the error of C1 increases to be 14 times worse than F1 for a fourfold decrease in the number of nodes lying within the port). A graphically obvious short-fall of the castellated approach is the poor representation of the port perimeter. The jagged nature of the castellations will naturally impose unrealistic constraints on the port flow. Particularly, the velocity normal to the wall of the perimeter of the port should be zero. With the fitted mesh this can be imposed reasonably accurately - the circular port being effectively represented by a many sided regular polygon - the face normals of which align locally to that of the circle being approximated. With the castellated approach, control of the secondary (axial, azimuthal) velocity components can only be performed by setting either or both to zero, to be consistent with neighbouring walls. In a corner cell for example, which is flanked by two blocked cells, both the axial and azimuthal velocities will be set to zero and the only possible flow direction is in the radial (through port) sense.

Each calculation was continued until the residual change in each and every solution variable was below 1.0×10^{-5} (defined as the largest change in a variable over all nodes within the solution domain divided by the maximum value of that variable). A large number of iterations, 10-15,000 were required for this due to slow convergence at the centre-line, where cell aspect ratios were unavoidably high. Indeed it is possible the solution may still not be completely converged on the centre-line (see discussion below). The rest of the solution field had converged within around 5000 iterations. Each calculation was performed initially with Hybrid differencing for each solution variable. QUICK was then used for the convective terms to establish if moving to a higher order scheme had any effect on the solution. This work is also reported in paper format, McGuirk and Spencer (1993).

6.2.1 Flow Field Predictions

As mentioned previously, convergence of each prediction was slow at the centre line due to the high aspect ratios of the cells. This problem arises when solving the

discretised equations 4.13 - if the magnitude of the influence coefficients ([A]) for an individual grid node are excessively different from each other, numerical round-off of the smaller values will ensure that the solution vector (ϕ) is swamped by the value(s) associated with the highest influence coefficient(s). Near the centre line the azimuthal influence coefficients may swamp those in the axial and radial sense due to the large cell aspect ratio. It is thus perhaps better to focus attention a little away from the centre line, particularly as this aspect ratio increases with grid refinement. Figure 6.4 thus shows the variation of axial velocity along a line parallel with the centre line at a radius of 20% of the core pipe radius for each of the six predictions in table 6.1. By moving attention away from the centre line, any concerns over the convergence problems in this region are reduced. The size and strength of the recirculation is indicated by the width and depth, respectively, of the negative portion of each curve. Looking at the castellated curves (outline symbols) shows a reasonable level of agreement between the two highest resolved grids in these two characteristics, suggesting grid independence. Compared to the castellated prediction the size of the recirculation is significantly under-predicted in F1. One reason for this could be the increase in numerical error due to mesh non-orthogonality, not only in the core but also in the annulus, as will be shown shortly. With the first increase in refinement of the fitted grid, F2, the recirculation size increases to be comparable to C2 and C3. On the final *level of fitted grid refinement, F3, the recirculation increases* further to have a similar size as C1 but comparable in strength to C2 and C3. This spread in prediction of the size of the upstream recirculation is cause for some concern. However, excluding F1, the impingement point predicted by each of the calculations lies within 1.5mm, suggesting the effective jet trajectory is consistently predicted. (note: the impingement point is the second zero crossing of the axial velocity profile). The magnitude of the maxima and minima of each curve appear to be correlated: a large and strong recirculation being accompanied by a high maximum velocity downstream of impingement. Higher centre line velocities are consistent with more of the jet's mass flow reaching the inner radii of the core. This may indicate that the lateral diffusion of the jet is over predicted in calculations F1 and F2. The differences between each prediction, thus appear to be due to differences in the predicted strength of impingement rather than jet trajectory.

Another good indicator of impingement strength is the level of turbulence at impingement. The distribution for each of the calculations is shown in figure 6.5. Clearly five of the curves have very similar distributions with almost identical maxima at impingement. Calculation C1 has a higher level of turbulent kinetic energy than the rest possibly due to the slight reduction in port area. This results because a smaller port will have a higher velocity through it for the same mass flow, thus creating a stronger impingement. The smaller recirculation of F1 is consistent with slightly reduced levels of turbulence within the core, particularly in the region of upstream recirculation.

Focussing attention on the near-centre line distribution of velocity and turbulent kinetic energy has led to an unclear indication of what grid density is required to reduce numerical error to an acceptable level in this flow. No experimental correlations exist which predict the size of recirculation for given flow conditions, but they are available for jet angle and discharge coefficient. Experimental evidence has also shown that the core recirculation is unsteady. To help clarify the level of grid independence of the current predictions, it is perhaps better to examine other flow details and global parameters.

In the next figure, 6.6, "streamlines" are presented for each of the 3 castellated calculations. These "streamlines" are the particle tracks that would result if massless particles were released in the mean flow field and constrained to lie in the $\theta=0^{\circ}$ plane. Although this is a rather artificial definition, it is believed to be the simplest way of obtaining a "global" view of the jet impingement/recirculation process. Each particle track has been released from the same location within each solution. All of the flow patterns agree well in both the core and annulus. The annulus flow of each can be categorised by that typified by that of figure 3.26(c), in which the separation bubble originating on the outer annulus wall is as large as the annulus (in the radial sense) and interacts strongly with the jet. The most noticeable difference between the three is in the nature of the upstream core recirculation, which has been examined in the previous two figures, again showing C2 and C3 agree well enough to imply that the solutions are grid independent.

The corresponding "streamlines" calculated for the fitted grids are shown in figure 6.7. This sequence confirms that the core recirculation of F1 is significantly smaller than the other predictions. Looking at the annulus stream traces shows that F1 has a different flow pattern than the other remaining fitted and castellated predictions - which all agree exceptionally well. The annulus flow pattern in F1 has switched to that typified in figure 3.26(b), in which the separation bubble on the outer wall does not interact with either the inner annulus wall or feed the jet. This switch from one mode of annulus flow to another could be an alternative explanation as to why F1 under predicts the size of the core recirculation, via a change in the jet characteristics. The problem definition of F1 is the same in every way to C1 upstream of the port in the annulus - excluding the deformations of mesh F1 which allow it to be fitted to the port. Hence the change in the predicted flow pattern can only have been bought about by the errors introduced by the appearance of mesh non-orthogonality which are predominant in what has been identified experimentally as a critical area of the flow. With increased mesh density, the annulus flow predicted by F2 and F3 are in agreement with the castellated predictions C2 and C3, suggesting the errors due to poor orthogonality have been reduced to an insignificant level.

Comparing the two finest mesh calculations, it can be seen that if the "leading-edge" streamline (that of the particle released closest to the centre line) of C3 did not bend backwards as it passes around the upstream extent of the recirculation then the agreement between it and F3 could be even better. This is perhaps further evidence that convergence close to the centre line is poor.

Considering the stream traces and centre line plots together show that at the highest two resolutions for both castellated and fitted grids (C2, C3, F2 and F3) the solutions agree well. Strong evidence that numerical error has been reduced to a insignificant level in the medium and fine grids. A further clear conclusion of this is that the additional effort of producing port-fitted meshes does not seem to influence the level of grid refinement needed to resolve the flow properties. Perhaps this is not surprising since large-scale flow features dominate in both the annulus and core.

6.2.2 Port Flow Detail

Since geometrical representation of the port is the second refinement considered (mesh density being the first), it is prudent to compare detailed flow properties in the port vicinity on both castellated and fitted meshes. Differences would be expected to be highest at the port exit where flow gradients are strongest. Figure 6.8 therefore shows the radial velocity (parallel to the port centre line) across the diameter coincident with the $\theta=0^\circ$ plane. Good agreement is seen between each of the predictions of radial velocity across this diameter. The C1 and F1 predictions do not fully describe the profile due to lack of resolution, particularly in regions of high rate of gradient change. The peak of the C1 profile is also high in absolute terms, a consequence of the port area being slightly undersized. The two highest resolution solutions for both castellated and fitted grids show excellent agreement.

The distribution of turbulent kinetic energy across the same port diameter, shown in figure 6.9, are also in very good agreement with each other, again excluding F1. It is clear that the different annulus flow history of F1 compared to the rest of the calculations has resulted in a significant reduction of the level of turbulence in the core of the jet. This is another factor influencing the core flow field which could further explain the reduction in core recirculation size of this calculation. Toward the edges of the port the k distribution for each prediction is quite similar as would be expected due to the imposed "wall" boundary conditions.

A better understanding of velocity distribution across the port diameter can be seen by presenting contour plots of each component over the port exit plane. These are presented in figure 6.10 for both C2 and F2, at which level the solution, on current evidence, is easily grid independent. The most striking difference between the castellated and fitted solutions is not surprisingly the presence of castellations in the contour levels close to the perimeter of the port. These unrealistic distributions rapidly disappear away from the port periphery to give very similar contour plots to the fitted solution. It is also noted that there is evidence of contour distortion around the computational corners of the fitted port, (at +/- 45° to the port's centre) where mesh distortion is at its highest. Away from the port perimeter not only are the distributions similar but so too are the absolute magnitudes. As was also seen in figure 6.8, the

castellated calculations predict a slightly higher radial velocity at the centre plane than the fitted ones. It is evident in the W velocity component contours that the velocity toward z=0 (the assumed symmetry plane through the port diameter) is higher in C2 than F2. One of the principle reasons for this is perhaps due to the tapering of the port. In a cylindrical polar mesh, azimuthal mesh planes taper in toward each other with decreasing radius. As z increases so too does this tapering effect; at z=0.01 of the port in this figure the taper angle reaches 11.6° (at the upstream and downstream edges there is no tapering when z=0.0). Because flow must pass tangentially over the walls defining the perimeter a funnelling effect will take place and the flow will be given a larger W component. Because of this effect the exit plane will also be slightly smaller than the inlet plane, but this is negligible over the relatively small thickness of this port. It is however the increased migration of flow toward the diameter of symmetry which results in a higher radial velocity for the castellated grid than for the fitted grids, which have parallel sided walls.

The final difference in the two types of port representation is the presence of increased U at the side of the fitted port. This could be due to the flow at the port exit plane experiencing the shearing action of the cross flow which is greatest at this point. Due to the nature of the unrealistic "jagged" boundary constraints of the castellated port this feature does not appear to develop. This could have some effect on the subsequent solution in terms of the strengths of the jet bound vortices for example.

All of the evidence based on the flow field and turbulence field indicates that mesh independent solutions are achieved at and above the second level of mesh density. Some difference is noted between the most refined castellated and fitted solutions, which are probably a result of differences in port exit characteristics brought about by differences in port representation. Different reasons may be advanced for the reduced accuracy of each of the two coarsest calculations. The shortfall of calculation C1 is that it poorly defines the port geometry, both in its description of the perimeter and actual open area. Calculation F1 however appears to suffer from increased numerical error due to mesh non-orthogonality. Care must therefore be used when adopting either approach at low resolution and the best approach chosen dependent upon what aspect of the flow is being considered. However, although the fitted approach does not affect

the grid density required for numerical accuracy it reduces the local errors due to the castellations. Therefore at reasonable grid densities the port-fitted mesh approach is preferable.

6.2.3 Global Parameters

Two parameters have been chosen in an attempt to summarise each solution at a global, performance level. The first is the discharge coefficient, a familiar experimental parameter, based upon the pressure difference across the liner wall. The method of evaluating C_d from computational results is dealt with later in section 6.3.2. The second parameter is the loss of total pressure due to turbulence generation which can also be evaluated from the data provided by CFD. Little(1993) has described how this turbulence-production related loss can be related to the overall pressure loss found in diffusers. Mechanical energy is lost as the fluid passes through the solution domain via the action of viscous and turbulent stresses (at high Re the second will obviously dominate). The work done by the mean flow against the turbulent stresses is also the energy transferred from the mean flow to the turbulent motion, i.e. the rate of production of turbulent kinetic energy. Thus the total loss of mechanical energy (total pressure) due to turbulence generation may be evaluated from;

$$\lambda = \int_{volume} \left(-\overline{\rho u_i u_j} \frac{\partial U_i}{\partial x_j} \right) dV$$

where the volume is that of the whole solution domain.

The effect of increasing the grid resolution on these parameters can be seen in figure 6.11. Although the predicted C_d of the castellated solutions is lower than those of the fitted it would appear that the two highest resolution calculations are in good agreement. The flatter nature of C_d for all of the fitted solutions is strong evidence that the fitted approach is better if there is any doubt over grid independence of the solution, particularly when interest is upon the predicted value of C_d - and consequent flow splits. This trend is again echoed in the loss parameter. The highest resolved calculations of each method are in good agreement but so too are the absolute values of

loss for the castellated and fitted methods, indicating convergence toward a common value.

All of the predictions reported so far have been calculated using Hybrid differencing. The dashed lines in figure 6.11 represent the same six calculations repeated with QUICK differencing for the velocity field. QUICK differencing has a higher order accuracy than Hybrid but is less robust. Any difference between solutions using QUICK and Hybrid are thus indicative of the presence of numerical error in the Hybrid solution at least. The QUICK predictions have not been reported at the detailed level since very little difference was observed in either the velocity or turbulence field compared with those of the Hybrid calculations reported. This is supported by the similarity of values of loss and C_d for each mesh. The most significant difference being that QUICK differencing predicted C_d's of around 1-2% higher than those of Hybrid. Because Hybrid differencing is more robust than QUICK and values of C_d were predicted more accurately with Hybrid it was chosen for all subsequent calculations.

Despite some initial confusion over grid independence when looking at centre-line distributions of axial velocity, a more detailed look at the flow field, jet characteristics and global parameters have all given a clear indication that the second level of resolution (C2/F2) is adequate to ensure numerical accuracy in this instance. It seems then of order 10^5 cells with of order 300 cells in the port will produce results which are grid independent.

6.3 Prediction of Discharge Coefficients

One of the characteristics used in the previous section to ascertain whether a solution was grid independent or not was the discharge coefficient. It has been previously discussed in chapter 3 how C_d has been evaluated experimentally. No open literature, however, discusses how C_d should be evaluated from CFD solutions in which discrete information of primitive variables over the whole of the solution domain is available.

This section thus describes a test problem which was set up to answer three fundamental questions:

- How should C_d be evaluated for a given port?

- How sensitive is C_d to changes in port geometry definition? This is important as it justifies whether the additional effort of describing port features such as chutes is worthwhile.

- If more than one port is included in a domain can the flow split between them be predicted? Moreover, will the effects of changing port geometry be detectable in terms of flow split changes brought about by the resultant C_d change?

The second and third points are related: if the ratio of C_d between each port is accurately predicted then it would be expected that the flow split through each would also be. Answering these questions will provide confidence in subsequent predictions in which flows for different ports are being compared, and also where multiple ports are present in a solution.

6.3.1 C_d Prediction Test Problem

In order to address the questions raised on the prediction of C_d and flow splits, a simple test problem was devised. The geometry of this test problem is shown in Figure 6.12 and consists of parallel annulus and core flows in a plane rectangular (rather than a cylindrical) geometry. This geometry was chosen principally to avoid the slow convergence due to the presence of a centre line as seen in the grid refinement section. The axial velocities of the air entering the annulus and core regions were set to 40.0 and 12.0 m/s respectively, and a small bleed flow of 5.0 m/s was also specified at exit to the annulus. At the exit to the core, a zero gradient boundary condition was imposed on all solution variables normal to the exit plane, allowing an exit velocity profile to develop. The liner surfaces and the outer annulus casing were defined as walls with no slip (wall function) conditions, and the remaining 3 bounding surfaces of the computational domain were defined to be symmetry planes as indicated in Figure 6.12.

The annulus flow can enter the core flow via two rows of circular ports in the liner with diameters chosen to give the hole plan areas as shown in Figure 6.12. Initially both ports are represented by plain holes and calculations are carried out for this geometry with the boundary conditions described above. Subsequently a chuted hole was

substituted for the plain hole of the upstream port. The chute used had a depth of 0.75 hole diameters, a thickness of 2mm, an inlet radius of 2mm and an exit plane angle, α, of 15 degrees. Using the same boundary conditions as above, the calculations were repeated to investigate the change in flow split between the ports (caused by the change in discharge coefficient of the upstream port), changes in the flow and turbulence field etc. To carry out this illustrative comparison a mesh of 60×40×30 nodes in the ξ, η and ζ directions was used. Within this mesh 10×11 nodes were used in the plane of the first port opening and 5×6 nodes resolve the second, fixed port. These port resolutions were chosen to be comparable to those used in typical combustor flow calculations.

6.3.2 Evaluation Of C_d

Figure 6.13 shows the pressure coefficient distribution around the plain port ($C_p = (p_{ann} - p) / (0.5 \rho U_{ann}^2)$). It can be seen that apart from the pressure gradient region across the port and the impingement region where some pressure is recovered, the pressure field is quite uniform. To calculate the C_d for each port the pressure difference across the liner was evaluated. This was done by calculating the mass weighted total pressure in the annulus, P_a, and the mass weighted static pressure in the core, p_c, half a port diameter upstream of the port. The ideal mass flow through each port could then be calculated from; $m_i = A_h \sqrt{2 \rho (P_a - p_c)}$. By comparing this with the actual mass flow through the port its discharge coefficient was then obtained via; $C_d = \dot{m}_a / \dot{m}_i$. The actual jet mass flow, m_a, was deduced by evaluating the difference in mass flow in the annulus upstream and downstream of the port. Calculating the jet mass flow by integrating over the port area was not as accurate, particularly when the port is resolved only by a few tens of mesh cells where velocity gradients will be quite high. The method described here to evaluate C_d is not the only method tried, but was chosen for two reasons; firstly it provides the quantities required with best accuracy and secondly is consistent with the theory behind the experimental procedures used to evaluate the same quantities.

Two other methods were investigated for evaluating C_d which attempted to exploit the information available within a computational solution. The first method was an

attempt to link the total pressure loss parameter (calculated by the method described in section 6.2.3) to C_d via some relationship. This approach was discarded because the port flow region was not the only loss generating mechanism in the flow field - others being impingement and upstream recirculation for example. For the flow scenario here this method would therefore be difficult to adopt. For a more fundamental, perhaps axis-symmetric, study of port flows this method could be developed and help investigate the loss mechanisms in greater detail.

The final method considered was to compare directly the pressure difference across the liner (evaluated as described above) with the mass weighted dynamic pressure in the jet, q_j. From the standard definition of C_d and continuity across the port:

$$C_d = \frac{\dot{m}_a}{A_h\sqrt{2\rho\,(P_a - P_c)}} \qquad \dot{m}_a = \rho A_h V_j$$

we can rearrange to get;

$$C_d^2 = \frac{\frac{1}{2}\rho V_j^2}{(P_a - P_c)} = \frac{q_j}{(P_a - P_c)}$$

Two problems were encountered with this approach. With the coarse representation of the port in this instance some doubt was placed on the accuracy of evaluating q_j, as already mentioned above in the context of evaluating the jet mass flow rate. However, even assuming that the mesh density was high enough to describe the velocity profile issuing through the port, thus allowing the mass weighted dynamic pressure to be evaluated accurately, it is questionable as to whether q_j should be evaluated at the port exit, or at the vena contracta. As figure 6.13 shows, the strong pressure gradient through the port extends well into the core, continuing to accelerate the flow. It would therefore be expected that the highest q_j would be seen at the vena contracta where the jet velocities are highest. Evaluation of the jet's stream tube (the surface formed by joining particle traces released around the port perimeter) becomes a problem, along with evaluation of q_j across its minimum cross-sectional area. The area ratio between the vena contracta and the port would also remain in the above equation since they are not equal and do not cancel in the re-arrangement.

Whilst these two alternative methods of evaluating C_d have not been developed further, they may prove useful in more fundamental studies of axis-symmetric flow through ports. The conventional method of evaluation adopted here and in subsequent analysis does nothing to help understand the differences in C_d between various types of port, but only helps us identify which will have the highest mass flow for a given pressure drop. With the absence of cross and bleed flows in more fundamental studies, evaluation of the required parameters would be more straightforward and could throw further light on the flow physics.

6.3.3 Test Problem Results

Figure 6.14 visualises the flow patterns obtained for the plain and chuted port designs using particle paths and focusing attention on the vicinity of the upstream port. Noticeable changes have been brought about in the jet trajectory with more vertical jet penetration resulting from the chuted design, as expected. This leads of course to a stronger impingement process and therefore an enlarged upstream penetration of the fluid. For the conditions chosen, only a small upstream vortex is obtained, (because the jets represent a smaller blockage to the crossflow than in other geometries considered in this thesis) but this has increased in both axial and vertical extent with the chuted port. The vena-contracta effect is also more visible in the plain hole than with the chuted geometry.

Quantitative assessment of the changed flow pattern is given in Figures 6.15 and 6.16 in terms of impingement plane profiles of axial velocity and turbulence energy immediately below the port entry locations, both profiles being non-dimensionalised with the entry core flow bulk velocity, $\overline{U}_c$. The upstream shift of the recirculation zone ahead of jet impingement for the chuted port can be clearly seen, with the zero velocity location lying almost exactly on the port geometrical axis, providing further evidence of the improved vertical jet trajectory This change in jet trajectory has had an influence on the flow throughout the entire solution domain, and, because it also influences the flow split between the holes (as shown below in Table 6.2), it clearly changes the flow pattern in the vicinity of the second port quite dramatically. The stronger impingement of the chuted port increases the turbulence level generated, as well as shifting this

upstream (see Figure 6.16), and the changed trajectory of the second jet has reduced its strength of impingement and hence associated turbulence production by a factor of around 2.

A comparison of bulk flow properties between the two test cases can be seen in Table 6.2 below. The predicted discharge coefficient increases by 15% from 0.67 to 0.77 on changing from a plain to a chuted design. The latter is in excellent agreement with the experimental correlation given in Lefebvre (1983) for plunged holes but the plain hole C_d is over predicted by some 15%. This is probably due to the presence of a vena-contracta effect in the plain hole flow pattern which influences the C_d value strongly; this has been noted by Wittig (1994) to be under-predicted by the k-ε turbulence model. The increase in C_d is accompanied by a shift of mass flow to the first row of holes from the second and this leads to an increase in the effective jet/cross flow ratio $(\overline{V}_j / \overline{U}_c)$ from 7.31 to 7.53. The pressure loss parameter $(\Delta p^* = (P_a-p_c)/P_a)$ across the liner is also reduced by some 14% by moving to a chuted geometry. Finally, the mean jet angle averaged over the whole port area goes up from $76°$ to $89°$. The mean jet exit angle for the plain port is in close agreement with the value of $72°$ obtained from the experimental correlation given in Adkins et al. (1986), though no equivalent correlation is yet available for chuted ports.

Parameter	Plain Port	Chuted port
C_d (prediction)	0.67	0.77
C_d (Lefebvre (1983))	0.58	0.76
C_{d2} (Adkins (1986))	0.59	-
$\overline{V}_j / \overline{U}_c$	7.31	7.53
Δp^*	7.90%	6.63%
θ	$76°$	$89°$
θ (Adkins [1])	$72°$	-
C_{d2} (prediction)	0.71	0.69
C_{d2} (Lefebvre (1983))	0.62	0.62
C_{d2} (Adkins (1986))	0.62	0.62

Table 6.2 Bulk flow properties of test problem

N.B. subscript 2 refers to downstream port (fixed geometry)

The results of this test case show that the accuracy with which C_d is predicted depends on the port geometry. For a plain port the C_d is over predicted, by around 15%, whereas the chuted port C_d is predicted quite well. The over prediction of C_d for the plain port is also echoed for the downstream port (C_{d2} - a plain port in both cases) which is also over predicted by 14% and 11% respectively. The probable reason for this is that the coarseness of the port representation cannot resolve the details of the separation at the entry to the sharp edged, plain port (forming the vena contracta). The chuted port however has inlet radiusing and the unresolved separation is not such a significant feature of the actual flow. In changing from a plain to chuted port however, even at this coarse port representation, the expected increase in C_d has been predicted.

6.4 Datum Flow

To provide data for a direct comparison between experimental and computational results several predictions were performed for the geometry and flow conditions corresponding to those performed with the test facility. As in the grid refinement study in section 6.2 only a thirty degree sector of the rig geometry was modelled, figure 6.17(a). An azimuthal symmetry plane was thus imposed through the centre of the jet and through the plane between jets. Boundary conditions identical to those shown in figure 6.1 were used except that the inlet flow conditions were taken from experimental measurements, shown in figure 6.17(b), and were imposed axis-symmetrically on the inlet plane. A uniform annulus exit velocity was used to give a 50% annulus bleed flow, and a zero gradient condition was imposed on the core exit to allow radial variation of flow properties exiting this plane. The experimental 'datum configuration' was thus matched as closely as possible.

A grid density similar to F2 in table 6.1 was chosen, beyond which no benefit was seen in moving to a mesh of higher resolution. The number of mesh lines in the radial direction(nj) was increased from 40 to 50 to reduce to some extent the high cell aspect ratio near the centre line. The resultant mesh can be seen in figure 6.18. Stretching functions can be seen to be used to good effect to ensure high mesh density in the port region with 252 nodes in the port area, which has been enlarged for clarity. Hybrid discretisation was used because little difference was seen between the Hybrid and

QUICK schemes during the grid refinement stage and Hybrid had proved the most robust, whilst also giving a better prediction of the port C_d.

The predicted velocity vectors on the symmetry plane through the port centre line are shown in figure 6.19. The vectors are plotted at each cell centre on this plane and it is clear a large amount of information is available from the CFD prediction. On the whole the prediction appears to agree reasonably well with the measurements, presented in a comparable form in figure 3.16. There are three principle differences in the velocity field which are obvious from a careful comparison of these two figures. The first is the nature of the separation region in the annulus from the outer annulus wall; the predicted separation point is 0.75 port diameters further upstream than measured. Despite this, the reattachment points are both at around 1.5 port diameters downstream. The second noticeable point is the absence of flow separation at the front edge of the port. The measurements indicate reverse flow entering the front edge of the port because of this, but no evidence of this is seen in the prediction, only a reduction in velocity. Low resolution of the mesh in this region is to blame for this. Prohibitive memory requirements prevent this required dramatic increase in mesh size being used to resolve this type of flow feature. Adaptive grid, multi-grid or multi-block grid methods could, however, prove useful in relieving this problem typical of single-block, structured grid practice. The final observable difference is in the size of the core recirculation. Both the axial and radial extent of the recirculation is predicted to be smaller than that measured. Probable reasons for the disparity in core size will become apparent as additional information is presented, but likely to be the result of several contributory factors, rather than any singular cause.

Figure 6.20 (a) to (d) shows the predicted turbulence field. The turbulent kinetic energy shown in figure 6.20(a) may be compared with the experimental distribution shown in figure 3.17. Features such as the low turbulence in the jet core can not be resolved on the measurement mesh, but on the whole, by comparing these figures it is seen the distribution of turbulence is reasonably well predicted except near jet impingement. The absolute levels of turbulent kinetic energy in the annulus match quite accurately, but, despite a good prediction of the core distribution, the absolute levels of k/U_c^2 are around half of the measured values. One explanation for this is that

the core contains all of the features which the k-ε turbulence model is generally accepted to be poor at predicting, i.e. highly curved, recirculating and impinging flow. Additionally, it was shown experimentally that the turbulence field contained a significant contribution associated with switching between two states of a bi-modal flow around the recirculation, which a steady-state k-ε model has no mechanism for describing this type of behaviour. The Boussinesq relationship (eq. 4.10) has been used to evaluate the normal stresses from the turbulence and velocity fields, and figures 6.20(b) to (d) show these. The comparative experimental measurements can be seen in figure 3.6 for the core and figure 6.12 for the annulus. Each of the normal stresses is under-predicted by a factor of around 2 to 3 in the core, consistent with the under-predicted turbulent kinetic energy. Clearly we are seeing that the computational methodology has several shortfalls in predicting the core flow physics, in particular the nature of the turbulence.

The velocity vectors presented in figure 6.19 are not the most convenient means for comparing the velocity field on the symmetry plane with those found experimentally. Particle tracks calculated through the predicted and measured flow fields enable easier comparison and are given in figure 6.21. The discrepancies between the core and annulus recirculations previously pointed out are highlighted to better effect here. The core recirculation is clearly seen to be under-predicted in size, both axially and radially. Both prediction and measurement indicate the impingement at around 13mm. Of more importance here though is the nature of the annulus flow fields. It is clear that the CFD model has predicted an annulus flow mode (as discussed in chapter 3.3) different to that measured. Looking at the velocity field in this way has hopefully shown why comparing velocity component profiles at each measurement location is not the most convenient way of validating the computational results, and has to be approached with some care.

To compare absolute magnitudes in velocity two axial locations have been chosen which highlight the region in which disparity between the measured and predicted recirculation sizes originates. Figure 6.22 shows the non-dimensional axial and radial velocity components along radial lines at x=+/-5mm on the symmetry plane. Considering only the annulus first, the radial and axial velocities are very well

predicted, excluding the axial velocity close to the outer wall. The prediction shows the flow is very close to separation from the outer wall at this point. Experimentation suggests this is not the case, and by x=5mm the difference has grown, and both axial and radial velocities are significantly different across much of the annulus. In the core it is clear that the radial velocity issuing from the port is under predicted at both x=-5 and 5mm. This is seen to have a large effect on the axial velocity close to the centre line for both axial locations. The core radial velocities measured at radii close to the inner wall will have some error associated with them, because at these locations data rates were low due to high levels of refraction and reflection. When the optical orientation of the laser has been optimised to measure radial velocity at port exit, the measured velocities are slightly lower bringing them into better agreement with those predicted, as shown in the next figure. However, the through port velocities are under predicted, which is consistent with the finding that the predicted impingement strength is weaker than measured.

On the whole it is apparent that CFD has predicted all of the large scale features of this flow problem, however on closer inspection, detailed but significant differences occur between the measurements and the prediction. One of the motivations of this work is to improve the representation of the jet entry profiles to the core, thus with significant differences between the prediction and the measurements, the question arises how well are the port exit conditions predicted, and can these be to blame for the poor core predictions. The distribution of each velocity component exiting from the port are presented in figure 6.23(a). Each measured component is indicated by separate symbols, and the predicted profiles are indicated by the solid lines. Agreement between predicted and experimental values is good enough that the individual predicted velocity components do not need distinguishing explicitly. The diameter across which the profiles are plotted is coincident with the symmetry plane through the centre of the port. The W velocity component is everywhere zero due to the imposed boundary conditions (the velocity normal to the symmetry plane is set to zero). Confirmation that this is a valid boundary condition is supported by the experimental measurements which are also zero. The distribution of axial and radial velocity over the back of the port is particularly well predicted, and this is echoed by the resultant flow angle distribution, shown in figure 6.23(b). Over the front half of the port the lack

of a predicted separation at the front edge appears to have had significant effect. The axial velocity component is under-predicted, and the obvious shear layer in the radial velocity profile has not been resolved. The injection angle over the front of the port is thus over predicted by $4°$. It is also clear that the radial velocity is also under-predicted over most of the diameter. This suggests that the predicted effective flow area through the port is larger than in actuality, supported in this plane because the separation is predicted to be smaller. Thus the peak velocity will be closer to the velocity averaged over the whole port area in the prediction. Encouragingly though the C_d evaluated from the prediction is 0.648, just over 1% of that measured for the same case, 0.639.

Figure 6.24 shows the axial velocity distribution on the axial planes x=10 and -10mm in the annulus. These have been mirrored about $\theta=0°$ for clarity and easier comparison with figure 3.13. The axial velocity distribution is predicted quite well upstream of the port at x=-10mm. One disparity between the prediction and experimental results is that the prediction shows the boundary layer near the outer wall is largest over the port - decreasing in thickness between ports (compare regions enclosed by $U/U_c=2.5$). Experimental evidence in figure 3.13 suggests the opposite to this, the boundary layers being thickest between ports. This could explain why the change from the high bleed flow mode to low bleed flow mode is predicted to occur just above 50% bleed, rather than just below as suggested by the experimental evidence. Without detailed boundary layer measurements and pressure field mapping it is difficult to explain or understand these differences. Higher peak velocities are also predicted at the very upstream edge of the port, $U/U_c=5.5$ compared with 4.5. Downstream of the port at x=10mm, the stronger predicted back flow into the port is quite evident (unshaded region), with axial velocity an order of magnitude greater. The separation on the outer wall is also predicted to be much larger in extent. It would appear that with the increased thickness of the boundary layer upstream and in-line with the port the size of the separation has been over-predicted. As a result of this the port is no longer fed completely from flow entering from upstream in the annulus. High negative axial velocities at the inner wall close to the rear of the port indicate where the deficit in feed is made up from. Generalising these effects it could be considered that ratio of radial to azimuthal influence of the port on the annulus flow is over predicted.

Investigation of the solution so far has been via comparison with experimental results. CFD analysis allows a better understanding of the flow pattern to be obtained than by typical experimental presentation alone. One example, which is of use here, is the ability to calculate particle tracks through the solution. 3D flow predictions can be difficult to interpret unless visualised interactively at a work station. However, the two views supplied in figure 6.25 present enough information to interpret the shape of the particle tracks predicted for the annulus flow. These particles have been released 0.5mm above the port perimeter and traced back along their route in the annulus from each point. The surface which could be formed by joining the neighbouring tracks can also be imagined. This surface is comparable to that sketched from flow visualisation in figure 3.27(b) of the perceived mean stream tube entering the port. The slight difference between the flow topologies is that in the prediction the kidney shaped catchment region on the inlet plane touches the outer annulus wall. Some of the flow entering the rear of the port must therefore enter from the recirculation behind the port. It is at this condition where the flow pattern changes from that of 3.27(b) to that of 3.27(c), when the recirculation on the outer annulus grows as large as possible in the radial sense and begins to feed the rear of the port.

6.5 Dilution Flow

Experimentally it has been shown that the dilution flow is characteristically different to primary port flow in both the core and annulus. In this respect the dilution configuration deserves attention to determine if CFD can predict the fundamentally different flow scenario any better or worse. The importance of this question is that most full combustor calculations will contain both types of port, if one is inaccurately predicted then the resultant flow split will be incorrect. However the C_d of each port could be wrongly predicted, but providing it is by the same amount for each port, the flow split will still be correct.

The velocity vectors for the dilution configuration are presented in figure 6.26. Looking back to figures 3.18 and 3.21 allows comparison with experimental results for the core and annulus respectively. Reasonable agreement can be observed; similar jet deflection, entrainment into the lee of the jet and distribution of reverse flow in the

annulus. Evidence that separation at the front lip of the port is being resolved can also be seen (this will be looked at in more detail later). Perhaps the most significant difference is where jet mixing occurs in the downstream region of the core. Experimentally it is observed that at x=90mm the jet velocity core has disappeared and the axial velocity at the centre line is constant out to a radius of around 10mm. In the prediction however the core flow passing along the centre line has not been accelerated to the same extent, with an obvious velocity deficit toward the centre line. Again this could be due to problems mentioned previously with the mesh properties close to the centre line.

The predicted turbulence field can be seen in figure 6.27. Comparing with the two experimental results, figures 3.20 and 3.22, shows similar trends to the datum flow. The distribution in both the core and annulus appear to be well predicted, but the absolute levels in the core are predicted to be about half of those measured. In contrast, in the regions where it was seen experimentally that the momentum of the jet was mixing with the flow along the centre line, similar or higher levels of k are seen. Around the port entry turbulence levels, measured and predicted, agree well. Whether this implies the jet turbulence levels are well predicted will be seen in the next section of this chapter when port shape effects are considered.

Direct comparison is shown in figure 6.28 of particle tracks calculated from the prediction with those calculated from experimental results. The experimentally observed change in annulus flow mode is also observed in the prediction. Differences in the shape of the recirculation into the rear of the port could be simply due to the reduced resolution of the experimental results (especially in the axial sense). One feature which appears to be accurately predicted is the entry point to the port at which the fluid from up and downstream in the annulus meet, at about x=2.5mm. In the core the jet trajectories agree well, though the upstream edge of the measured jet is slightly further downstream in the core. This is due to a larger than predicted separation from the front lip of the port.

Figure 6.29 presents the axial and radial velocities over the same radial lines as for the datum case given in figure 6.22. In the annulus the prediction and measurements are in

close agreement. However, as with the datum prediction, the velocities in the core are poorly predicted particularly around the influence of the jet. Some concern may be cast over the radial velocity measurements in the last 5% of the core radius due to the significant beam distortion experienced. Although radial and velocity corrections have been made to account for this (via the use of the ray tracing algorithm described in section 2.4.2) no correction for the azimuthal position can be made. Away from this region of concern, the largest disagreement between prediction and measurement is in the U distribution at x=5mm between 15<r<30mm. It would appear that the region of shear at the upstream extent of the jet is underpredicted, as indicated by the velocity gradient in this orientation, $\frac{\partial U}{\partial r}$. It would be tempting to blame this on the turbulence model however the next figure shows it to be more likely to be due to the poor prediction of the jet entry profiles.

A comparison of the predicted jet exit profiles with measurements optimised to capture this region of the flow with minimum error is given in figure 6.30. The predicted V profile is not dissimilar to the predicted primary jet profile (figure 6.23). The measurements however show that a quite different jet profile should be expected. The predicted shear at the front of the port is much less than the measurements suggest - *explaining why the levels of shear* at the upstream edge of the jet within the core are also underpredicted. Neither is the characteristic peak in radial velocity predicted at the rear of the port. The trends in the axial velocity distribution are followed by the prediction, but like the primary configuration, they are much less pronounced. Despite the poor prediction of velocity components over much of the port, the flow angle entering the core is quite well predicted, excepting the rear quarter of the port. It is easy to be over critical of the predicted jet profiles at this stage, but it must be remembered what the alternatives are. Compared to adopting mass averaged values of U and V for the jet in a prediction of the core flow only, this coupled prediction shows a much better representation of the jet characteristics. To improve on the current situation experimental measurements would need to be made over the whole port area and then imposed on a mesh of at least comparable density as used here. This final option is against the ethos of this thesis, which hopes to provide information on how to *better model the port flow*, rather than rely upon measurements in difficult areas. The C_d calculated for this prediction is 0.715, representing an increase of 10% compared to

the primary configuration. This is quite large compared to the 2% experimental increase and 3% increase predicted by the Lefebvre (1983) correlation. This really reiterates the finding that the dilution jet characteristics are not as well predicted as the primary jets are. It may be expected from this result that in multi-port calculations flow splits would be over predicted for ports with the lowest bleed ratios, since the Cd would be over predicted.

Figure 6.31 shows the predicted axial velocity distributions in the annulus upstream and downstream of the port, which may be compared to the experimental equivalent in figure 3.24. The prediction has been again mirrored about $\theta=0^\circ$ for comparison. The prediction appears to over-predict the velocity into the front edge of the port, where the non-dimensionalised velocity, U/U_c, is 1.75, compared to the experimental value of 1.25. This is echoed at the rear of the port, where again the velocity at the edge is high. The shape of the region containing backflow at x=10mm is quite similar to that of the measurements, though the prediction shows that the flow is separated all the way around the outer wall, which is not quite the case from experimental evidence. Naturally the slight asymmetry observed in the measurements is not apparent.

The complex nature of the predicted annulus flow field is displayed in figure 6.32. The flow paths into the rear of the port are perhaps somewhat artificial since these are the *tracks of particles following the mean velocity field*, through a region of high turbulence intensity. However, combined with the primary annulus flow field in figure 6.25, the predictions support the results of flow visualisation and changes expected in flow topology that occur between these two levels of bleed in the annulus. The streamtube as described previously for figure 6.25 issuing backwards from the port perimeter describes a catchment region on the inlet plane which, with decreased bleed, is now bounded by the outer annulus wall. Because this catchment region is less than 80% of the inlet area (the proportion which will enter the port) flow must enter the port from outside of this catchment - resulting in the complex flow behind the port.

It would appear that the prediction of the primary and dilution flow configurations both suffer from deficiencies but in different areas. The mode of flow in the annulus of the primary setup was predicted to be different to observation (though this error may be

over emphasised since 50%bleed represents the condition at which the flow mode may change) and the turbulence levels in the core were substantially underpredicted. Again the turbulence in the core of the dilution configuration was under predicted but the annulus flow showed good agreement with measurement. The jet characteristics of the dilution case were badly predicted when compared to the primary case, and this was echoed in the predicted C_d. Because the accuracy of prediction is dependent upon the flow condition care must be taken when performing multi port calculations, such that flow splits match those expected.

Velocities into the very edge of the port were higher than measured for both primary and dilution flows, in what were otherwise well predicted annulus flow fields. This may explain the poor jet characteristics predicted to some extent. However the increased U momentum into the port would be expected to be seen at exit, but the U profiles at exit to the port are underpredicted compared to measurements. Although care was taken to ensure a mesh density was chosen to minimise numerical accuracy, it appears that in the port region higher mesh densities may be required. The mesh resolutions used, and higher, are however not practical for modelling of full combustor geometries. To model the port flow in coupled calculations the way forward will be to use one of or a combination of multi-block, multi-grid, adaptive or unstructured meshing techniques. With good prediction of the turbulence levels and distribution in the annulus the k-ε model appears to be adequate, but this is certainly not true in the core. The core flow field has not been focused on for this reason, with levels of k up to a factor of 4 under-predicted at impingement. The shortfalls of the k-ε closure for jets in confined crossflows are well documented so poor predictions may be expected.

6.6 Port Shape Effects

Inclusion of the port in the computational domain providing coupling of the internal and external aerodynamics has shown that the ability to predict C_d accurately depends upon the flow configuration. Some care is thus needed with multiple port calculations which have ports with different bleed ratios. Producing geometrically accurate ports within the mesh took a significant amount of work, as reported in the previous chapter,

but it needs to be asked whether this effort is rewarded with predicted differences in C_d for the ports? To answer this, table 6.3 below shows the predicted C_d for each port.

Port Shape	Plain		Chuted		D shaped	
flow condition	Primary	Dilution	Primary	Dilution	Primary	Dilution
C_d Prediction	.648	.715	.648	.724	.635	.737
C_d Measured	.639	.649	.812	.875	.647	.661
α Prediction	72.3°	79.5°	75.6°	79.6°	74.1°	74.8°

Table 6.3 Predicted Discharge Coefficients and Jet Exit Angle

It is clear that although the C_d is (overly) sensitive to flow condition, little difference is seen in C_d due to changes in port geometry. The chuted geometry stands out in particular, with a substantially underpredicted C_d for both flow conditions. This is contrary to the results of the test problem in section 6.3, in which C_d was predicted to increase due to the addition of a chute. The jet angle, α, (based on the mass flow averaged through port velocities) changes little between calculations, though this reflects the experimental results which showed each port had a similar exit angle distribution (see figure 3.38).

To establish why C_d for the chuted port is under-predicted compared to the experimental measurements requires a more detailed look at the flow properties within the port. In figure 6.33 the distributions of through-port velocity and turbulent kinetic energy are presented for each port shape on its exit plane with primary jet flow conditions. Clear similarities can be seen between the plain and D-shaped ports which both have peak velocities toward the rear and off-set from the centre plane, (z=0 plane) located at around (x,z)=(0.096m,0.005m). The region of peak velocity for the chuted port covers a larger area than the other two ports and the $V/V_j = -1.5$ contour passes through the symmetry plane. At the centre-rear of each port the local peak turbulence levels are similar, but is found to be slightly higher for the plain port. What may be considered the potential core of the jet is illustrated bounded by the first (unevenly spaced) contour level of $k/V_j^2 = 0.001$. Again this core has a similar nature for each of the ports, and is not necessarily associated with the highest radial velocity for each port. It is at the upstream edge of the port where the chuted port is most different from

the other two. The levels of turbulence in this region are 3-4 times greater for the chuted port than the other two. Looking at the radial velocity in this region all three ports exhibit similar amounts of reverse flow (positive radial velocity) indicating separation of the jet from the upstream inlet edge of the port. Experimentally however, it was seen that for the chuted port the radial velocity distribution was more evenly distributed over the plan of the port and the region of separation was much smaller than the other two ports. Because the discharge coefficient and the exit velocity distribution are inextricably linked, and each port has a similarly predicted velocity distribution then each will have a similarly predicted C_d. It would appear from this that the flow has not been accurately resolved in the upstream half of the chuted port which has led to an under-prediction of its discharge coefficient.

Additional port exit characteristics are shown in figure 6.34, namely the secondary velocity components and jet exit angle, $\alpha = \tan(V/U)$. Each of the figures 6.34 (a) to (c) use the same scale for vector length. By considering the shorter vectors in (b) it is clear that the effect of the chute is to reduce the magnitude of these secondary velocities (U,W). The net result of this is that the jet exits the chute more perpendicularly than for the other two ports, being around or over 80° for much of the port. What can also be seen is that the recirculating fluid around the front of the port moves around the outer perimeter of the port to be then entrained by the jet.

To better quantify the comparison between these predictions and the corresponding experimental results, figure 6.35 presents U/V_j, V/V_j and α across each port diameter coincident with the symmetry plane. In this figure the circles represent the experimental measurements and the lines show the corresponding CFD predictions. Considering the through port velocity first, some discrepancy is seen between the two data sets for each port. On this diameter V/V_j is slightly under-predicted for the rear three-quarters of both the plain and D-shaped port, but over-predicted for the chuted port. The plain and D-shaped ports were seen experimentally to have a region of reverse flow at the front of the port, indicated by negative V/V_j over x/r_{port} of -1.0 to around -0.7. The steep gradient, i.e. high shear stress, between this region and the core of the jet, $(V/V_j > 1.0)$ has been smeared by the predictions, indicating that the flow has not been fully resolved in this region. The effect of over prediction of velocity at

the front of the port is that the peak non-dimensionalised velocity rearwards is reduced (to satisfy continuity). Remembering that this is only one diameter of the port, the effects of this smearing accumulate over the full port area to result in an under-prediction in radial velocity of about 7% at the port centre-line.

Little difference is seen in the predicted distribution of V/V_j between the chuted port and the other two ports. However, it was seen experimentally that the reverse flow region at the front of the port was significantly reduced by the inclusion of a chute. This, in turn, produced a lower peak value of V/V_j, since with a more even through port (radial) velocity, V/V_j will become closer to a uniform value of 1.0 over the whole port. It is apparent that at the front of the port the effects of including the chute are not predicted, and the effect of over-predicting the reverse flow region in this case has a detrimental effect on the predicted flow through the remainder of the chuted port.

The axial velocity and exit flow angle (defined in figure 3.15(a)) is well predicted for the rear half of both the plain and D-shaped ports. However, the flow at the front of the port is not being properly resolved. In the grid refinement study no benefit was seen in increasing the number of nodes in the port from 260 (similar to that used here of 252) to 480. To resolve flow detail at the upstream edge of the port it is thus probable that the mesh density requires more than doubling. The only practical way of achieving this level of resolution is to move to an embedded grid method, or maybe a multi-grid method, which were unfortunately beyond the scope of this work.

Figure 6.36 which presents the turbulent kinetic energy across the same port diameter as the previous figure. Again for the plain and D-shaped ports the levels of k are comparatively well predicted over the rear three-quarters of the port, whereas it is grossly under-predicted in the region of high shear between the separated flow and the jet core. It was in this region that the shear layer had been smoothed out in the prediction, which has obviously led to an under prediction of k. This would suggest that the k-ϵ turbulence model may be adequate for modelling the port flow but the lack of resolution of the velocity gradients - as apparent in the previous figure - is to blame for the poor prediction of k at the front of the port.

In figure 3.37 experimental results were presented which were taken to see if changing the port shape had any effect on the approach flow in the annulus. Figure 6.37 thus presents the predicted flow fields associated with this experimental configuration of a dilution port flow scenario, R=2.0, B=50%. The results are presented slightly differently here, with the figures being split into velocity vectors and streamlines, rather than plain and D-shaped ports. This is done because only one half of the port has been modelled and it makes it easier to see the difference between the two predictions with the plain port results plotted using positive rθ, and D-shaped port results using negative rθ. The differences between the two predictions are quite small, though the reverse flow of the plain port penetrates slightly further upstream than for the D-shaped port. This echoes what was found experimentally, though the increased width of the upstream approach flow in this plane being captured by the D-shaped port over that of the plain port was not predicted. In other respects the predictions appear, from this evidence, to have captured the mean annulus flow field quite well.

Continuing the look at the flow in the annulus for the dilution flow configuration, figure 6.38 shows the axial velocity on the axial plane coincident with the rear of the port for the chuted and D-shaped ports (figure 6.31 presents the same information for the plain port). Again, comparing all three of these velocity distributions shows each flow pattern is quite similar. A slight difference which can be seen is the strength of reverse flow into the rear of the plain port is slightly higher than the other two. To compare these predictions with the experimental results figures 3.24, 3.35(a) and 3.35(b) need to be considered for the plain, chuted and D-shaped ports respectively. As with the comparison between experimental and predicted port exit profiles, it can be seen that there is good agreement of the measured axial velocity distribution for the plain and D-shaped port, but for the chuted port do not match as closely. Principally the reverse flow into the chuted port is predicted to be similar in nature to the other two ports, but in practice it is much reduced. Because this flow feeds the port it probably contributes to the poorer prediction of jet characteristics for the chuted port over the other two. It is hard to determine the cause of this discrepancy, but it is suspected that the inlet radiusing to the chuted port is not being well resolved. It is this radiusing which allows more of the upstream flow to be directly swallowed by the port and also help prevent the flow separation, thus reducing the reverse flow region in the exit plane

of the port. A poorly resolved inlet radius may therefore influence both of these inter-related features.

To complete the picture of the effects of port description within each prediction, the resultant velocity field and turbulence field on the $\theta=0^\circ$ plane are given for the D-shaped and chuted ports with a primary port like flow condition. (For the plain port these are given in figures 6.19 and 6.20(a) respectively.) Not surprisingly the resultant core flow fields are quite similar for each of the three port shapes, particularly when considering the similarities seen between each of the port exit profiles. In particular, the size and position of the core upstream recirculation (shaded next to the centre-line) is virtually the same for each prediction. The biggest differences occur in the D-shaped port prediction when compared to the plain and chuted port. Firstly the region of reverse flow into the port from the annulus is reduced for the D-shaped port where it is seen that the separation region on the outer annulus wall is not connected to the reverse flow region on the inner wall, as it is in the other two cases. At around a bleed ratio of 50% it was seen experimentally to be the point at which flow modes in the annulus changed for the plain port (see section 3.4). It is suggested by this calculation that changing the port shape affects the bleed ratio at which the flow mode changes from that where the outer annulus separation interacts with the port flow (figure 3.38 (b)) to that where it does not (figure 3.38(a)). This predicted change in flow mode does not appear to have a significant (predicted) effect on the port exit characteristics when considering the similarities between the plain and D-shaped ports as presented in figures 6.33-6.36. However, the increased backflow into the plain port may explain why it has a higher peak value of turbulent kinetic energy ($k/V_j^2 = 0.059$) at the rear of the port compared to the D-shaped port ($k/V_j^2 = 0.034$). A similar reduction in k/V_j^2 was also measured experimentally and can be seen by looking back to figure 6.36(a) and (c).

Also of note in this comparison of the resultant flow for the three ports is the region of reverse flow in the wake of the jet as it issues into the core. For the D-shaped port this wake is much larger than that found behind the jet for either the chuted or plain ports. This is also accompanied by an increase in the levels of turbulence behind the jet as can be seen in figure 6.40, where levels of k/U_c^2 have almost doubled in this region

when changing from a chuted to D-shaped port. As discussed in section 3.5.3, distinct frequencies in the velocity spectra in the wake of the jet were measured experimentally for the D-shaped port but not for chuted or plain ports (Daly (1994)). This suggested a vortex shedding process was occurring off the rear of the jet, similar in nature to a vortex-street. Figure 6.41 illustrates how this is supported using evidence from the computational predictions presented here. In this figure streamlines are given which are forced to remain in the first computational plane away from the core liner wall by setting the perpendicular velocity component (principally radial) to zero. The velocity vectors on the plane defining the wall are given in order to indicate the port exit area, and the shapes of the plain circular port (a) and the D-shaped port (b) can clearly be seen (since the velocity on the wall is zero vectors are not seen around the port). A striking difference in the predicted core cross-flow can be seen. For the plain port a singularity can be seen in the lee of the jet which the cross-flow spirals in towards. This point represents the start of the centre of the bound vortex line, and through entrainment, fluid within this vortex is drawn radially inward with the jet. In the case of the D-shaped port a distinct "separation" occurs between the cross-flow and the rear corner of the "D" shaped jet. This fluid spirals back into the rear of the jet where it is then entrained. In this process, however, two forced vortices are formed (remembering this flow field is mirrored about the port centre-line) on each corner of the "D". This scenario is the classic starting point for the description of how Von-Karman vortex streets are formed behind cylinders (i.e. one vortex becomes dominant, enlarges and is shed, allowing the other to become dominant and a cyclic shedding of the vortices begins). Naturally in a time-averaged Reynolds-stress adaptation of the Navier-Stokes equations such time dependent behaviour cannot be resolved - especially when symmetry is imposed where, for a vortex street, it does not exist. However it is clear that with both the experimental evidence of strong periodicity in the azimuthal velocity component and the predicted flow field which will probably be periodic a vortex shedding mechanism is occurring.

Resolving the details of port geometry has had mixed success on the resultant predicted flow fields. Many of the predicted detailed flow features for the plain and D-shaped port agree with experimental evidence quite well. However, contrary to the results of the test problem in section 6.3.3, expected changes in the flow field for the

chuted port have not been seen (e.g. the increased C_d and decreased core recirculation size). These discrepancies have been attributed to poorly predicted port exit characteristics. In particular, the radial velocity through the chuted port was found experimentally to have an almost "top-hat" distribution. With low resolution of the port exit (as in the previous test problem) this type of distribution is easily represented. However with the increased resolution employed here, a smearing of the shear layers has occurred in the same way as it has for the plain and D-shaped ports.

6.7 Symmetry Constraints and Annulus Swirl

One common feature of many CFD predictions is the assumption of symmetry boundary conditions on certain planes. In most of the calculations reported so far in this chapter, only one twelfth of the full flow domain has been modelled by assuming planes of flow symmetry on azimuthal planes between ports and through port centre lines (coincident with geometrical symmetry). Evidence described in chapter 3 and that given in the preceding section showed that features appeared in the flow which did not satisfy these assumptions of symmetry, particularly in the port entry. Removing the planes of symmetry from the CFD predictions may therefore allow the predicted solution to exhibit flow features which would otherwise be suppressed. Cyclic conditions were not available within the flow solver employed, thus to avoid the need for symmetry conditions and also allow the introduction of an annulus swirl velocity component, a full $360°$ of the geometry was modelled. There were therefore two purposes to the investigation reported here; to look at the effect of removing imposed symmetry conditions and also to provide a comparison with the identical configuration except with swirl introduced into the annulus flow.

Initially it was attempted to model exactly the same geometry as that shown in figure 6.17, but it was difficult to generate a suitable grid. Figure 6.42 shows an axial section through this initial grid, coincident with each of the port's centre lines. There is significant grid distortion around each port, evident in this figure. Of more concern is the mis-alignment of the grid lines with the expected flow direction through the ports. This is of concern because numerical error can be shown to be greatest where the flow is not aligned with the grid line direction - particularly in the jet region where

velocities and gradients of flow properties are high. Secondly, the grid is symmetric about two diameters, whereas the geometry is symmetrical about 12 diametral lines (6 through port centre-lines and 6 bisecting the port centre-lines). This mis-match would result in the flow direction relative to the grid direction being different for each port. Numerical accuracy is affected by the orientation of the flow to the grid and thus the mis-match described may then be blamed as a cause of solutions which do not exhibit symmetry about the 12 planes expected. This is one of many examples of the limitations when fitting structured grids to complex geometries.

To avoid the problems outlined above the number of ports was reduced to 4, the geometry for which is shown in figure 6.43. This allowed a grid to be generated which was better suited than that generated for a geometry with six ports. Figure 6.44(a) shows the resultant surface mesh with one quarter section removed. It can be seen in figure 6.44(b) that the radially inward flowing jets will also be aligned with principle grid directions and that the grid has common lines of symmetry with the geometry. These two features make the grid much more suitable than the best structured grid which could have been fitted to a six-hole geometry. Interestingly, a more efficient use of the grid is possible within the core as the problems of high grid concentration at the centre line has been avoided, which is unavoidable with the previously used wedge-shaped domains. Excluding the ports, the regions of high mesh distortion are now isolated to where the corners of the computational mesh have been incorporated into the perimeters of the cylindrical walls. These distortions have been arranged to be between ports and thus away from areas of strong flow gradients, and away from where unsymmetric flow features may occur. Naturally the larger region being modelled here required some compromise with mesh resolution. Keeping the same mesh density as calculation F2 in section 6.2 would require somewhere between 8-12 times the number of mesh nodes which was prohibitive with available hardware. Port resolution was thus downgraded to be similar to that in calculation F1 (section 6.2) in which the port opening is now resolved by 80 (10*8) mesh nodes. Justification for this can be made since we are moving attention away from predicting the detailed nature of the port flow toward the resulting flow structures in the annulus with removal of symmetry, and then inclusion of annulus swirl.

Apart from the inclusion of annulus swirl, identical flow conditions were imposed on these two calculations, viz; a uniform core inlet velocity of 0.3m/s, an annulus inlet velocity of 0.204m/s and an annulus exit velocity of 0.00408m/s. These gave a jet to core flow velocity ratio of 4.0 and a bleed ratio of 2%. As observed experimentally, port vortices were most likely to occur at the lowest bleed ratios. A minimal level of bleed flow was chosen since with no bleed flow convergence was very slow in the near-stagnant region of the downstream annulus. A bleed ratio of 2% was thus chosen to ensure that conditions were favourable to produce possible flow asymmetries whilst ensuring a converged solution could be achieved. Results from these calculations are not directly comparable to any experimental measurements reported in chapter 3 due to the larger hole pitch to diameter ratio (no time was available for these measurements to be made).

Comparing the plots of velocity vectors on a diametral plane through two port centre lines for the calculations with and without annulus swirl, figure 6.45, shows a number of differences. At first inspection both calculations exhibit the same flow structures; jet impingement, core recirculation, jet entrainment, etc., consistent with those of previous calculations. However, two distinct differences can be observed in the core flow field. With the introduction of annulus swirl the size of the upstream recirculation has reduced and the axially deflected merged jet is more diffuse, this can be seen on the core exit plane as a less pronounced maximum axial velocity at the centre line and wider spread. These differences are consistent with the trends found experimentally, though the predicted reduction in the size of the core recirculation was not as pronounced. This is a clear indication that, in an otherwise identical calculation, swirl in the annulus can be predicted to have significant effect on the core flow. This is further confirmed in figure 6.46 in which the turbulent kinetic energy distribution on the same plane is presented. Experimentally it was seen that annulus swirl decreased the level of k/U_c^2 at impingement slightly, but here its level is not predicted to fall, and the region enclosed by the highest contour level has increased. Despite the experimentally found trends not being echoed in the turbulence field around impingement, it is significant that there is sensitivity of the core to annulus effects. Again, the poor agreement is likely to be due to the weaknesses of the k-ε turbulence closure as previously indicated in predicting the impingement region. In the lee of the

jets at their largest curvature, a near-stagnant region is accompanied by an increase in k/U_c^2 slightly downstream (this can be seen in figure 6.46 labelled A and B). This is in agreement with the experimental results, and indicates that away from impingement the turbulence model is adequate to represent the core flow.

To summarise the previous two figures, the centre line variation of axial velocity and turbulent kinetic energy are presented in figure 6.47. The distribution of U/U_c clearly shows the reduction in the size of the recirculation and reduced centre line velocity downsrteam of impingement with the inclusion of annulus swirl. The turbulence distribution only shows a notable difference due to the reduction in the size of the recirculation, with the maximum value at impingement being the same for both calculations.

It has been seen that annulus swirl has affected the flow prediction quite significantly. Because of the lack of experimental evidence for this geometry and the mesh resolution being lower than would be recommended for numerically accurate results in the light of the mesh refinement study, an in depth comparison has been avoided. However, what has not yet been considered is the effect of the removal of any planes of assumed symmetry within the solution domain. Figure 6.48 presents the secondary velocity vectors and radial vorticity contours for several mesh planes over one of the ports in a prediction in which no annulus swirl was present. The mesh planes are almost, but not quite, planes of constant radius within this region, thus the radius quoted for each plane is that at which the port centre line intersects the plane. On the five planes above the port (figure 6.48(a)-(e)) it is clear from the velocity vectors that a vortex is present at all radii through the annulus. From the accompanying radial vorticity plots it can be seen the level of vorticity associated with this vortex is also constant across the width of the annulus with its core at just below -60.0 rad s^{-1}. Upstream of the vortex the five vorticity contours appear symmetrical, when comparing the regions of $0<\Omega_r<20$ with $-20<\Omega_r<0$, though this symmetry is not present in the downstream annulus. Looking to the plane just below the port exit evidence of the vorticity is still present within the core of the jet, and noticing the change in scale, the eye of the vortex is still at the same level as within the annulus.

The regions of high vorticity in the lee of the jet are indicative of the bound vortices associated with a jet in cross flow.

The presence of this vortex is quite surprising, even though the flow conditions have been set to maximise the chance of observing one and also that they have been observed in practice. The geometry and imposed boundary conditions are symmetrical along with the governing equations, so what generates this vortex? It would appear that a symmetrical back flow from the annulus into the rear of the port is unstable, in much the same way as that of a separation and vortex structure behind a long cylinder. However, as the back flow from one side begins to dominate a self-stabilising flow structure occurs, unlike the cylinder in which it is well known a periodic oscillation is set up. The stabilising mechanism is not clear from available information but it is thought that a whole-scale circumferential skew in the flow downstream of the row of ports maintains this, and the other vortices, predicted over each of the ports. Moreover, since the net axial velocity in the downstream annulus is small, there is not a sufficient convective force of the cross-stream. The structure of the predicted vortices is however different to that observed during flow visualisation. What was described in figure 3.30 as the dominant vortex has seen to be predicted, however, the minor vortex which was seen to link neighbouring ports has not. This could be due to the increased pitch spacing between ports, but has brought about the result that each vortex in this prediction rotates in the same sense (all with negative radial vorticity).

Figure 6.49 presents exactly the same results for the case with annulus swirl introduced. The nature of the through port vortex, and its magnitude is very similar to the previous case with no swirl. This is strong evidence that the vortex is not due to any tiny amount of upstream swirl in the annulus. It can be seen that the flow fields with and without swirl are quite similar, but with the introduction of annulus swirl the flow field has been rotated with respect to the port centre line.

Table 6.4, below, shows the changes in the jet characteristics with the introduction of annulus swirl (refer back to figure 3.49 for a graphical definition of α and β).

Parameter	No Swirl	12° Swirl
C_d	0.724	0.722
$\alpha = \tan^{-1}(\overline{V_r}/\overline{U})$	82.05°	82.15°
$\beta = \tan^{-1}(\overline{V_r}/\overline{W_\theta})$	89.97°	87.63°

Table 6.4 C_d and Jet Exit Angles for Four Hole Geometry

The overbar on the velocities denotes in this instance the mass averaged velocity though the port, i.e.

$$\overline{U} = \frac{\int_{A_h} \rho V_r U \, dA}{\int_{A_h} \rho V_r \, dA}$$

etc. The trends shown in this table agree well with those found experimentally. The slight reduction in Cd is consistent with the 0.7-1.3% reduction observed experimentally (table 3.5). Similarly the change in predicted flow angles are consistent with the measured distributions across a port diameter given in figure 3.49(b). Over the measured diameter a skew from perpendicular injection of around 2-3° is seen, due to the 12° swirl component in the annulus.

In figure 6.50 the distribution of axial velocity is seen on the axial plane coincident with the rear of the four ports, at x=10mm. This figure is presented such that positive U is out of the page, and convention for positive annulus swirl velocity is in the anti-clockwise sense. The distortion of the core distribution of U due to the mis-aligned jets of the case with annulus swirl can clearly be seen when compared to the virtually symmetrical case with no swirl, particularly in the centre line region. Surprisingly the distributions in the annulus are quite similar. The reason for this is that in figure 6.50(a), with no annulus swirl, the predicted though port vortex has resulted in an unsymmetrical distribution of U which is very similar in nature to that observed with annulus swirl. Experimentally it was seen with a bleed of 20% that the distribution on this plane without annulus swirl was reasonably symmetrical (figure 3.24(b)), though towards the outer wall, the region of reverse flow was skewed to one side of the port,

much as seen here. With annulus swirl, measurements showed distributions behind the port to be significantly distorted (figure 3.46(b)), with the region of backflow being moved increasingly away from the port centre line with increasing radius.

The approximate location of one of the port vortices for each case has been marked with a V. For the case with no swirl this re-iterates that each vortex sits on the same side of each port and rotates in the same sense, unlike the experimentally found contra-rotating pairs of vortices.

With doubt over the ability of current CFD methods to accurately predict the core flow (due to low resolution and inadequacies of the k-ε model) and the lack of supporting experimental evidence for the four hole geometry, a detailed examination of this will not be considered. However, figure 6.51 shows the distribution of axial angular momentum flux though the core and annulus. For the case without annulus swirl it is interesting to note that a small amount of axial angular momentum is present in the downstream core, which is likely to be due to the through port vortices. The negative vorticity over each port indicates a clockwise vortex looking onto the ports, figure 3.8(a)). As these vortices are bent downstream by the core crossflow the rotational sense of each will become positive in the axial sense, explaining the significant angular momentum flux. Experimentally no momentum flux in the core exit was observed without annulus swirl. However, one reason for this is that the port vortices - though unsteady - were contra-rotating, thus as they were deflected downstream the opposite rotational sense of each would cancel.

With the introduction of annulus swirl it is apparent from figure 6.51 that all of the angular momentum is conserved as the flow passes through the port. The initial value agrees well with the analytically obtained value of $M_x=0.00408kgm^2s^{-2}$ from the imposed boundary conditions. The axial angular momentum then decays quite quickly in the downstream of the core, approximately 30% lost by x=0.1m. This could explain why a loss of 16% beyond that expected was seen in the experimental measurements, i.e. due to turbulent dissipation. Ikeda (1993) noted in predictions of confined swirl flow with interferential cross jets that the k-ε closure resulted in rapid swirl momentum decay, compared with both experiment and the Reynolds stress model.

In both cases, with and without annulus swirl, a common characteristic is the pronounced drop to similar levels of negative M_x at the rear of the port in the annulus. This would account for the skewing of the axial velocity distributions in the previous figure. This drop is then matched by an almost matched increase in the core. It is possible that this mechanism is related to the generation of the through port vortex, such that the overall angular momentum is conserved when taking into account all components.

6.8 Combustor Sector Model

6.8.1 Introduction

The conclusion of chapter 5 saw the development of two meshes (figures 5.13 and 5.14) which described the geometry of a sector of an actual combustor (similar to the one shown in figure 1.3). Based on the evidence from the grid refinement study of section 6.2 it is unlikely that the mesh resolution around the ports will be sufficient for the flow physics to be accurately predicted in these regions. However, the mesh size represents the largest which could be practically handled by the computational hardware at the time of this study. It is clear that in order to perform coupled internal/ external calculations some compromise has had to be made on the port mesh resolution. This is a situation which is constantly changing with the rapid development of computational hardware and numerically accurate predictions will soon be possible. Despite these limitations the meshes are of a density comparable to, or greater than, calculations on similar geometries which have been published in open literature or those which are performed in industry.

The purpose of the work reported in this section is to determine whether the computational methods described and developed for this study can predict changes due to the inclusion of port features (e.g. chutes) at contemporary mesh densities for typical combustor geometry. It had been observed in the past that predictions of this particular combustor geometry had produced unrealistic temperature exit profiles, Priddin (1995). Two areas of doubt over the model used were that chute features had not been resolved, nor was the internal flow prediction properly coupled to the external (annulus) flow.

An initial attempt to answer these questions proved unsatisfactory for a number of reasons, but the lessons learnt proved the importance of providing accurate descriptions of the boundary conditions to CFD models. The initial attempt used a model of only one half of a combustor sector. Planes of symmetry were thus assumed on planes through and between burner centre-lines. As a result of this, the swirl component of the air issuing from the airswirler around the burner head (see figure 1.3) could not be modelled and an unrealistic core flow field resulted. In addition it was discovered that the cooling rings upstream of each row of ports required modelling. Without extracting air through the rings they represented forward facing steps to the annulus flow. By looking back to figure 5.14 the steps can be seen downstream of the second row of ports on the top liner surface. These steps produced a separation region on the combustor liner immediately upstream of the ports, providing unrealistic port entry velocity profiles. Slots were thus introduced upstream of the ports, as can be seen in the close-up view in figure 5.14, to allow flow through the film cooling rings.

6.8.2 Boundary Conditions

The flow around the head of the combustor was not included in the calculation due to the desire to keep the mesh density as high as possible in the region of interest. Additionally, experimentally obtained velocity profiles were available at the inlet planes of this calculation, for the diffuser/combustor head geometry being modelled, Denman (1992). These velocity profiles are presented in figure 6.52 for each annulus. Airswirler characteristics were also available, Brocklehurst (1994), to allow it to be fully represented and this is shown in figure 6.52(b). A zero gradient exit plane from the core was applied to allow exit profiles to develop, whilst the annulus exit velocity was fixed to produce the flow splits discussed below. Planes between burners were assumed to be planes of symmetry, implying adjacent airswirlers were contra-rotating, which is not the case in practice. However, cyclic boundary conditions were not available in the employed flow solver and this compromise must be accepted. Justification for this can be made because we are comparing only the two resultant predictions with each other. The mass flow exiting from features along each annulus

was fixed to match the flow splits found at design conditions, which are given in the table below.

Feature	Actual splits % Design Flow	Modelled splits % Renormalised
Outboard 1st cooling ring	4.85	6.3
Outboard primary jet	8.62	[11.3]
Outboard 2ndcooling ring	3.75	4.7
Outboard dilution jet	10.52	[13.7]
Outboard ignored features	9.82	0
Outboard bleed flow	4.15	5.4
Inboard 1st cooling ring	3.35	4.3
Inboard primary jet	5.56	[7.3]
Inboard 2nd cooling ring	2.74	3.6
Inboard dilution jet	10.75	[14.0]
Inboard ignored features	7.8	0
Inboard bleed flow	3.91	5.1
Fuel injector air	18.91	24.3
Ignored head features	5.27	0
Totals	100%	100%

Table 6.5 Actual and Modelled Combustor Flow Splits (Boyce 1995)

Mass flow through features which were not modelled was ignored in the calculation and the final column presents the re-normalised flow splits. Accounting of the flow splits was done in this way to ensure a consistent pressure drop across the inner and outer combustor liner resulted. This practice developed during the preliminary study prevented the total pressure in the inner and outer annuli becoming significantly different since they are not directly connected within this computational domain. Bracketed values in the final column are those which were not fixed in the calculations reported here, since one aim of these predictions is to allow the mass flow splits through the rows of air admission ports to be determined. However, the mass flow through the cooling rings was fixed because they were poorly resolved (only one cell thick) and accurate prediction of the mass flow through them could not be expected. Despite poor representation of the cooling rings, their inclusion was important to ensure the velocity distribution in the annulus upstream of the port was adequately modelled.

6.8.3 Flow Splits

The table below shows the percentage of total combustor flow passing through each row of ports predicted for the plain port and chuted port geometry compared to those of the re-normalised design conditions.

Port	Design	Plain Ports	Chuted Ports
Inner Primary	7.3	5.5	5.1
Inner Dilution	14.0	16.8	16.2
Outer Primary	11.3	7.4	7.7
Outer Dilution	13.4	17.6	17.3

Table 6.6 Port Flow Splits as Percentage of Total Flow

Slight differences in flow splits can be seen between the two predictions, but these differences are small compared to the difference between each prediction and the design conditions: the calculation for each port geometry over-predicts the flow through the secondary ports and under predicts the flow through the primary ports. This anomaly can, however, be accounted to the absence of some of the annulus flow which would feed liner features downstream of the dilution ports which have not been modelled. The effect of removing this flow from each annulus is that each row of ports has a reduced bleed flow past it. Using the correlation presented in Lowe (1994) to predict the C_d for the actual compared to the renormalised flow condition of the outer annulus ports suggests a decrease in C_d of 21% for the secondary ports and a decrease of 9% for the primary ports due to the bleed increase. Because the mass flow through each port is proportional to its discharge coefficient, a shift of 12% of the combined port flows would be expected from the dilution to the primary ports: equivalent to 3.0% of the total combustor flow. The C_d correlation of Lowe(1994) only holds for plain ports, thus applying the above argument to the plain port prediction results in the estimated flow splits as given in the table below.

Port	Design	Plain Ports
Inner Primary	7.3	7.1*
Inner Dilution	14.0	14.2*
Outer Primary	11.3	10.4*
Outer Dilution	13.4	14.6*

Table 6.7 Flow Splits Accounting for Bleed Fraction Differences (*)

Clearly a much better agreement can be seen between the prediction and design conditions, when taking into account the bleed flow effect. A consequence of this effect of differences in actual and modelled bleed flows is that care must be taken in coupled calculations to include as many of the annulus exit flow features as possible in order to match the bleed fractions at each row of ports. Adding the ignored annulus flow to the annulus exit flow to address this problem was seen to give poor results in the preliminary studies of this section. In particular, this caused the predicted total pressure in each annulus to be significantly different. In practice a large total pressure difference cannot occur, but because the annuli are not directly connected in this calculation, and because of changes in modelled compared with actual flow splits, a different pressure loss in each annulus may occur.

A fairer comparison of the ability of CFD to predict flow splits between port rows in this case would therefore be to compare predicted port C_d s, as given in the table below.

Port	Lowe (1994)	Plain Ports	Chuted Ports
Inner Primary	0.601	0.657	0.669
Inner Dilution	0.594	0.652	0.756
Outer Primary	0.568	0.573	0.661
Outer Dilution	0.561	0.631	0.698

Table 6.8 Predicted Port Discharge Coefficients

Values of C_d given by the Lowe correlation may only be compared to those of the plain port calculation, since no effect of the chute is accounted for. However, the Lowe correlation has been applied using the same bleed fractions as obtained from the plain port calculation. The C_d of the inner annulus ports are both over predicted by 9% compared to Lowe's correlation. Because both are over-predicted by the same amount, it is found the correct flow split is obtained between the inner annulus ports as seen in table 6.6. In the outer annulus the primary port discharge coefficient is over predicted by only 0.9% whereas the dilution port is over predicted by 12.5%. This results in a bigger disparity between the actual and estimated splits for these ports as also seen in table 6.6, where more of the flow is predicted to pass though the dilution port. Obtaining the correct flow split from coupled calculations can therefore be seen not to

be dependent upon the C_d being accurately predicted, but that it is consistently over/ under-predicted for each port. Incorrect prediction of each C_d will naturally effect the liner pressure drop and probably the jet velocity profiles. However, because the accuracy with which the C_d can be predicted depends upon the resolution of the port - hence of the issuing jet - it could be argued the only way to improve the prediction of the jet is to increase the grid resolution to allow it to be better resolved. This suggests that even with detailed experimental measurements of each jet profile, the prediction of the core flow field could not be improved since the jet profile would be discretised onto the boundary grid with only the same coarse resolution. Considering that in these calculations the open area of the primary ports are resolved by 30 cells and the dilution ports by 36 it is surprising, given the results of the grid refinement study (section 6.2), that the discharge coefficients are as well predicted as they are. It is also clear that the effect of introducing chutes to the calculation has the expected effect of increasing the discharge coefficients of each port. Assessing the accuracy of these increased values is difficult though, because each chute is of slightly different geometry and no suitable correlations exist which predict them.

The final sequence of figures in this thesis present information on the resulting flow field through various planes of this calculation, with the plain port configuration prediction, (a), above the chuted port prediction, (b). The first of these, figure 6.53, shows the velocity vectors on the central azimuthal plane through the airswirler and two of the primary port centre-lines. Quite clearly, the predicted effect of the chute is immediately obvious: the jets conditioned by the chutes penetrate the internal field much more strongly forming a mutual impingement point, whereas the plain port jets are much more diffuse and are deflected downstream in the combustor.

The difference in the velocity field is not as distinct when moving to a plane through two of the secondary ports as shown in figure 6.54. Here the flows are quite similar, but detail can be identified which supports the trends in predicted C_d's. Looking at the direction of the velocity vectors downstream of the impingement point shows that with chutes the flow is roughly directed toward the mid-radius of the exit plane. In the plain calculation they are more directed toward the inner radius. This is consistent with the comparative increase in predicted C_d of the inner port when adding a chute to that of

the outer port. A relatively stronger inner jet would have the result as seen, deflecting the flow from impingement out to a larger radius.

The increased strength and penetration of the chuted port over the plain ones is further seen in figure 6.55 showing the resultant turbulence fields. For the secondary ports turbulence near impingement has been increased by around 50% on this central plane through the centre-line of the primary ports. Indeed without chutes the impingement of the primary ports has not been predicted at all, resulting in a threefold decrease in predicted turbulent kinetic energy. The overall effect of the increased turbulence predicted for the chuted ports would be to increase mixing within the combustor. Calculations with additional ports port features resolved can therefore predict changes in the levels of mixing occurring within the combustor even with what may be considered a low density mesh in the port region.

An alternative way of assessing the influence of the chutes on the calculation is to look at a property of the combustor exit plane. Indeed part of the motivation of this work was to understand if improving port representation could change the predicted exit temperature distribution. Because these calculations were isothermal, naturally the exit temperature profiles will both be equal and uniform. However, by solving for a conserved scalar, ϕ, for which the inlet conditions are zero in the annulus and 1.0 at the airswirler, an indication of the aerodynamic mixing could be obtained by looking at the distribution of ϕ at the exit plane of the combustor. This quantity may be considered a concentration, i.e. being the proportion of the local air which has entered through the airswirler. The more uniform the exit distribution is would indicate that more mixing had occurred. The primary influence on this exit profile will be the effectiveness of the mixing between port and combustor flow.

Firstly figure 6.56 shows the axial distribution of concentration along the length of the combustor on the central plane through the primary port centre-lines. It can be seen in this figure how the concentration reduces left to right in the core from 1.0 at the air swirler to around 0.25 at the combustor exit plane (which is the fraction of air entering the domain through the airswirler). Again the much stronger jets issuing into the core can be seen by the increased length of what may be considered their potential core.

This is indicated by a concentration of zero (unshaded) within the core of the jet since no mixing with the internal air has yet occurred.

More importantly, the predicted concentration can be seen on the exit plane of the combustor in figure 6.57. On this plane the concentration can be seen to be much more uniform for the chuted ports than for the plain ports. Which would be the most suitable is not really an issue here, it is the exit temperature distribution which is of more importance. However, a more uniform concentration indicates more complete mixing, and more complete mixing would result in a more uniform exit temperature. Thus what is significant is the resultant change in this distribution brought about by the introduction of chutes on the ports to an otherwise identical prediction. A clear indicator that changes to port representation within CFD predictions can have large scale consequences on the resultant flow field.

6.9 Closure

Commissioning of experimental facilities, described in chapter 2, is often though of as an experimental pursuit, however it has an equivalent and important role for CFD studies. The grid refinement section investigated implementation of CFD methods to a typical port flow problem, demonstrating the required level of mesh density to minimise numerical error. This phase of work also compared two methods of geometrical representation of the port, e.g. castellated and fitted meshes. The fitted approach introduced additional error due to increased mesh distortion, but once a mesh density independent solution was reached the port fitted mesh produced the most realistic results. A test problem was then developed which demonstrated three points. Firstly that C_d could be determined in a fashion consistent with experimental methods - though others are suggested. Secondly that differences in C_d due to port geometry changes can be predicted, and these follow expected trends. Finally the flow split between ports could be determined for problems containing more than one port.

A computational study has then been conducted for the geometry of the experimental rig. Inlet boundary conditions were taken from experimental measurements to accurately resolve actual velocity and turbulence distributions. Success of the CFD method was mixed. The annulus velocity and turbulence fields were generally well

predicted using the k-ε turbulence model, and further clarification that distinct flow modes exist in the annulus was found (discovered experimentally, and dependent on the bleed ratio). Flow through the port and jet exit characteristics were predicted with some success but success depended upon the shape of the port, the mesh density used to represent the port and the flow conditions. This may throw some suspicion on calculations of multi-port calculations which contain ports of various types each with varying flow conditions: if C_d of each port is predicted with different levels of accuracy then it is likely that the resultant flow splits will not be correct. Limited success was found in predicting the core flow field. Reasonable predictions of the mean velocity field were obtained, but levels of turbulence were grossly under-predicted, particularly around impingement. It is likely that the k-ε turbulence is the biggest source of error in this respect, and previous workers have found this in similar flow scenarios.

Removal of an imposed plane of symmetry through the centre of a port resulted in a through port vortex being predicted at low bleed ratios. This suggests that care should be used when setting up symmetry planes in the feed annulus of such flows. A component of swirl was introduced to the annulus flow and this was seen to predict the significant effects on the core flow seen experimentally, though no back to back comparisons were possible for this scenario.

The final predictions in this chapter demonstrated that port representation in combustor sector calculations can have large scale effects on the resultant flow field. In particular, exit temperature distributions could be significantly altered by the levels of mixing predicted when including the chute details of each port rather than using plain ports.
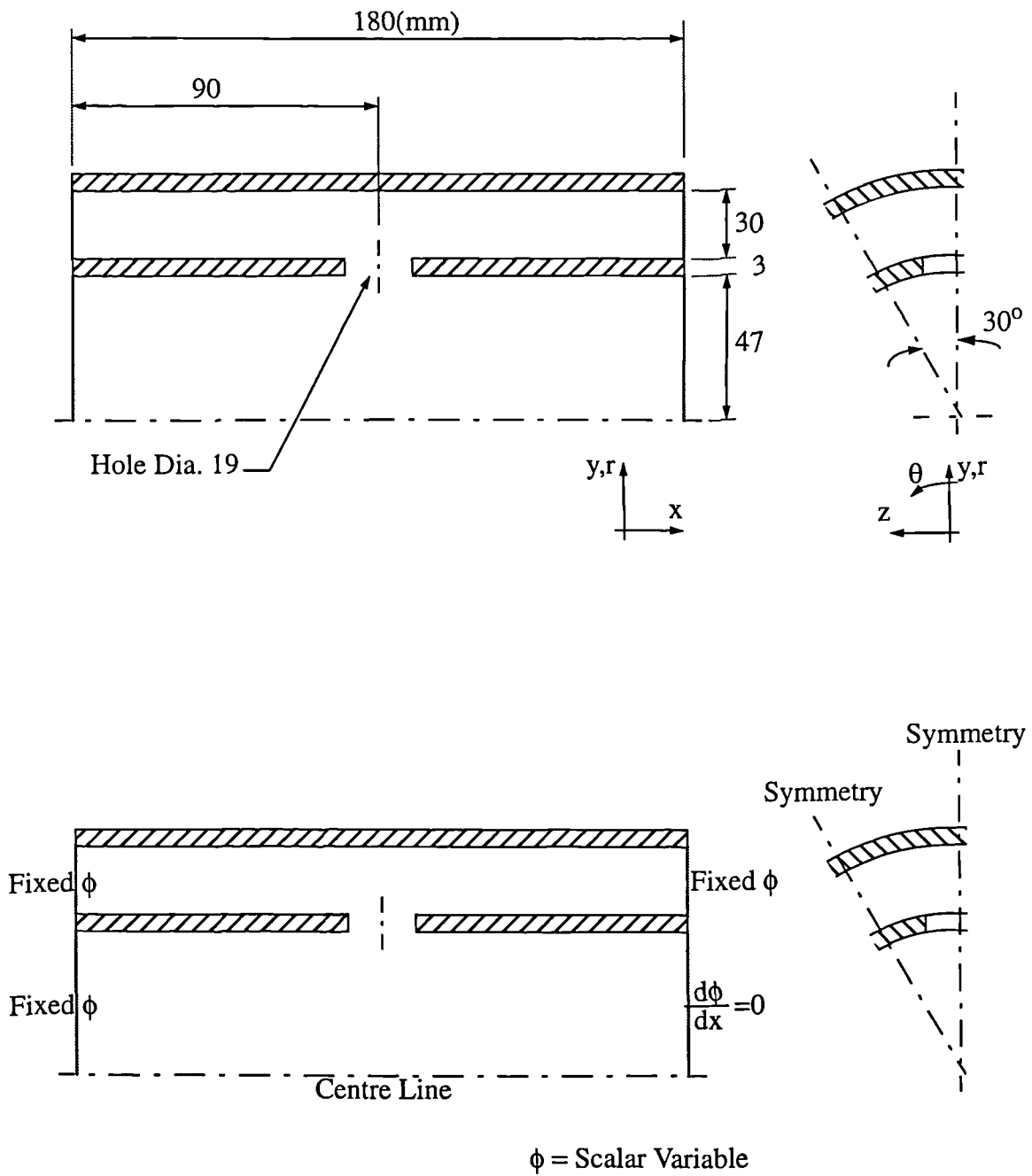
Figure 6.1 Geometry and Boundary Conditions For Grid Refinement Study

Mesh C1

(and Initial Mesh F1,
pre-port module)

Port Detail Mesh C1

Port Detail Mesh F1
(post-port module)
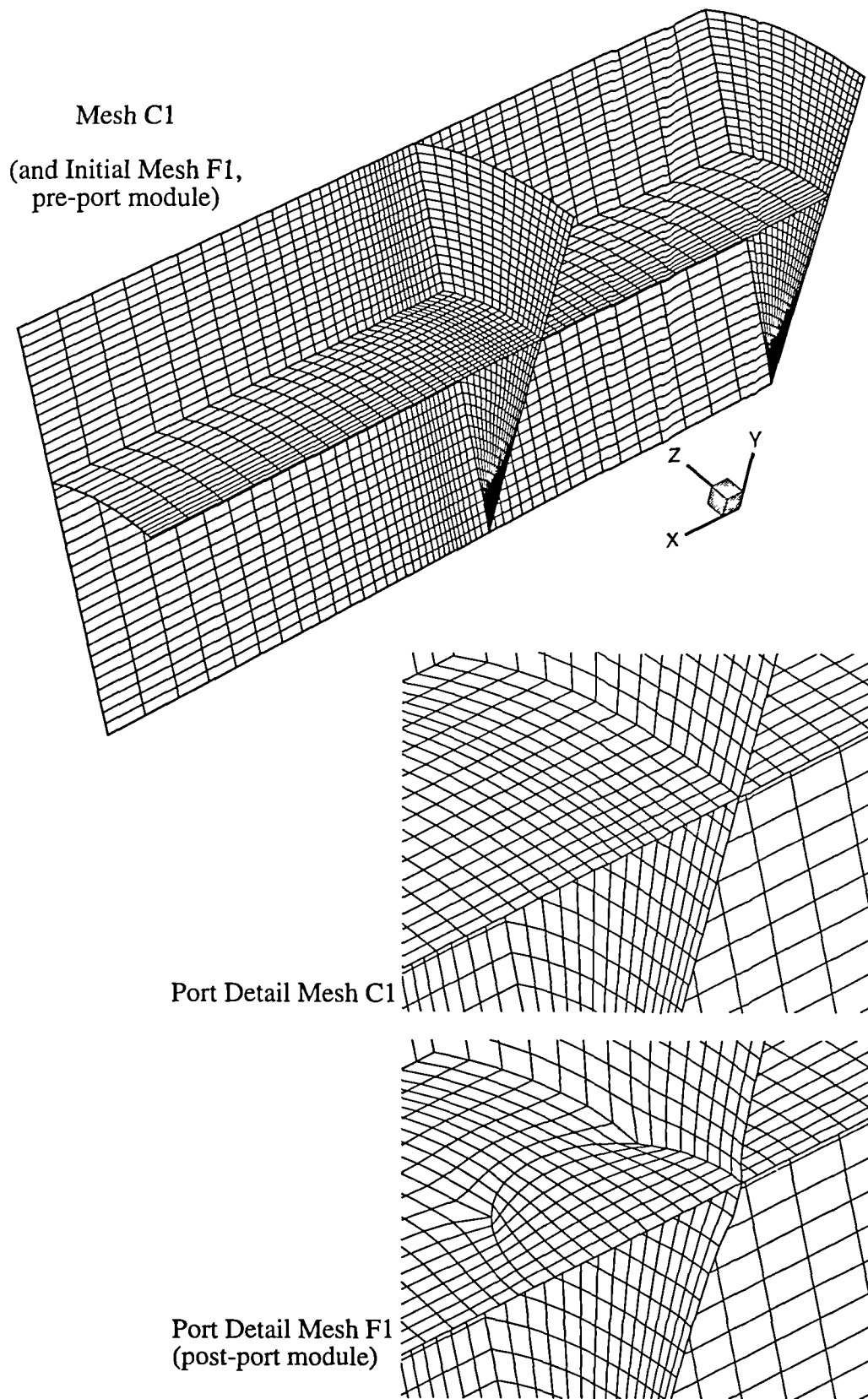
Figure 6.2 Coarsest Meshes for Grid Refinement Study (C1 & F1).
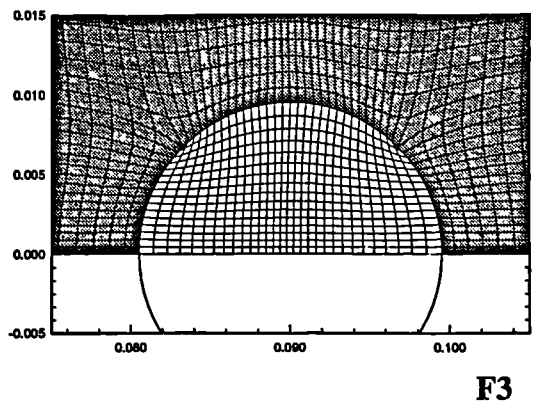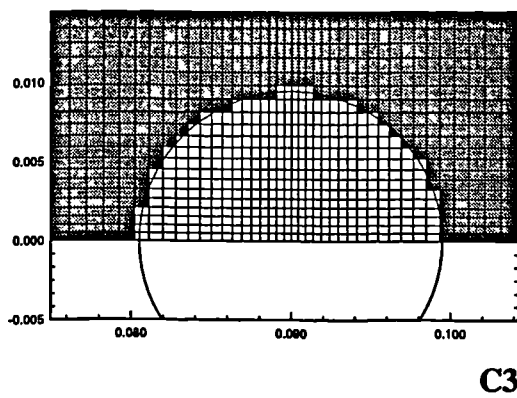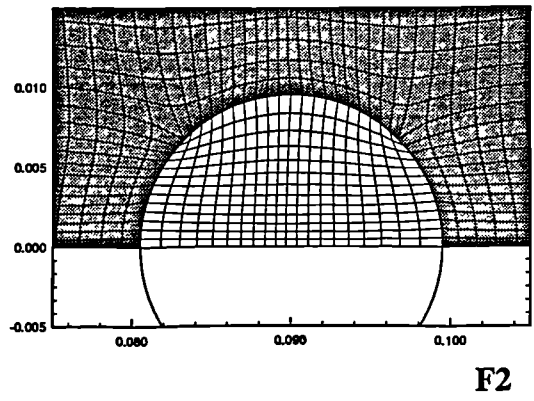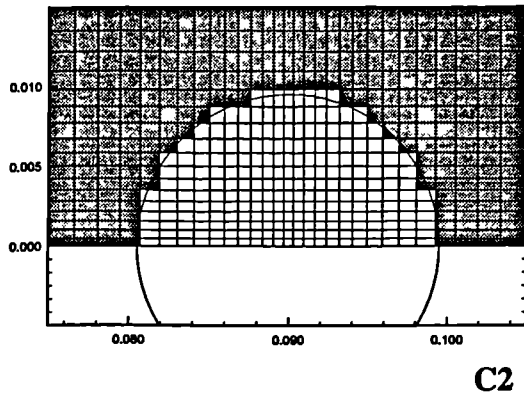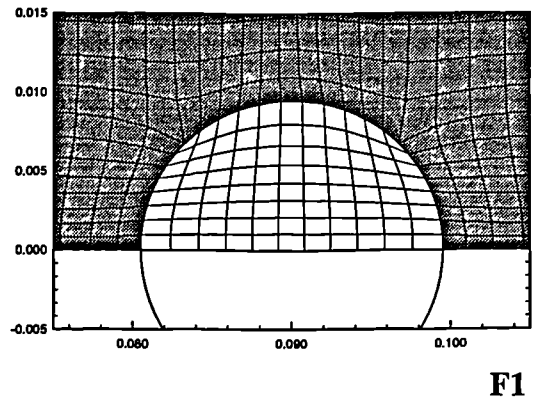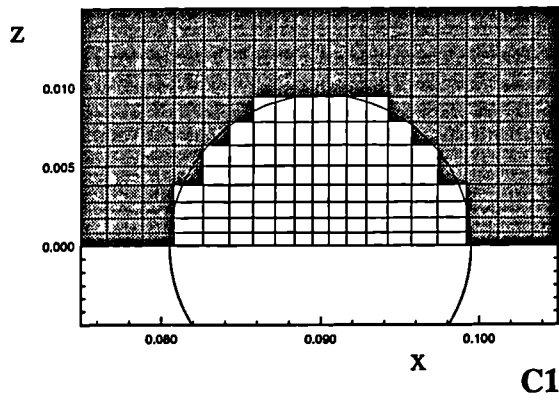
Figure 6.3 Port Detail At Each Level of Mesh Refinement

N.B. r=0.01m, θ=0.0°
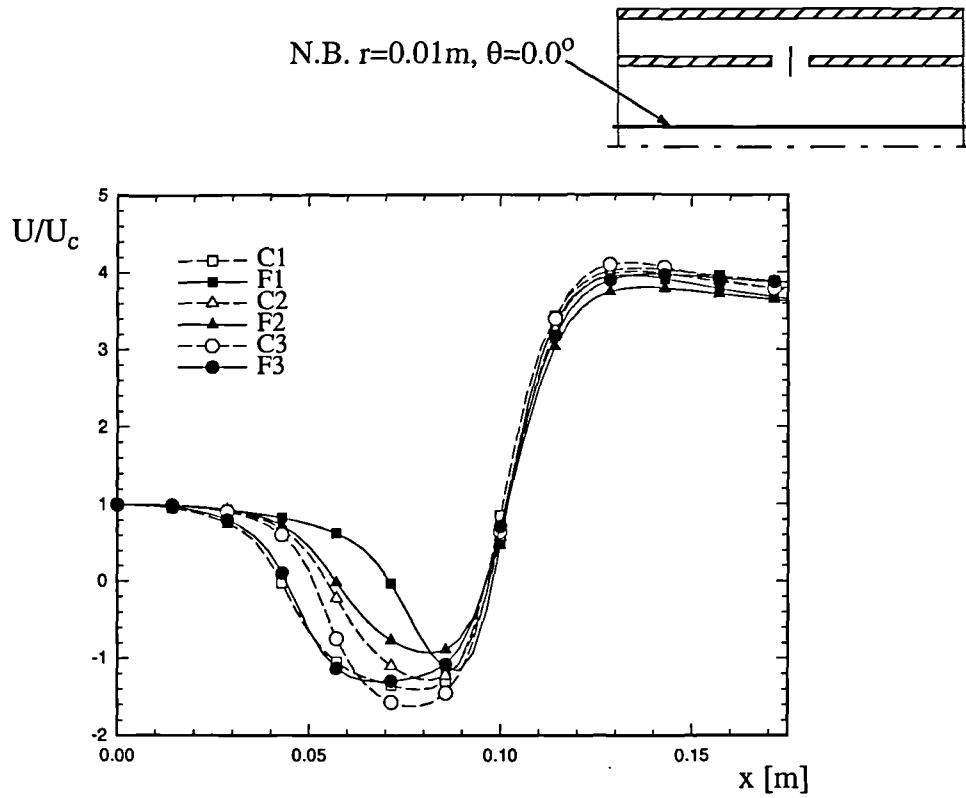
Figure 6.4 Axial Distribution of U/U_c Along r=0.01m, θ=0.0°
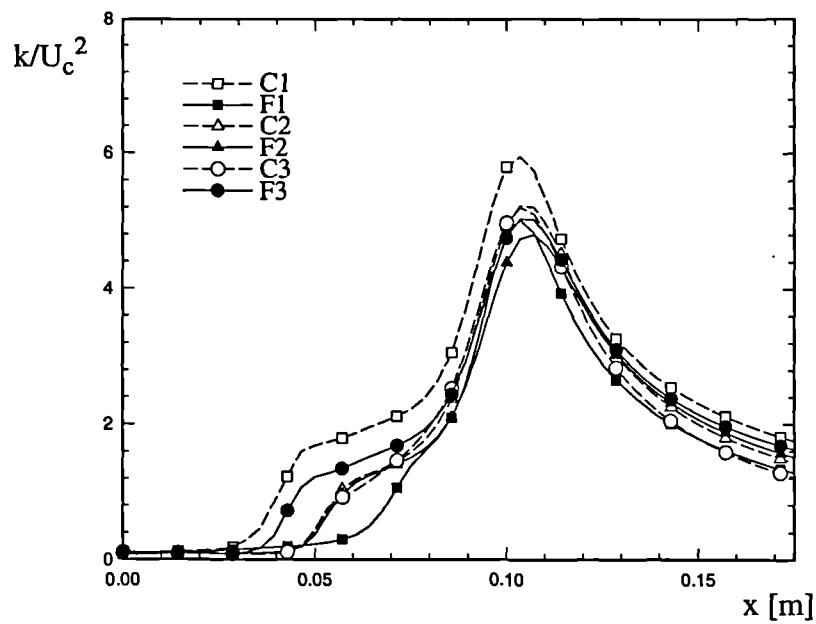
Figure 6.5 Axial Distribution of k/U_c^2 Along r=0.01m, θ=0.0°
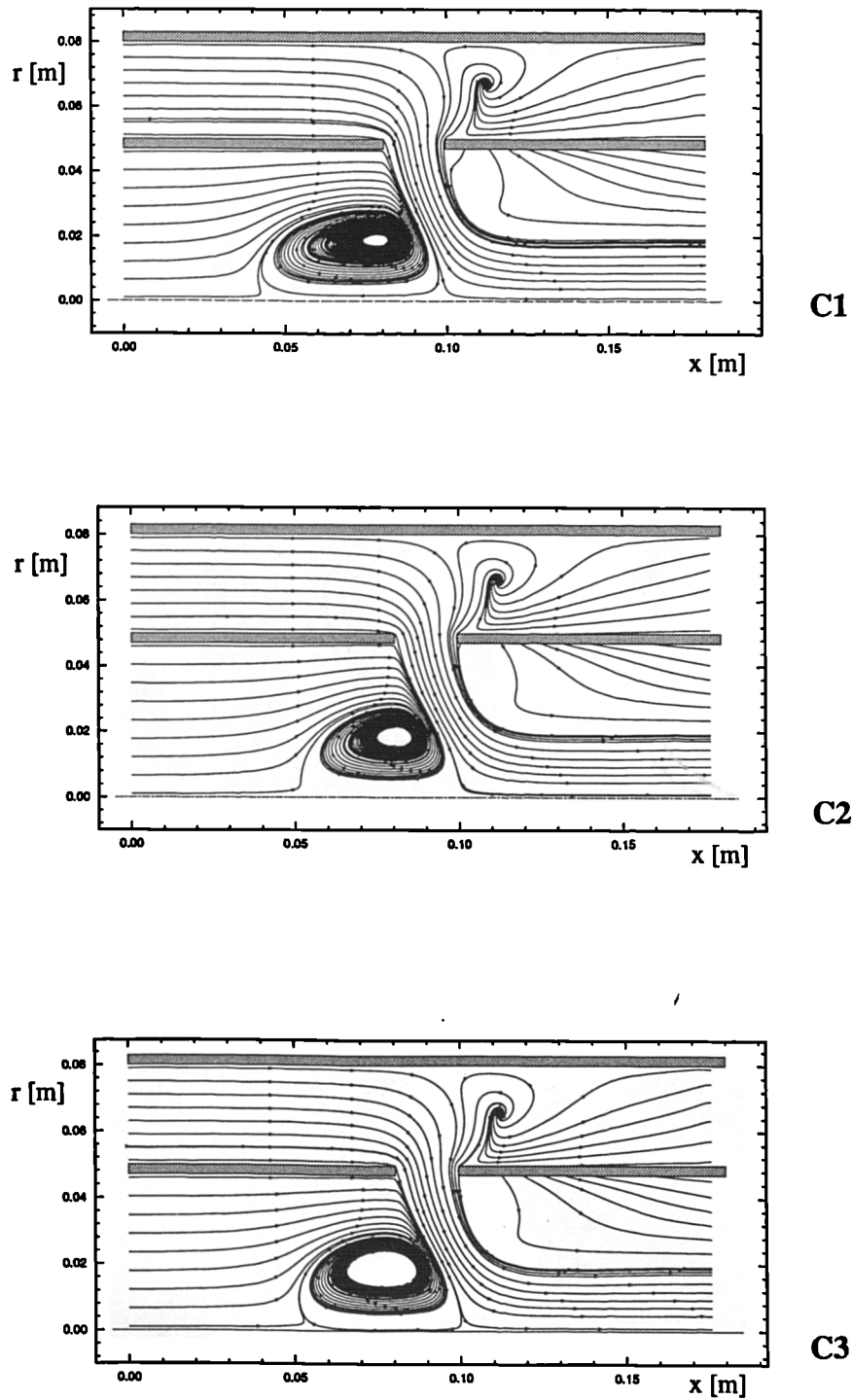
Figure 6.6(a) Predicted Flow Patterns for Castellated Ports

F1

F2

F3
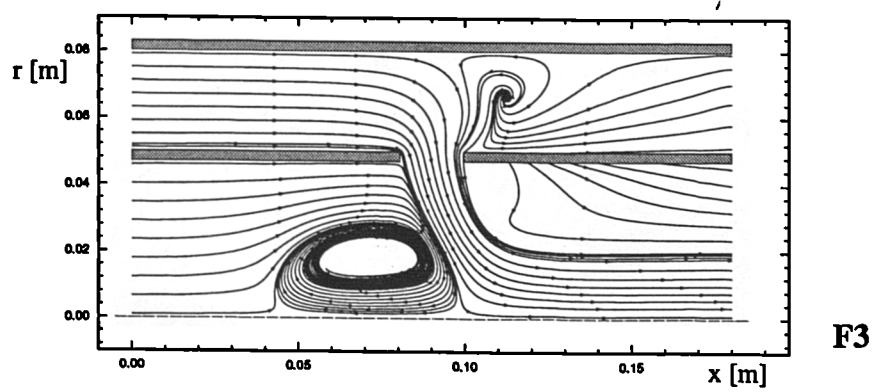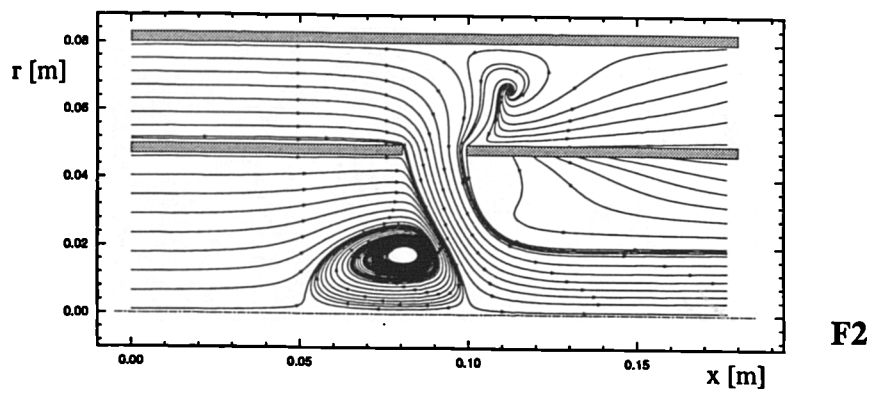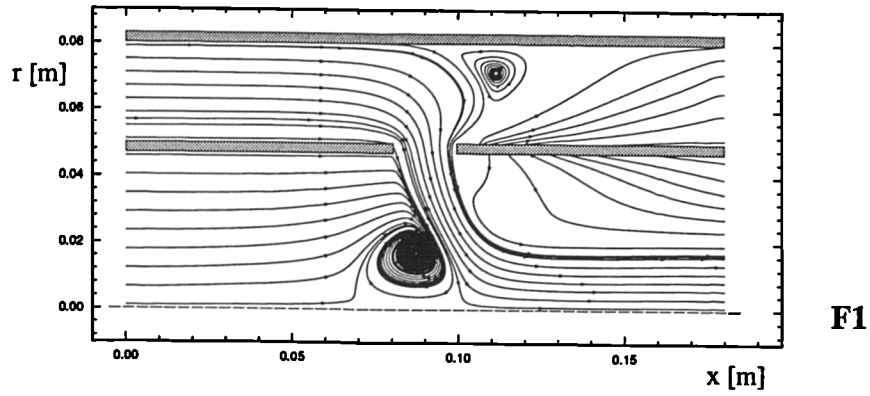
Figure 6.7 Predicted Flow Patterns for Fitted Ports
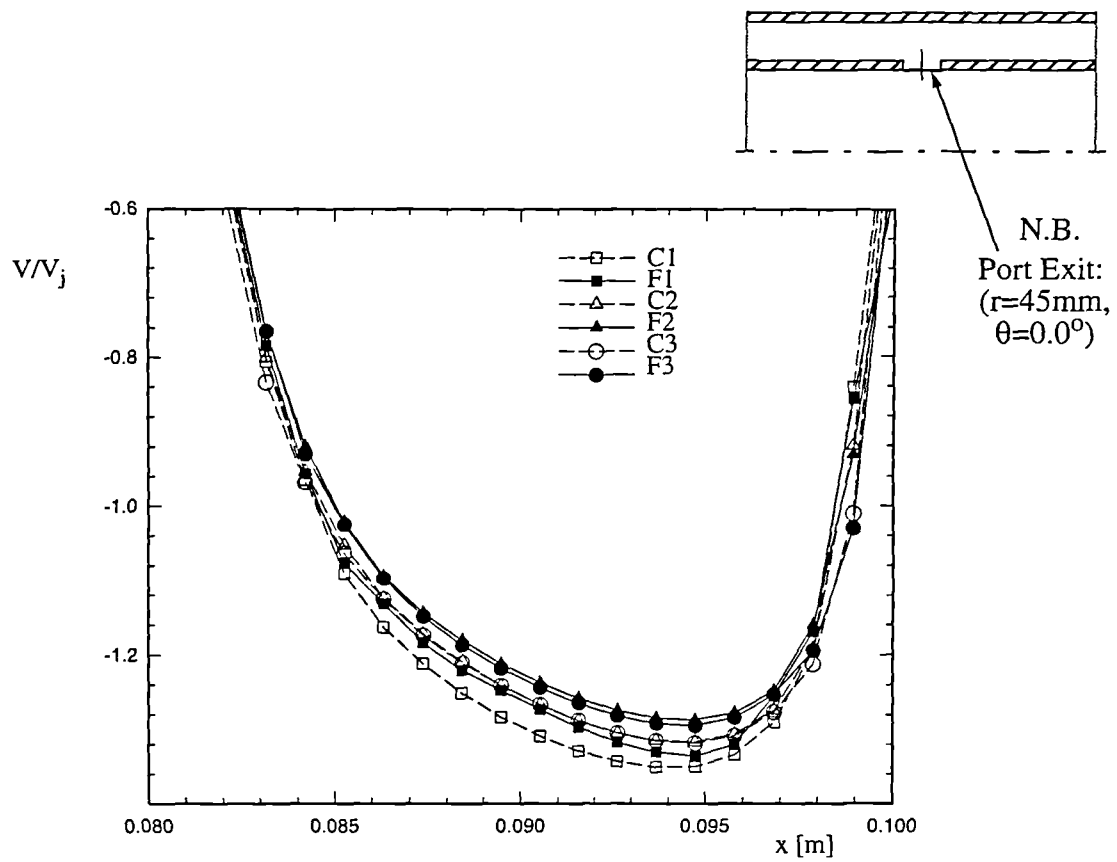
Figure 6.8 Radial Velocity Across Port Diameter
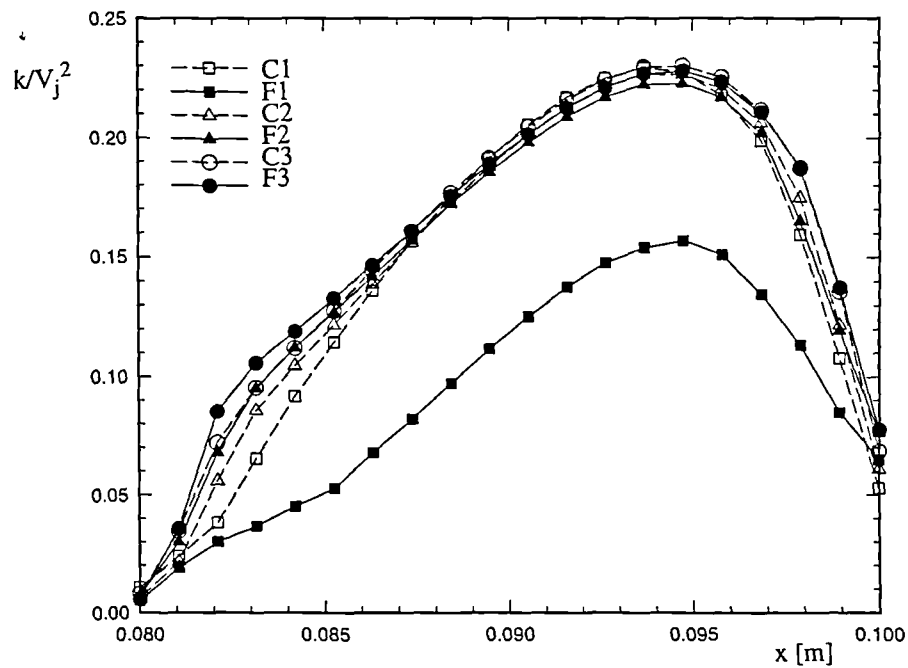
Figure 6.9 Turbulent Kinetic Energy Across Port Diameter
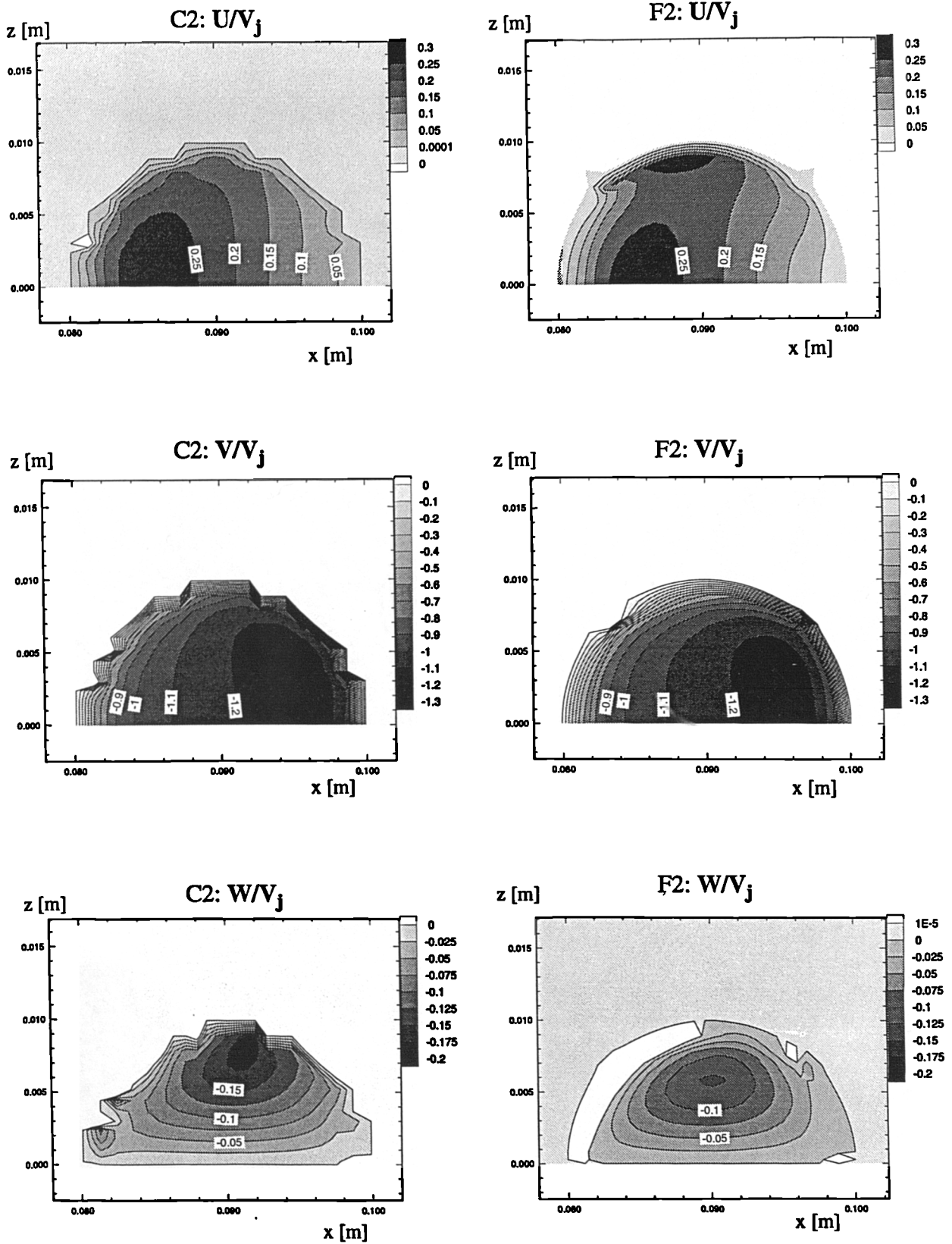
Figure 6.10 Port Exit Velocity Distribution For Castellated and Fitted Meshes
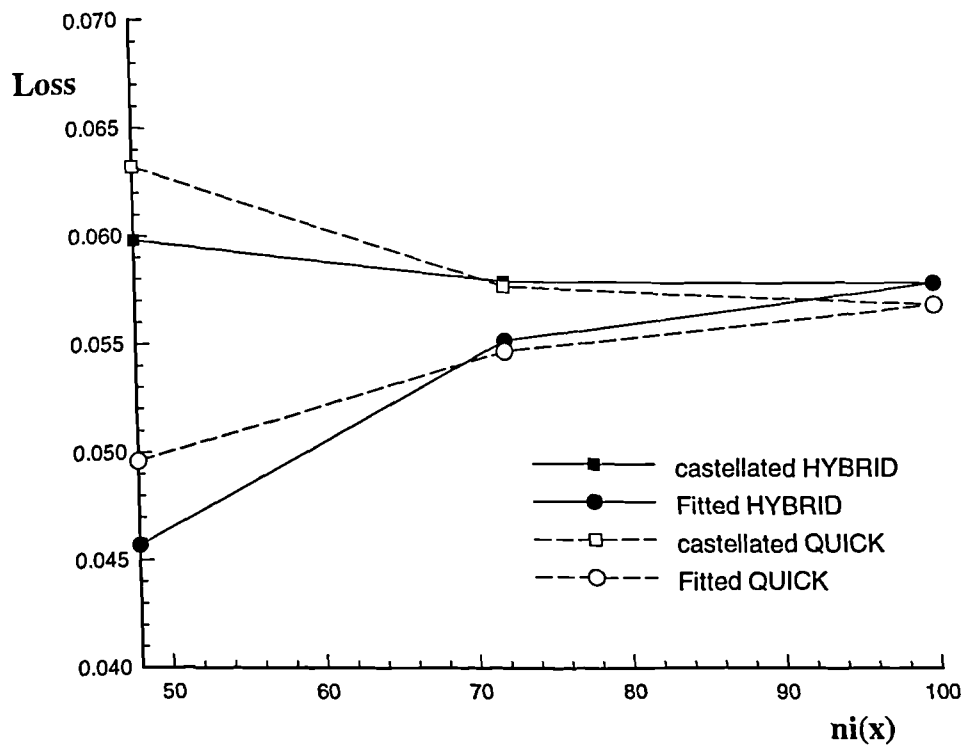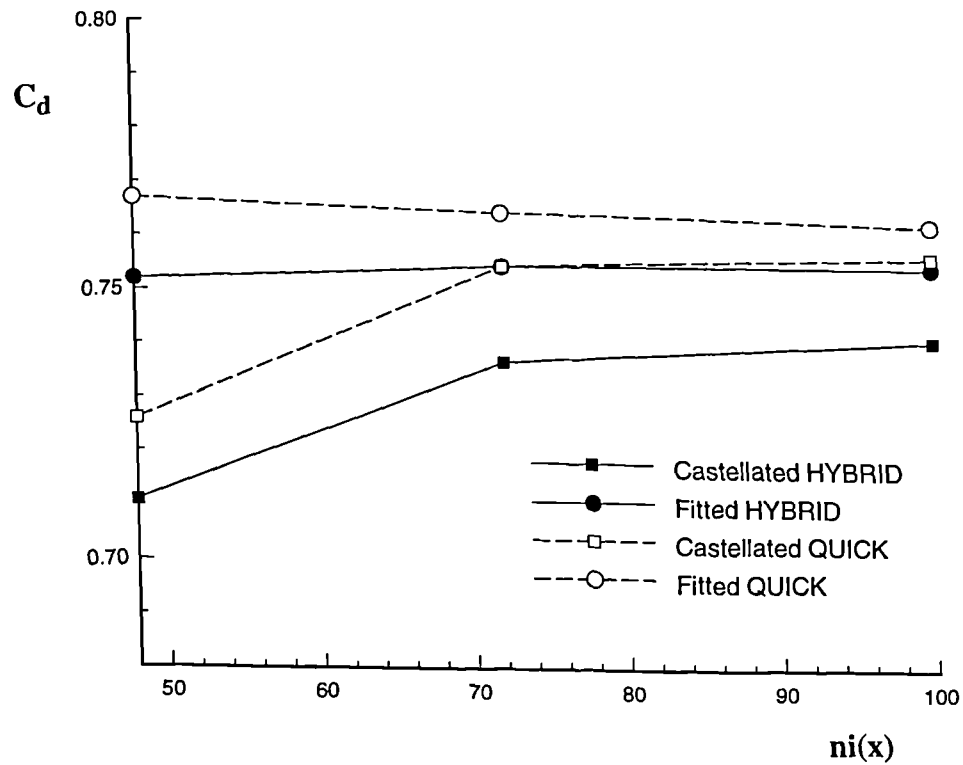
Figure 6.11 Effect of Grid Resolution on C_d and Total Turbulent Loss

— — — — Symmetry planes

•••••••••••••• Boundary of modelled region
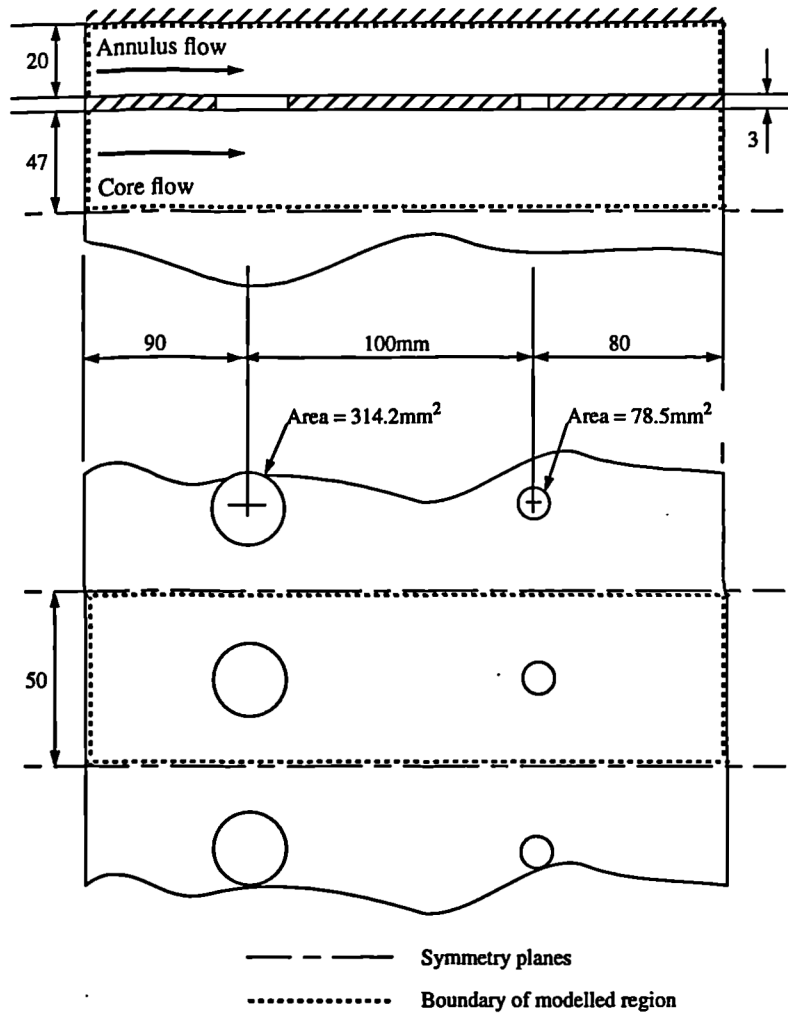
Figure 6.12 Rectangular Test Geometry
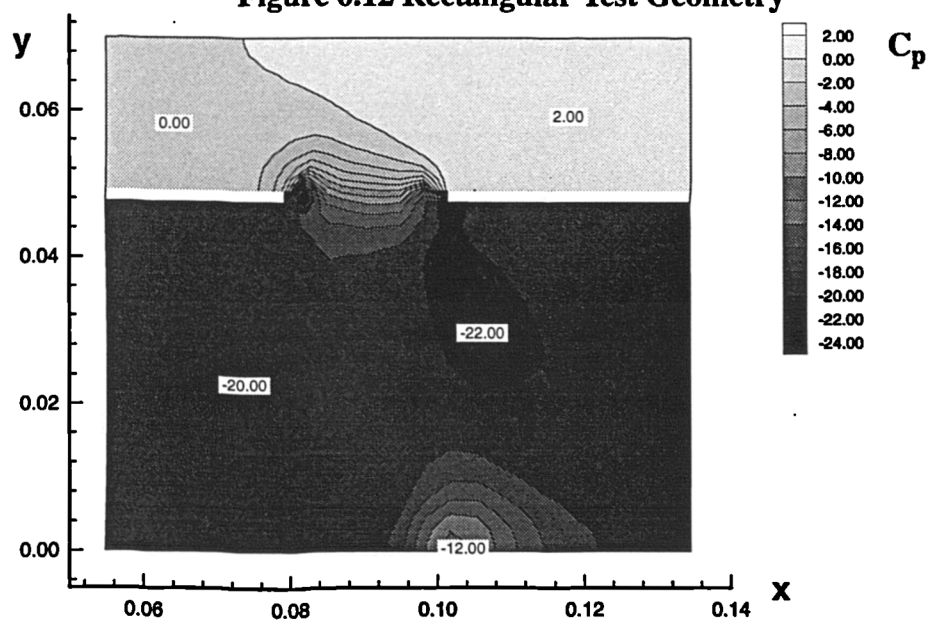
Figure 6.13 Pressure Coefficient Around Upstream Port
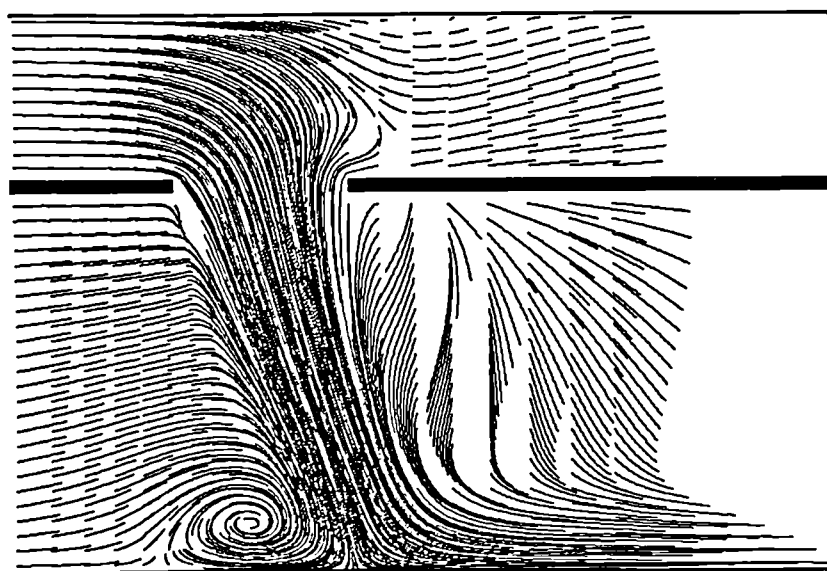
(a) Plain port
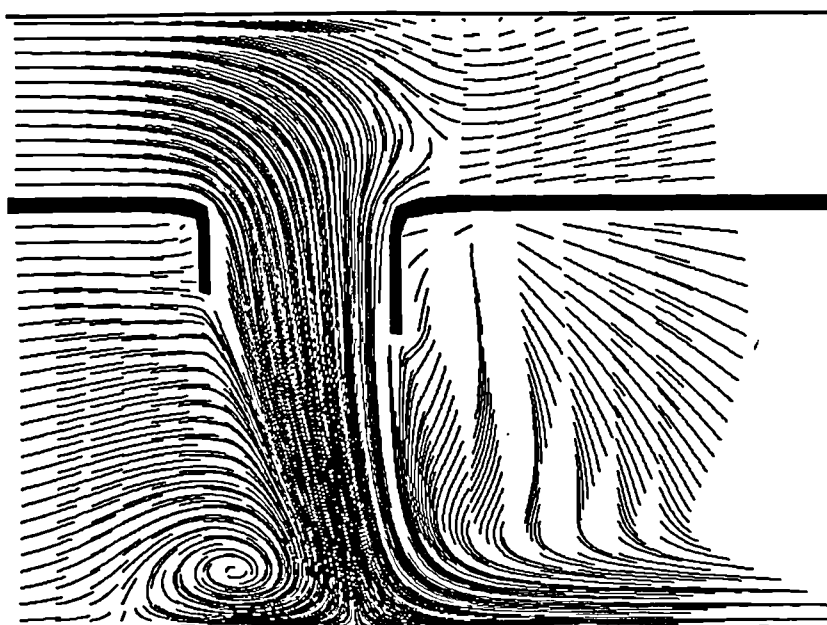
(b) Chuted port

Figure 6.14 Streaklines On Symmetry Plane Through Upstream Port
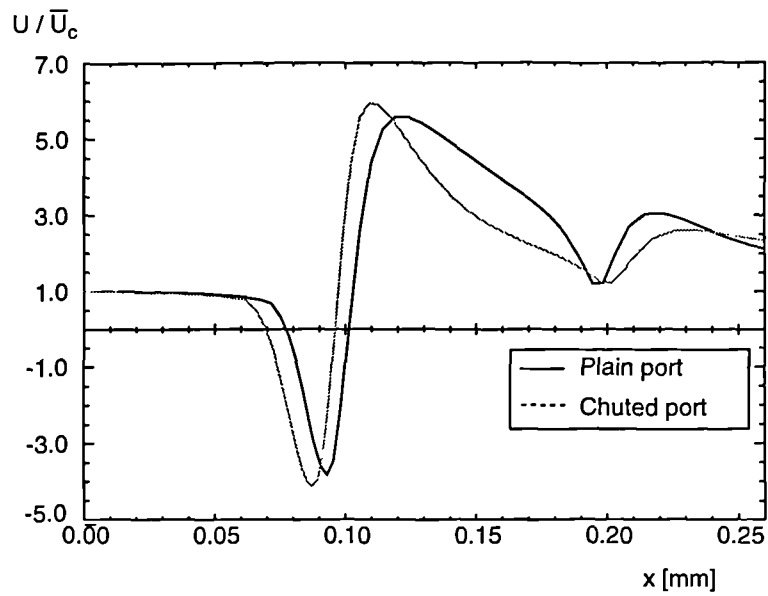
Figure 6.15 Axial Velocity Profile on Plane of Impingement
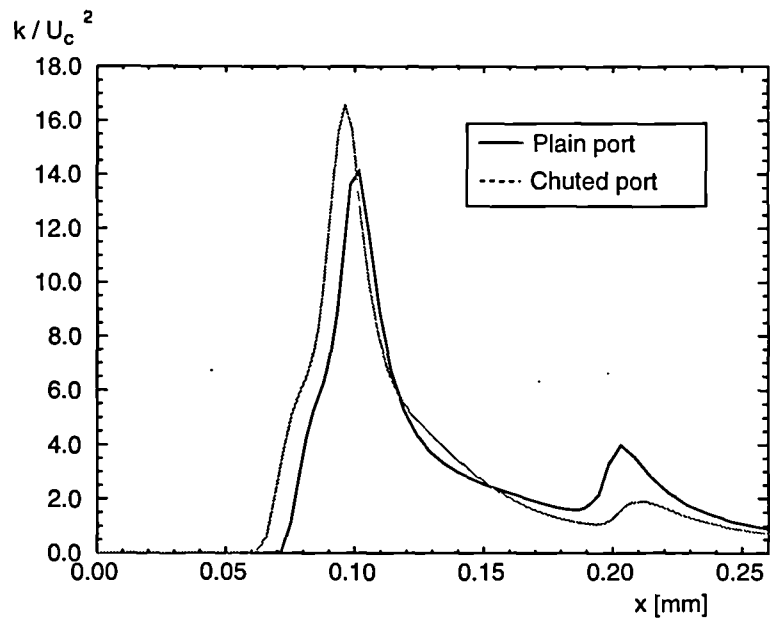
Figure 6.16 Turbulent Kinetic Energy on Plane of Impingement
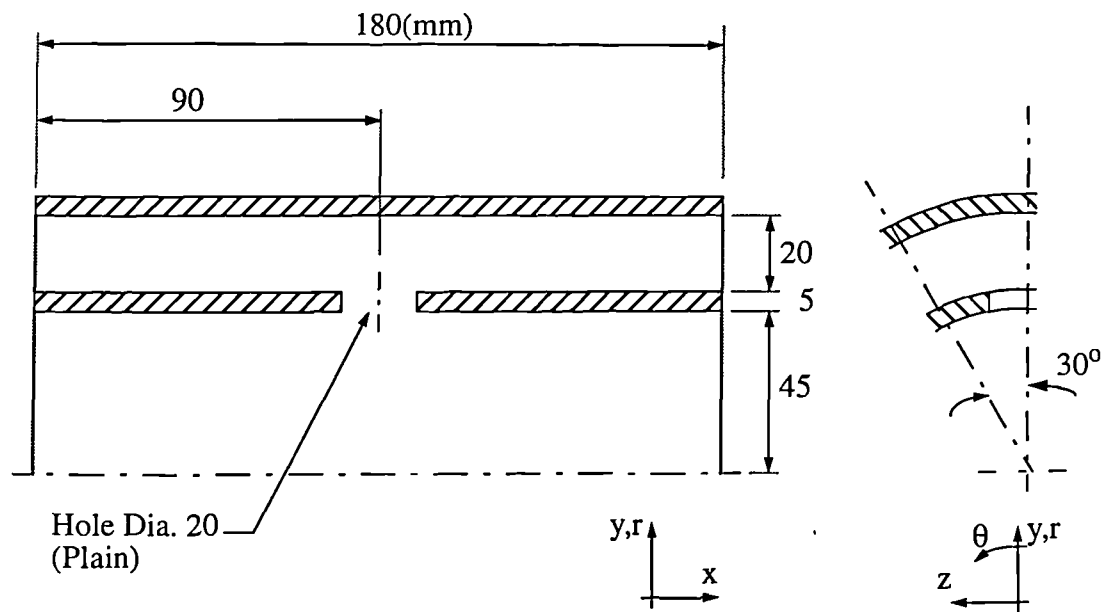
Figure 6.17(a) Geometry of Test Rig (With Assumed Symmetry)
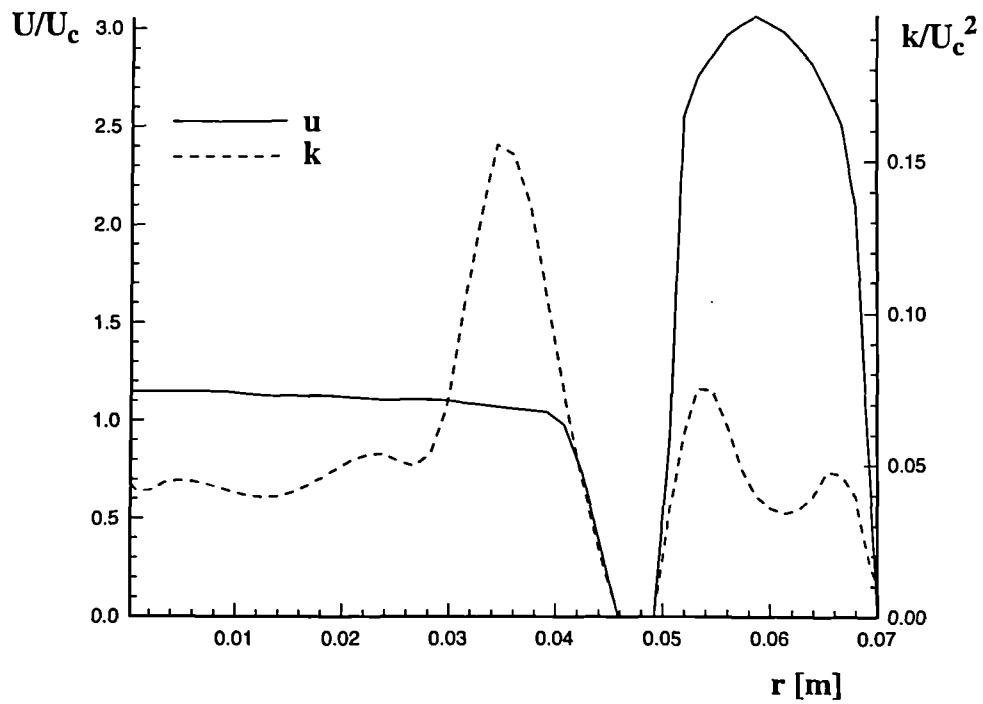
Figure 6.17(b) Inlet Velocity and Turbulence Profiles For Rig Modelling
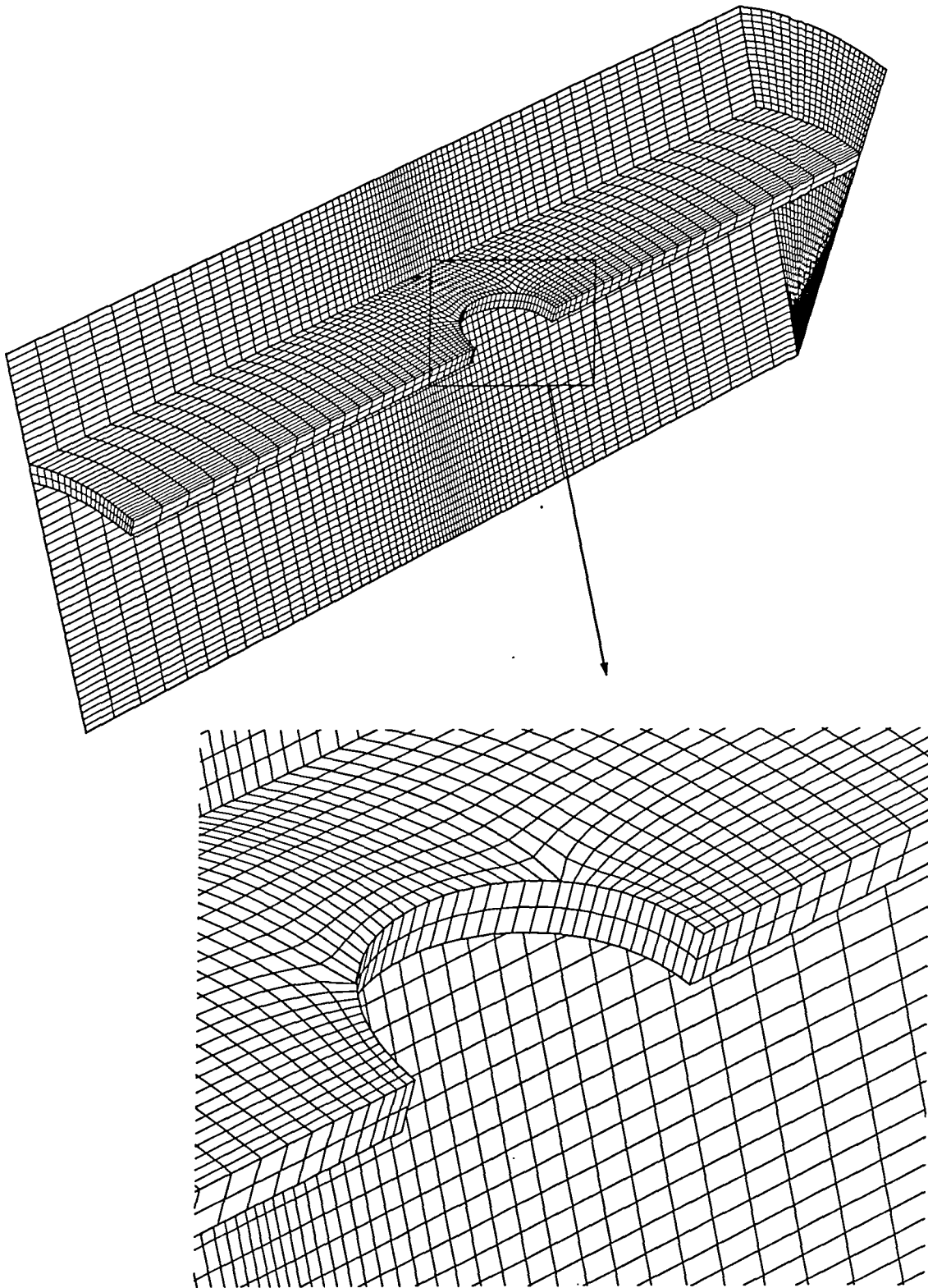
Figure 6.18 Mesh Fitted to Plain Port
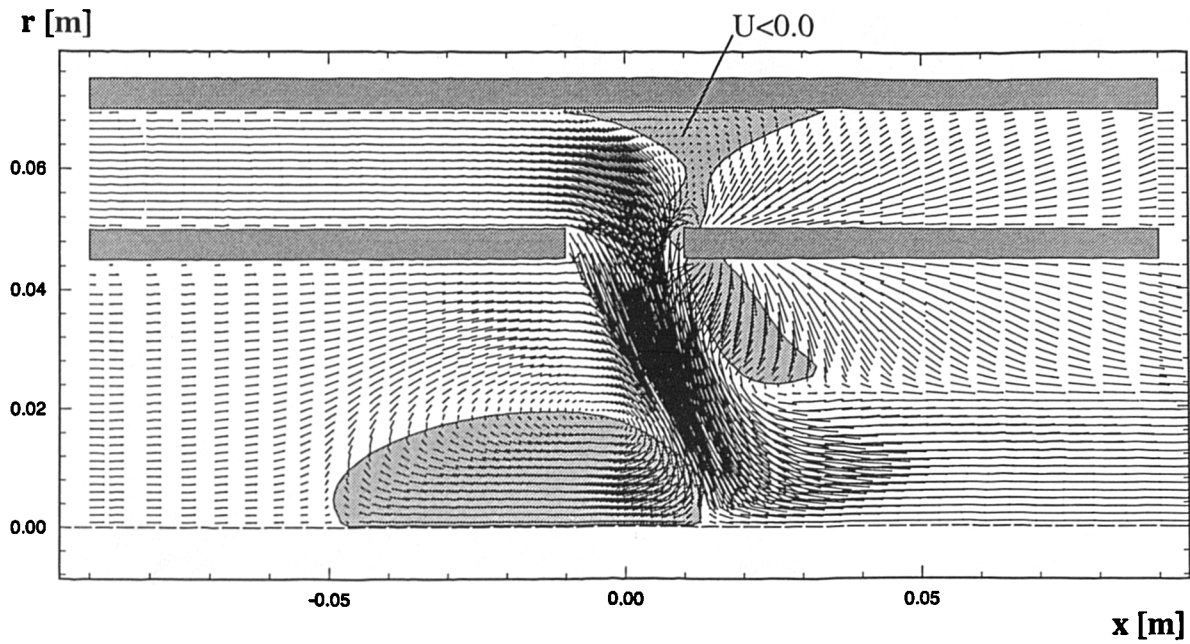
Figure 6.19 Predicted Velocity Field for Datum Case
Plain Port, R=5.0, Bleed=50%
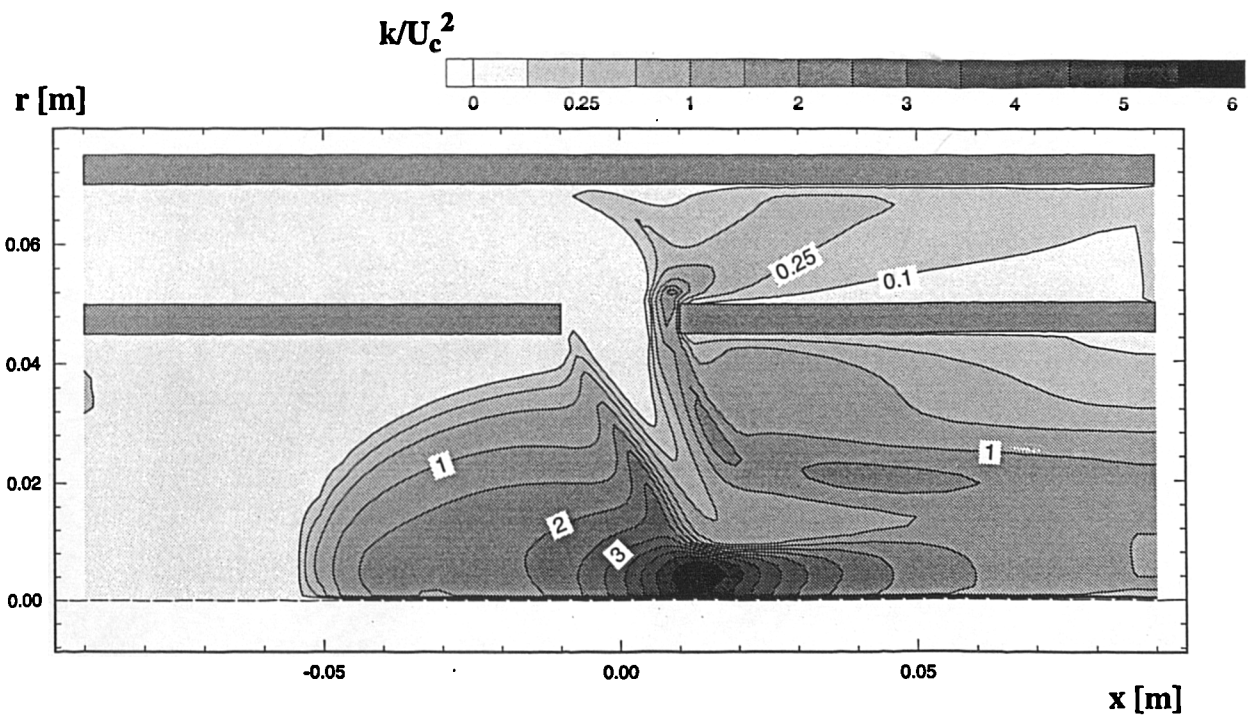
Figure 6.20(a) Predicted Turbulence Field for Datum Case - k
Plain Port, R=5.0, Bleed=50%

NB: increments:
0 to 0.5 in 0.1
0.5 to 5 in 0.5

(b) uu/U$_c^2$

(c) vv/U$_c^2$

(d) ww/U$_c^2$
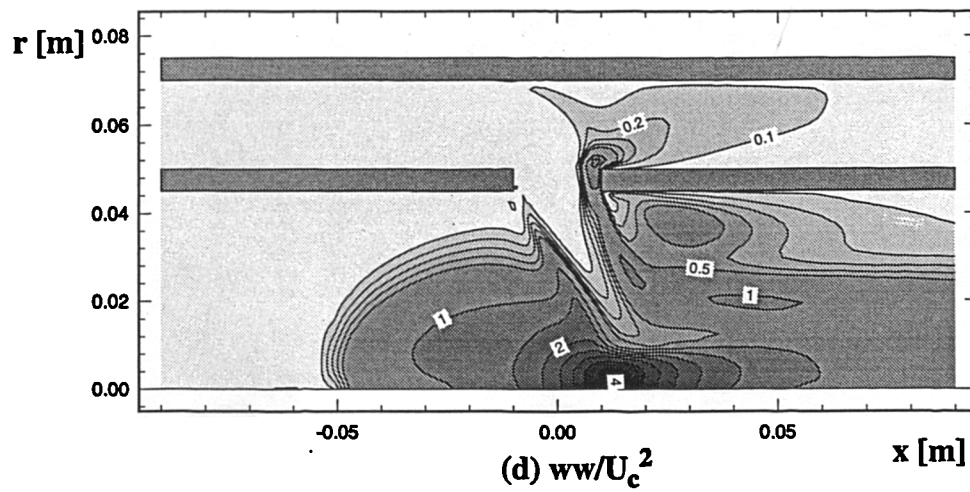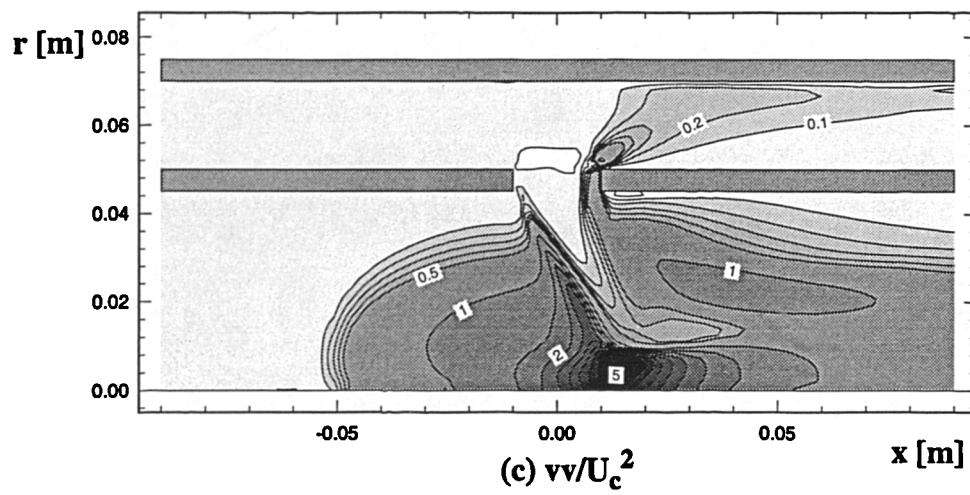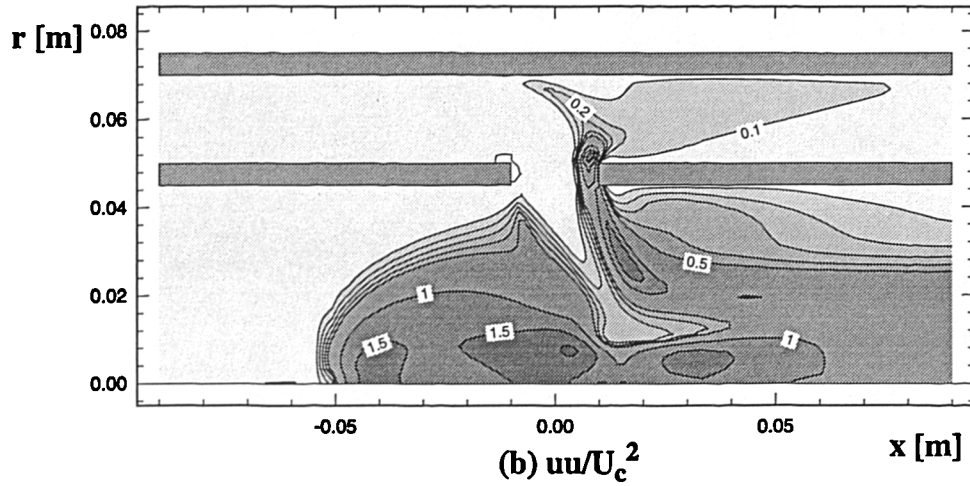
Figure 6.20(cont) Predicted Turbulence Field for Datum Case - Normal Stresses
Plain Port, R=5.0, Bleed=50%
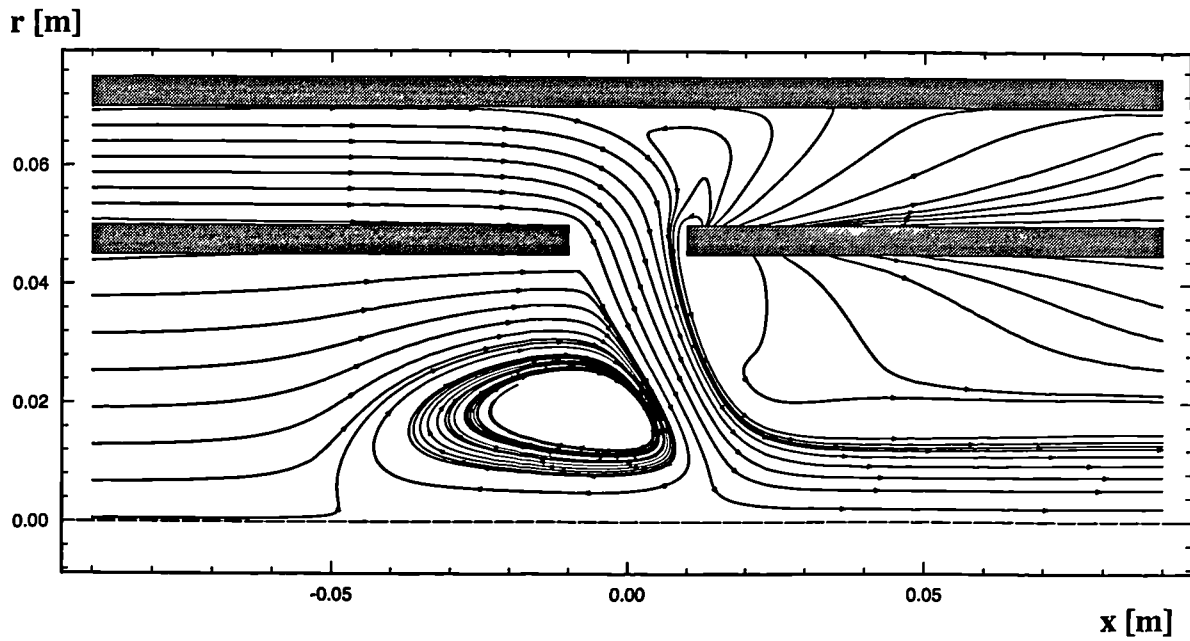
(a) Prediction
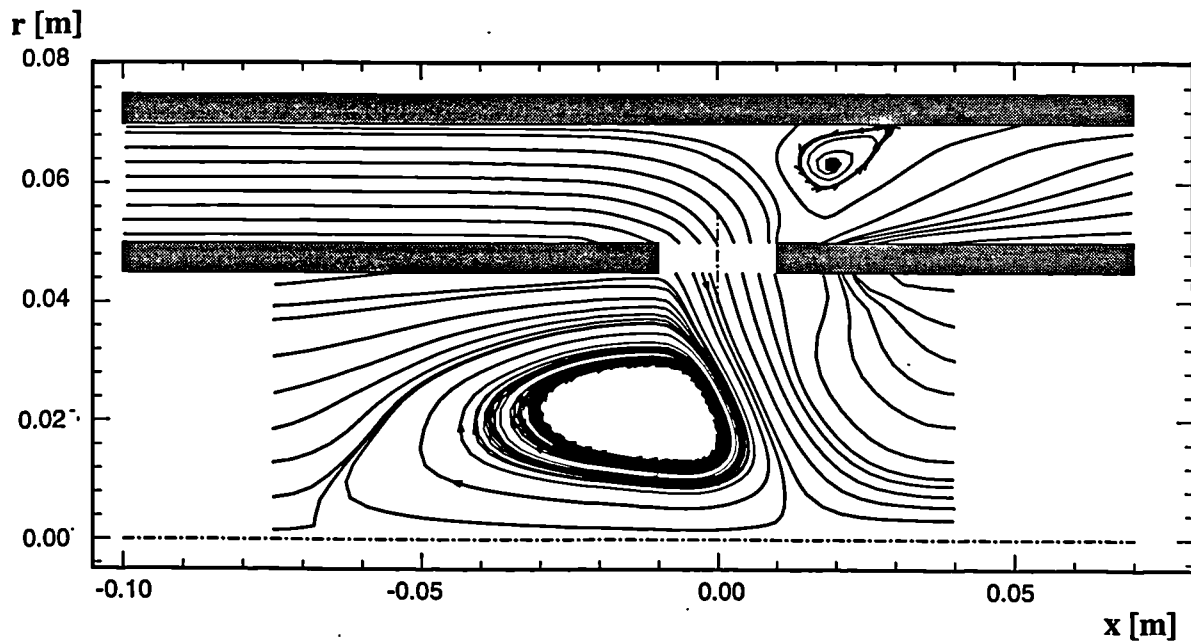
(b) Measurements

Figure 6.21 Particle Tracks On Symmetry Plane for Datum Case
Plain Port, R=5.0, Bleed=50%
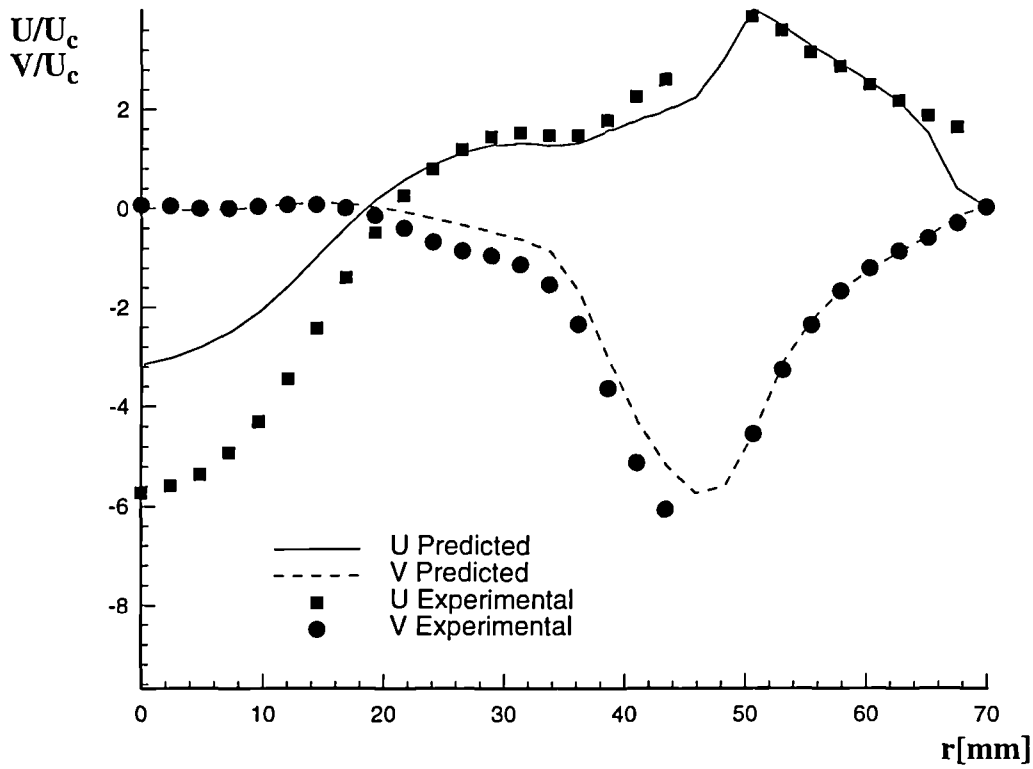
(a) x = -5mm
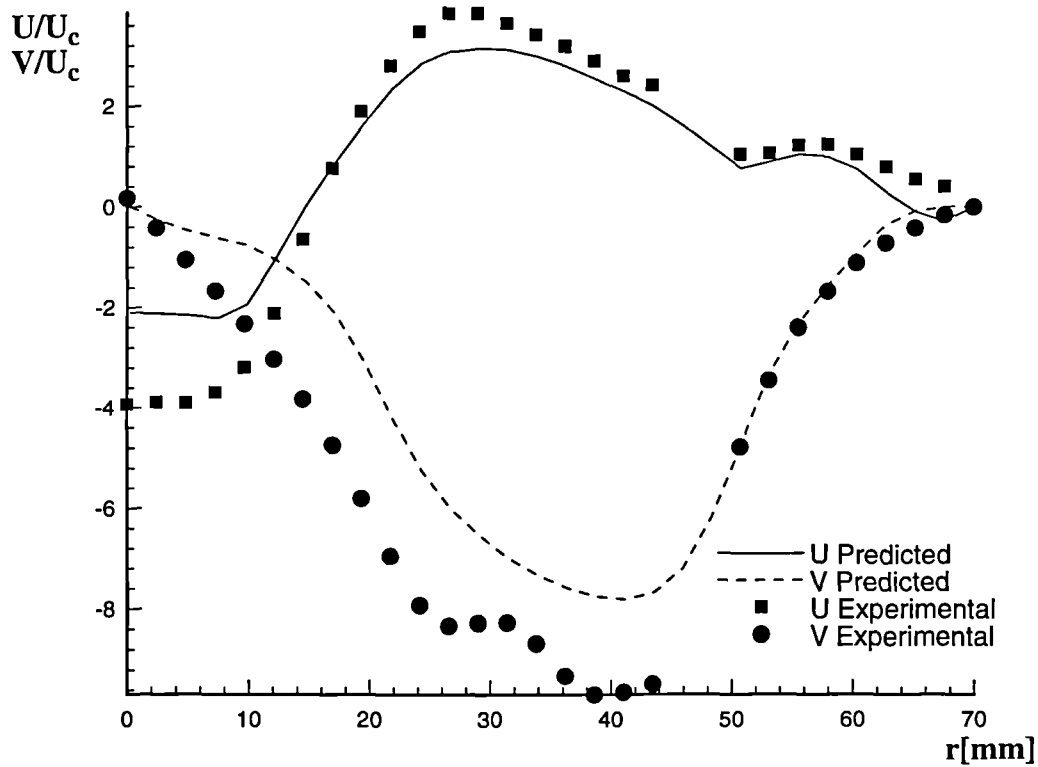
(b) x = 5mm

Figure 6.22 Velocity Profiles at x=-5 and x=5mm, θ=0°, Datum Case
Plain Port, R=5.0, Bleed=50%
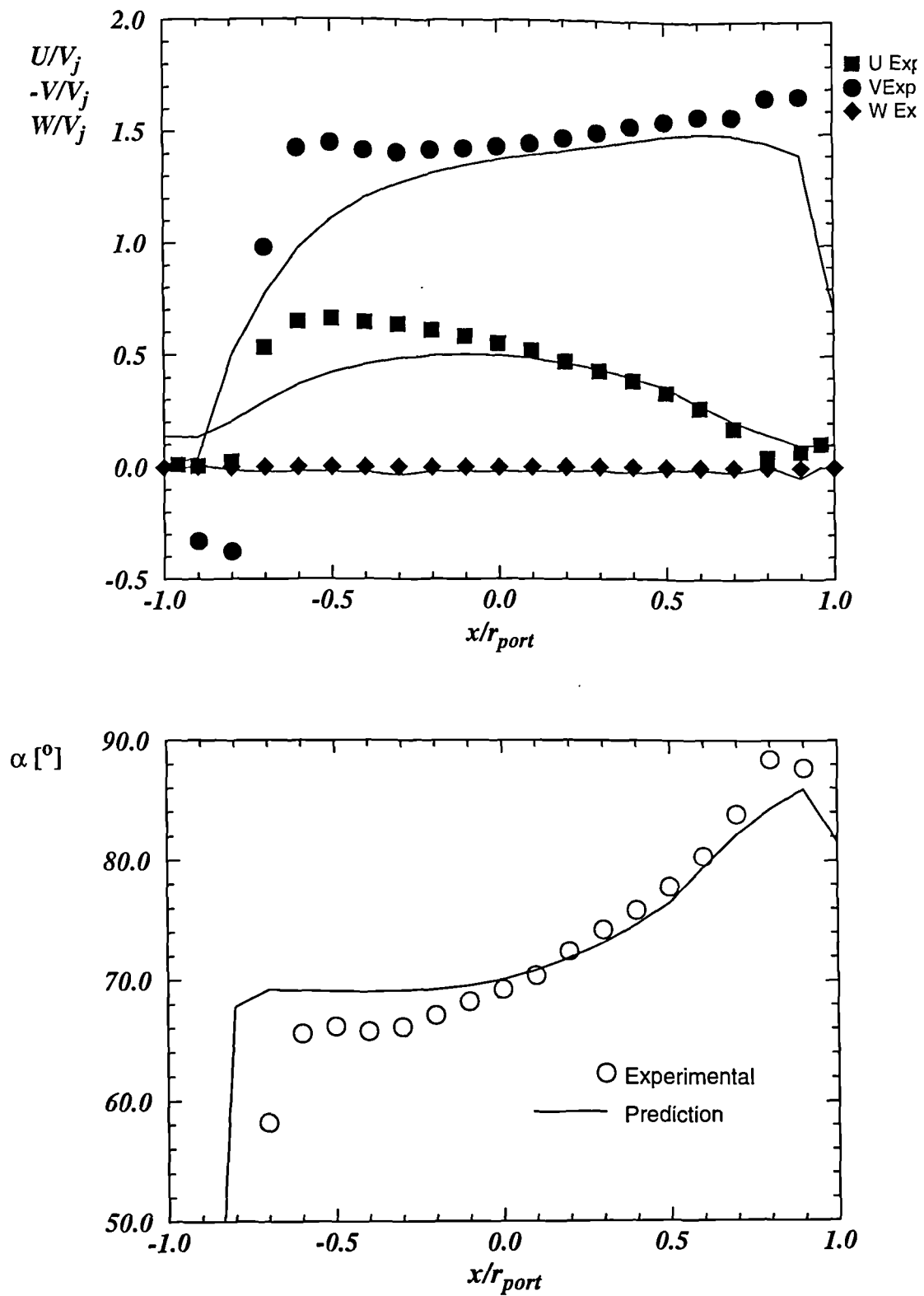
Figure 6.23 Jet Exit Velocity and Flow Angle for Datum Case
Plain Port, R=5.0, Bleed=50%
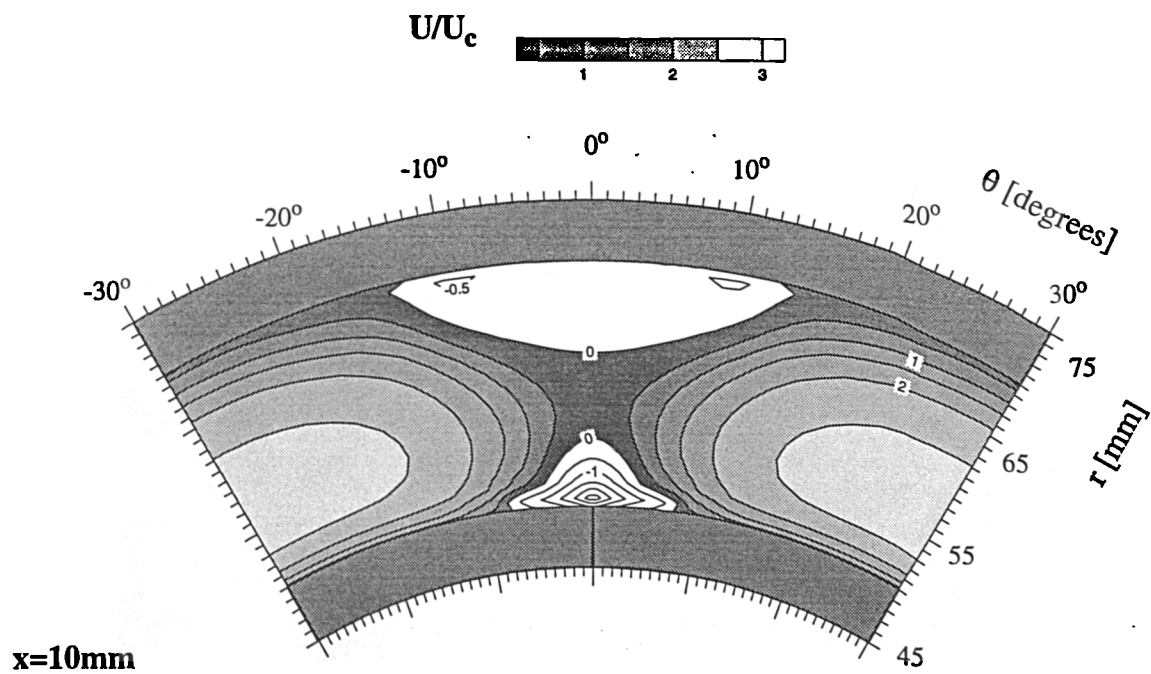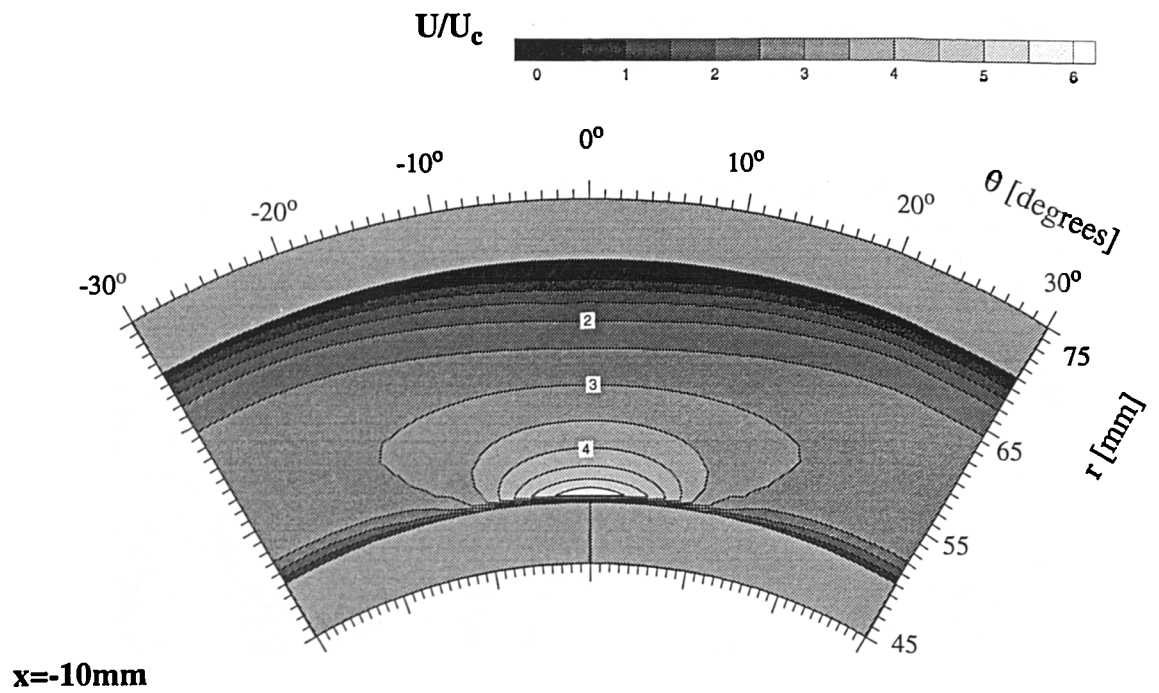
Figure 6.24 Axial Velocity Distribution in Annulus on x=-10 and x=10 Planes
Plain Port, R=5.0, Bleed=50%
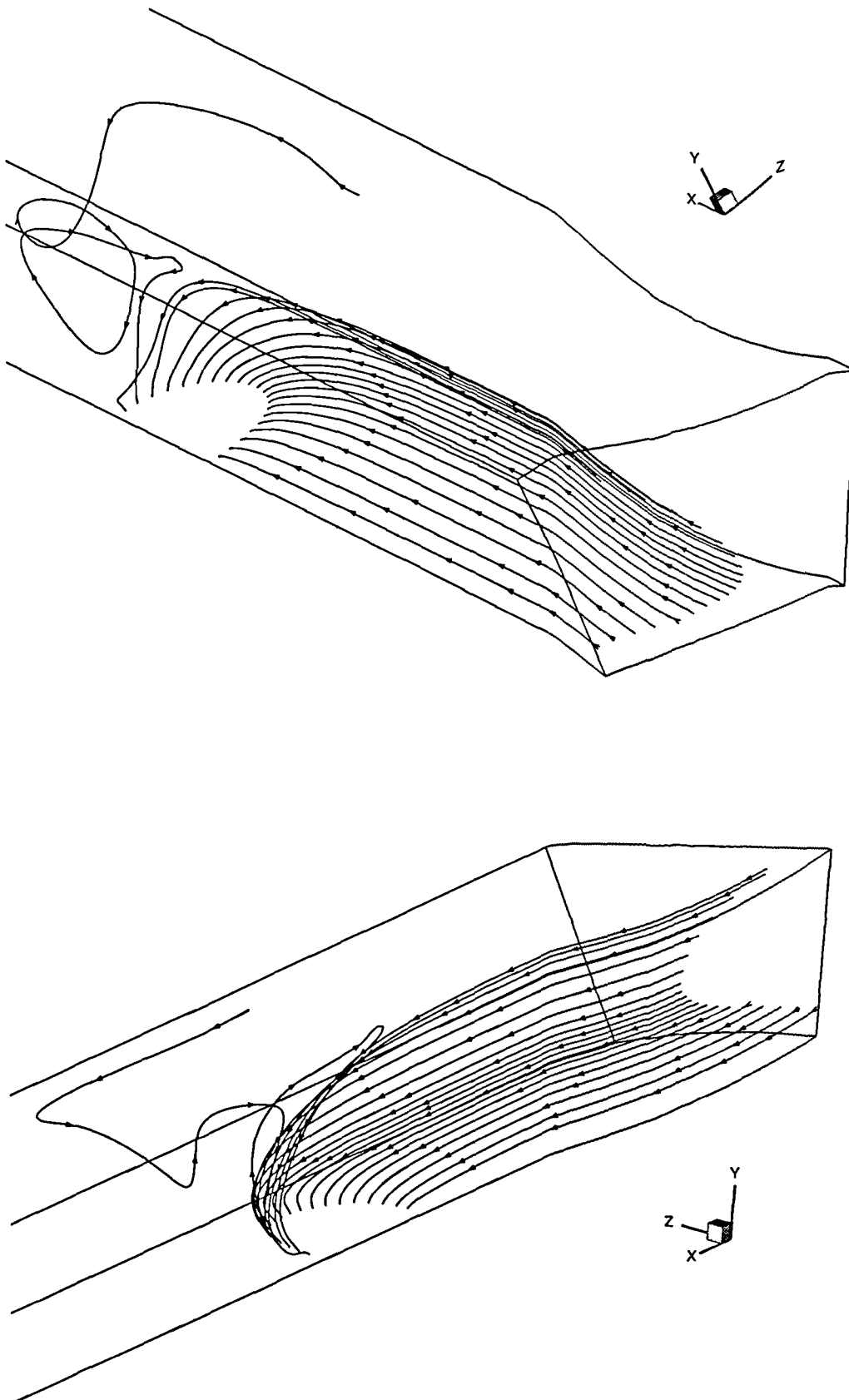
Figure 6.25 Reverse Particle Tracks Released From Port Perimeter
Plain Port, R=5.0, Bleed=50%
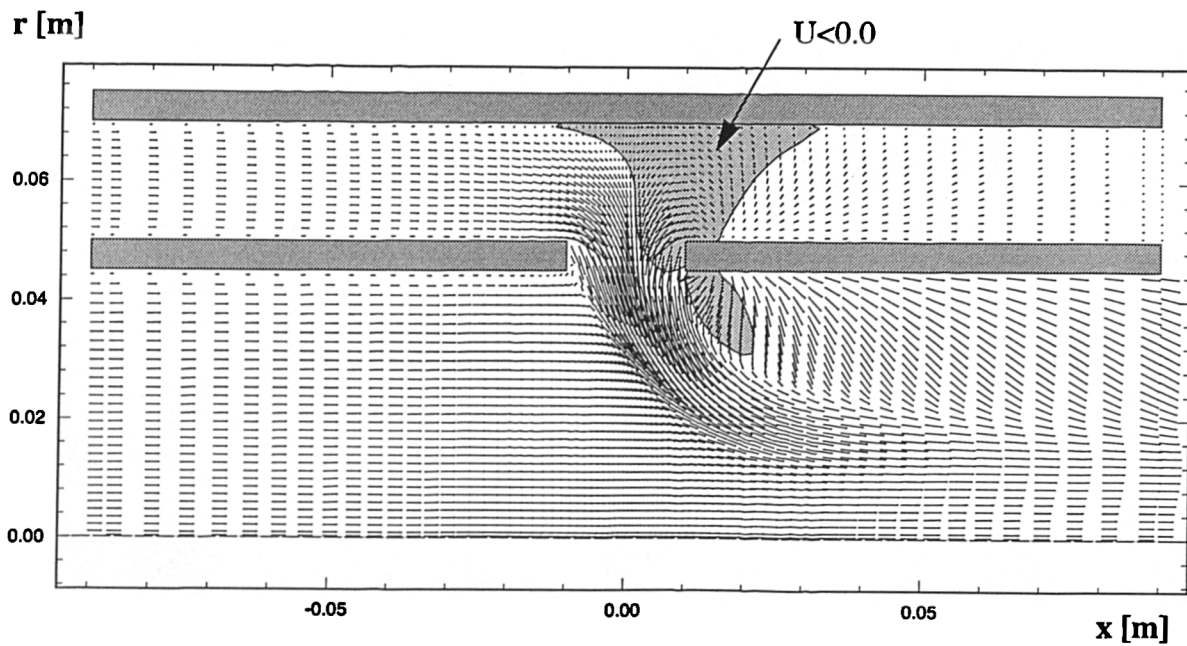
Figure 6.26 Predicted Velocity Field for Dilution Configuration
Plain Port, R=2.0, Bleed=20%
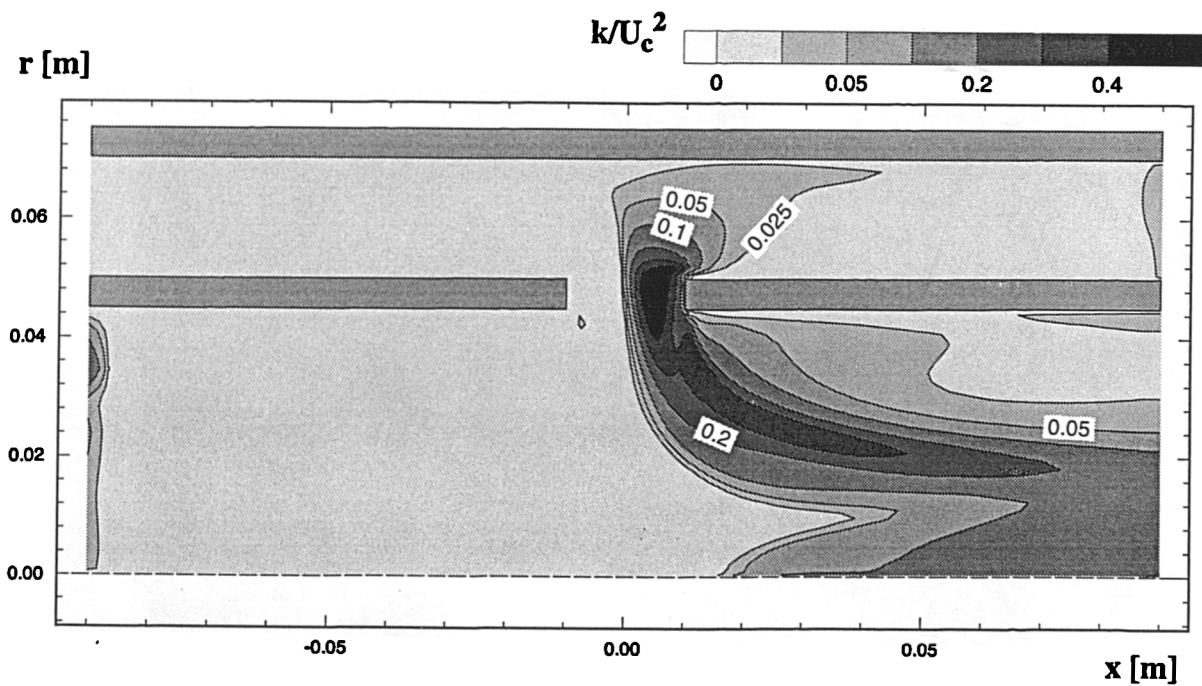
Figure 6.27 Predicted Turbulence Field for Dilution Configuration
Plain Port, R=2.0, Bleed=20%
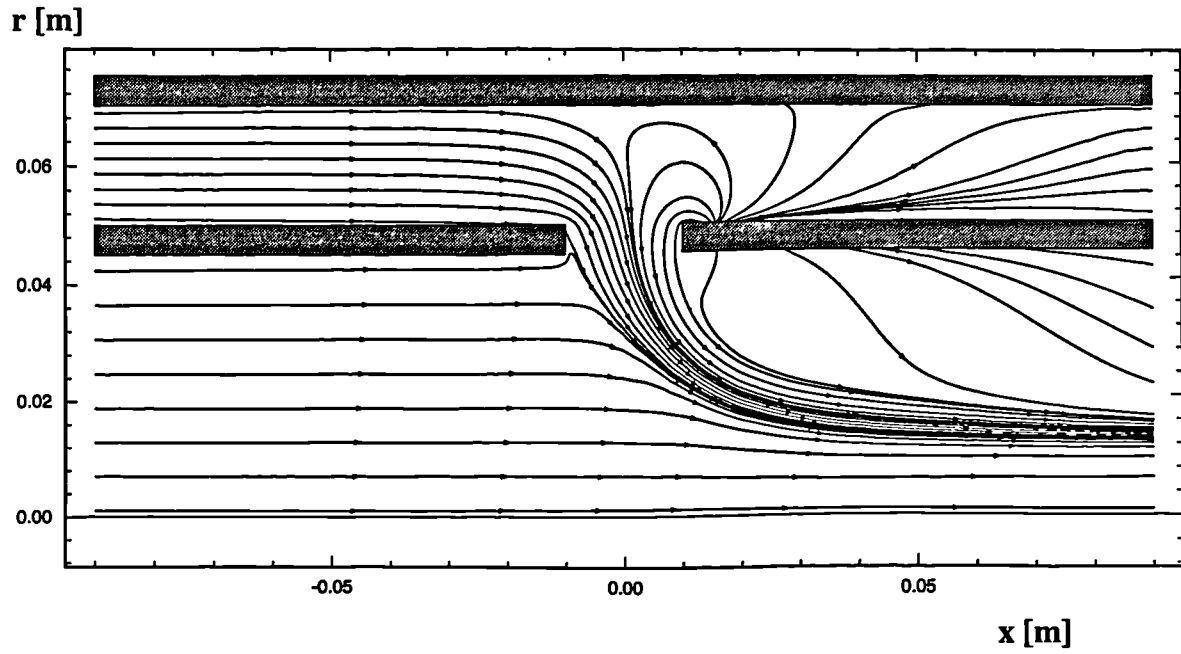
(a) Prediction
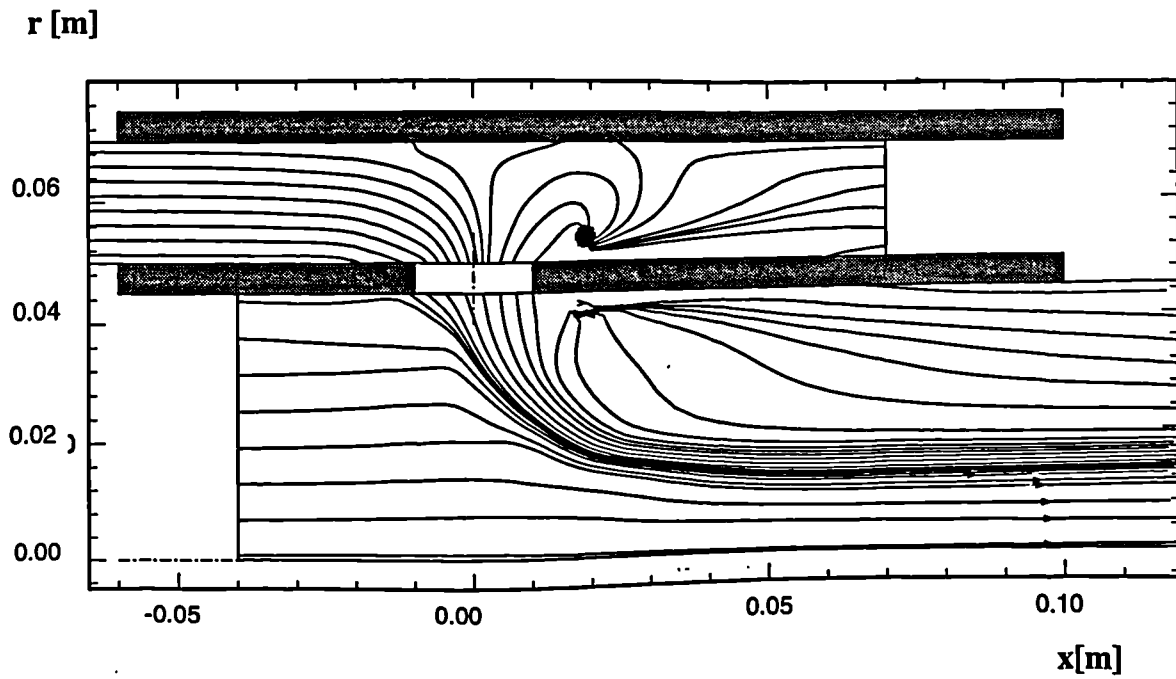
(b) Measurements

Figure 6.28 Particle Traces For Dilution Configuration
Plain Port, R=2.0, Bleed=20%
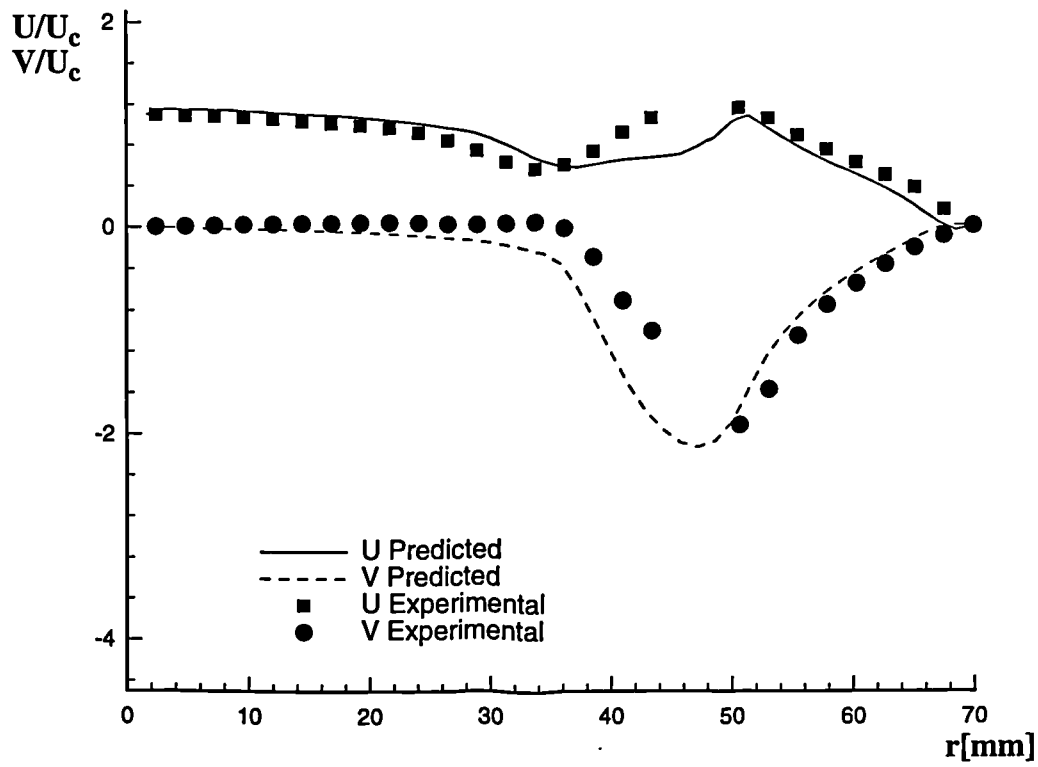
(a) x = -5mm
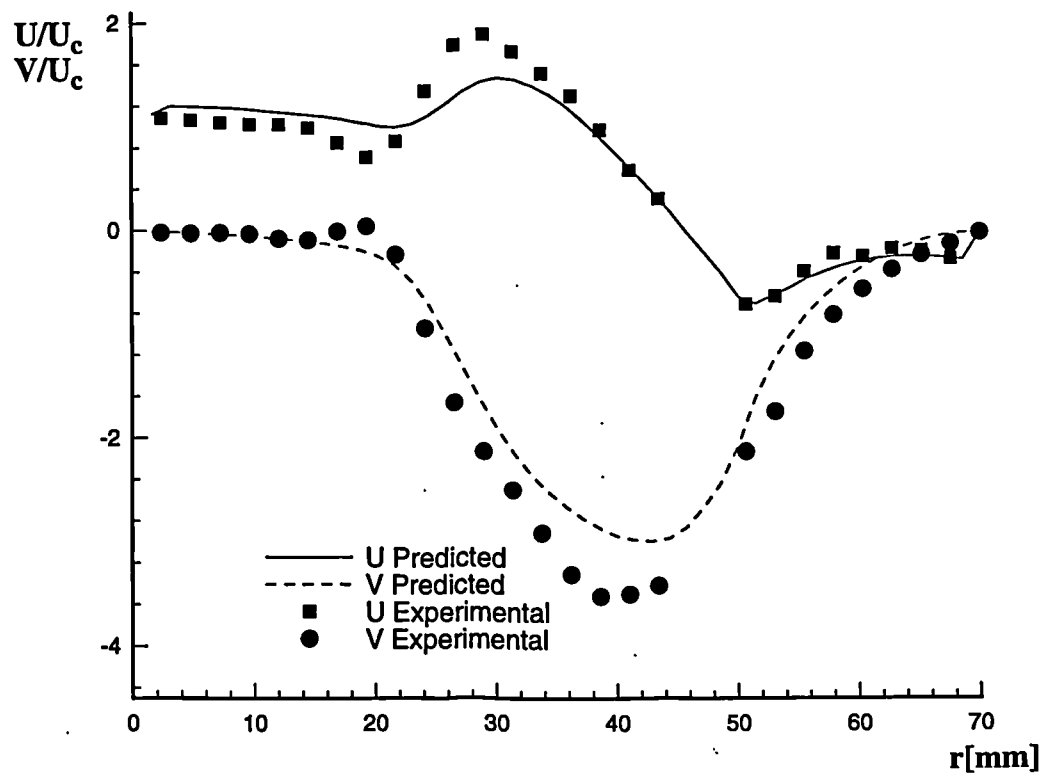
(b) x = 5mm

**Figure 6.29 Velocity Profiles at x=-5 and x=5mm, $\theta=0^\circ$, Dilution Flow
Plain Port, R=2.0, Bleed=20%**
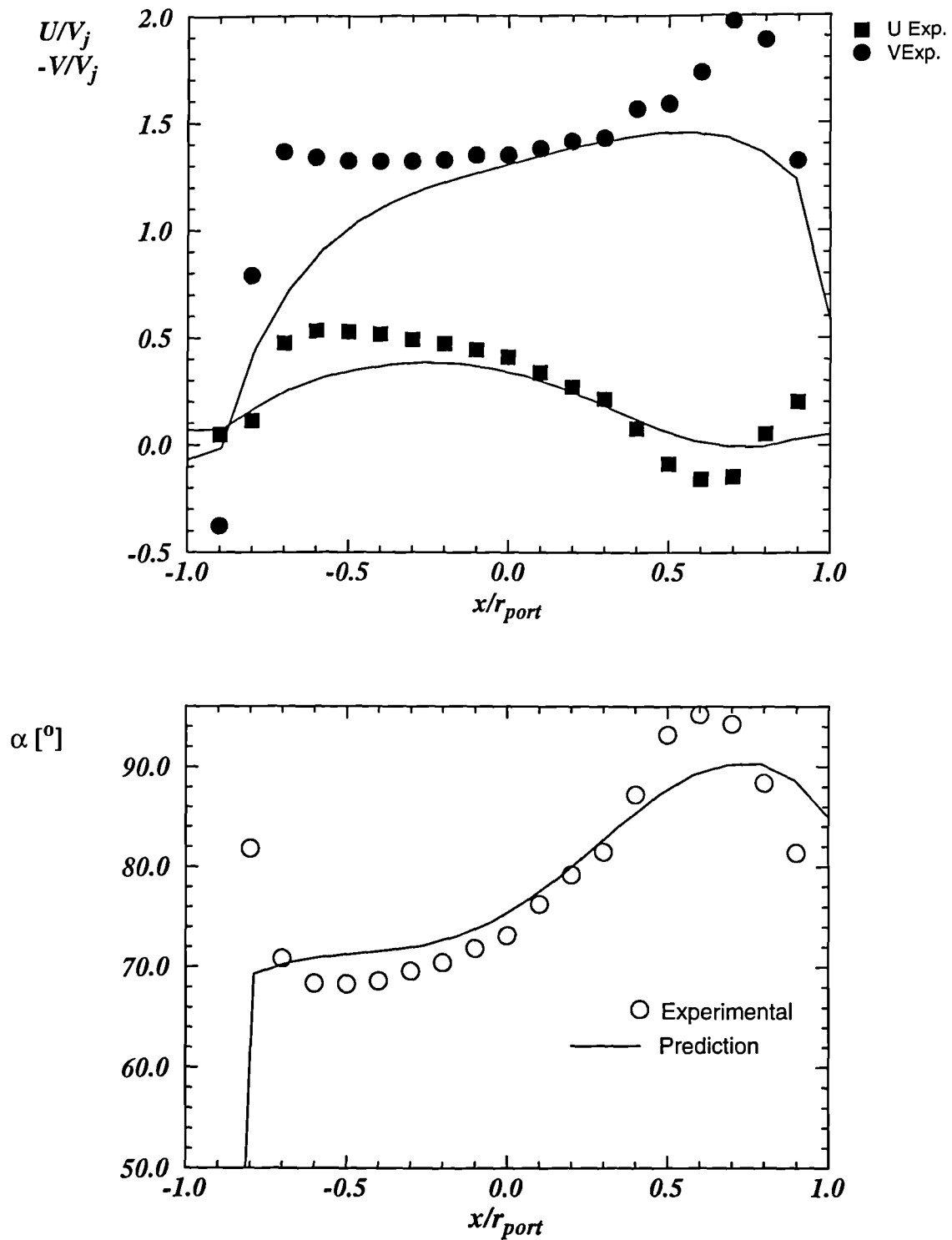
Figure 6.30 Jet Exit Velocity and Flow Angle for Diluiton Configuration
Plain Port, R=2.0, Bleed=20%

x=-10mm

x=10mm
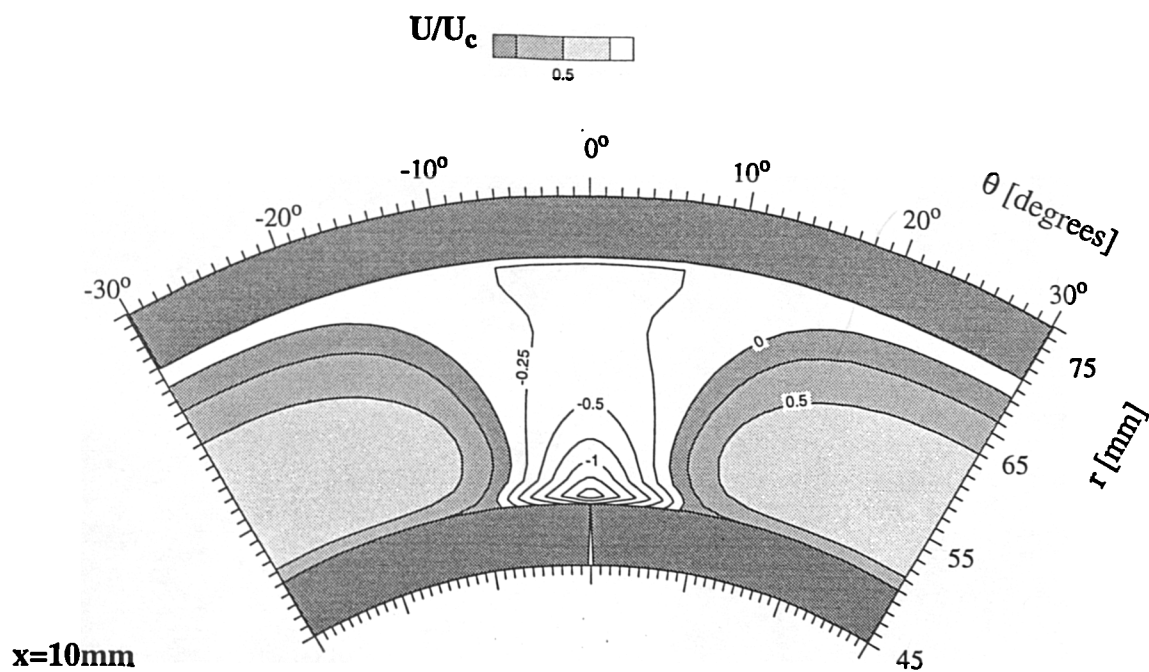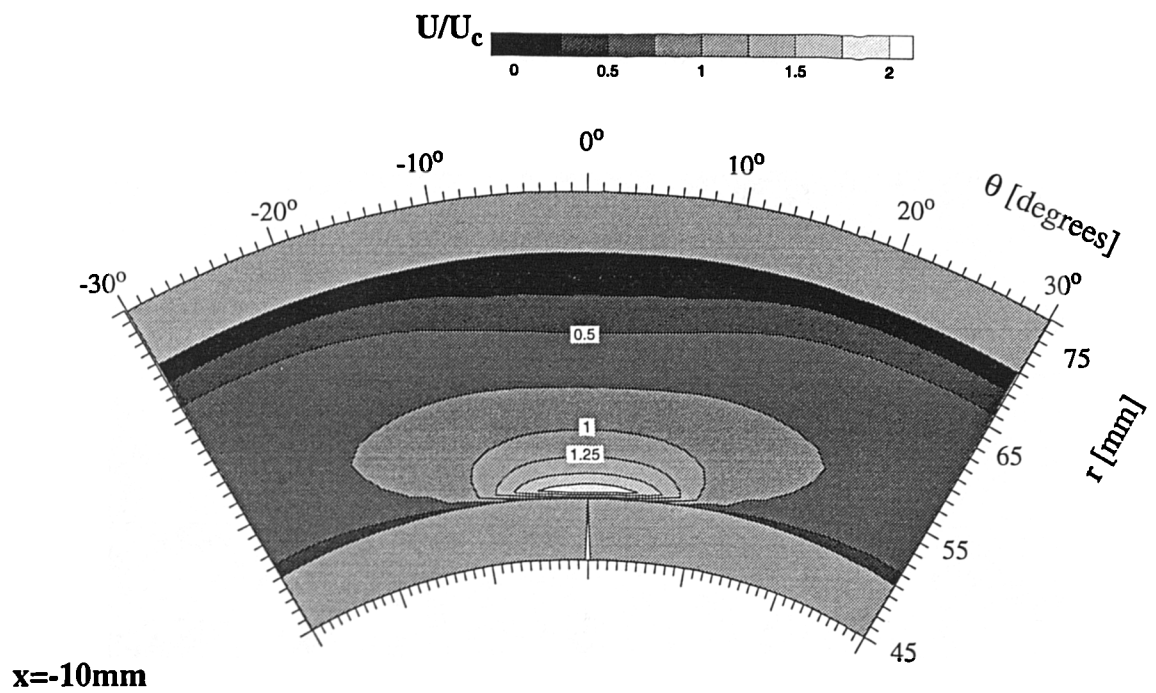
Figure 6.31 Axial Velocity Distribution in Annulus on x=-10 and x=10 Planes
Plain Port, R=2.0, Bleed=20%
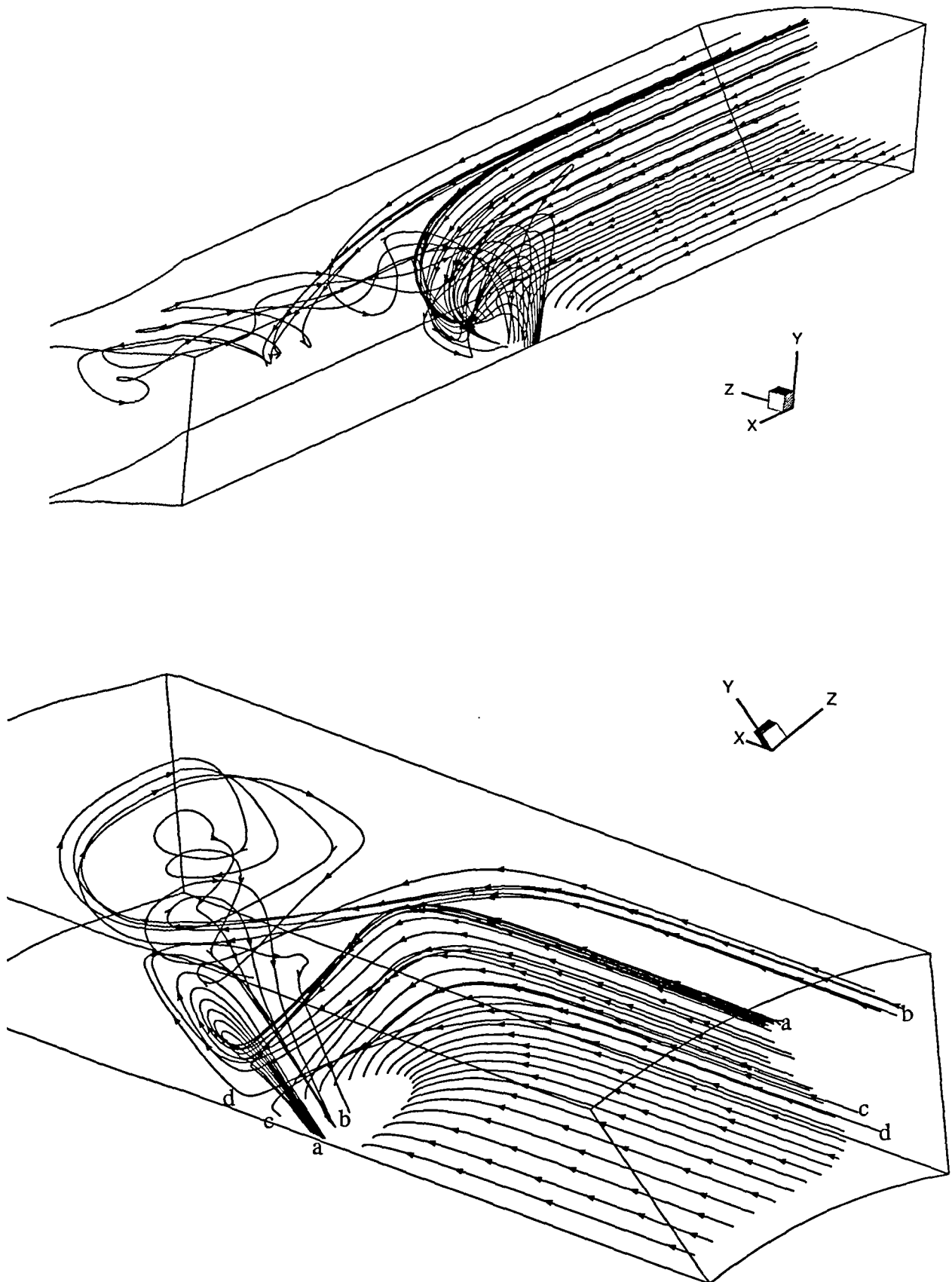
Figure 6.32 Reverse Particle Tracks Released From Port Perimeter
Plain Port, R=2.0, Bleed=20%
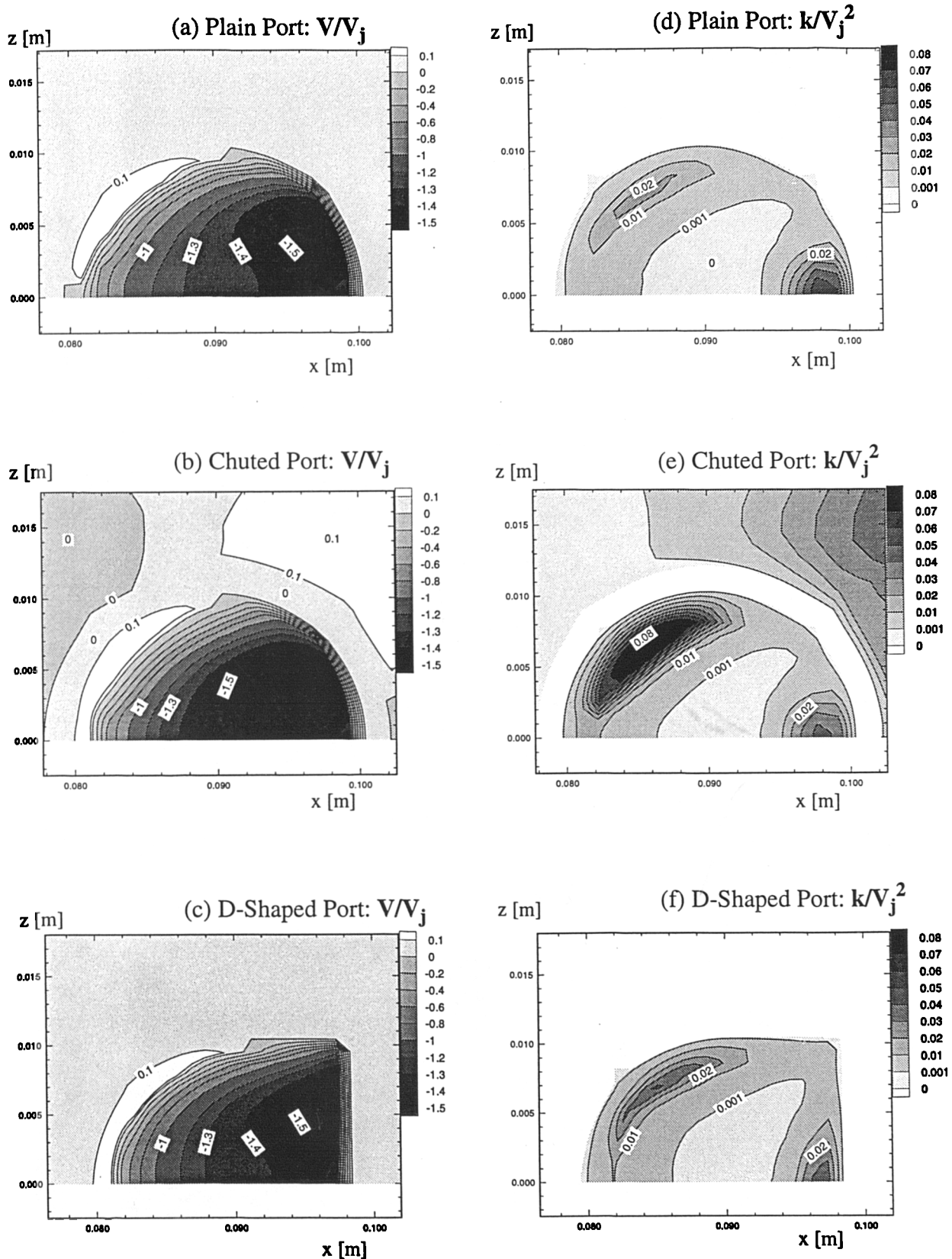
Figure 6.33 Port Exit Radial Velocity and Turbulent Kinetic Energy Distribution
R=5.0, Bleed = 50%
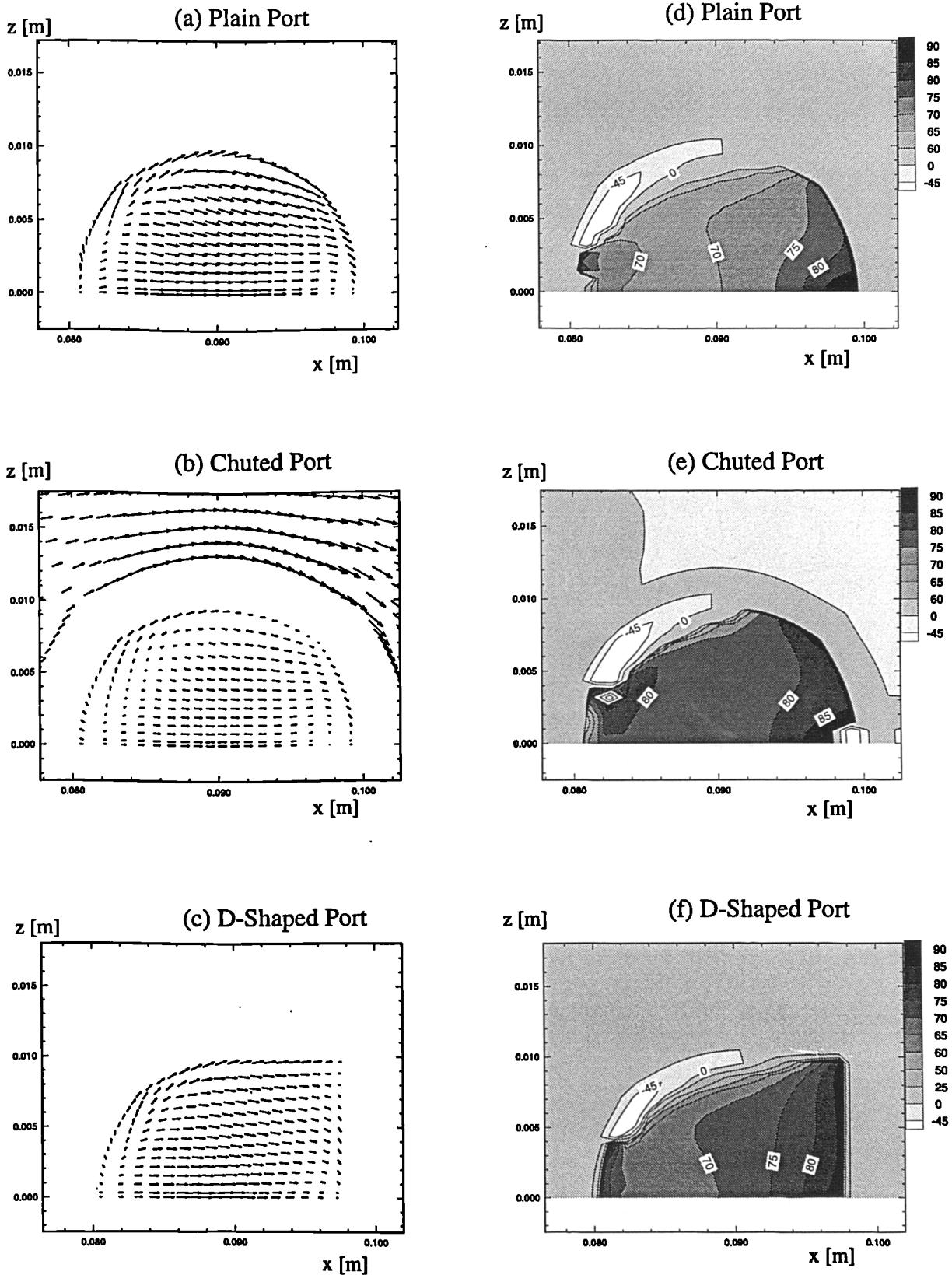
Figure 6.34 Port Exit Secondary Velocity Vectors and Flow Angle, α.
R=5.0, Bleed = 50%
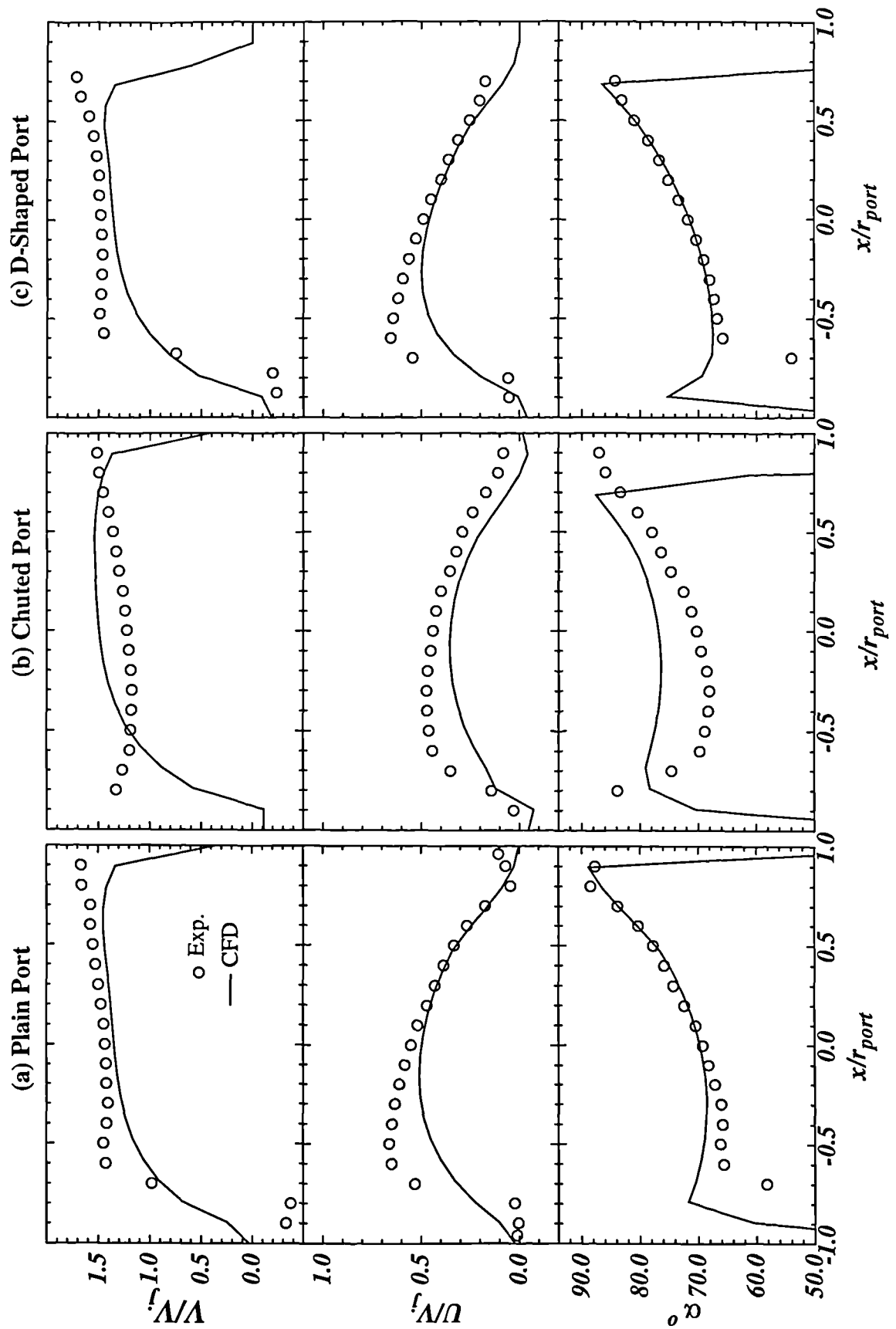
Figure 6.35 Predicted and Experimental Port Exit Characteristics
R=5.0, Bleed = 50%
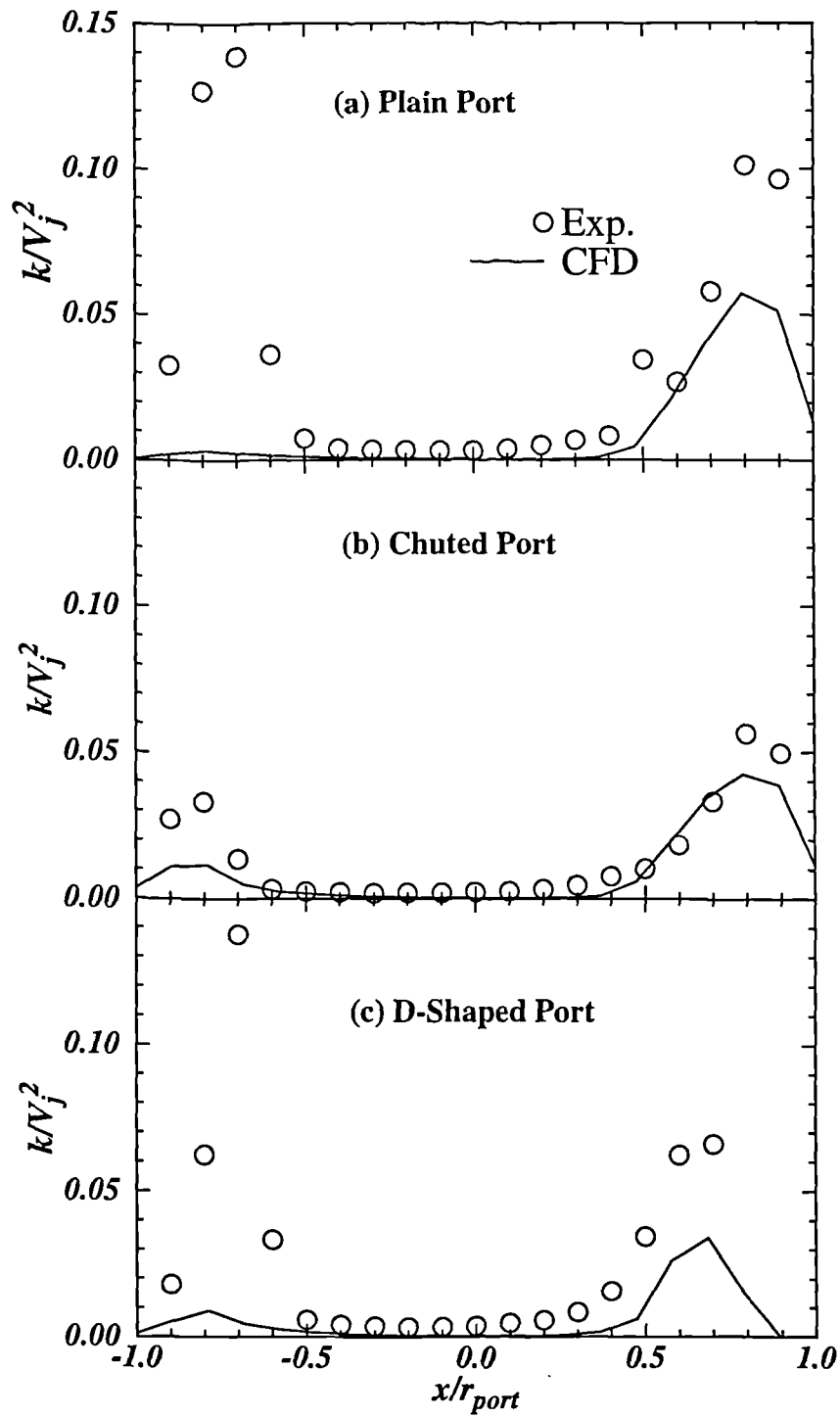
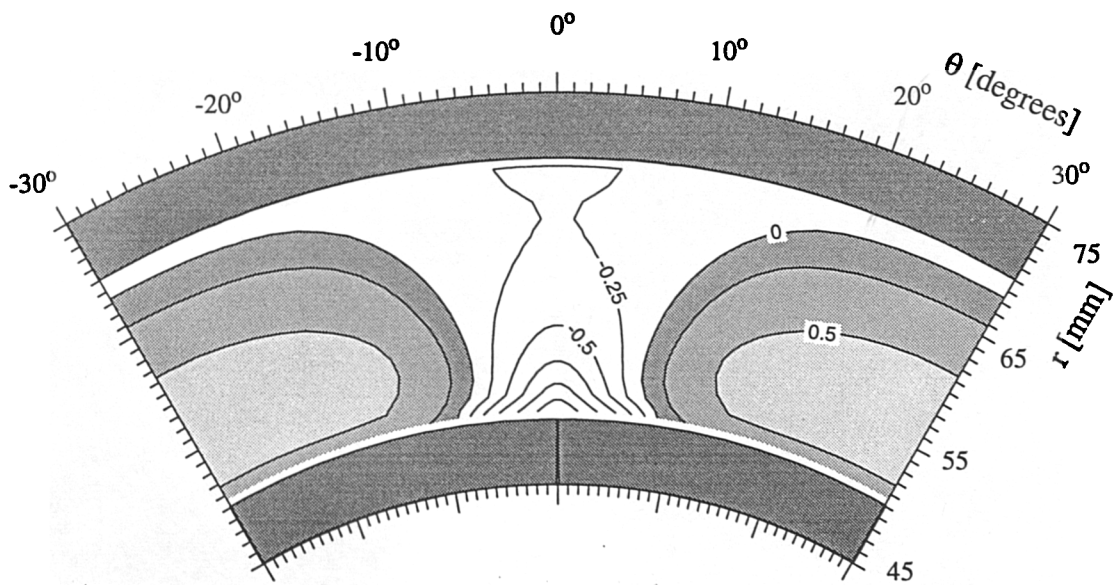**Figure 6.36 Port Exit Turbulent Kinetic Energy Profiles**
R=5.0, Bleed = 50%

(a) Velocity Vectors   x [mm]

(b) "Streamlines"   x [mm]
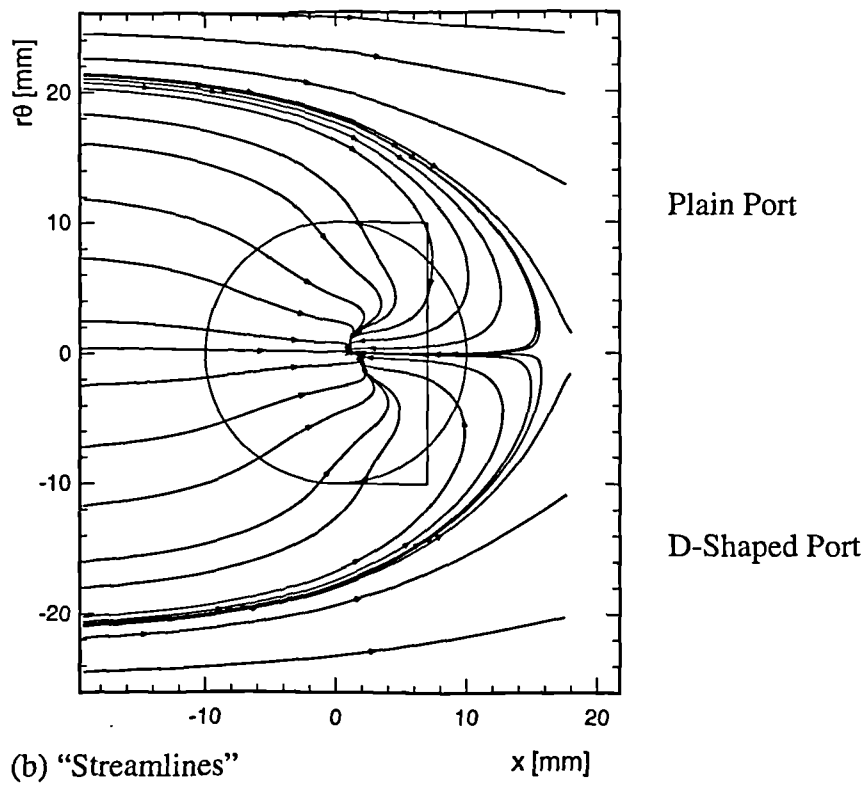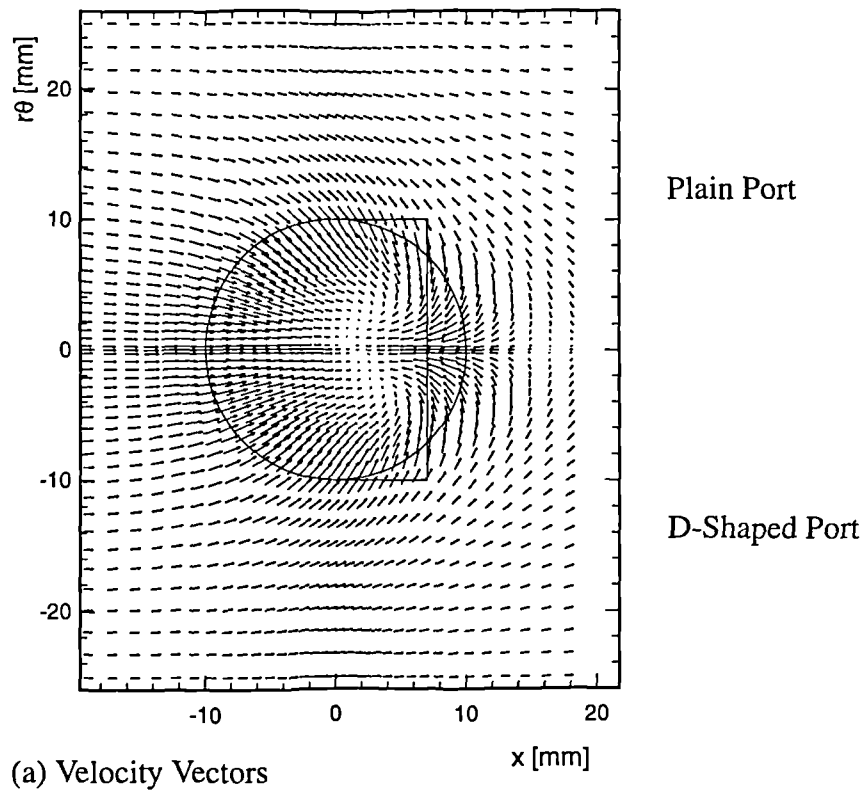
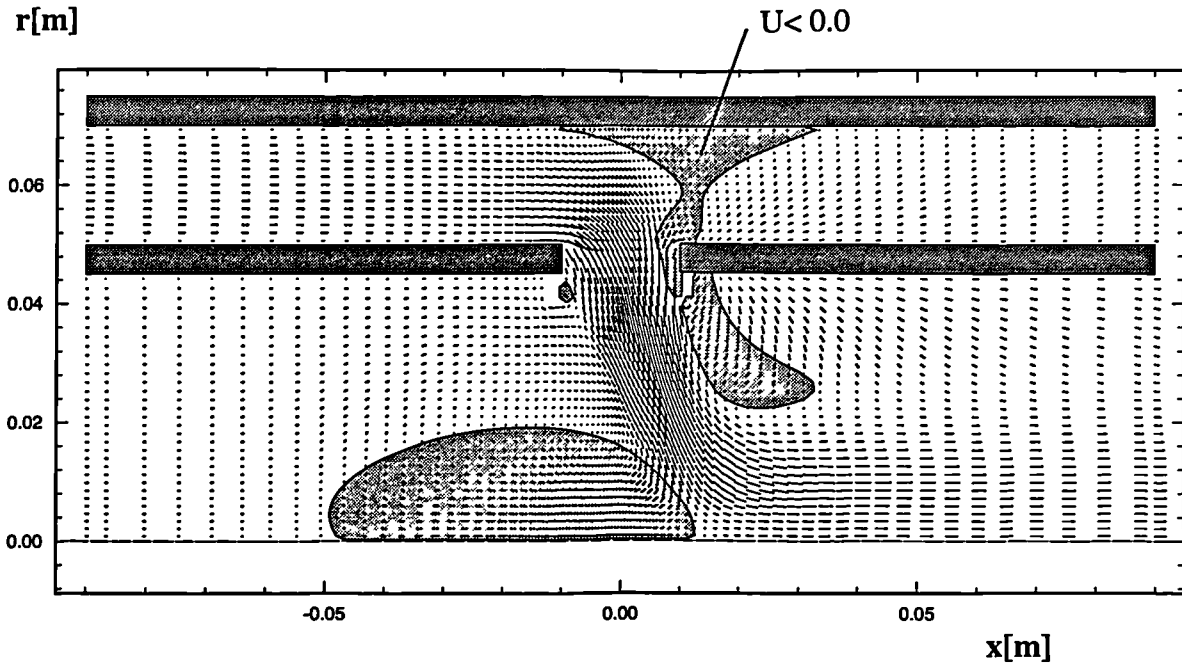**Figure 6.37 Secondary Velocity Components Near Inner Annulus Wall**
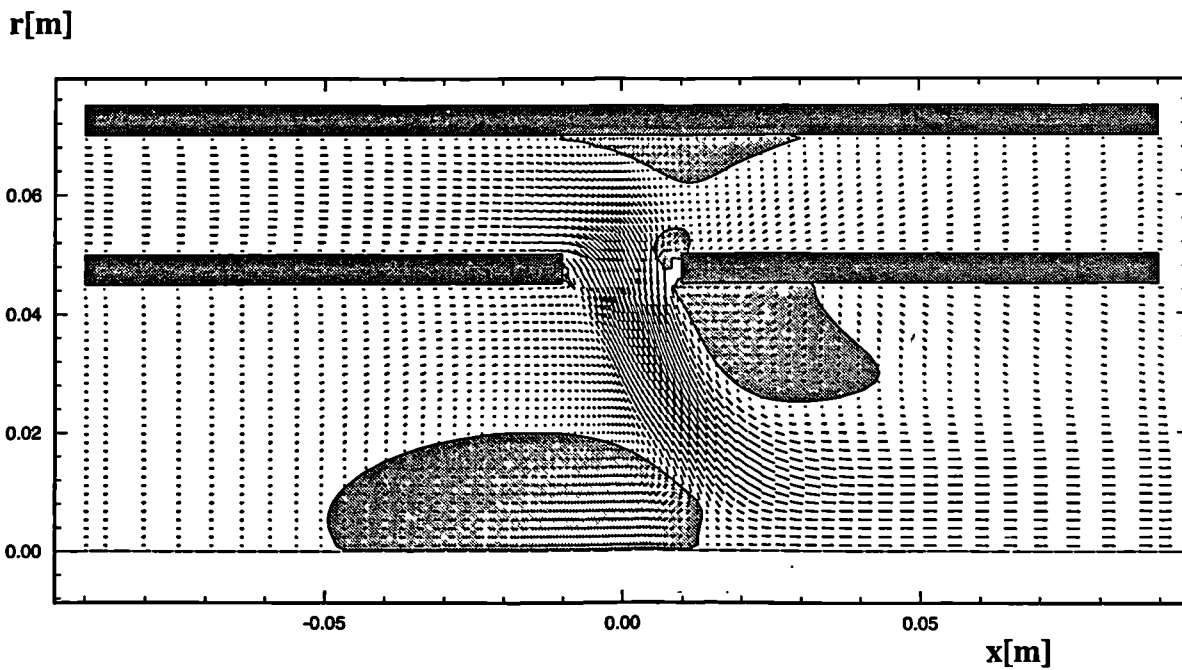R=2.0, Bleed = 20%
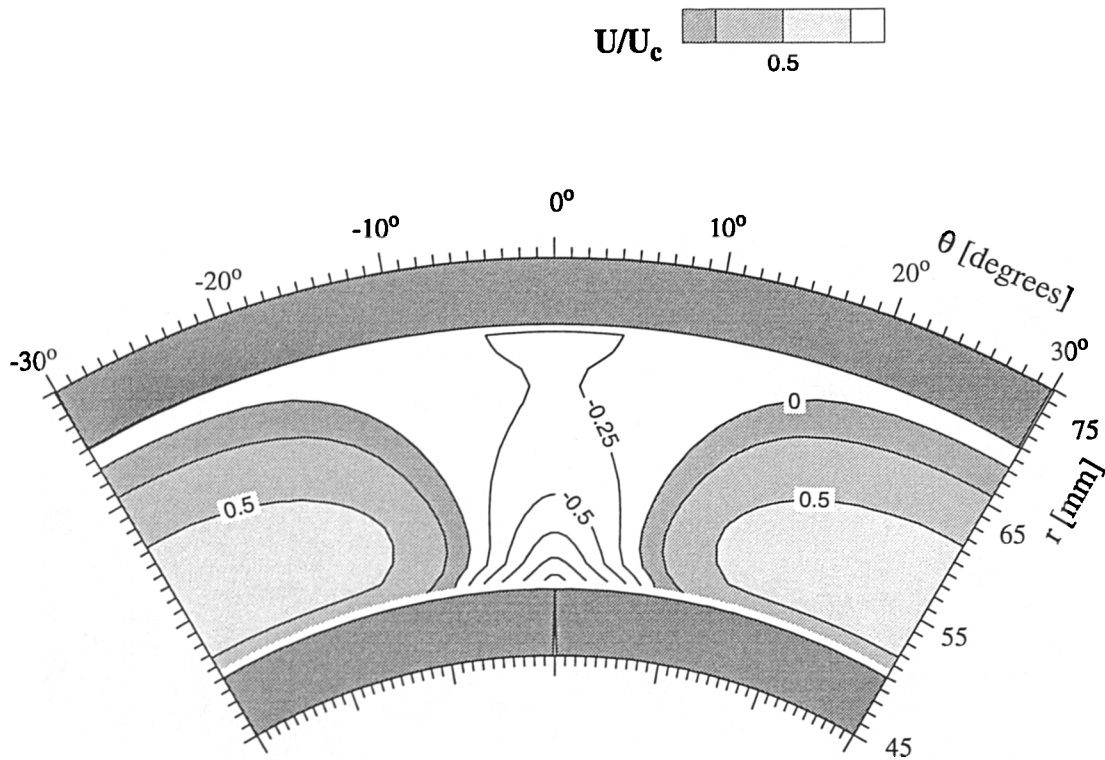
(a) Chuted Port, x=10mm

(b) D-Shaped Port, x=7mm

Figure 6.38 Axial Velocity Distribution on Axial Plane Downstream of Port
R=2.0, Bleed = 20%

(a) Chuted Port

(b) D-Shaped port

Figure 6.39 Velocity Field on θ=0° plane
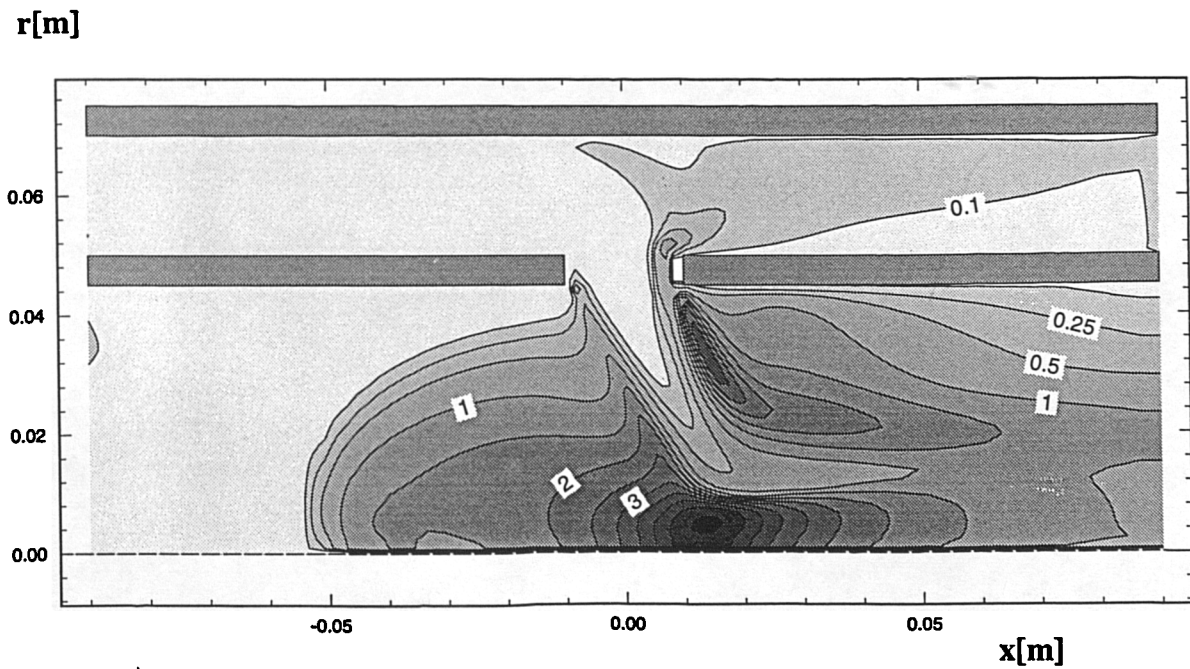R=5.0, Bleed = 50%
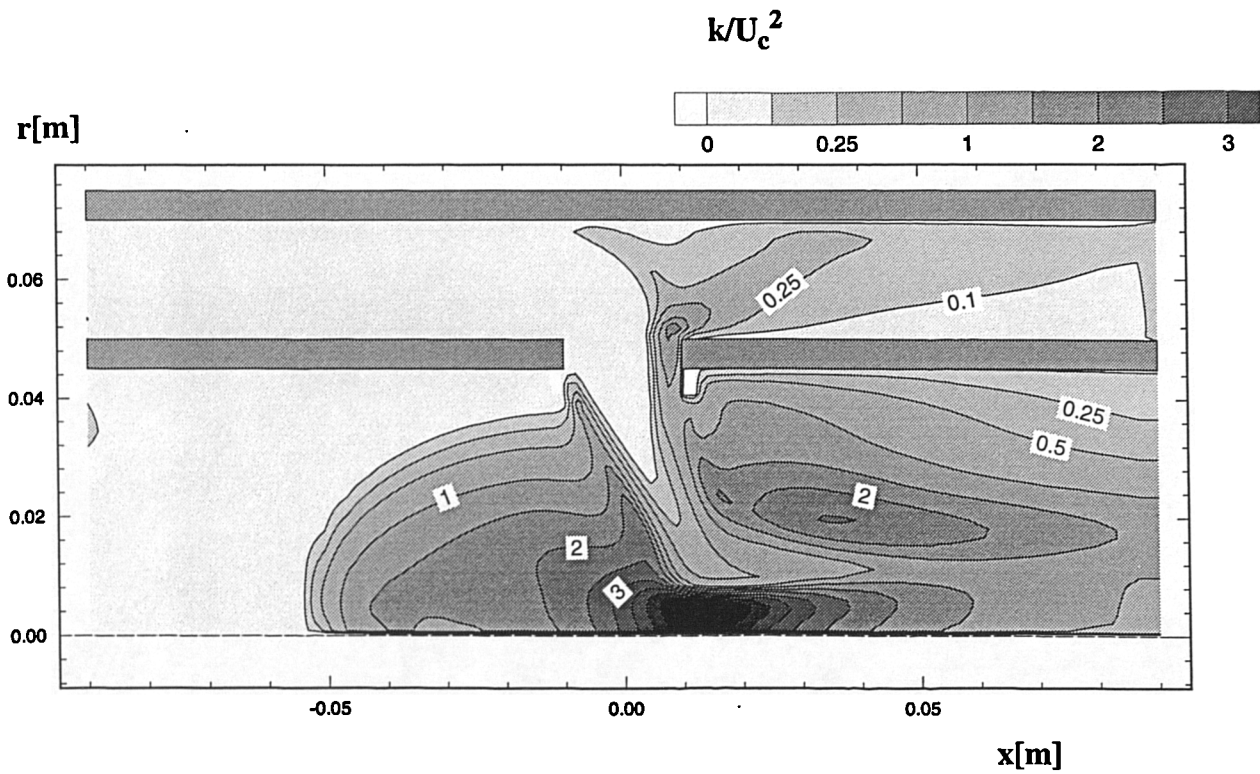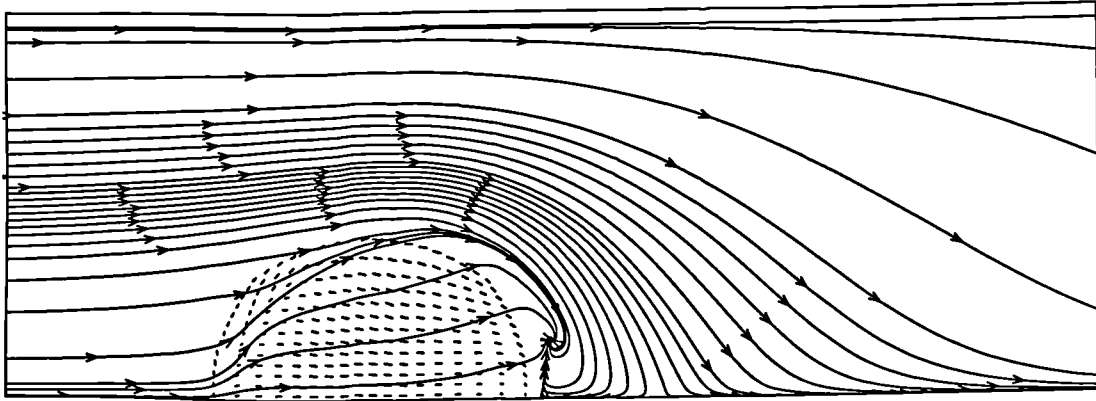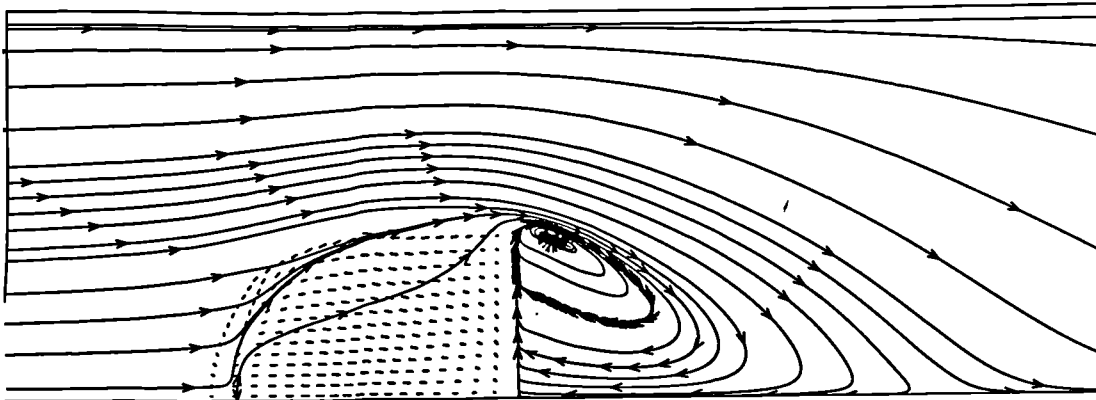
$$k/U_c^2$$

(a) Chuted Port

(b) D-Shaped port

Figure 6.40 Turbulence Field on θ=0° plane
R=5.0, Bleed = 50%

(a) Plain Port

(b) D-Shaped Port

Figure 6.41 Predicted Streamlines on Radial Plane in the Core Close to Port Exit
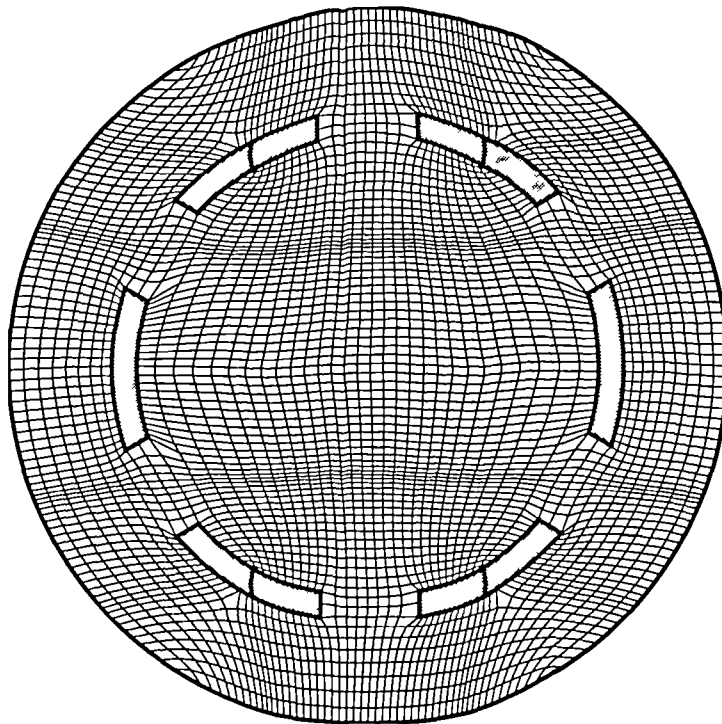
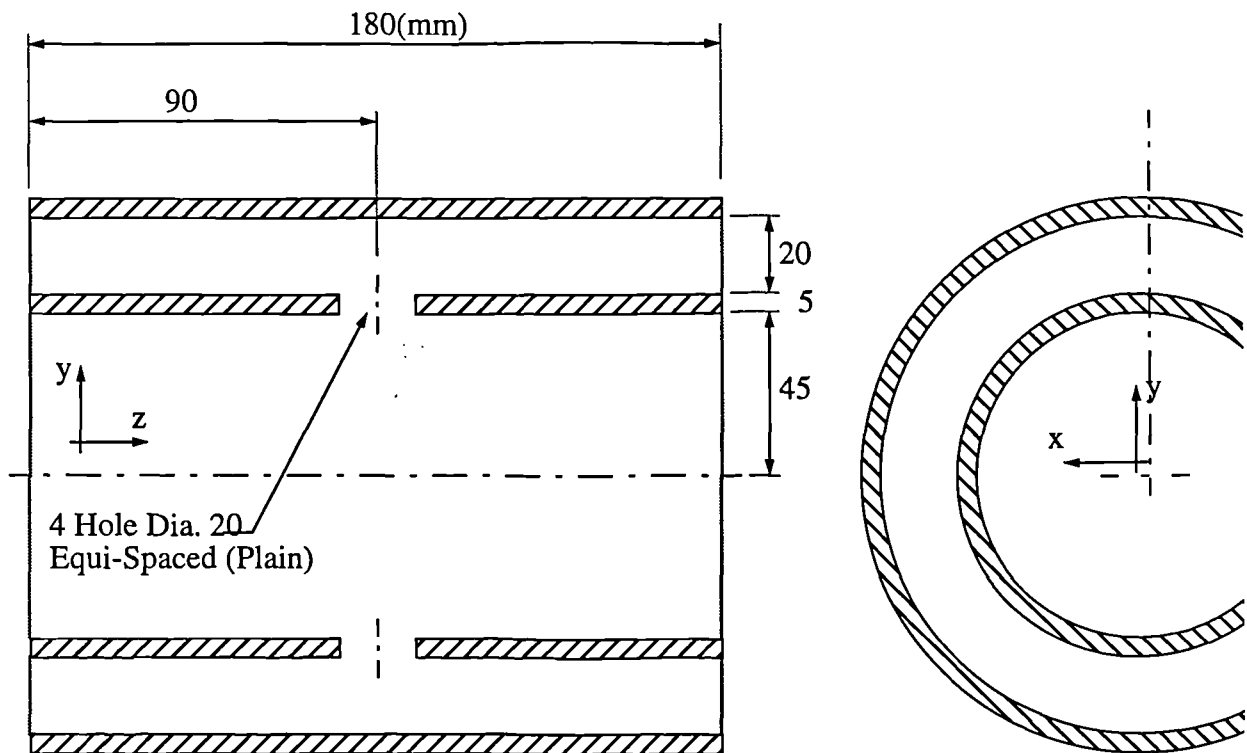**Figure 6.42 Ill-Conditioned Structured Mesh For Six-Hole Geometery (fig. 6.17a)**

Figure 6.43 Adopted Four-Hole Geometery

(a) Surface Mesh (Quarter Removed)

(b) Axial Plane Through Port Centre-Lines
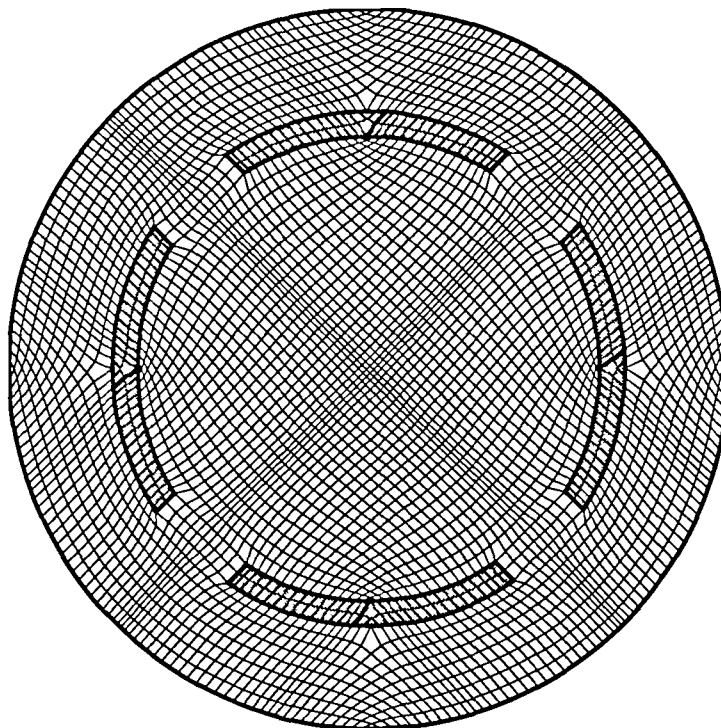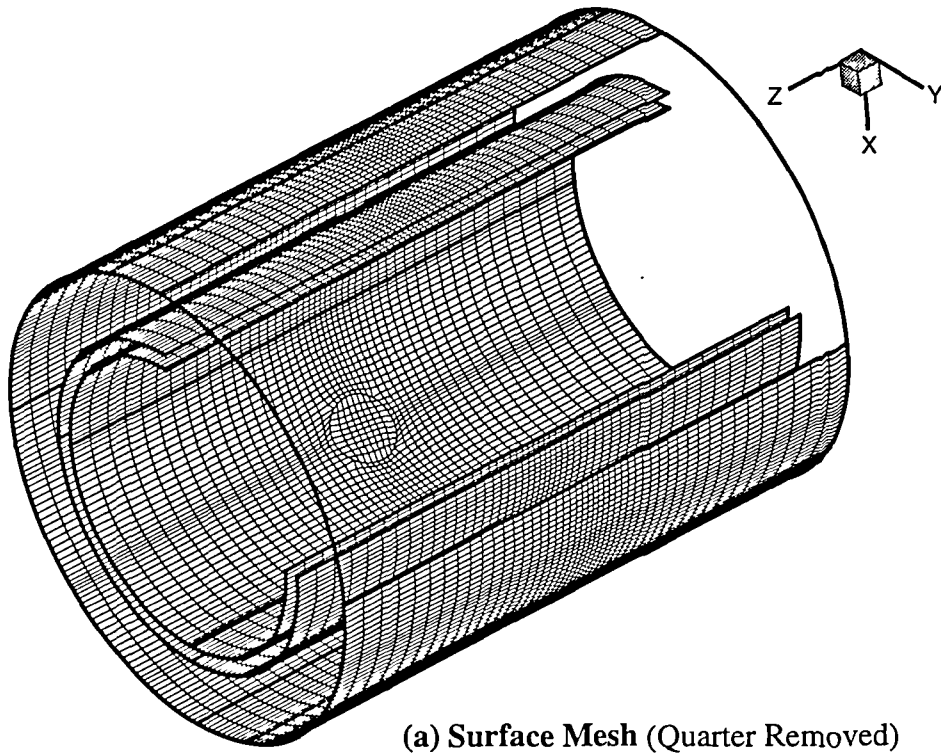
Figure 6.44 Improved Mesh Using Four-Hole Geometery
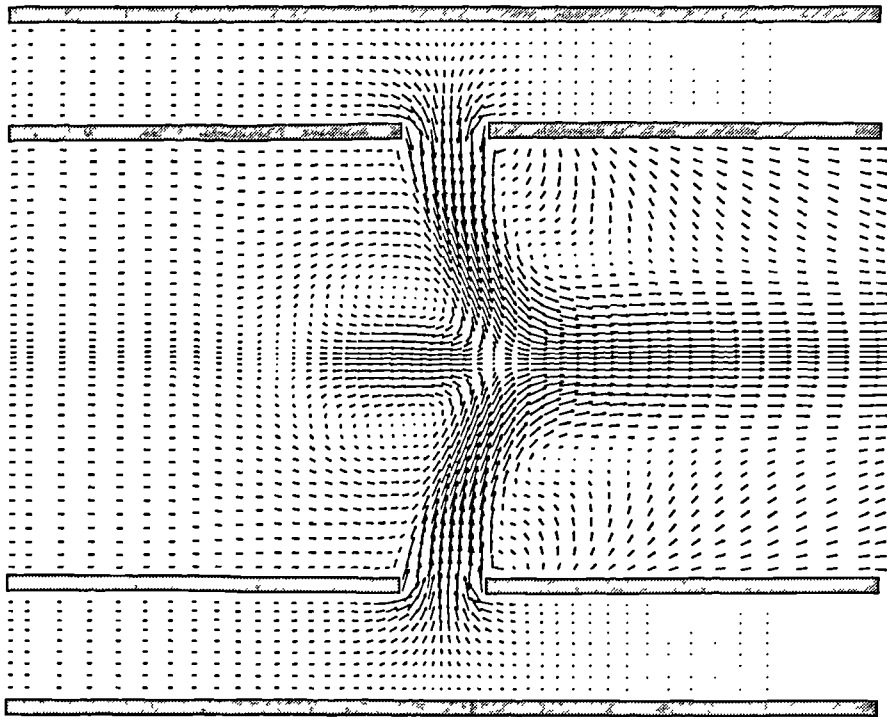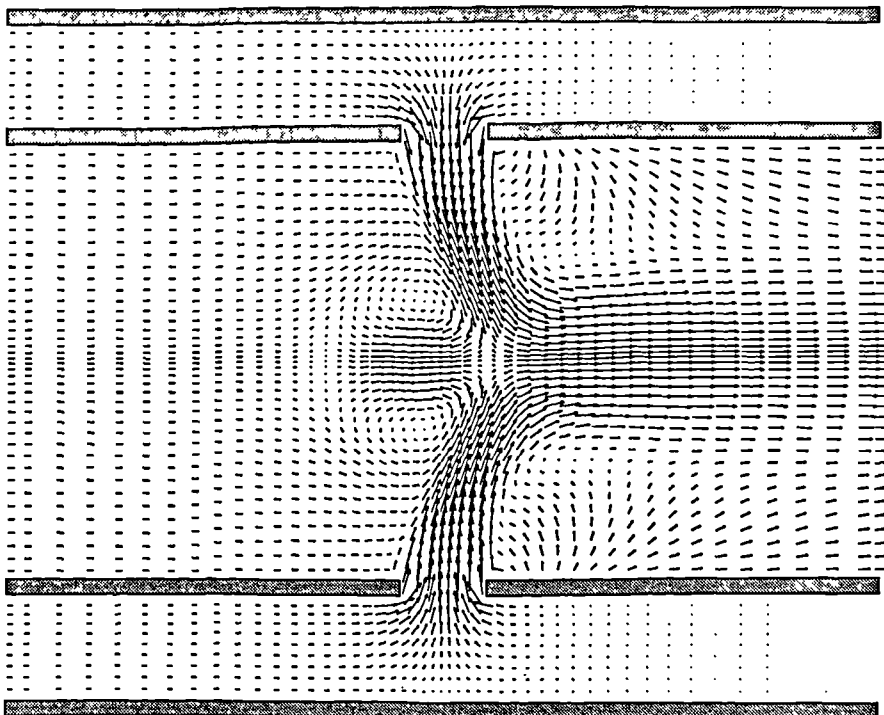
(a) $W_a/U_a=0.0$

(b) $W_a/U_a=0.215$

Figure 6.45 Velocity Vectors on Diametral Plane of Symetrey
Plain Port, R=4.0, Bleed=2%
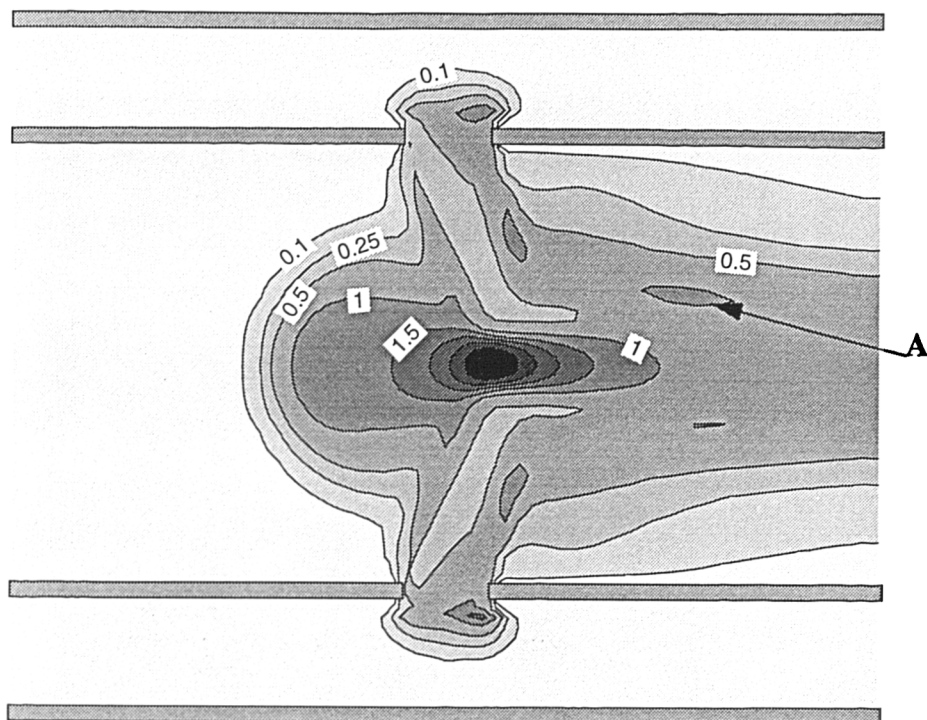
(a) $W_a/U_a = 0.0$
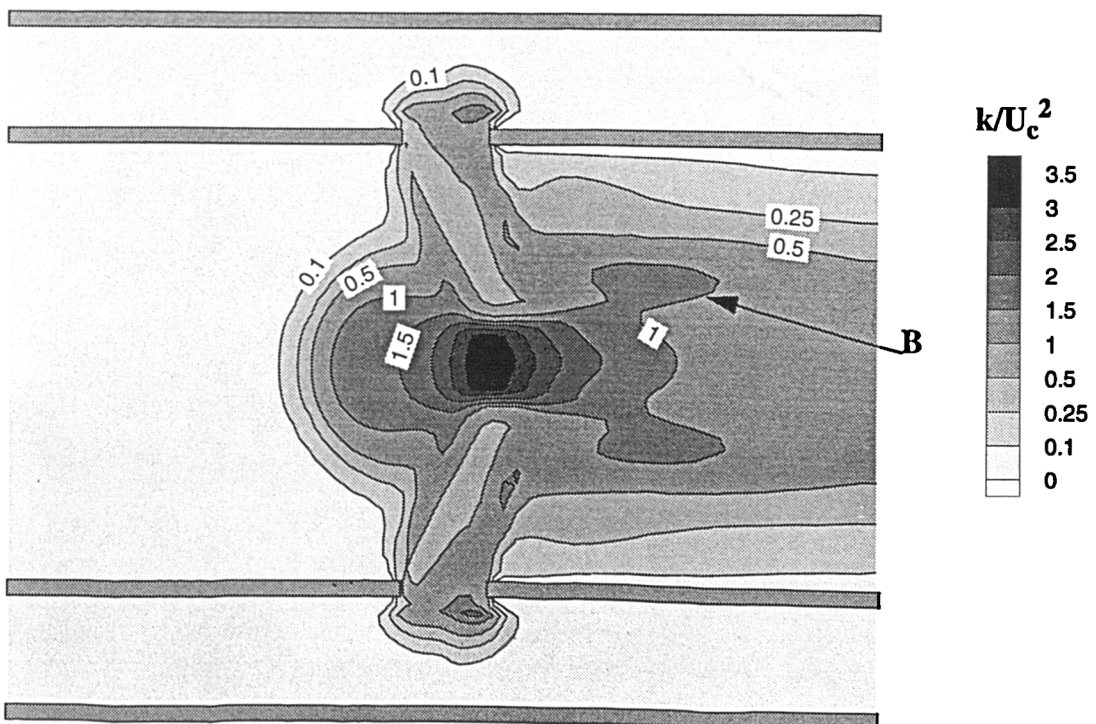
(b) $W_a/U_a = 0.215$

Figure 6.46 Turbulent Kinetic Energy on Diametral Plane of Symetrey
Plain Port, R=4.0, Bleed=2%
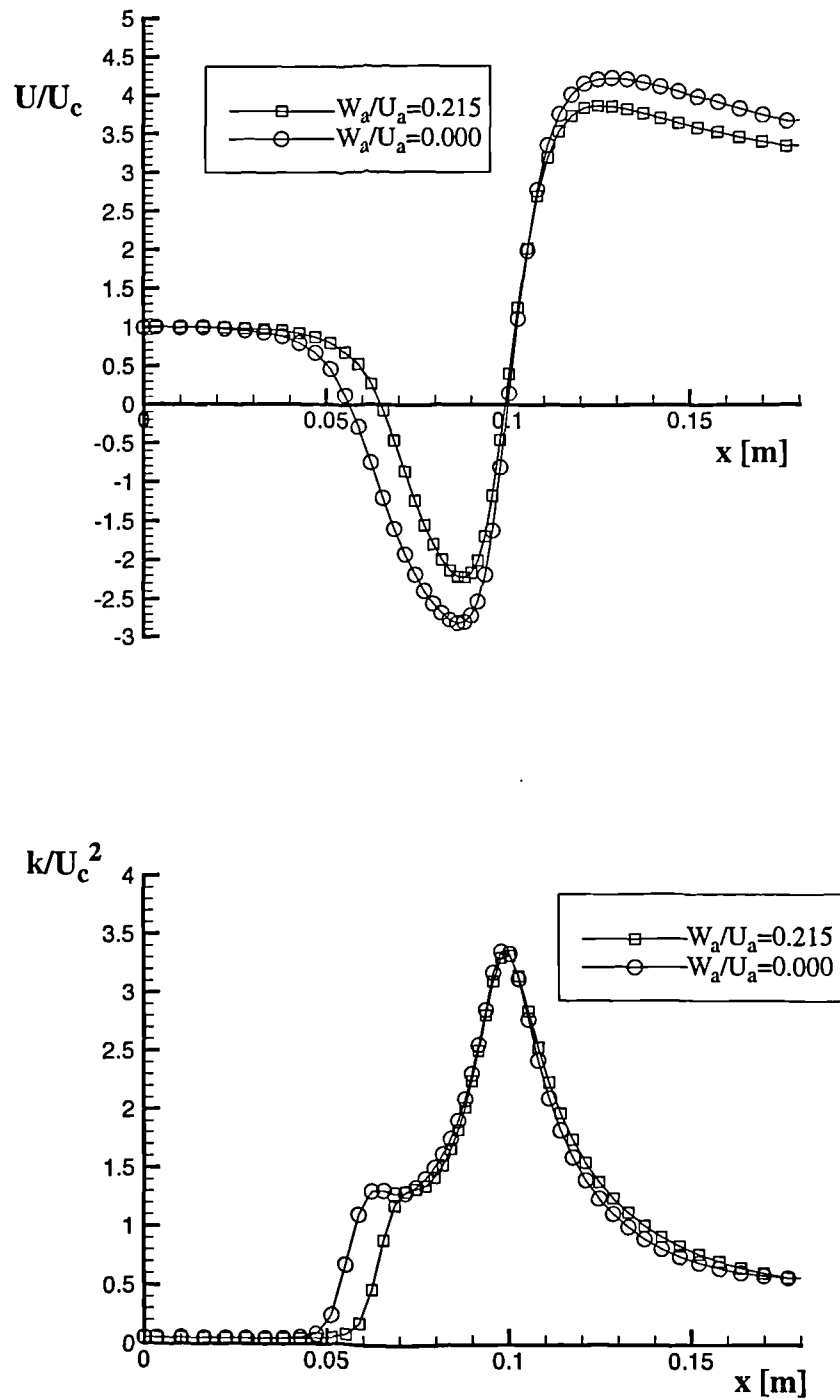
Figure 6.47 Axial Velocity and Turbulent Kinetic Energy Along Centreline
Plain Port, R=4.0, Bleed=2%

(a) mesh plane:
r≅68.5mm (on port centreline)

Ω_r

20.0
0.0
-20.0
-40.0
-60.0

(b) mesh plane: r≅62.9mm

Ω_r

20.0
0.0
-20.0
-40.0
-60.0

(c) mesh plane: r≅57.6mm

Ω_r

20.0
0.0
-20.0
-40.0
-60.0
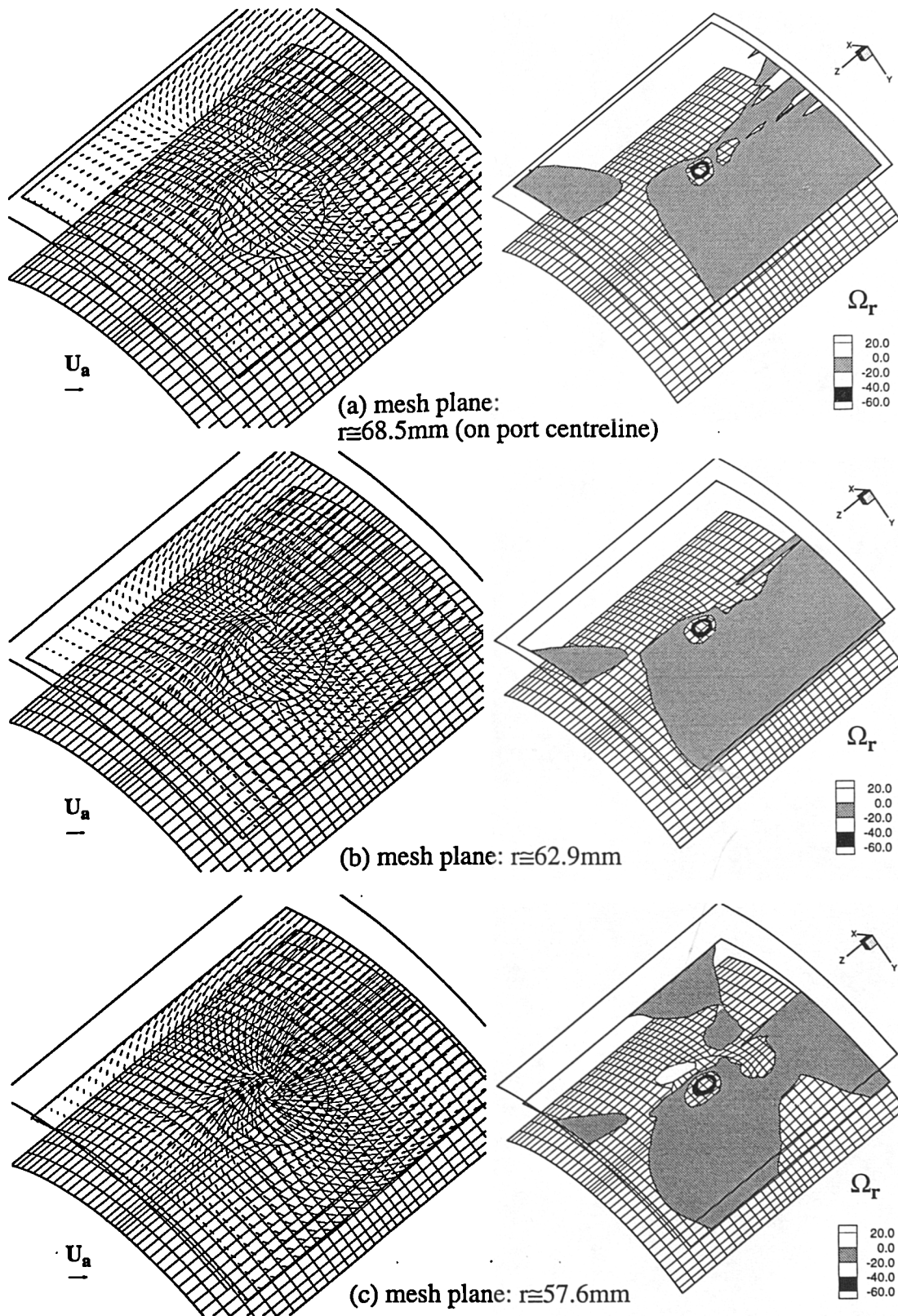
Figure 6.48 Secondary Velocity Vectors and Radial Vorticity Over Port
Plain Port, R=4.0, Bleed=2%, W_a/U_a=0.0

(d) mesh plane:
r≅52.4mm (on port centreline)

(e) mesh plane: r≅50.5mm

(f) mesh plane:
r≅42.5mm (below port exit)
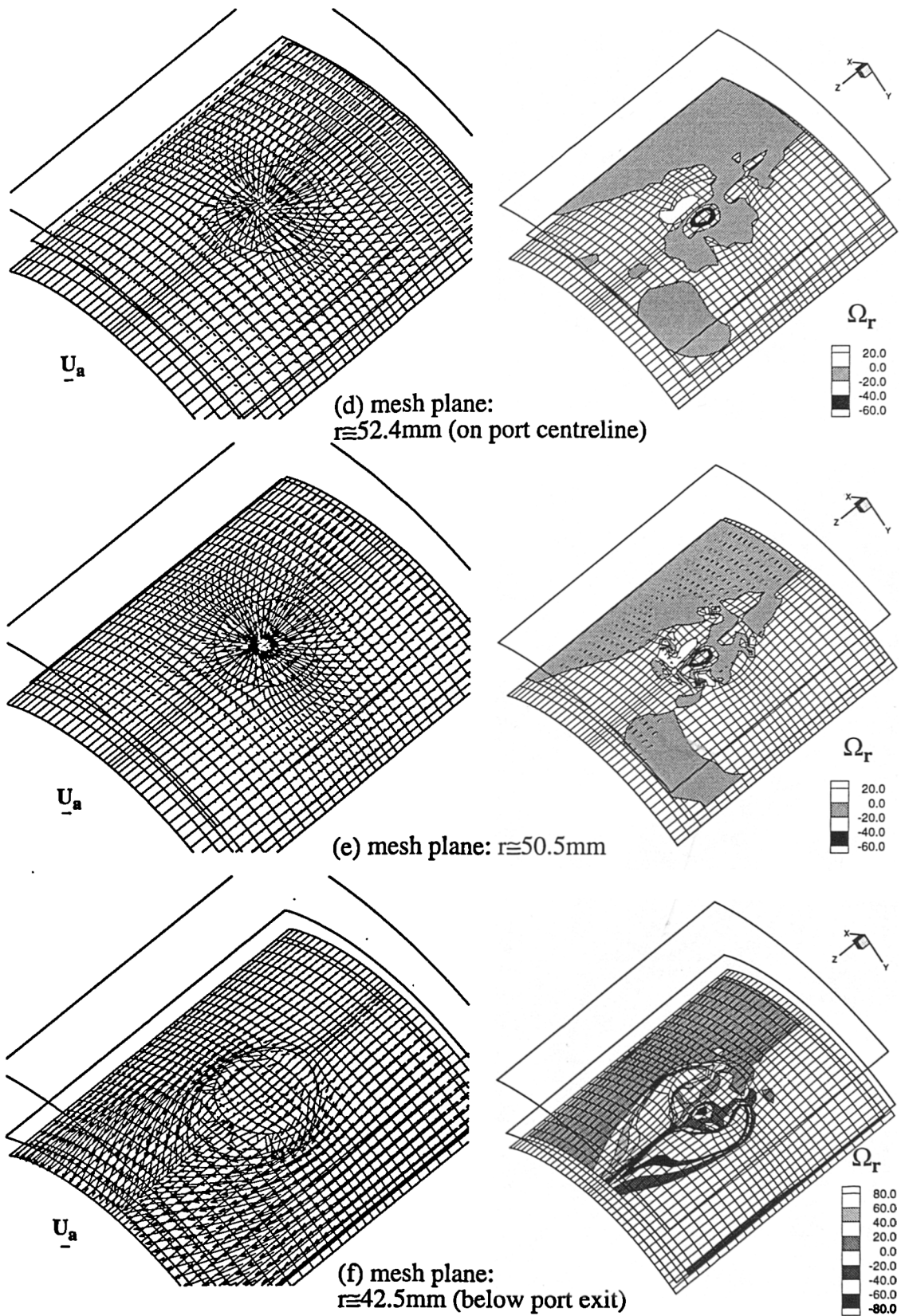
Figure 6.48(cont.) Secondary Velocity Vectors and Radial Vorticity Over Port
Plain Port, R=4.0, Bleed=2%, W_a/U_a=0.0

(a) mesh plane:
r≅68.5mm (on port centreline)

(b) mesh plane: r≅62.9mm

(c) mesh plane: r≅57.6mm
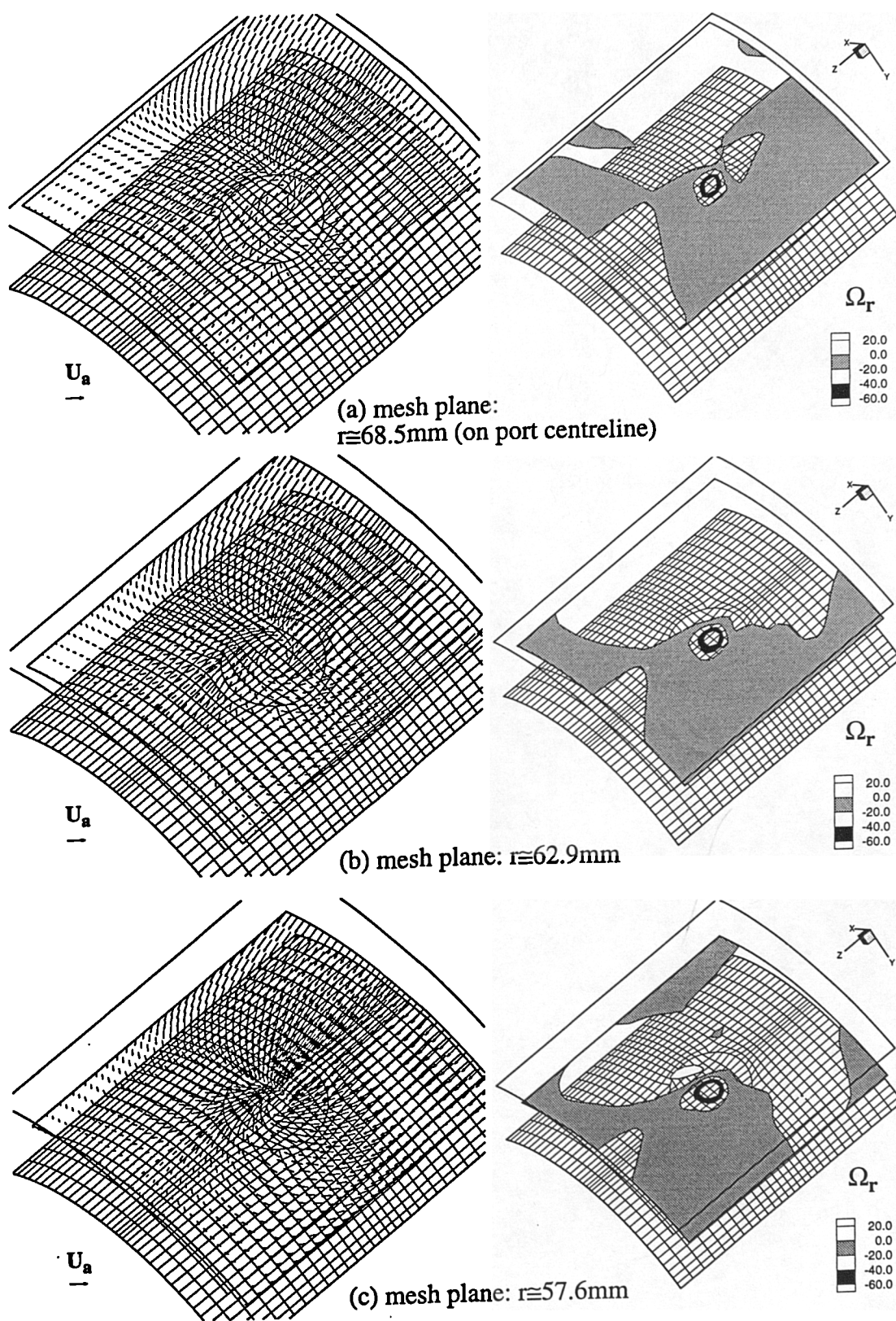
Figure 6.49 Secondary Velocity Vectors and Radial Vorticity Over Port
Plain Port, R=4.0, Bleed=2%, W_a/U_a=0.215

(d) mesh plane:
r≅52.4mm (on port centreline)

(e) mesh plane: r≅50.5mm

(f) mesh plane:
r≅42.5mm (below port exit)
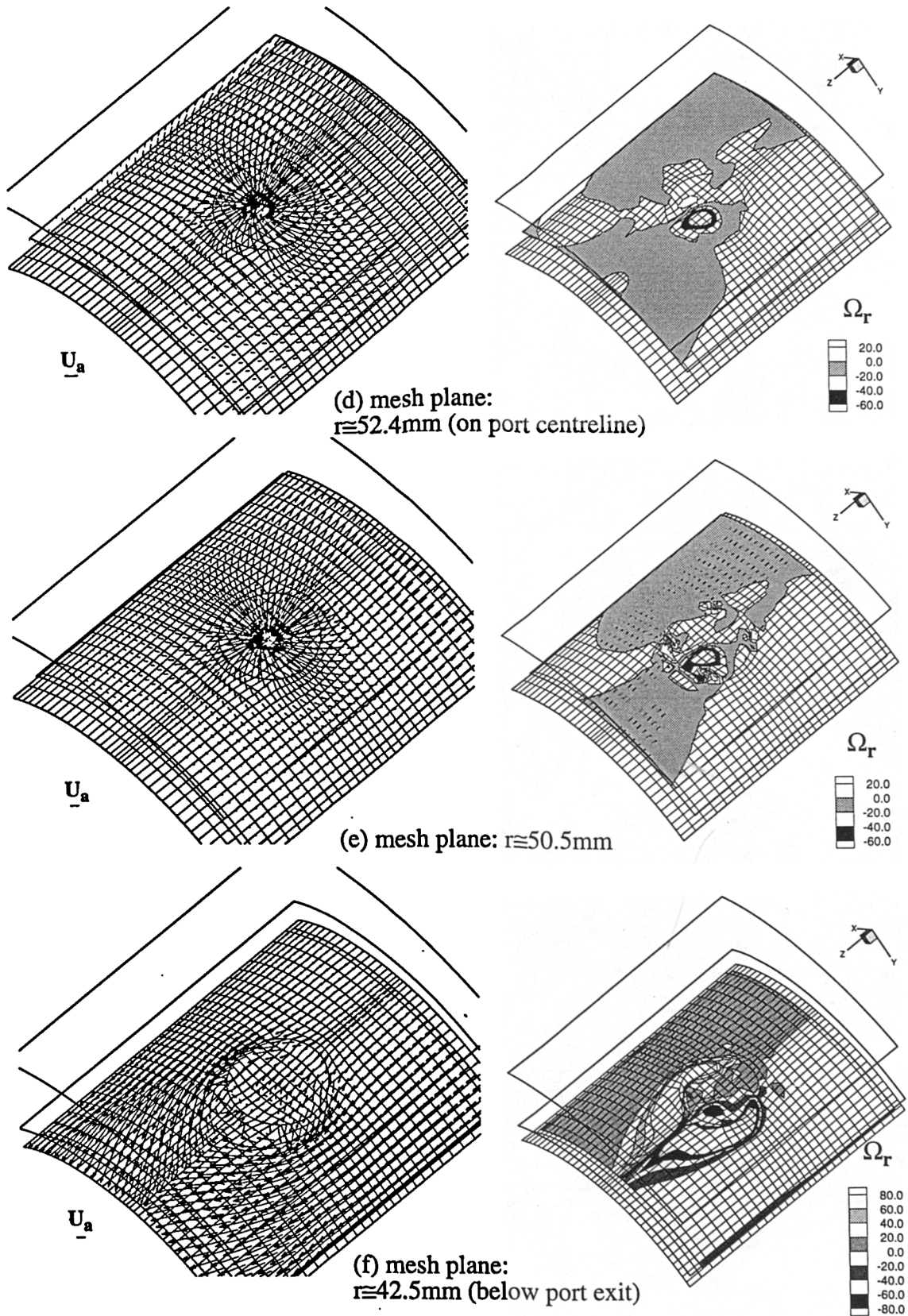
Figure 6.49(cont.) Secondary Velocity Vectors and Radial Vorticity Over Port
Plain Port, R=4.0, Bleed=2%, W_a/U_a=0.215
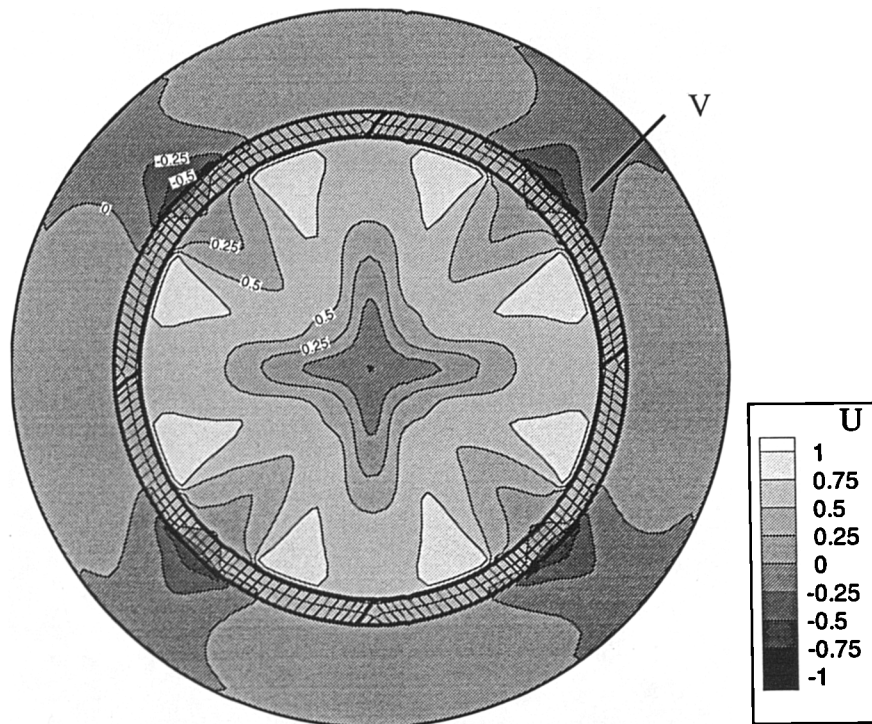
(a) $W_a/U_a = 0.0$

(looking upstream)
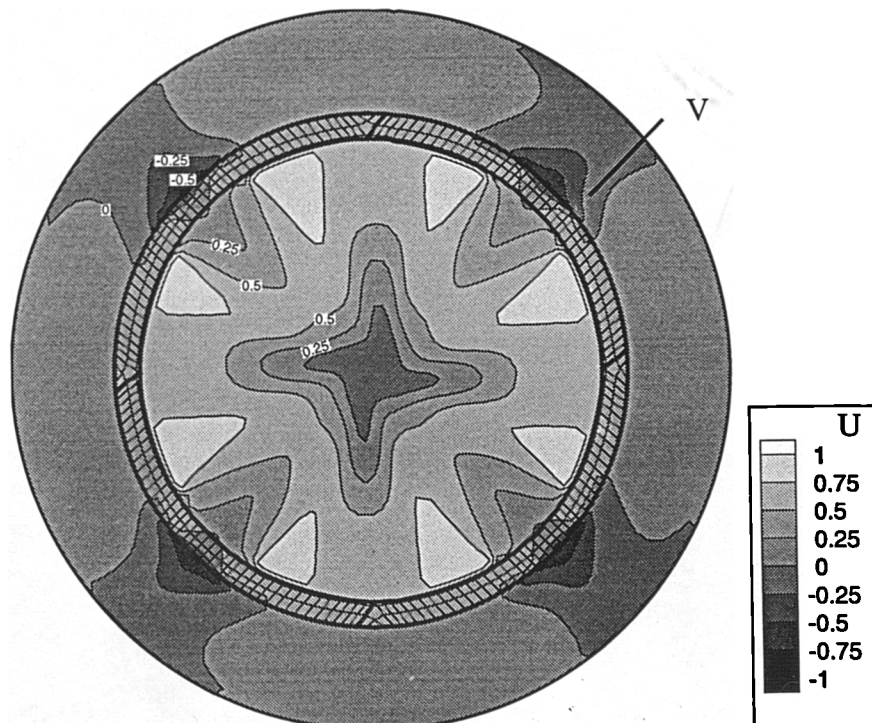
(b) $W_a/U_a = 0.215$

Figure 6.50 Axial Velocity Distribution on Plane x=10mm
Plain Port, R=4.0, Bleed=2%
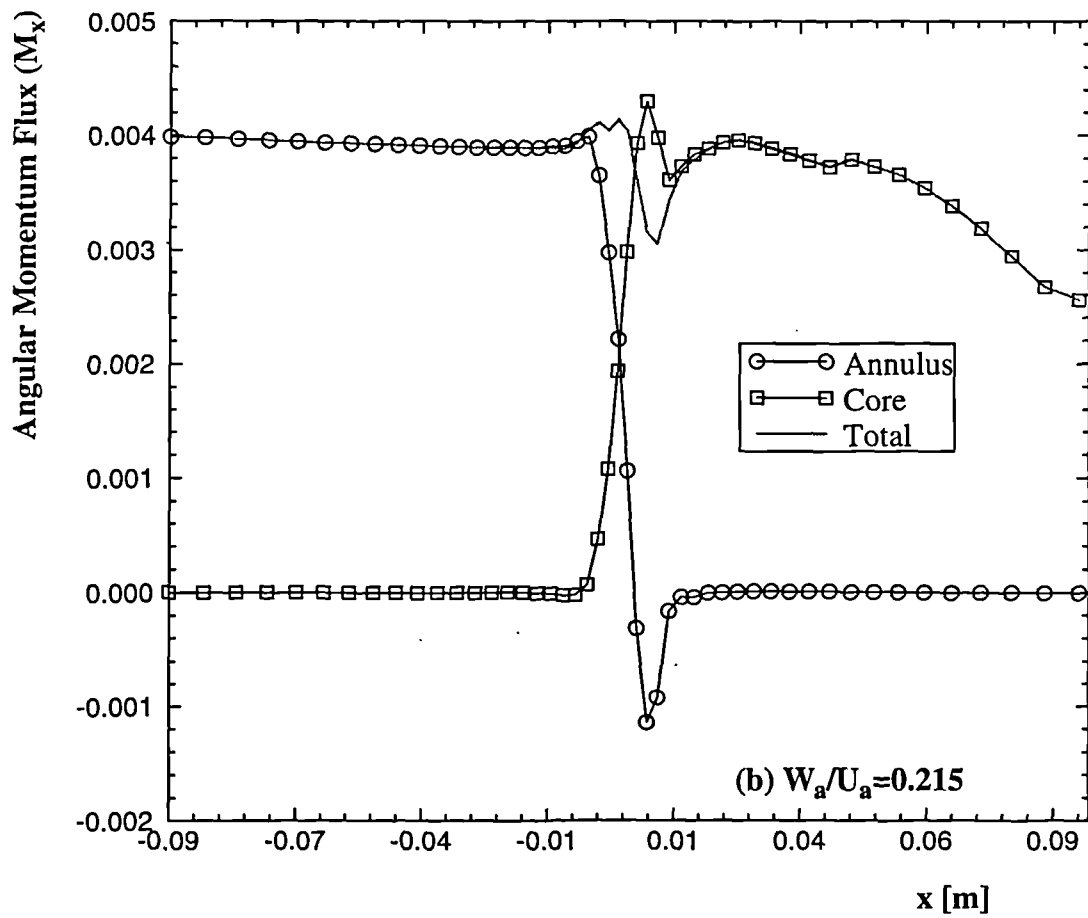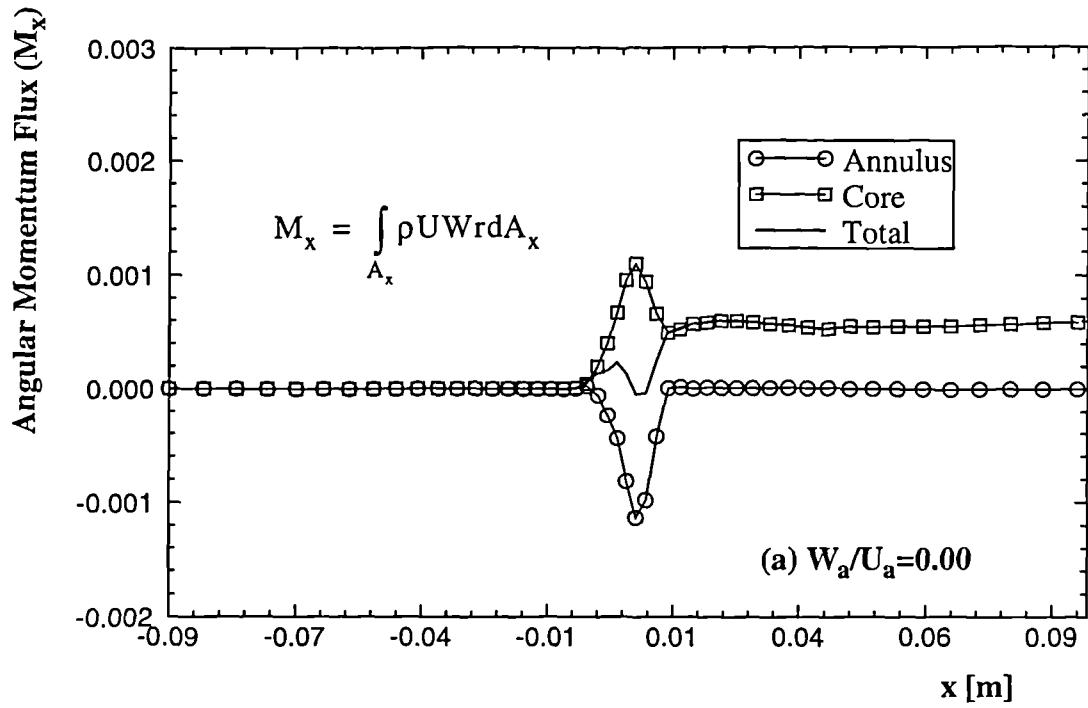
Figure 6.51 Total Axial Angular Momentum
Plain Port, R=4.0, Bleed=2%
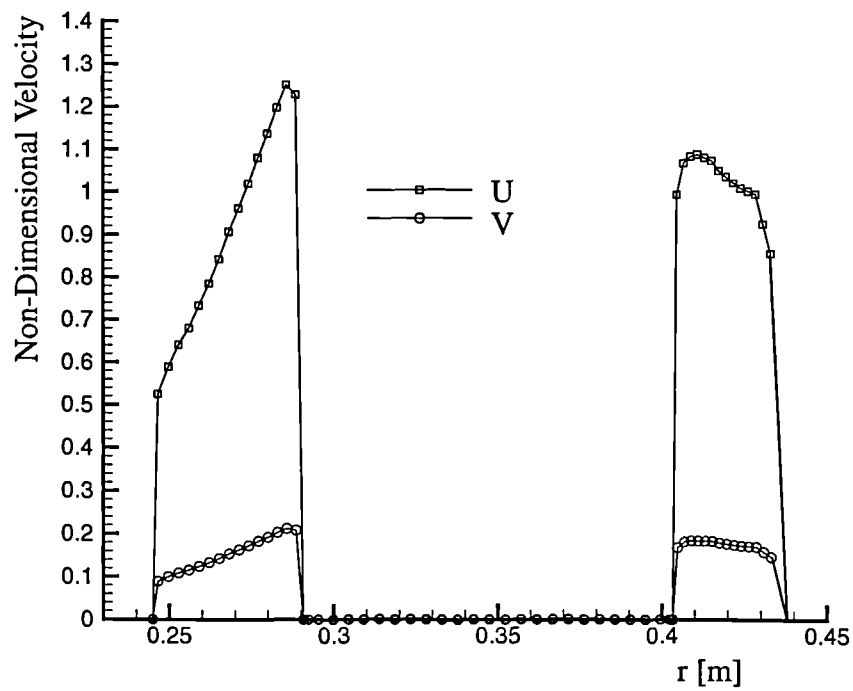
(a) Annulii Inlet Velocity Profiles
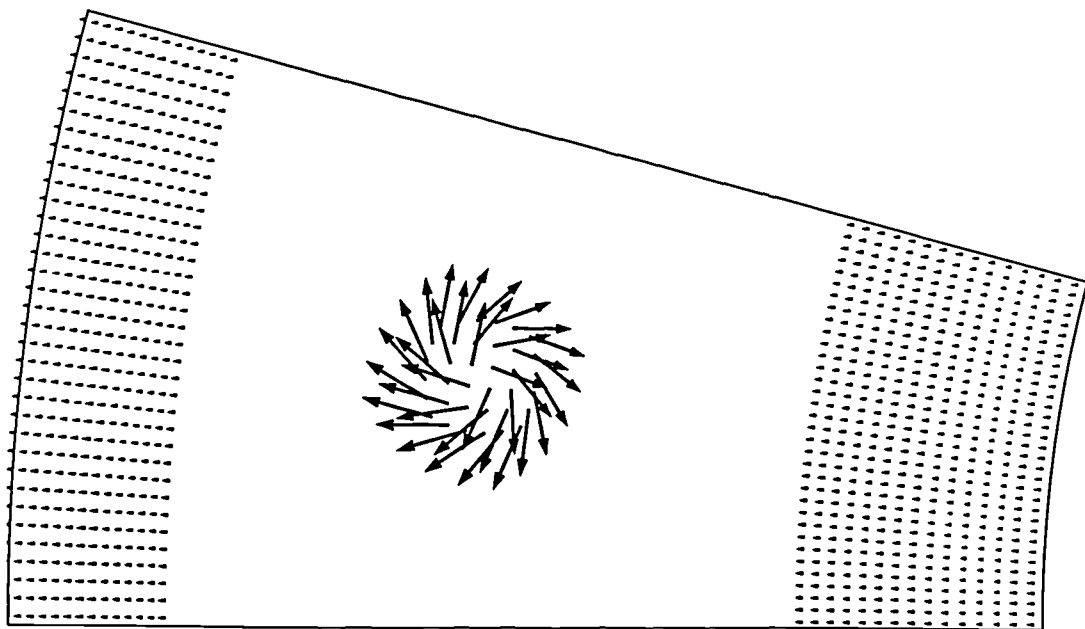
(b) Air-Swirler Representation

Figure 6.52 Combustor Sector Inlet Velocity Definitions

(a) Plain Ports

(b) Chuted Ports
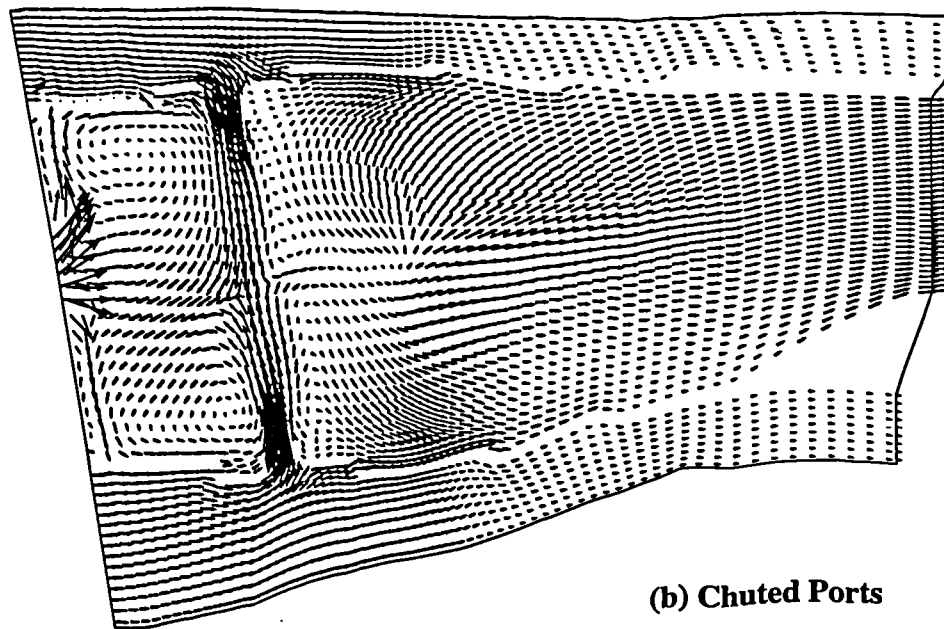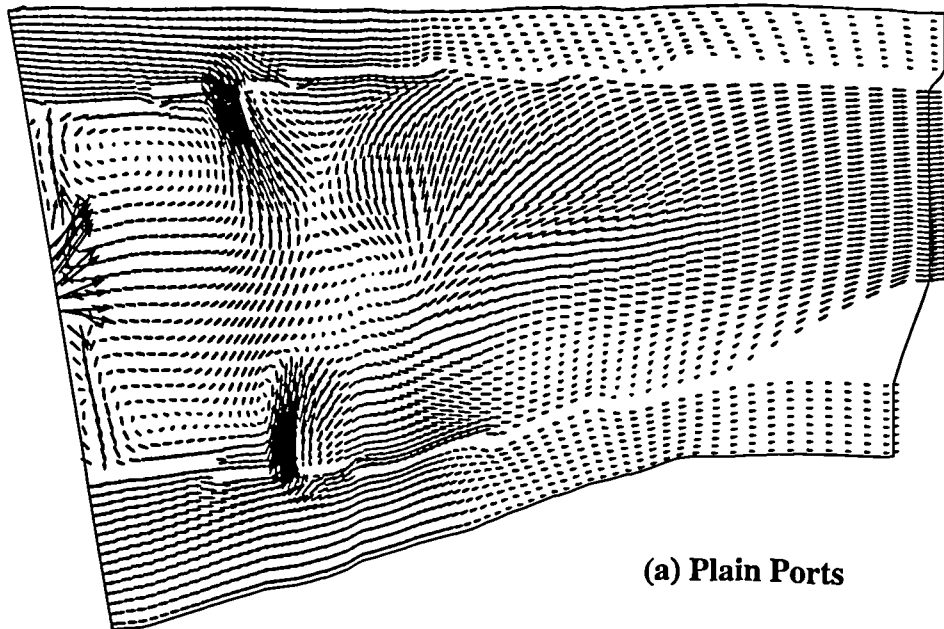
Figure 6.53 Velocity Vectors on Plane Through Air-Swirler Centre-Line

(a) Plain Ports

(b) Chuted Ports
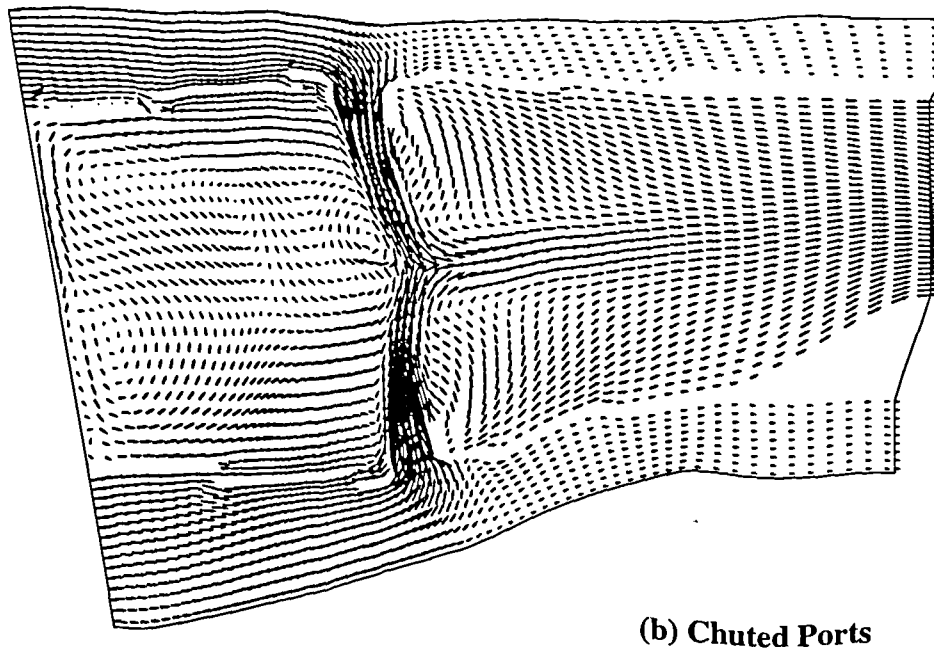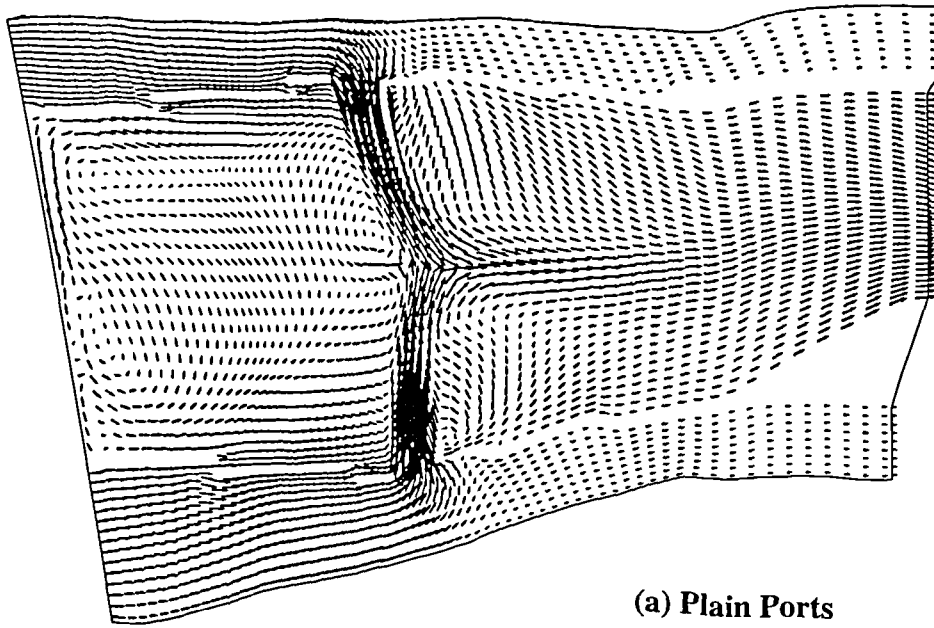
Figure 6.54 Velocity Vectors on Plane Through Secondary Port Centre-Lines

$$k \ [m^2/s^2]$$

(a) Plain Ports

$$k \ [m^2/s^2]$$

(b) Chuted Ports
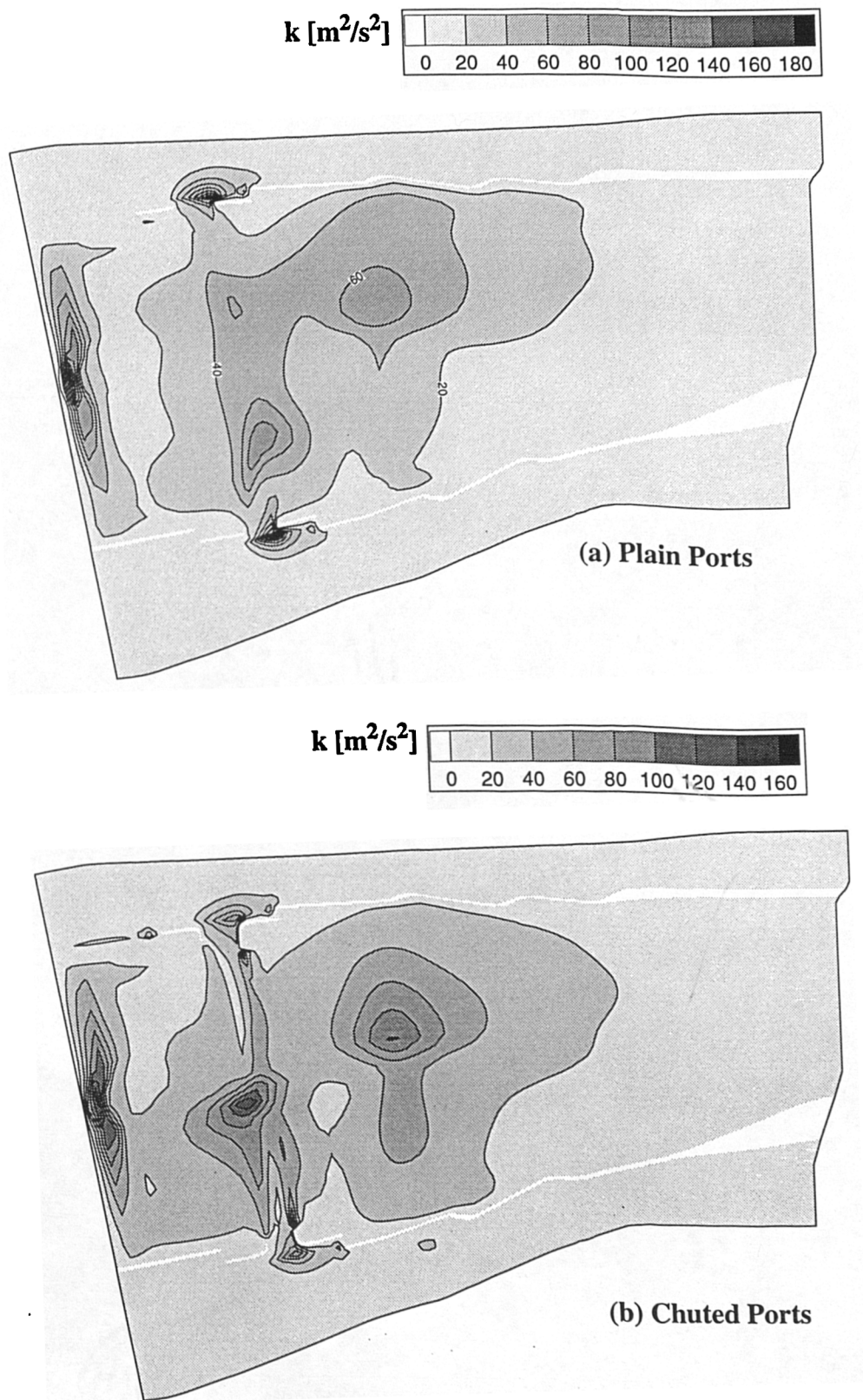
Figure 6.55 Turbulent Kinetic Energy Distribution on Plane Through Air-Swirler

(a) Plain Ports

(b) Chuted Ports
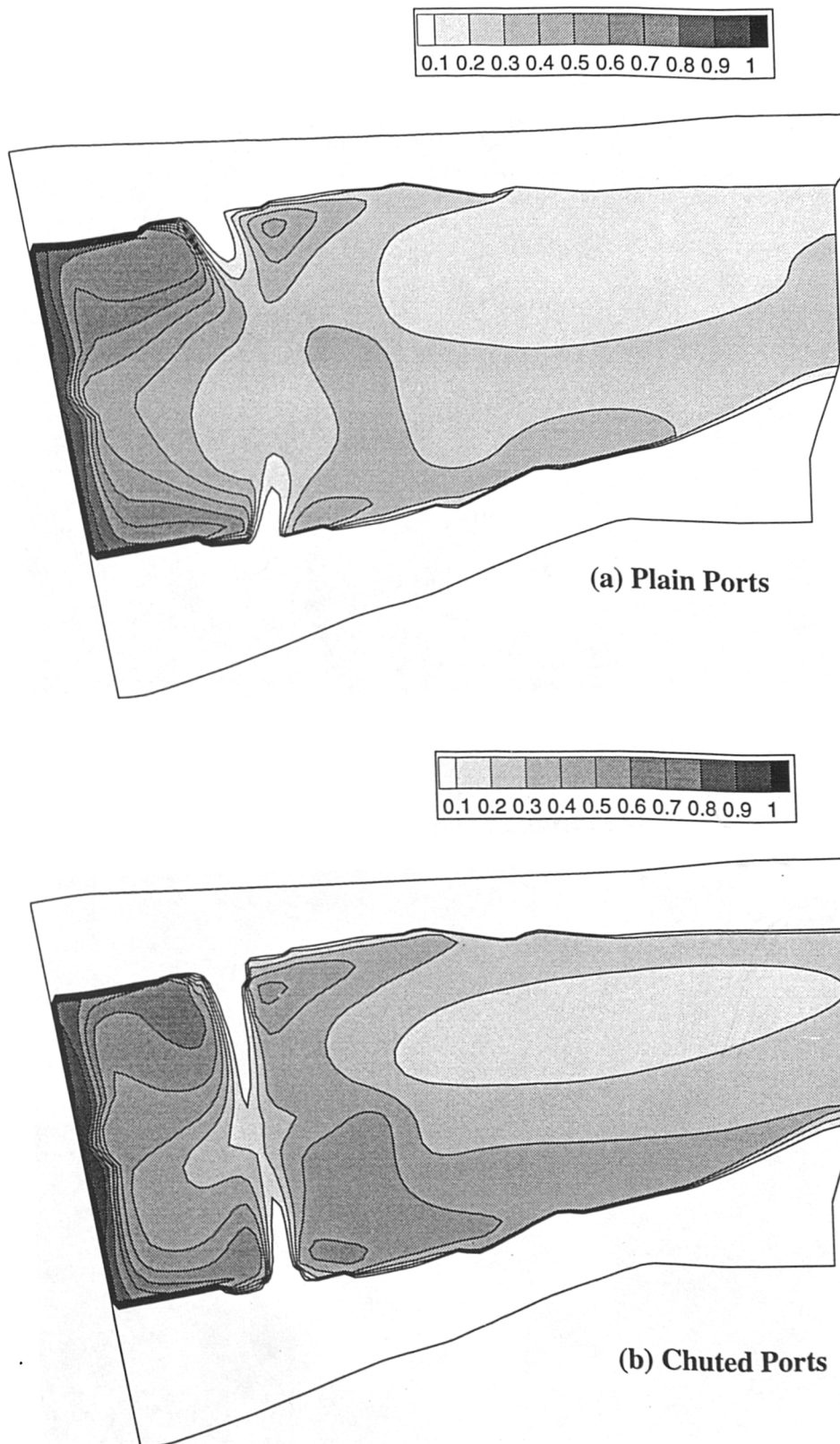
Figure 6.56 Concentration on Plane Through Air-Swirler Centre-Line

(a) Plain Ports

(b) Chuted Ports
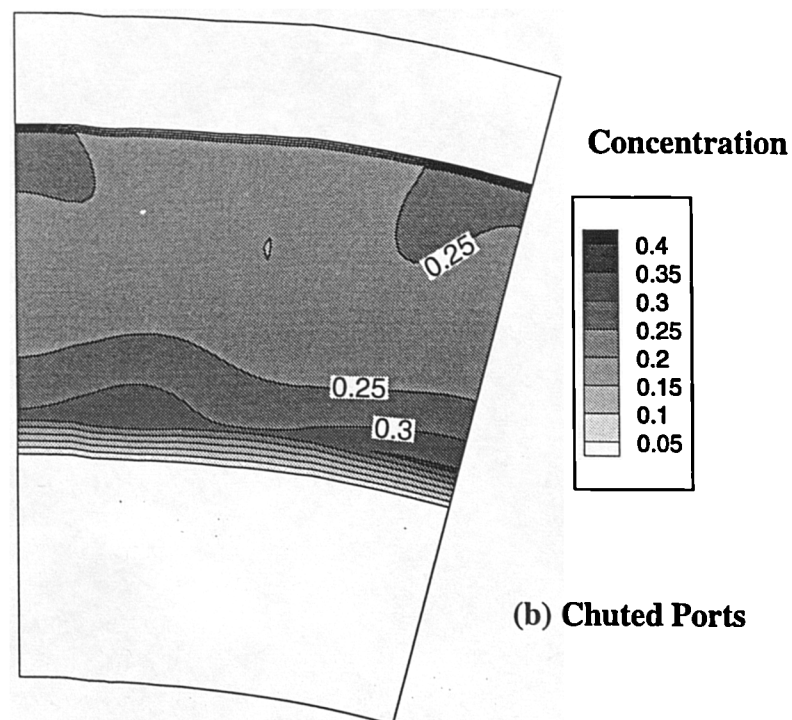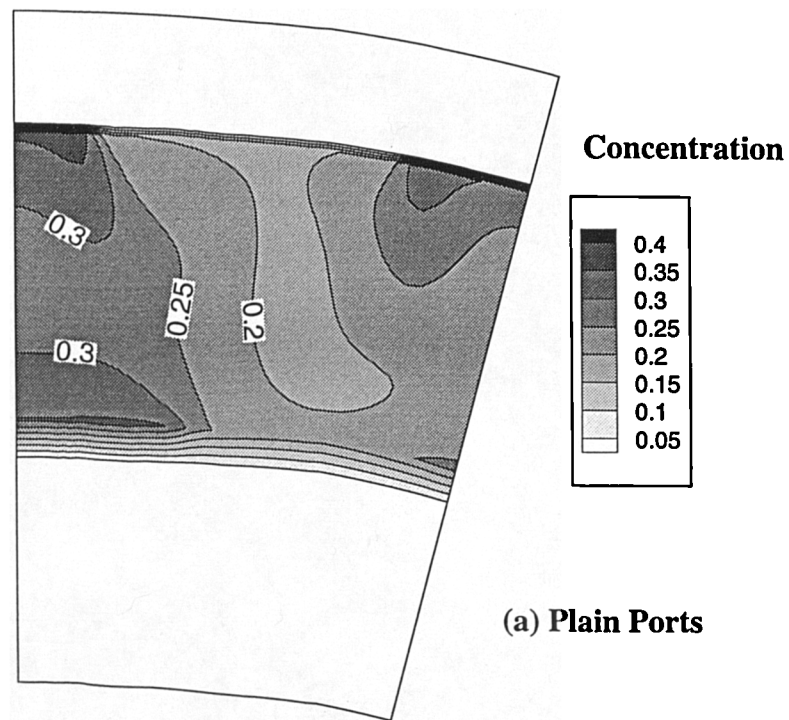
Figure 6.57 Concentration on Combustor Exit Plane

Chapter 7

Conclusions

7.1 Conclusions

A combined experimental-computational study has been carried out on the flows associated with gas turbine combustor air-admission ports. The experimental work was conducted using a water analogy rig built with perspex to allow LDA instrumentation to map the flow field. The CFD approach solved the Reynolds-Averaged Navier-Stokes equations using a k-ε closure for the turbulence model. A non-orthogonal implementation of this allowed meshes to be fitted to the port shapes considered. With the thread of each approach following common ground, the conclusions drawn from each will be discussed together.

The overall aim of this study has been to improve modelling techniques which are used to both; a) determine the flow splits between the various ports of a combustor and b) define the characteristics of the jets issuing from those ports to use as boundary conditions for internal combustor CFD predictions. It is in this context in which the conclusions will be discussed.

Coupling of the combustor internal/external flow fields has allowed flow splits and jet characteristics to be predicted implicitly within a solution domain. For single port calculations the flow split is trivial since the port mass flow rate will be fixed by the boundary conditions. Successfulness of the prediction of jet characteristics was found to depend on several factors;

* flow conditions: The predicted velocity field issuing from a port with primary port like flow conditions was predicted comparatively better than that for the dilution port-like flow condition.

* port resolution: It was apparent that test cases with comparatively low resolution predicted the effects of including port chutes, whilst at higher resolution port characteristics appeared relatively insensitive to changes in port shape.

* port geometry: Compared to the effects of flow conditions port geometry had little effect on the predicted discharge coefficients. At low mesh densities C_d for plain circular and D-shaped ports was over-predicted to be similar to the well predicted C_d of the chuted port. At higher mesh densities C_d of the plain and D-shaped ports was well predicted, but the chuted port C_d was under-predicted.

On the whole port exit velocity distribution was well predicted over the rear half of the ports, but the separation of the flow from the upstream inlet edge of the port was poorly resolved. This led to a smearing of the high velocity gradients found

experimentally in this region. Despite this, the exit angle of the flow from the port was well predicted over most of the port. It also has to be remembered what the alternative to these predicted jet characteristics is. For example, using results from the predictions reported here, would be more representative of a jet characteristics than a uniform, mass-averaged velocity being applied over the port for subsequent, internal only, calculations.

The k-ε model used was found to be quite poor at predicting the turbulence levels within the core, being quite badly under-predicted, though on the whole the resultant core velocity fields agreed well with experimentation.

The feed annulus flow and port flows were generally well predicted, except in the upstream region of the port as mentioned. Experimental and computational evidence was found to suggest that there are three distinct flow modes which may occur within the feed annulus. The mode will depend upon the bleed ratio past the port as well as geometrical considerations. At low bleed ratios it was found experimentally that flow structures occurred which resulted in an intermittent formation of through-port vortices. No evidence was found that this was accompanied by a reduction in C_d. Vortex interaction between ports was also observed to result in contra rotating pairs of port vortices. Planes of symmetry were removed from one calculation and similar through-port vortices were predicted. However the interaction with neighbouring ports did not appear to be resolved, and each port vortex rotated in the same sense.

Introducing swirl into the feed annulus was found to have large effects on the internal, core, flow field. The feed annulus flow field did not appear to change radically due to swirl, but, from the perspective of the port, skewed such that the approach angle to the port changed. However, a slight deflection of the jets resulted which created an axial swirl component in the core. This had the effect of reducing the size of the upstream core recirculation. CFD predicted these trends well but no direct comparison was possible. With $15°$ of swirl a reduction in C_d of upto 8% was measured for chuted ports. This effect is not catered for by any combustor design procedures and warrants investigation beyond that here, particularly if swirl is thought ever to be present at compressor exit.

A final prediction for an actual combustor demonstrated that the methods developed in this thesis can have quite significant effects on the internal flow field. The inclusion of chutes at port exit was seen to radically change the primary port characteristics, for example, which without chutes did not impinge, but with chutes did impinge. The cumulative effect was demonstrated to have a significant consequence on the exit temperature pattern.

7.2 Further Work

In isolating one portion of combustor aerodynamics to produce a simplified flow problem a surprising number of areas in which useful work could be done to further our understanding have presented themselves.

Experimentally, flow unsteadiness provides perhaps the biggest scope for work of a fundamental nature. By using two lasers it would be worthwhile performing cross-correlations of velocity fluctuations to see if the unsteady character of the annulus at low bleed ratios in any way dictate the nature of core unsteadiness. The character of the through port vortices and their origins would help in how to truly design away from such undesirables. Much of this work is suitable for final year undergraduate projects now that the facility is built and experimental techniques have been developed. Naturally it would also be possible to test a larger range of port geometries, and possible flow control devices to examine or develop their desired effects. PIV could be utilised, which may also be able to shed some light on the origin of the flow unsteadiness. An example of results from a demonstration of PIV on the experimental facility is given as a taster in figure 7.1. Clear similarities between this (uncalibrated) image and those predicted and measured above port exit can be seen.

The partial success of coupling the internal/external fields has shown more development is required before calculations of complete combustors can be performed. However the information on jet characteristics obtained from such an approach may complement current 1D annulus flow prediction methods in providing additional information for the boundary conditions for the internal calculation.

Computational effort could perhaps be put to best use developing embedded techniques for locally resolving port details within solution domains that do not require the same mesh density as the port and resulting jet. This may produce the most useful step toward increasing the accuracy of coupled annulus/core calculations. More complex methods of resolving the port may also provide useful such as adaptive grid or multi-grid methods. Poor predictions of the core flow may well be improved by using a Reynolds-Stress turbulence closure, and this would warrant further investigation. The benefit of moving to this extra level of complication may not be great for the annulus flow field, which was reasonably well predicted.

Time dependent calculations or even LES studies would be useful in uncovering the nature of the core flow unsteadiness, seen as bi-modal behaviour. LES may also be able to show how the through port vortices are formed, for which PIV could provide suitable validation.
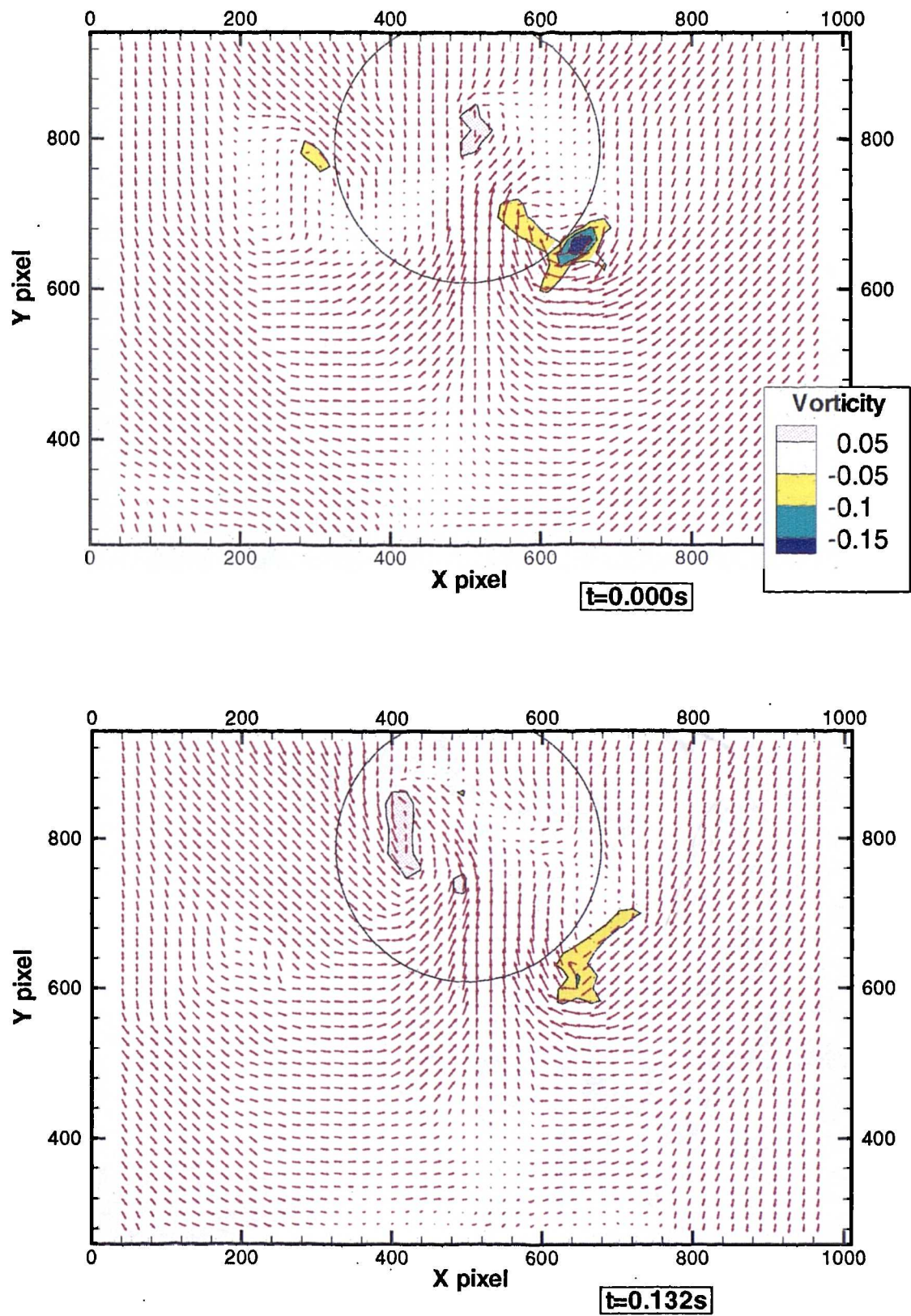
Figure 7.1 Demonstration of PIV Applied to Annulus/Port Flow

References

Adkins,   R.C. and Gueroui, D. (1986) "An Improved Method For Accurate
             Prediction Of Mass Flows Through Combustor Liner Holes."
             ASME Paper 86-GT-149.

Anreopoulos, J. and Rodi, M. (1984) "Experimental investigation of Jets in Cross-
             Flow."
             J. Fluid mech., Vol. 138, pp.97-127.

Baker,   S. and McGuirk, J.J. (1992) "Multi-Jet Annulus/Core-Flow Mixing -
             Experiments and Calculations."
             ASME Paper 92-GT-111.

Baker,   S. J. (1992b) "Combined Combustor/Annulus Flows : Isothermal
             Experiments and Predictions"
             Ph.D. Thesis, Imperial College of Science.

Bevington,   P. R. and Robinson, D. K. (1992) "Data Reduction and Error Analysis
             for the Physical Sciences"
             McGraw-Hill

Bicen,   A.F. (1981) "Refraction Correction For LDA Measurments in Flows
             With Curved Optical Boundaries."
             Imperial College, Fluids Section, FS/81/17.

Bicen,   A.F., McGuirk, J.J. and Palma, J.M.L.M. (1989) "Modelling Gas
             Turbine Combustor Flow Fields In Isothermal Flow Experiments."
             Proc. Instn. Mech. Engnrs. Vol.203, pp. 113-122.

Boadway,   J.D. and Karahan, E. (1981) "Correction of Laser Doppler Anemometer
             Readings for Refraction at Cylindrical Interfaces."
             DISA Information, No. 26, pp. 4-6.

Boussinesq, J. (1877) "Essai sur la Theorie des Eaux Courantes."
             Mem. Pres. Acad. Sci. 23, pp. 1-680..

Bradshaw,   P. (1973) "Effects of Streamline Curvature on Turbulent Flow."
             AGARDograph No. 169.

Brocklehurst, H. (1994) "Fuel Injector Definition for the Phase Five Combustor."
             Rolls-Royce plc. Report CRR 90209.

Boyce,   R. (1995) *Private Communication.*

Carrotte,   J.F. and Stevens, S.J. (1990) "The influence Of Dilution Hole Geometry
             on Jet Mixing."
             J. of Eng. for Gas Turbines and Power, Vol, 112, pp. 73-79.

Carrotte,   J.F. (1990b) "An Experimental Investigation Into The Mixing Of
             Dilution Jets."
             Ph.D. Thesis, Loughborough University of Technology.

Carrotte,   J.F. (1994) *Private Communication.*

Carrotte,   J.F. (1995) "Detailed Measurements on a Modern Combustor Dump-
             Diffuser System."
             J. of Eng. for Gas Turbines and Power, Vol, 117, pp. 678-685.

Castro,   I.P. and Jones, J.M. (1987) "Studies In Numerical Computations Of
             Recirculating Flows."
             Int. J. For Numerical Methods in Fluids, Vol. 7, pp. 793-823.

Close,   D. (1991) "Discharge Coefficients of Plain and Plunged Holes - Data
             Analysis."
             Rolls-Royce Report CRR00340.

Coupland,   J. and Priddin, C.H. (1986) "Modelling the Flow and Combustion In A
             Production Gas Turbine Combustor."
             Turbulent Shear Flows 5. Ed. F. Durst et al. Springer Verlag, 1986.

Daly,   J. (1994) "Annulus/Port Flows" Final Year Project Report.
             Dept. Transport Technology, Loughborough University of Technology.

Denman,   P.A., Carrotte, J.F. and Wray, A.P., (1992) "Phase 5 DIffuser Research -
             Performance Comparison of a Dump and Short Faired Diffuser System"
             Dept. AAETS report TT92R02, Loughborough University.

Doerr,   Th., Blomeyer, M. and Hennecke, (1995) "Optimization of Multiple
             Jets Mixing With a Confined Crossflow."
             ASME Paper 95-GT-313.

Durst,   F., Melling, A. and Whitelaw, J.H. (1976) "Principles and Practice of
             Laser Doppler Anemometry."
             Academic Press.

Durst,   F. and Tropea, C. (1984) "Advanced Laser Doppler Anemometry."
             UMIST Course Notes.

Eccles,   N.C. and Manners, A.P. (1997) "Structured Grid Generation Using a
             CAD Solid Model for an Aero-Gas Turbine Combustion System"
             Numerical Grid Generation, 1997.

General Electric, (1996) "New Product Information - Low Emission Combustor"
             Internet page: http://www.ge.com/geae/services/npi.htm

Hay,   N. and Spencer, A. (1992) "Discharge Coefficients Of Cooling Holes
             With Radiused and Chamfered Inlets."
             J. of Turbomachinery Vol. 114 pp. 701-706.

Huang,   Z., Low, M.S., Kawall, J.G. and Keffer, J.F. (1991) "Structural Features
             Of A Heated Round Jet In Cross-Flow."
             Proc. 8th Symposium On Turbulent Shear Flows. Paper No. 25-1.

References

Ikeda,   Y. and Nakajima, T. (1993) "Calculation of Confined Swirl Flow with Interferential Cross Jets."
9th Symposium On Turbulent Shear Flows. Paper No. 6-2.

Jones,   W.P., Sodha, M.N. and McGuirk J.J. (1989) "Calculation of The Flow in a Sector of An Annular Combustor."
Proc. Instn. Mech. Engnrs. Vol. 203, pp. 187-193.

Jones,   W.P. (1980) "Models For Turbulent Flows With Variable Density and Combustion."
Prediction Methods for Turbulent Flows, ed. W. Kollman, Hemisphere.

Jones,   W.P. and Launder, B.E. (1973) "Prediction of Low Reynolds Number Phenomena With A two Equation model Of Turbulence."
Int. J. Heat and Mass Transfer, 16, p1189.

Karki,   K.C., Oechsle, V.L. and Mongia, H.C. (1990) "A Computational Procedure For Diffuser-Combustor Flow Interaction Analysis."
ASME Paper 90-GT-35.

Koutmos,   P. and McGuirk, J.J. (1989) "Isothermal Modeling of Gas Turbine Combustors: Computational Study."
J. Propulsion Vol. 7, No. 6.

Launder,   B. E. and Spalding, D.B. (1974) "The Numerical Computation of Turbulent Flows"
Computer Methods in Applied Mech. and Eng., Vol. 3, pp.269-289.

Launder,   B. E. (1992) "An Introduction to the Modelling of Turbulence"
Turbulence Modelling for CFD Applications, UMIST short course.

Lefebvre, A.H. (1983) "Gas Turbine Combustion."
McGraw-Hill, New York.

Lefebvre, A.H. (1995) "The Role of Fuel Preparation in Low-Emission Combustion."
Jnl. of Eng. for Gas Turbines and Power, vol. 117, pp.617-654.

Leonard,   B.P. (1979) "A Stable and Accurate Convective Modelling Procedure Based Upon Quadratic Upstream Interpolation."
Comp. Meth. Appl. Mech. Eng., Vol. 19 pp. 59-98.

Lin,   C.A. and Lu, C.M. (1993) "Modeling Three-Dimensional Gas-Turbine Combustor Model Flow Using Second-Moment Closure"
AIAA Jnl., vol. 32, No.7, pp. 1416-1422.

Little,   A.R. and Manners, A.P. (1993) "Predictions of the Pressure Losses in 2D and 3D Model Dump Diffusers."
ASME Paper 93-GT-184.

Lowe,   D.R. (1994) "A Review of Airflow Correlations..."
Rolls-Royce Report, DNS 13297.

Manners,   A.P. (1992) "Computational Fluid Dynamics"
             Course notes, Dept. AAETS, Loughborough University.

Manners,   A.P. (1988) "The Calculation Of The Flows In Gas Turbine combustion
             Systems."
             Ph.D. Thesis, University of London.

Manners,   A.P. (1987) "The Calculation of The Flow Through Primary and
             ·Dilution Holes."
             Rolls-Royce report CRR00290.

Margason,   R. J. (1993) "Fifty Years of Jet in Cross Flow Research"
             AGARD-CP-534, pp. 1-1 to 1-41.

McGuirk,   J.J. and Palma, J.M.L.M. (1992) "Calculations of The Dilution System
             in an Annular Gas Turbine Combustor."
             AIAA Journal Vol. 30, No. 4.

McGuirk,   J.J. and Spencer, A. (1993) "CFD Modeling Of Annulus/Port Flows."
             ASME Paper 93-GT-185.

McGuirk,   J.J. and Spencer, A. (1995) "Computational Methods For Modelling
             Port Flows In Gas-Turbine Combustors."
             ASME Paper 95-GT-414.

Merdjani,   S. (1989) "Study Of Jet Mixing In An Isothermal Model Of A Gas
             Turbine Combustor Zone."
             PhD Thesis, Univ. of Leeds 1989.

Patankar,   S.V. and Spalding, D.B. (1972) "A Calculation Procedeur for Heat,
             Mass and Momentum Transfer in Three-Dimensional Parabolic Flows."
      ↳   *Int. J. Heat and Mass Transfer, 15, p1787.*

Patankar,   S.V. (1980) "Numerical Heat transfer and Fluid Flow."
             Hemisphere.

Platten,   J.L. and Keffer, J.F. (1971) "Deflected Turbulent Jet Flows"
             Trans. ASME, Jnl. of Applied Mechanics, Vol.38.

Press,   W.H, Teukolsky, S.A., Vetterling, W.T. and Flannery, B.P., (1992)
             "Numerical Recipies in FORTRAN The Art of Scientific Computing."
             Cambridge University Press, 2nd Ed.

Priddin,   C.H., (1995) *Private Communication.*

Quick,   J.W., Gartshore, I.S. and Salcudean, M. (1993) "The Interaction of
             Opposing Jets."
             Proc. 9th Symposium On Turbulent Shear Flows. Paper No. 6-4.

Ramsey,   J.W. and Goldstein, R.J., (1971) "Interaction of a Heated Jet with a
             Deflecting Stream"
             Trans. ASME, Jnl. of Heat Transfer, Vol. 93.

References

Rhie,   C.M. and Chow, W.L. (1982) "A Numerical Study of The Turbulent
             Flow Past an Isolated Airfoil."
             AIAA-82-0998.

Soni,   B.K., McClure, M.D. and Mastin, C.W. (1986) "Geometry/Grid
             Generation In N+1 Easy Steps."
             Numerical Grid Generation, Pineridge Press, pp. 83-94.

Stull,   F.D., Craig, R. R., Streby, G. D. and Vanka, S.P., 1985, "Investigation of
             a Dual Inlet Side Dump Combustor."
             Journal of Propulsion and Power, Vol 1, No. 1, Jan., pp. 83-88.

Shyy,   W., Braaten, M.E. and Burrus, D.L. (1988) "Study of Three-
             Dimensional Gas Turbine Combustor Flows."
             Int. J. Heat Mass Transfer Vol. 32, No. 6.

Shyy,   W., Braaten, M.E. and Sober, J.S. (1987) "A Three-Dimensional Grid
             Generation Method For Gas Turbine Combustor Flow Computations."
             AIAA Paper No. AIAA-87-0204.

Sivasgaram, S. and Whitelaw, J.H. (1986) "Flow Characteristics Of Opposing Rows
             Of Jets In a Confined Space."
             Proc. Instn. Mech. Engnrs. Vol. 200, pp. 71-75.

Srinivasan, R., Berenfeld, A. and Mongia, H.C., (1983) "Dilution Jet Mixing
             Program Phase I Report."
             NASA CR-168031, Nov.

Srinivasan, R., Coleman, E. and Johnson, K., (1984) "Dilution Jet Mixing Program
             Phase II Report."
             NASA CR-174624, June.

Srinivasan, R., Myers, G., Coleman, E. and White, C., (1985) "Dilution Jet Mixing
             Program Phase III Report."
             NASA CR-174884, Sep.

Tennekes,   H. and Lumley, J.L., (1974) "A First Course in Turbulence."
             The MIT Press.

Thomas,   P.D. and Middlecoff, (1982) "Numerical Generation of Composite
             Three-Dimensional Grids by Quasilinear Elliptic Systems"
             Numerical Grid Generation, Elsevier/North Holland, New York.

Thompson,   J.F. Warsi, Z.U.A. and Mastin, C.W. (1985) "Numerical grid
             Generation: Foundations and Applications."
             New York; Oxford: North-Holland.

Turner,   J. T., (1990) "Application of LDA in Liquid Flows"
             LDA Short Course Lecture Notes, UMIST

Warsi,   Z.U.A. and Tiarn, W.N. (1986) "Surface Mesh Generation Using Elliptic Equations."
Numerical Grid Generation, Pineridge Press, pp. 95-110..

Wittig,   S., Kim, S., Jakoby, R. and Weissart, I. (1994) "Experimental and Numerical Study of Orifice Discharge Coefficients in High Speed Rotating Disks"
ASME Paper 94-GT-142, 39th ASME IGTE, The Hague, Netherlands.